Behavior of jointed rock masses: numerical simulation and lab testing

To the Faculty of Geosciences, Geoengineering and Mining
of the Technische Universität Bergakademie Freiberg
approved

THESIS

to attain the academic degree of
Doctor of Engineering
Dr.-Ing.
submitted

by Dipl.-Ing. Lifu, Chang
born on June 15, 1986 in Shanxi, China

Reviewers: Prof. Dr. habil. Heinz Konietzky, Freiberg
Prof. Dr. habil. Jens Engel, Dresden
Prof. Dr. Renliang Shan, Beijing

Date of the award, 17.08.2017

Acknowledgements

I am pleased that I have spent precious four happy years at the Geotechnical Institute of TU Bergakademie Freiberg. This work would not have been be possible without the help, encouragement, friendship, and guidance of so many people, to all of whom I wish to express my sincere thanks.

I wish to express my deepest gratitude to my supervisor Professor Heinz Konietzky, Director of the Geotechnical Institute, TU Bergakademie Freiberg. I really appreciate his insight, guidance, meticulous review, understanding, enthusiasm and continuous support during my doctoral study. I will always remember his quick feedbacks and effective suggestions.

I would also like to thank the reviewing committee, Professor Jens Engel and Professor Shan for their revisions and suggestions. Hereby, I take the chance to sincerely thank my previous supervisor, Professor Renliang Shan who introduced this field to me and gave me great encouragement and help through my post-graduate studies. I also wish to thank all my colleagues at the Geotechnical Institute. In particular, I would like to thank Mrs. Angela Griebsch for her friendly help whenever needed, Dr. Martin Herbst for resolving my programing problems and for improving my writing in English, Mr. Gerd Münzberger and Dr. Thomas Frühwirt for their assistance during my laboratory work. I also want to thank Mr. Ismael, Mohamed Ahmed, and all of the Chinese colleagues for their kind support.

I would like to give special thanks to my parents, my sister, my girlfriend and other relatives for their unconditional love and support.

Finally, I also would like to thank the China Scholarship Council (CSC) and Deutscher Akademischer Austauschdienst (DAAD) for financially supporting my study in Germany.

Abstract

The anisotropic behavior of a rock mass with persistent and planar joint sets is mainly governed by the geometrical and mechanical characteristics of the joints. The aim of the study is to develop a continuum-based approach for simulation of multi jointed geomaterials. There are two available numerical techniques for the strain-stress analysis of rock masses: continuum-based methods and discontinuum based methods. Joints are simulated explicitly in discontinuous methodology. This technique provides a more accurate description for the behavior of a rock mass. However, in some projects, the explicit definition becomes impractical, especially with increasing number of joints. Besides, the calculation efficiency will be significant reduced as the number of joints increases within the model. Considering the above mentioned shortcomings of the discontinuous method, the continuum-based approach is widely used in rock mechanics. Within the continuum methods, the discontinuities are regarded as smeared cracks in an implicit manner and all the joint parameters are incorporated into the equivalent constitutive equations.

A new equivalent continuum model, called multi-joint model, is developed for jointed rock masses which may contain up to three arbitrary persistent joint sets. The Mohr-Coulomb yield criterion is used to check failure of the intact rock and the joints. The proposed model has solved the issue of multiple plasticity surfaces involved in this approach combined with multiple failure mechanisms. The multi-joint model is implemented into FLAC and is verified against the distinct element method (UDEC), analytical solutions, and experimental data. Uniaxial compression tests with artificial rock-like material (gypsum) are carried out in the laboratory in order to verify the developed constitutive model and to investigate the behavior of jointed specimen. Samples with two crossing joints covering more than 20 angle configurations and two different property sets were prepared and tested.

Simulation results are in good agreement with experimental observations. The developed model is applied to two potential practical applications: the stability analysis of a slope and a tunnel under different stress conditions. Finally, the main achievements of the whole PhD study are summarized and future research work is proposed.

Table of Contents

List of Figures

List of Tables

Notation

a	material constant related to *GSI* and Hoke's law
A_e	anisotropy parameter
b	material constant related to the rock mass
c, c_j^i $(i=1,2.3)$	cohesion and joint cohesion, respectively
C, C^I	compliance matrix for rock mass and for intact isotropic rock, respectively
C_j^i $(i = \alpha, \beta, \gamma)$	compliance matrix for joint plane i
C_{eq}	equivalent compliance matrix for rock mass
D	second-order stiffness tensor
D^{α}	disturbance factor
D_0	diameter of tunnel
D_{EP}	elasto-plastic constitutive tensor
D^T	transposed matrix of the second order stiffness tensor
E	elastic modulus
E_i $(i = 1, 2, 3)$	Young's modulus in the plane of isotropy
E'	Young's modulus in the direction normal to the plane of isotropy
E_m, E_{eq}	elastic modulus of intact rock and for the equivalent rock mass, respectively
$f^{s,i}$ $(i = 0,1, 2, 3)$	shear failure envelops for rock matrix and joint set, respectively
$f^{t,i}$ $(i = 0,1, 2, 3)$	tensile failure envelops for rock matrix and joint set, respectively
F^{trial}	strength reduction factor
F	plastic potential function
$g^{s,i}$ $(i = 0,1, 2, 3)$	shear potential functions for rock matrix and joint set, respectively
$g^{t,i}$ $(i = 0,1, 2, 3)$	tensile potential functions for rock matrix and joint set, respectively
G, G'	shear modulus of rock and for any plane normal to the plane of isotropy
G_{ij} $(i,j = 1, 2, 3)$	shear moduli in planes parallel to the local coordinate planes
h, h_1, h_2	functions to separate the failure envelope
I_1	first principal invariant of stress tensor
j_{α}^i $(i = 1, 2, 3)$	critical failure angle for joint set i
J_f	joint factor
J_2, J_3	second and third principal stress invariants

k_n, k_s	joint normal stiffness and shear stiffness
k	slope of the line relating maximum and minimum principal stress
K_i (i = 1, 2, 3)	stiffness of joint set i
κ	vertical earth pressure coefficient
L^{α}	transformation matrix for joint plane
m_i	constant related to the rock type
m_b	Hoek-Brown parameter
Q, Q_j	plastic potential function
R_σ, R_σ^T	stiffness transformation matrices
R_ε, R_ε^T	compliance transformation matrices
s	material constants related to *GSI* and rock damage
S^{α}	joint spacing for joint set α
S_i (i=1, 2, 3)	number of joints per 1 meter for joint set i
v, v'	Poisson's ratio and Poisson's ratio in different directions, respectively
α	angle between two joints
α_{min}, α_{max}	maximum and minimum failure angle, respectively
α_1, α_2	inclination angles for joint 1 and 2 measured from horizontal
α_j	critical joint angle measure from horizontal direction
β	joint inclination angle measured from vertical
β_i (i=1, 2, 3)	inclination angle of weak plane
$\Delta[n]^d$, $\Delta[n]'^d$	global and local correction components for weak plane, respectively
ζ	coefficient of correlation
ε_i (i = 1, 2, 3)	total strain for corresponding principal stress directions
ε_i^e (i = 1, 2, 3)	related elastic strain for corresponding principal stress directions
ε_j^{α}	strain increment for joint set α
ε_{pl}	plastic strain
ϕ, ϕ'	friction angle and effective friction angle of the intact rock, respectively
ϕ_j^i (i = 1, 2, 3)	friction angle for the joint set i
ϕ^{trial} , ϕ_j^{trial}	trial value for rock matrix and joint friction angle, respectively
ψ, ψ_j	dilation angle for rock matrix and joints, respectively
λ	plastic multiplier

$\lambda^{s,i}$ (i = 1, 2, 3)	plastic multiplier for joint shear failure
$\lambda^{t,i}$ (i = 1, 2, 3)	plastic multiplier for joint tensile failure
θ	inclination angle measured from horizontal
θ_j^i (i = 1, 2, 3)	joint angles which measured counterclockwise from the global x axis
ρ	density of rock
σ, σ_n, σ^t	tensile stress, normal stress and intact rock tensile strength, respectively
σ_1, σ_3,	maximum and minimum principal stresses, respectively
$\sigma_j^{t,i}$ (i = 1, 2, 3)	joint tensile strength for joint set i
σ_β	normal stress acting on the fracture plane
σ_{ci}	unconfined compressive strength of the intact rock
σ_c, σ_u	uniaxial compressive strength and uniaxial compression stress
$\sigma_{ia,}$	compressive strength of the intact samples under confining pressure
σ_{ja}	compressive strength of jointed sample under confining pressures
$\sigma_{ij,}$ σ'_{ij} (i= 1, 2, 3)	global and local stress components, respectively
$\sigma'^{s,i}$	local stress correction components on the joint plane
σ_i^{trial}	trial elastic stress
σ_i^N *(i = 1, 2, 3)*	new stress state components
σ_i^O *(i = 1, 2, 3)*	old stress state components
τ, τ', $\tau_j^{i\prime}$	shear stress components in the global and local coordinates, respectively

1 Introduction

1.1 Object and scope

The stability and safety of civil engineering or mining structures have a profound relation to the strength and failure patterns of rock masses. Rock masses are characterized by discontinuities of quite different scale ranging from a few millimeters to several kilometers. Such discontinuities have a remarkable influence on the anisotropy of rock masses including deformability, permeability and strength. Jointed rock masses generally exhibit reduced stiffness, higher permeability and lower strength compared to intact rock. Various analytical, numerical and empirical methods are suggested in order to take into account the influence of discontinuities on the mechanical behavior of rock masses. With the ongoing development of computer based simulation techniques, more sophisticated models have been developed in recent years and it is possible to incorporate more aspects of rock mass behavior into the simulations.

In this thesis, a new equivalent continuum constitutive model named multi-joint model is formulated and implemented into FLAC for the stress-strain analysis of jointed rock masses. This model is suited for rock masses containing up to three arbitrary orientations of joints and spatial distribution. The equivalent compliance matrix of the rock mass is established and the Mohr-Coulomb yield criterion is used to check the failure characteristics of the intact rock and the joints. A series of uniaxial compressive tests on special artificial rock-like materials (gypsum) are carried out to study the strength anisotropy and the failure pattern of jointed specimens. Three sample categories containing more than 20 joint angle configurations were prepared and tested. Lab test results are compared with continuum and discontinuum based numerical simulations as well as analytical solutions to verify the developed constitutive model. Additionally, the term "joints" in this thesis represents all the discontinuities in rocks such as bedding, faults and fractures.

1.2 Research strategy and structure of thesis

The research strategy underlying this thesis is illustrated in Figure 1.1. Objective of research and literature review are included in chapter 1 and 2, respectively. Constitutive relationship for equivalent continuum multi-joint model is presented in chapter 3, which contains equivalent continuum compliance matrix for the proposed model and multi surface plasticity as well as the coordinate transformation between the local and global system and the plastic corrections of the intact rock and joint sets. Lab testing and numerical simulations for multi-jointed samples are studied in chapter 4 and 5. There, results of the uniaxial compression strength (UCS) tests and the corresponding failure types of tested lab samples are presented. Also, numerical simulation results and analytical solutions for these experiments are given for comparison. Two practical applications based on the developed simulation approach are documented in chapter 6. Finally, a summary of the thesis and an outlook are given in chapter 7.

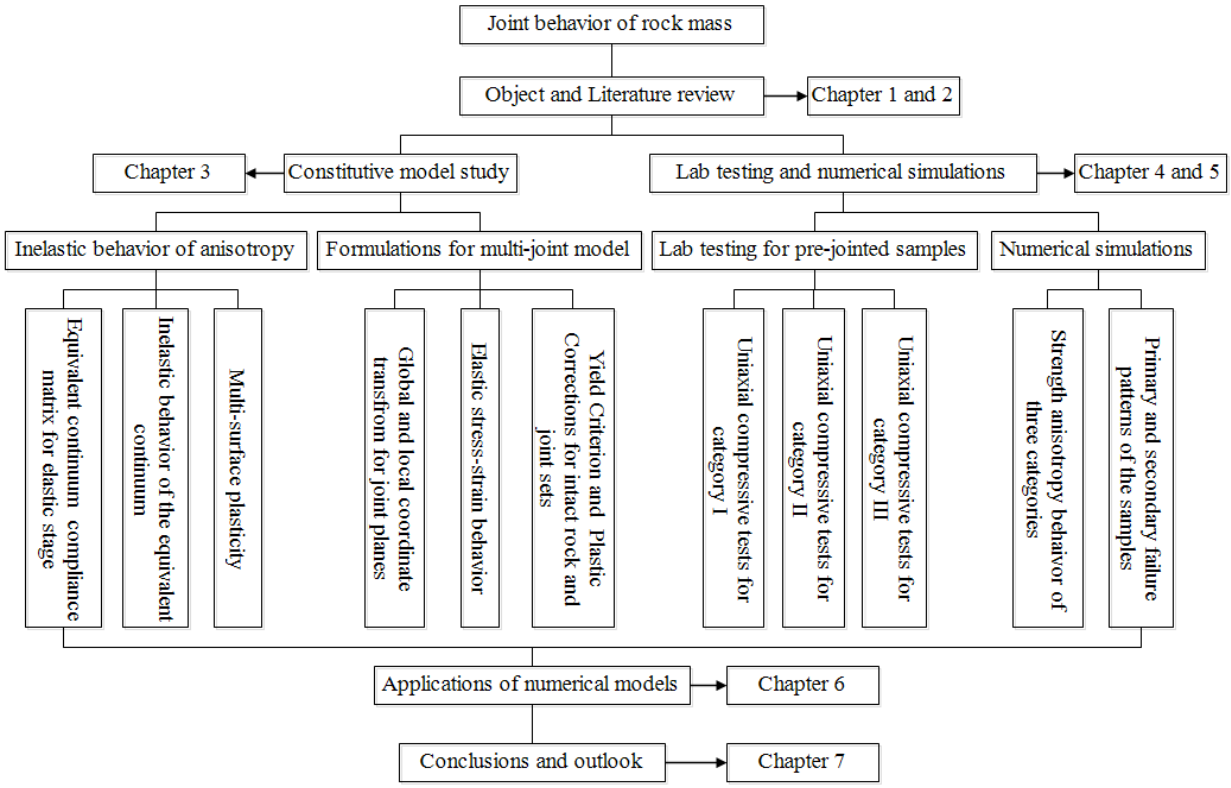

Figure 1.1 Research strategy and structure of thesis

2 State of the art

2.1 Overview

Rock is defined as a naturally occurring solid which consist of at least one mineral component. There are three general classes of rocks: igneous, sedimentary, and metamorphic. Through the extensive studies of the behavior of rocks since the 1960's, it was found that most rocks behave anisotropic. Intact rocks with discontinuities at different scale, ranging from several millimeters to hundreds of meters, form a rock mass. Both, micro- and macro-scale discontinuities are generated during the processes of rock formation. There are two kinds of micro-scale cracks. One type of micro features is produced during the formation of rocks. They are related to the grain size and have a natural orientation. The other type of micro-scale discontinuities is caused by either tectonic or construction disturbances. They are commonly regarded as disordered and randomly distributed.

Most foliated metamorphic rocks, such as schists, slates or gneisses, contain a natural orientation of their flat/long minerals or a banding phenomenon which results in anisotropy in their mechanical properties (Bagheripour et al. 2011). Figure 2.1a shows textural anisotropy in form of layering and intersection of planar fabric structures in a metamorphic slate.

(a) (b)

Figure 2.1 Typical geological features of metamorphic and sedimentary rocks: (a) textural anisotropy of a slate, (b) sample of stratified sedimentary: shale bedding

One of the special geological features of sedimentary rocks is the stratification. Rocks like sandstone, shale or sandstone-shale alterations are often characterized by the presence of bedding planes. Figure 2.1b shows bedding in a shale. Igneous rocks such as volcanic foam or vesicular basalt have micro-scale bubbles which are usually stochastically distributed. Generally, igneous rocks show no remarkable fabric anisotropy. Some metamorphic rocks have inherent anisotropy due to the formation process and the corresponding constituent minerals such as slates, gneisses or schists. A set of parallel weak planes, i.e. the foliations and schistosity-planes, control strength of the rocks. In addition to the bedding, some sedimentary rocks have joints and faults. These weak discontinuities affect the strength behavior of rocks. These two corresponding types of anisotropy are illustrated in Figure 2.2: inherent plane anisotropy, e.g. bedding and induced plane anisotropy, e.g. fracture.

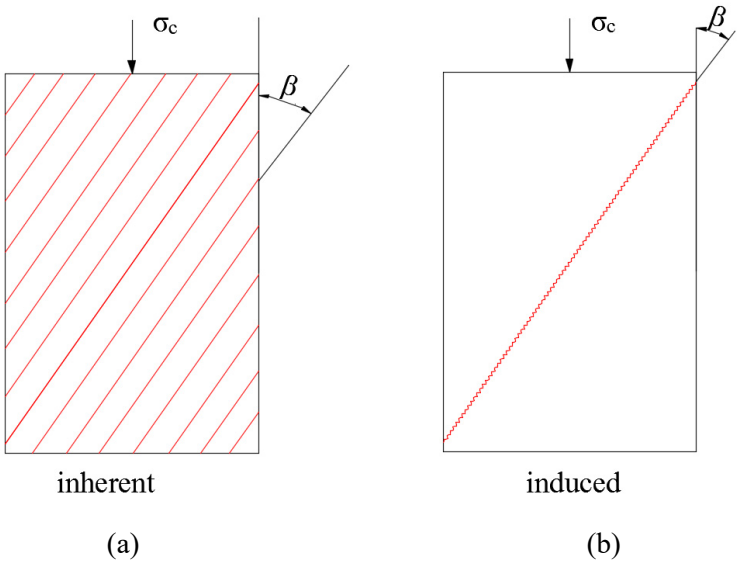

Figure 2.2 Inherent and induced anisotropy

Macro-scale discontinuities are formed during geological or tectonic activities. Such features are defined as (i) cracks and fractures, (ii) bedding planes and (iii) shear planes and faults (Salager 2013). The macro-scale discontinuities have a profound influence on the mechanical properties of rock masses such as deformability, permeability and strength.

Rock properties are affected by macro- and micro-scale discontinuities in the following way: (1) nonlinear deformation characteristics and reduced stiffness, (2) reduced strength, (3) anisotropic behavior, especially if rock mass is characterized by different joint sets. Because of the nature of

geological discontinuities, the rock mass behavior is very different from that of intact rock. Jointed rock masses generally exhibit lower stiffness, higher permeability and lower strength compared to intact rock (Alireza 2013). The importance and the role of discontinuities in a rock mass has been realized by geo-engineers and is still an active research topic. Different methods like analytical solutions, empirical methods, numerical simulations, lab testing and in-situ (large scale) testing, back-analysis of failure modes and rock mass classifications are used to study the influence of discontinuities on the mechanical behavior of rock masses.

2.2 Theoretical research background

The rock mass deformation behavior and the mathematical description of the failure processes are very complex. The properties of the intact rock can be acquired from lab tests, but other parameters like the length, orientation and properties of discontinuities are not easy to obtain. Rock deformation depends mainly on the elastic deformability and the strength characteristics. Deformation modulus and Poisson's ratio correspond to Hooke's law which is only valid under the assumption of an isotropic linear elastic response. Rock exhibits nearly Hook’s behavior in the elastic range.

In a real rock mass, the rock matrix is intersected by discontinuities and consequently deformations of the rock mass become anisotropic. For an anisotropic rock mass, 21 elastic constants are used to describe the rock mass deformability in general (Jaeger 2009). If symmetries exist the number of parameters can be reduced like for the isotropic model, the transversely isotropic model and the orthotropic model. These specific constitutive models are described in more detail in the following chapter.

2.2.1 Hooke's law and material symmetry

If a material is assumed to be linear-elastic and homogeneous the famous Hooke’s law can be applied. In tensor form this relation is given by (Timoshenko et al. 1970; Jaeger et al. 2007):

$$\sigma = D\varepsilon \tag{2.1}$$

where D is a second-order stiffness tensor which has 36 elastic constants. Equation (2.1) can be expanded as:

$$\begin{bmatrix} \sigma_1 \\ \sigma_2 \\ \sigma_3 \\ \sigma_4 \\ \sigma_5 \\ \sigma_6 \end{bmatrix} = \begin{bmatrix} D_{11} & D_{12} & D_{13} & D_{14} & D_{15} & D_{16} \\ D_{21} & D_{22} & D_{23} & D_{24} & D_{25} & D_{26} \\ D_{31} & D_{32} & D_{33} & D_{34} & D_{35} & D_{36} \\ D_{41} & D_{42} & D_{43} & D_{44} & D_{45} & D_{46} \\ D_{51} & D_{52} & D_{53} & D_{54} & D_{55} & D_{56} \\ D_{61} & D_{62} & D_{63} & D_{64} & D_{65} & D_{66} \end{bmatrix} \begin{bmatrix} \varepsilon_1 \\ \varepsilon_2 \\ \varepsilon_3 \\ \varepsilon_4 \\ \varepsilon_5 \\ \varepsilon_6 \end{bmatrix} \tag{2.2}$$

The stress tensor elements are $\sigma_1 = \sigma_{11}$, $\sigma_2 = \sigma_{22}$, $\sigma_3 = \sigma_{33}$, $\sigma_4 = \sigma_{23}$, $\sigma_5 = \sigma_{13}$ and $\sigma_6 = \sigma_{12}$. The components of the strain tensor are $\varepsilon_1 = \varepsilon_{11}$, $\varepsilon_2 = \varepsilon_{22}$, $\varepsilon_3 = \varepsilon_{33}$, $\varepsilon_4 = 2\varepsilon_{23}$, $\varepsilon_5 = 2\varepsilon_{13}$ and $\varepsilon_6 = 2\varepsilon_{12}$. ε_4 to ε_6 represent the shear strains. For an anisotropic rock mass without physical symmetry, 36 elastic parameters are required to establish the stiffness matrix, 21 of them are independent. If symmetries exist number of constants are reduced. In some cases, it is more convenient to use the compliance matrix. The compliance matrix C is the inverse of the stiffness matrix. The corresponding stress-strain relation can be written as:

$$\varepsilon = C\sigma \tag{2.3}$$

2.2.1.1 Orthotropic rock

An orthotropic rock has two or three mutually perpendicular planes as shows in Figure 2.3 (a). Principal coordinate axes are defined in the directions normal to those planes. The incremental strain-stress relations in the local axes can be written as follows (Lai et al. 2009):

$$\begin{bmatrix} \Delta\varepsilon_1 \\ \Delta\varepsilon_2 \\ \Delta\varepsilon_3 \\ \Delta\varepsilon_4 \\ \Delta\varepsilon_5 \\ \Delta\varepsilon_6 \end{bmatrix} = \begin{bmatrix} \frac{1}{E_1} & -\frac{\nu_{12}}{E_2} & -\frac{\nu_{13}}{E_3} & 0 & 0 & 0 \\ -\frac{\nu_{21}}{E_1} & \frac{1}{E_2} & -\frac{\nu_{23}}{E_3} & 0 & 0 & 0 \\ -\frac{\nu_{31}}{E_1} & -\frac{\nu_{32}}{E_2} & \frac{1}{E_3} & 0 & 0 & 0 \\ 0 & 0 & 0 & \frac{1}{G_{12}} & 0 & 0 \\ 0 & 0 & 0 & 0 & \frac{1}{G_{13}} & 0 \\ 0 & 0 & 0 & 0 & 0 & \frac{1}{G_{23}} \end{bmatrix} \begin{bmatrix} \Delta\sigma_1 \\ \Delta\sigma_2 \\ \Delta\sigma_3 \\ \Delta\sigma_4 \\ \Delta\sigma_5 \\ \Delta\sigma_6 \end{bmatrix} \quad (2.4)$$

This model involves nine independent elastic constants:

E_1, E_2, E_3 Young's moduli in the directions of local axes,

G_{23}, G_{13}, G_{12} Shear moduli in planes parallel to the local coordinate planes,

$\nu_{12}, \nu_{13}, \nu_{23}$ Poisson's ratio where ν_{ij} characterizes lateral contraction in local direction i' caused by loading in local direction j'.

2.2.1.2 Transversely isotropic rock

One special kind of orthotropic material is transversely isotropic material (Figure 2.3 b). Transverse isotropy is often used to describe rocks with one dominant system of layers (e.g., bedding, layering or foliation). Transversely isotropic rock takes a plane of isotropy into consideration. It has same properties in all directions perpendicular to a rotational symmetry axis, which is normal to the plane of isotropy (Jaeger 2009). This material is characterized by five independent elastic constants: E, E', ν, ν', G'. The shear modulus G can be calculated by the following equation:

$$G = E/2\,(1 + \nu) \quad (2.5)$$

The strain-stress relations are expressed as:

$$\begin{bmatrix}\varepsilon_1\\ \varepsilon_2\\ \varepsilon_3\\ \varepsilon_4\\ \varepsilon_5\\ \varepsilon_6\end{bmatrix} = \begin{bmatrix} \frac{1}{E} & -\frac{\nu}{E} & -\frac{\nu'}{E'} & 0 & 0 & 0 \\ -\frac{\nu}{E} & \frac{1}{E} & -\frac{\nu'}{E'} & 0 & 0 & 0 \\ -\frac{\nu'}{E'} & -\frac{\nu'}{E'} & \frac{1}{E'} & 0 & 0 & 0 \\ 0 & 0 & 0 & \frac{1}{G} & 0 & 0 \\ 0 & 0 & 0 & 0 & \frac{1}{G'} & 0 \\ 0 & 0 & 0 & 0 & 0 & \frac{1}{G'} \end{bmatrix} \begin{bmatrix}\sigma_1\\ \sigma_2\\ \sigma_3\\ \sigma_4\\ \sigma_5\\ \sigma_6\end{bmatrix} \tag{2.6}$$

where:

$E = E_1 = E_2$	Young's modulus in the plane of isotropy.
$E' = E_3$	Young's modulus in the direction normal to the plane of isotropy.
$v = v_{12}$	Poisson's ratio characterizes lateral contraction in the plane of isotropy when tension is applied in the plane.
$v' = v_{13} = v_{23}$	Poisson's ratio characterizes lateral contraction in the plane of isotropy when tension is applied in the direction normal to it.
$G = G_{12}$	Shear modulus for the plane of isotropy.
$G' = G_{12} = G_{23}$	Shear modulus for any plane normal to the plane of isotropy.

Transversely isotropic behavior appears at the macro scale due to the planes of weaknesses which are found in most of the metamorphic rocks such as: slates, gneisses and schists.

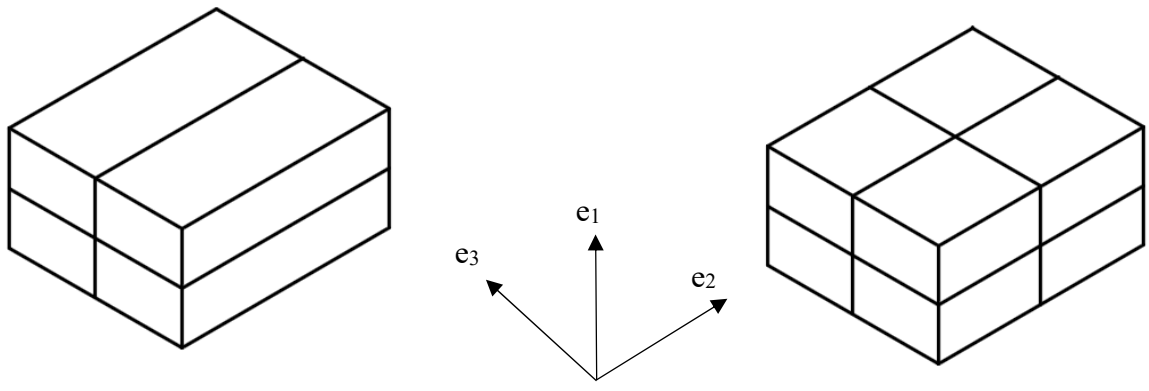

(a) orthotropic rock

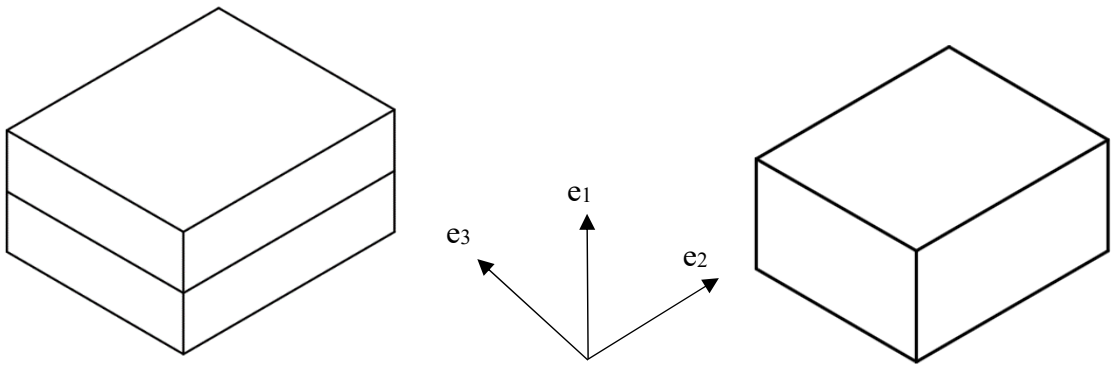

(b) transversely isotropic rock (c) isotropic rock

Figure 2.3 Different symmetries for rock masses: (a) orthotropic rock with two and three symmetry planes, (b) transversely isotropic rock, (c) isotropic rock

2.2.1.3 Isotropic rock

An isotropic rock can be considered as a special case of transversely isotropic rock. The compliance matrix of an isotropic material can be established by three elastic constants, i.e. Young's modulus, E, Poison's ratio, ν, and shear modulus G (Goodman 1989), although only two parameters are independent, because the shear modulus can be expressed by Young's modulus and Poison's ratio. The strain-stress relationship can be written as follows:

$$\begin{bmatrix} \varepsilon_1 \\ \varepsilon_2 \\ \varepsilon_3 \\ \varepsilon_4 \\ \varepsilon_5 \\ \varepsilon_6 \end{bmatrix} = \begin{bmatrix} \frac{1}{E} & -\frac{\nu}{E} & -\frac{\nu}{E} & 0 & 0 & 0 \\ -\frac{\nu}{E} & \frac{1}{E} & -\frac{\nu}{E} & 0 & 0 & 0 \\ -\frac{\nu}{E} & -\frac{\nu}{E} & \frac{1}{E} & 0 & 0 & 0 \\ 0 & 0 & 0 & \frac{1}{G} & 0 & 0 \\ 0 & 0 & 0 & 0 & \frac{1}{G} & 0 \\ 0 & 0 & 0 & 0 & 0 & \frac{1}{G} \end{bmatrix} \begin{bmatrix} \sigma_1 \\ \sigma_2 \\ \sigma_3 \\ \sigma_4 \\ \sigma_5 \\ \sigma_6 \end{bmatrix} \tag{2.7}$$

The strength and deformation behavior of jointed rock mass might be influenced by the rotation of intact blocks or slip along the joints. For such cases the strain-stress relationship of the rock mass cannot be calculated using Hooke's law but requires more sophisticated methods such as the equivalent continuum method or discontinuum methods. The next section contains a brief

comparison of these methods available for deformation and strength analysis of jointed rock masses.

2.2.2 Stress-strain analysis for jointed rock masses

The behavior of a jointed rock mass is potentially anisotropic, non-linear and stress path dependent due to the discontinuities. Experimental investigations, analytical and empirical methods have been used to develop an approach to study the influence of discontinuities on the mechanical rock mass behavior. Two numerical techniques are used: continuum-based methods and discontinuum based methods as shown in Figure 2.4.

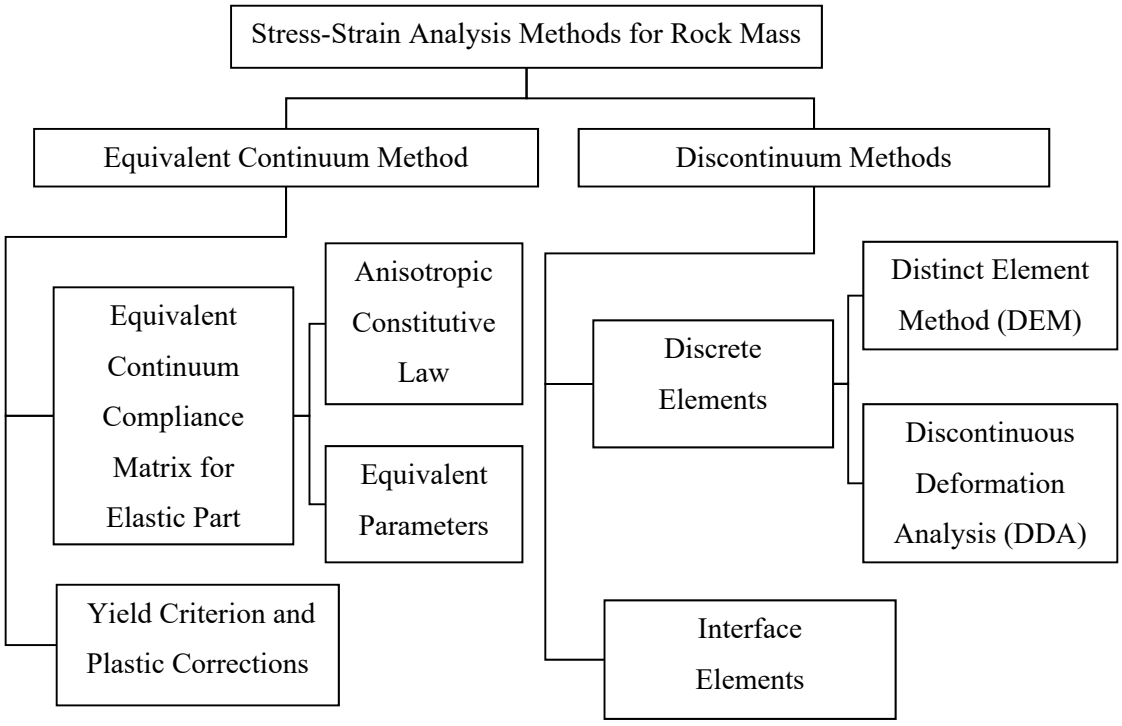

Figure 2.4 Classification of numerical approaches to simulate jointed rock masses

Discontinuum methods consider the rock mass as an assemblage of rigid or deformable blocks connected along discontinuities. In continuum methods, the discontinuities are considered as smeared cracks and all the joint parameters are incorporated into the equivalent constitutive equations.

2.2.2.1 Discontinuum-based methods

A discontinuous based approach considers the existence of contacts or interfaces between discrete bodies. Several discontinuum based methods are available for the analysis of anisotropic rock masses, such as the Distinct Element Method (DEM), the Discontinuous Deformation Analysis Method (DDA), the Finite Element or Finite Difference Method with interfaces (FEM-IF) or the Extended Finite Element Method (X-FEM). The latter two mentioned methods are only extensions of continuum methods; they do not fulfill all requirements of Discrete Element Methods.

DEM was first introduced by Cundall (1971) and developed to study the stability of rock masses. Later it has been extended towards particle based research (e.g. Walton, 1993; Ding et al. 2010; Chen et al. 2015), studies on microscopic mechanisms in granular material (Vychytil et al. 1997; Yoshida et al. 2004; Konietzky, 2017) and research on crack development in rocks and concrete (Donze et al. 2009; Scholtes et al. 2012; Chen et al. 2015). DDA was originated by Goodman and Shi (1985) and further developed by Shi (1996, 2002). This method uses series approximations to supply an increasingly complex set of strain patterns that is superimposed for each block (Itasca 2007). The primary objective of this method was to compute large displacements of discontinuous materials in rock mass structures.

In geomechanics, interfaces such as joints, faults or bedding planes are used to described planes on which sliding or separation can occur. In a Finite Element model, discontinuities are added explicitly by using joint or interface elements. The so-called "Goodman joint element" (Goodman et al. 1968) is a four node one-dimensional joint element, widely used in FEM codes and applied to many practical rock engineering problems. Examples of such type of elements include also the joint elements developed by Pande et al. (1990), Jing et al. (2003), Riahi et al. (2010); Mahabadi et al. (2012). Several expressions have been derived for two- and three-dimensional approaches and multiple joint sets. More information about these derivations can be found in Fossum (1985), Singh (2002) and Li et al. (2010).

Interface models have significant drawbacks whenever large-scale opening or sliding of the joints occur. Although in principle there is no restriction in respect to the number of interfaces or the

complexity of their intersections, usually such an approach is not suitable to model more than several simple interfaces. DEM and DDA methods have no such restrictions: old contacts can be broken and new ones can be established and contact modes can change (Riahi and Hammah 2010). DEM or DDA methods should be used instead of the interface method for more complicated situations.

2.2.2.2 Equivalent continuum methods

Equivalent continuum approaches use the principles of continuum mechanics to establish corresponding constitutive relations for rock masses. Hooke's law for orthotropic, transversely isotropic or isotropic rocks are used with equivalent parameters for the compliance matrix (e.g. Wittke 1984, 1990).

For heavily jointed rock masses equivalent continua can be used. Barton (2002) relies on the Q-system, Diederichs and Hoek (2006) combined equivalent elastic parameters with the GSI values. Diederichs et al. (2006) assumed that the rock mass deformability is isotropic, which is only acceptable for massive rock or heavy jointed rock. For more complicated situations, the equivalent rock mass parameters depend on orientation, spacing etc. of discontinuities. Discontinuity parameters can be integrated into the constitutive equations of the equivalent continuum using the concept of conservation of energy for the work done on the representative elementary volume (REV) (Agharazi, 2012).

The equivalent continuum method can be divided into three parts, the equivalent continuum compliance part (incremental elastic law), the yield criterion and the plastic corrections part. There are several assumptions for this method: first, the joints should be persistent and planar; second, all stresses are carried by the intact rock and joint sets transmit no stress; third, the total strain of the REV is related to the intact rock deformation and the displacement along the joints. Singh (1973) proposed the average strain energy density to establish the constitutive equations for the heterogeneous elastic matrix with three orthogonal joint sets in a rock mass. The method using the REV and non-linear elasto-plastic joints was developed by Cai et al. (1992). Both, Singh and Cai used non-persistent joints which lead to a problem to find out the proper REV for the rock masses. Oda et al. (1993) introduced a crack tensor to represent the joint geometry and developed an elastic

stress-strain relationship for rocks with random joints. A simple practical method to characterize the strength and stiffness of jointed rock masses was presented by Sitharam (2001, 2007). In his method, the effect of joints in the rock mass was taken into account by a joint factor. These obtained relations are incorporated into a non-linear FEM code to perform the equivalent continuum analysis. Bobet et al. (2009) improved a discontinuous deformation analysis method which treats the rock mass as a discontinuous medium. Zhang (2006) developed further the Goodman's joint element model and derived the equivalent method for rock masses with multi-set joints in a global coordinate system. Rihai (2008, 2010) proposed a method which takes into account the influence of micro moments on the behavior of the equivalent continuum based on the Cosserat theory. A more accurate description of the mechanics of jointed rock can be obtained using the micropolar (Cosserat) continuum. Dawson (1995) developed micropolar elastic and elastoplastic models for jointed rock. Agharazi et al. (2012) developed a jointed rock model which uses a three dimensional equivalent continuum constitutive model for the stress-strain analysis of fractured rock masses. Will (1999) implemented a multi-surface plasticity model into a FEM code with internal iterations in case of touching several plasticity surfaces at the same time.

2.2.2.3 Continuum Methods versus Discontinuum Methods

For a jointed rock mass, discrete methods provide an accurate description of the rock mass behavior because of their discontinuous nature. The benefit of discontinuum models is that it can be used to simulate a wide variety of rock mass situations, including both, micro- and macro-scale discontinuities. The restricted number of blocks and the duration of a simulation, each limited by the computational power are current disadvantages in using discontinuum based codes.

Continuum methods provide an alternative way to solve problems of jointed rock masses. The numerical discretization does not consider joints in an explicit manner, which reduces model size and increases computational efficiency. Continuum models can still be used if the data base about the geometry of discontinuities is limited. Several failure criteria can be used. The compressive and tensile strength of intact rock can be obtained by lab tests. The influence of joint sets can be taken into account by the Geological Strength Index (GSI) or through rock mass classification systems. The greatest challenge for continuous modeling is to select a proper constitutive law

which is appropriate for the particular problem. Different constitutive laws require different parameter sets and may result in different outputs. Parameters obtained from lab testing refer to small specimens of intact rock, therefore scale effects should be taken into consideration. A rock mass composed of mainly intact rock or by small rock pieces in relation to the overall model size can be treated as a continuous rock. Figure 2.5 illustrates this scale effect for a tunnel.

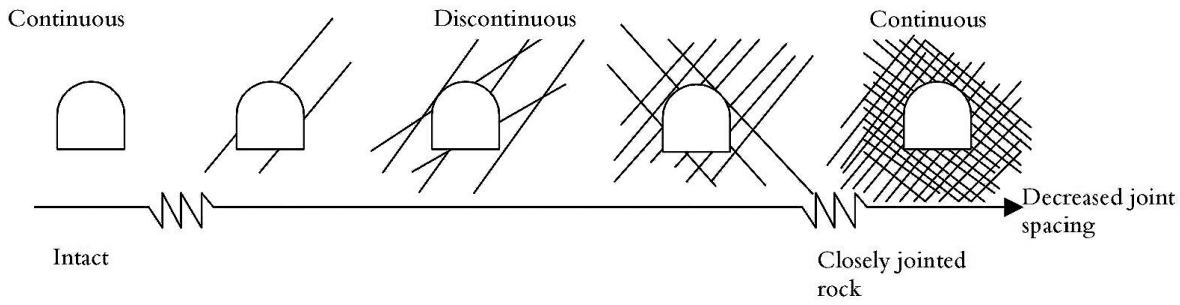

Figure 2.5 Continuous and discontinuous approach for rock masses (Edelbro, 2003)

2.3 Deformation of jointed rock masses

Deformation of the rock mass consists of two parts: deformation of the intact rock and the displacement along/across the joints. A lot of research about the deformation characteristics of rock joints was carried out in the last decade (e.g. Jade et al. 2003; Cai et al. 2006; Chen et al. 2007; Prudencio et al. 2007, Nguyen 2013).

2.2.3.1 Types of joints and corresponding simplifications

Lin et al. (2006) proposed a two-scale modeling concept within the framework of the manifold method. Their approach categorizes the joints in a rock mass into two sets according to their impact on overall kinematics. Discontinuities were denoted as primary and secondary discontinuity set. The primary discontinuities have a dominant influence on the mechanical behavior of the rock mass at large-scale and consist of highly persistent discontinuities like faults or bedding planes. The primary discontinuities should be modeled explicitly. Small-scale randomly distributed joints which are usually limited in size are named secondary discontinuities. These secondary joints have limited impact on the large-scale rock mass deformation. Due to the stochastic distribution

of the secondary joints, equivalent continuum parameters should be used and the rock matrix can still be treated as an isotropic material. The rock mass can be considered as an assemblage of intact rock blocks with downgraded mechanical properties (Agharazi, 2012). This two-scale concept is illustrated in Figure 2.6.

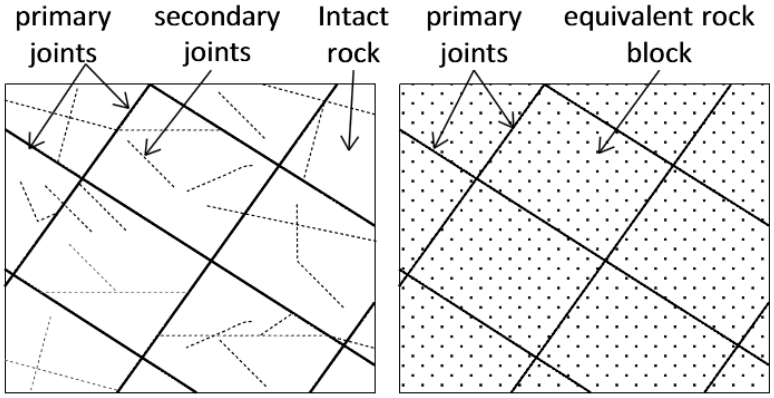

Figure 2.6 Rock mass with two-scale joints (Agharazi, 2012)

The roughness of joint surfaces is of paramount importance for the mechanical and hydraulic properties of a rock mass. Jiang et al. (2006) developed a new model using a 3-dimensional fractal evaluation method of roughness characterization combined with the Projective Covering Method (PCM). Jiang's (2006) approach is a new way to accurately evaluate the roughness of rock joint surfaces and shows how joint roughness influences the hydro-mechanical behavior of rock joints. In Wang's studies (2009, 2014), the shear strength of the joint was estimated using Barton's empirical formula which uses joint roughness coefficient (JRC), uniaxial compressive strength of joint wall (JCS) and the joint basic friction angle (ϕ_b). In this research, joints are assumed to be persistent and planar.

2.2.3.2 Failure behavior

A constitutive relationship should reproduce the main physical phenomena. In terms of elasto-plasticity and failure pattern the following types can be distinguished: brittle, elastic-perfect plastic and strain softening behaviour (Lee et al. 2008; Salager et al. 2013). The harder igneous and some metamorphic rocks usually fail in a brittle manner (Figure 2.7 a). Perfect plastic behaviour means that the rock mass deform at a constant stress level (Figure 2.7 b). Jointed rock mass can best be described by strain softening behaviour as shown in Figure 2.7 (c).

A large number of uniaxial compressive tests were conducted by Singh et al. (2005) on jointed specimens having various orientations of interlocking joints. Singh (2002, 2005) proposed four dominating failure modes for a jointed rock mass: (a) splitting of intact material of the elemental blocks, (b) shearing of intact block material, (c) rotation of the blocks, and (d) sliding along the critical joints, as shown in Figure 2.8.

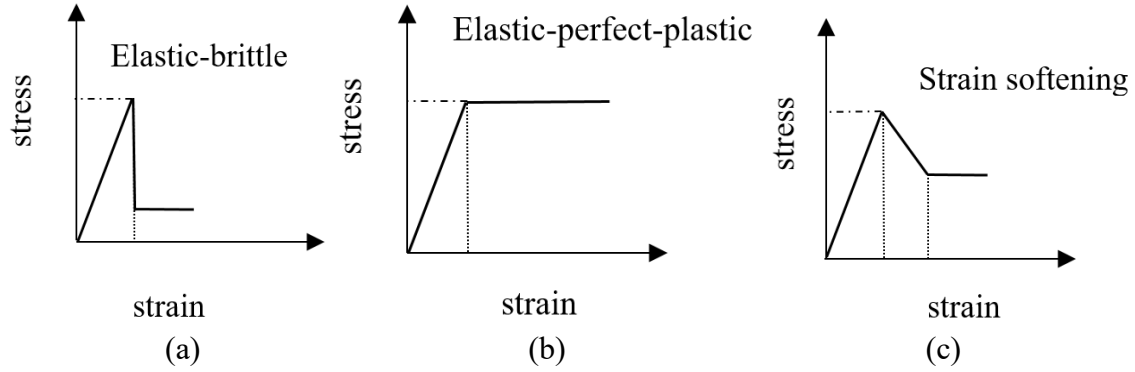

Figure 2.7 Schematic illustration of elasto-plastic behaviour: (a) brittle, (b) perfectly plastic, (c) strain softening

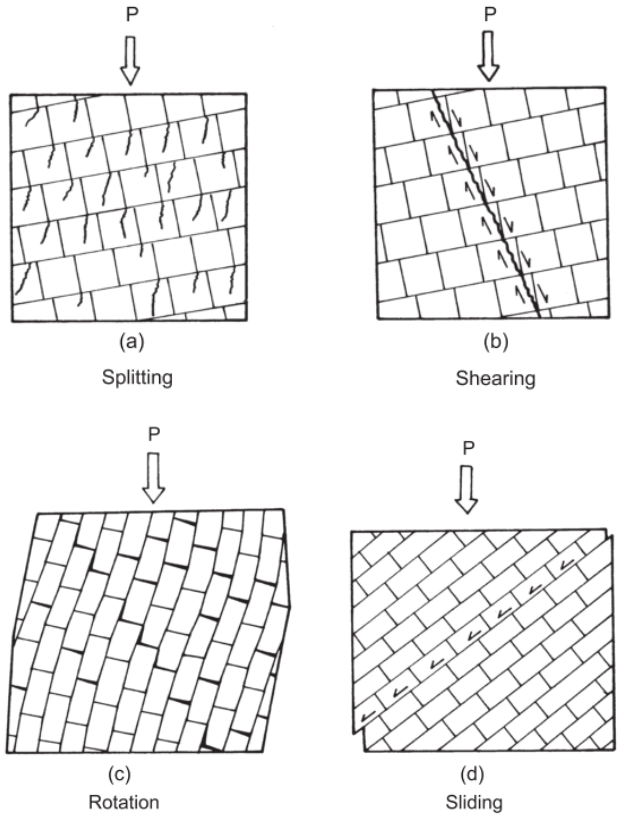

Figure 2.8 Sketches of failure modes (Singh et al. 2005)

2.2.3.3 Deformation types

Deformability of the discontinuities can be described by normal and shear stiffness. Experiments (Goodman 1976; Bandis et al. 1983) show that the normal displacement of joints follows a non-linear relationship with the applied normal stress (hyperbolic function). Goodman (1976) proposed two shear displacement models for joints: the constant shear model and the constant displacement model. Misra and Marangos (2010) developed a joint deformation model which has a linear elastic intact rock using the Mindlin contact principle of joint stiffness. Barton et al. (1986) concluded that the shear stiffness should be lower than the normal stiffness which is more reasonable to explain anisotropic deformations in rock masses. Barton (1986, 2007) carried out and analyzed a series of flat jack and plate loading tests in-situ. Based on experimental results he defined three deformation types as shown in Figure 2.9. The main features of rock mass deformation for each type are provided in Table 2.1.

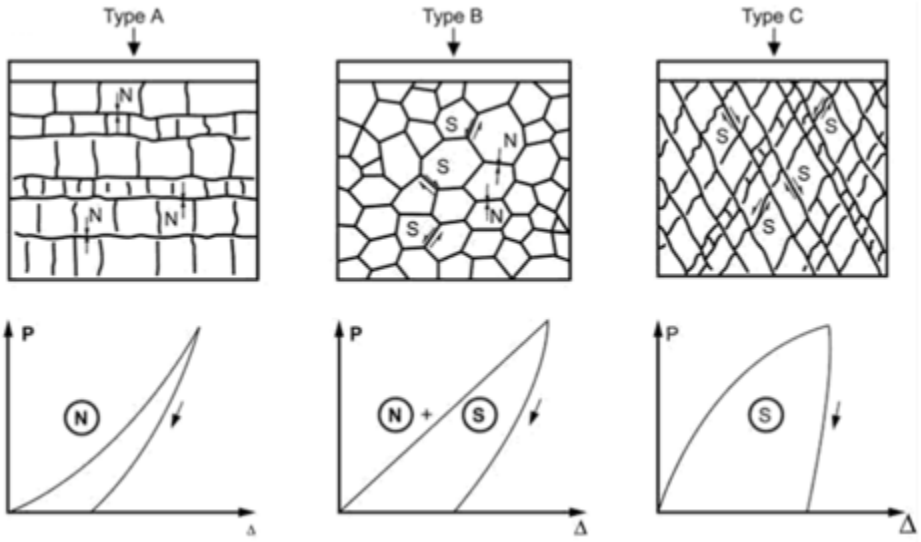

Figure 2.9 Conceptual pressure-deformation curves due to normal-closure and shear-displacement components (Barton 1986)

Table 2.1 Characteristics of load-deformation patterns for jointed rocks (Barton 2007)

Type	Dominant Model	Shape	Hysteresis	Lateral Expansion	Poisson's Ratio
A	Normal	Concave	Small	Small	Low
B	Normal+Shear	Linear	Moderate	Moderate	Medium
C	Shear	Convex	Large	Large	High

2.3 Experimental investigations

2.3.1 Lab testing

In the past several decades, a great amount of lab tests with samples containing a single joint or joint set under confined and unconfined conditions have been carried out to investigate the effect of joint orientation and failure characteristics of jointed rocks (Donath 1964; Bary 1967; Brown, 1970; Kulatilake et al. 2001; Singh et al. 2002; Tiwari et al. 2004; Kumar et al. 2005). The following review focus on tests, which consider one joint/joint set, two joints/joint sets and three systematically intersected joint sets.

Donath (1964) conducted experiments with one joint using Martinsburg slate. Shale and slate experiments were done by Allirote et al. (1974). Sandstones tests were performed by Ramamurthy et al. (1988). Singh et al. (2001) worked on the anisotropic response of gneisses and schists. Artificial material samples with some pre-existing discontinues have been extensively tested by Tien and Tsao (2000) and Tiwari et al. (2004).

Although many experiments have been conducted on rocks with a single joint or joint set, only few experimental studies considered rock masses with multiple, interconnected joints or joint sets (Yang et al. 1998; Kulatilake et al. 2001; Ghazvinian et al. 2012; Xiao et al. 2014).

Cubic samples with two or three joint sets were tested under uniaxial compression by Yang (1998). The dimensions of the samples are 125 × 100 × 300 mm (length, thickness, height). All of these specimens were made of a plaster-sand mixture. Schematic views of Yang's models are shown in Figure 2.10. Joint 2 is a vertical joint, and joint 1 (characterized by γ_1) and joint 3 (characterized by γ_3) are interconnected joint sets. 10 different orientations for γ_1 (two joint sets), and six combinations of γ_1 and γ_3 (three joint sets) were considered. The surface of the joint planes are rough. Yang identified three different failure modes: splitting fracture of the rock blocks, sliding along the joints and mixed failure. The experiments also reveal that more joint sets lead to a weaker behavior of the rock mass in terms of strength and deformation. Another series of tests with a plaster-sand mixture were conducted by Kulatilake (2001). The samples size is

125 × 86 × 300 mm. Two intersected joint sets with several types of combinations of joint orientations ranging from 0º to 40º were used. Conclusions of Kulatilake are similar to those of Yang.

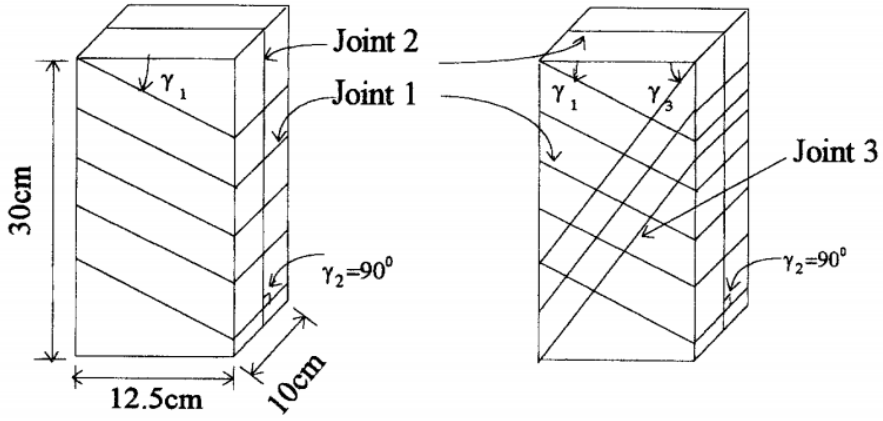

Figure 2.10 Schematic representation of samples with two and three joint sets (Yang et al. 1998)

A series of triaxial compression tests with two perpendicular joints of different orientation were done by Ghazvinian et al. (2012). The tests were conducted for dip angles β ranging from 0º to 45º (15º intervals) in order to examine the response for any possible inclinations of perpendicular dipping joints. The artificial plaster specimens were tested under various confining pressures. The curves of peak strength versus joint angles are shown in Figure 2.11. A new parameter A_e (a dimensionless parameter) is used to represents the anisotropy effect as follows:

$$A_e = \frac{\sigma_{ia} - \sigma_{ja}}{\sigma_{ia}} \tag{2.8}$$

where σ_{ia} is the compressive strength of the intact samples under confining pressures, and σ_{ja} is the compressive strength of the anisotropic samples (pre-existing joint) under the same confining pressure. A_e can vary from 0 to 1.

Deformation and strength of columnar jointed rock mass exhibit significant anisotropy. Cylindrical specimens (cement like material) under uniaxial compression with no more than two joint sets with different dip angles ranging from 0° to 90° were used to investigate the anisotropy of

columnar jointed rock masses (Xiao 2014). Xiao (2014) summarized four types of failure mode for columnar jointed specimen under uniaxial compression. The deformation and strength curves, respectively, resembles the "U" shape, with minimum strength value for 30° measured from the vertical direction.

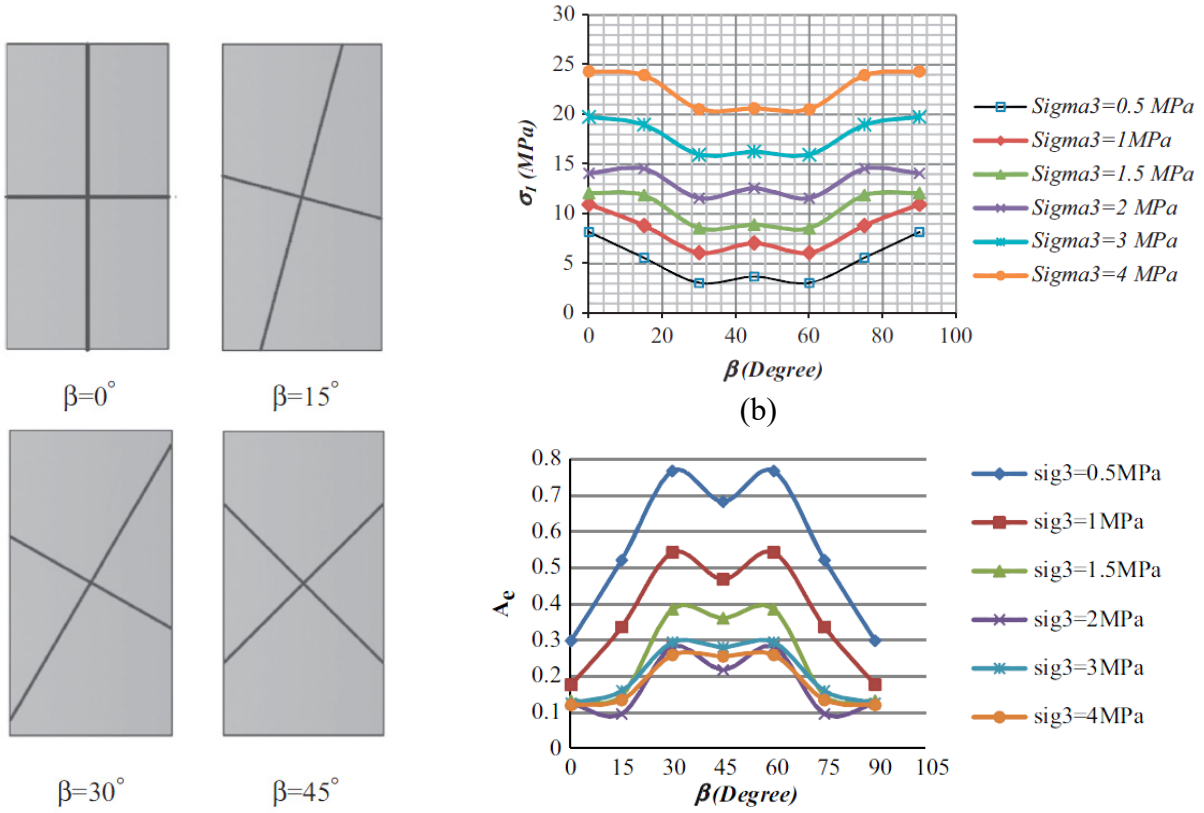

Figure 2.11 Anisotropy effect of perpendicular jointed rock: (a) sketches to introduce joint configurations, (b) peak strength for different joint orientations, (c) anisotropy parameter A_e vs. joint orientation for various confining pressures (Ghazvinian, 2012)

2.3.2 In-situ testing

Large scale in-situ tests on rock masses have been conducted in many projects in order to obtain the deformation modulus of the rock mass. The most common test is the plate loading test (Hucka, 1965; Bieniawski, 1978; Ünal, 1997). Some other in-situ tests such as stress measurements, direct shear tests or wave velocity tests will not discussed here. Palmström (2001) has improved the plate

loading test and developed the plate jacking test (PJT), which measures the deformations by extensometers inside drill holes. In order to study the deformation mechanism of the weak layer in diabase dikes under long-term loading at a hydropower dam foundation in China, a large-scale compressive creep test using a rigid bearing plate were performed by Yang et al (2014). Weak mineralized zones in underground mines at greater depths are intensely fractured and highly altered. In order to overcome the absence of in situ geotechnical data, a portable plate loading device (PPLD) was designed and applied by Kallu et al. (2016). Test procedures and data reduction methods were developed to limit potential sources of error associated with the PPLD test which exerts low cost and allows relatively quick in situ deformability tests on weak rock masses.

2.4 Empirical failure criteria and analytical solutions for a jointed rock

2.4.1 Mohr-Coulomb strength criterion

The Mohr-Coulomb strength criterion is widely used in geotechnical engineering (e.g. Zhao, 2000; Obara et al., 2004; Palchik, 2006). According to the criterion, the shear strength is defined as:

$$\tau = c + \sigma_n \tan \phi \tag{2.9}$$

where τ is shear strength of the shear plane, c is the cohesion, σ_n is the normal stress acting on the shear plane and ϕ is the friction angle. This criterion is often applied in rock mechanics for shear failure in rock matrix, at rock joints and also for rock masses. The criterion can also be described in principal stresses as:

$$\frac{\sigma_1}{\sigma_3} = \frac{2c\cos\phi}{\sigma_3(1-\sin\phi)} + \frac{1+\sin\phi}{1-\sin\phi} \tag{2.10}$$

In many cases the criterion is expressed as:

$$\sigma_1 = \sigma_c + k\sigma_3 \tag{2.11}$$

where σ_c is the uniaxial compressive strength, k is the slope of the line relating σ_1 to σ_3. The friction angle ϕ and the cohesion c can be calculated using the following equations:

$$\sin\ \phi = \frac{k-1}{k+1} \tag{2.12}$$

$$c = \frac{\sigma_c(1-\sin\ \phi)}{2\cos\ \phi} \tag{2.13}$$

when $c = 0$, the slope of the line is given as:

$$\frac{\sigma_1}{\sigma_3} = \frac{1+\sin\phi}{1-\sin\phi} = k \tag{2.14}$$

Substituting Eq. (2.10) and Eq. (2.13) into Eq. (2.9), the criterion can be re-written:

$$\sigma_1 = \sigma_3 \frac{1+\sin\ \phi}{1-\sin\ \phi} + \frac{2c\cos\ \phi}{1-\sin\ \phi} \tag{2.15}$$

The failure envelope in the principal stress space is shown in Figure 2.12 (a), the uniaxial compressive and tensile strength, σ_c and σ_t, are given as:

$$\sigma_c = \frac{2c\cos\phi}{1-\sin\phi} \tag{2.16}$$

$$\sigma_t = \frac{2c\cos\phi}{1+\sin\phi} \tag{2.17}$$

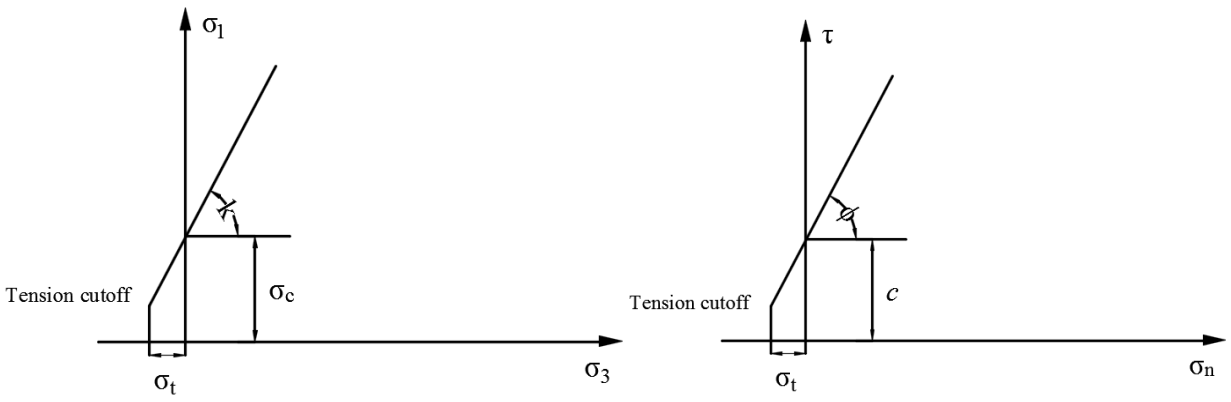

Figure 2.12 Mohr-Coulomb failure criterion: (a) in principal stress space, (b) in normal stress - shear stress space

Since rock cannot sustain large tensile stresses, a tension cut-off is often included. In fact, these parameters are not constant with damage accumulation under different confining pressure. Therefore, several non-linear failure criterions were developed to describe the damage process of rocks and rock masses.

2.4.2 Empirical failure criteria for rock masses

Strength and deformation of jointed rock masses can be expressed as the function of intact rock properties and certain joint factors. Joint factors can be related to rock mass classification systems. Such empirical relations are obtained by statistical analysis of a large amount of data (Arora 1987; Ramamurthy et al. 2004; Maji 2007). One of the most popular non-linear failure criterion is the modified Hoek-Brown criterion (Hoek et al., 2002; Chen et al. 2015) which is based on the mechanical behavior of intact rock, but can also include properties of the discontinuities incl. their spatial distribution. The criterion is formulated by principal stresses σ_1 and σ_3. The general expression of this criterion is:

$$\sigma_1' = \sigma_3' + \sigma_c \left(m_b \frac{\sigma_3'}{\sigma_c} + s \right)^b \tag{2.18}$$

where σ_c is the uniaxial compressive strength of intact rock, m_b is a reduced value of the constant m_i, which characterize the rock type and can be expressed as:

$$m_b = m_i \exp\left(\frac{GSI - 100}{28 - 14D}\right) \tag{2.19}$$

The parameters s and b are constants for the rock mass expressed by:

$$s = \exp\left(\frac{GSI - 100}{9 - 3D}\right) \tag{2.20}$$

$$b = \frac{1}{2} + \frac{1}{6}\left(e^{-GSI/15} - e^{-20/3}\right) \tag{2.21}$$

GSI is the geological strength index and D is a disturbance factor. Equivalent Mohr-Coulomb parameters (c, ϕ) can be defined by linearization of the non-linear Hoek-Brown criterion (Chakraborti & Konietzky 2012). The relationship between Hoke-Brown and the equivalent Mohr-Coulomb criteria are shown below (Yang et al. 2006):

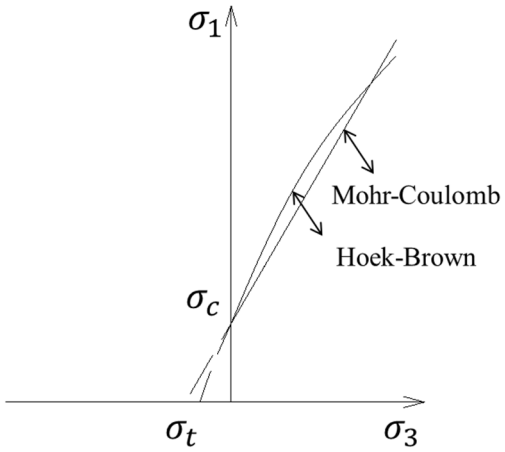

Figure 2.13 Comparison between Hoek-Brown and Mohr-Coulomb failure

The equations for effective angle of friction ϕ' and effective cohesive strength c' are:

$$\phi' = \sin^{-1}\left[\frac{6am_b(s+m_b\sigma'_{3n})^{a-1}}{2(1+a)(2+a)+6am_b(s+m_b\sigma'_{3n})^{a-1}}\right] \tag{2.22}$$

$$c' = \frac{\sigma_{ci}\left[(1+2a)s+(1-a)m_b\sigma'_{3n}\right](s+m_b\sigma'_{3n})^{a-1}}{(1+a)(1+2a)\sqrt{1+(6am_b(s+m_b\sigma'_{3n})^{a-1})/((1+a)(1+2a))}} \tag{2.23}$$

where $\sigma_{3n} = \sigma'_{3max}/\sigma_{ci.}$ and σ'_{3max} is the upper limit of confining stress as shown in Figure 2.13.

Li (2008) and Rafiai (2011) compared several conventional failure criteria for the prediction of the rock mass strength such as the Bieniawski–Yudhbir and the Ramamurthy empirical failure criteria. For the numerical model introduced in the following chapters, the Mohr-Coulomb criterion was used as constitutive model for the rock matrix and for the joints (Agharazi et al. 2012). Non-linear empirical relationships were obtained with equivalent rock mass parameters or joint factors (J_f) according to different rock mass characterization systems (Edelbro 2007; Cundall et al. 2008; Sitharam, 2009).

2.4.3 Analytical solution for a jointed rock

2.4.3.1 Analytical solution for strength anisotropy

Comprehensive theories based on various rock failure phenomena have been proposed (Jaeger and Cook, 1979; Brzovic et al. 2007; Itasca 2007). Different failure pattern for samples under uniaxial tension and uniaxial/triaxial compression are shown in Figure 2.14 (a). The analytical solution can be expressed using the shear and normal stresses acting on the fracture plane as illustrated in Figure 2.14 (b). Corresponding formulas are given as follows:

$$\begin{cases} \sigma_\theta = \frac{1}{2}(\sigma_1+\sigma_3)+\frac{1}{2}(\sigma_1-\sigma_3)\cos 2\theta \\ \tau_\theta = \frac{1}{2}(\sigma_1-\sigma_3)\sin 2\theta \end{cases} \tag{2.24}$$

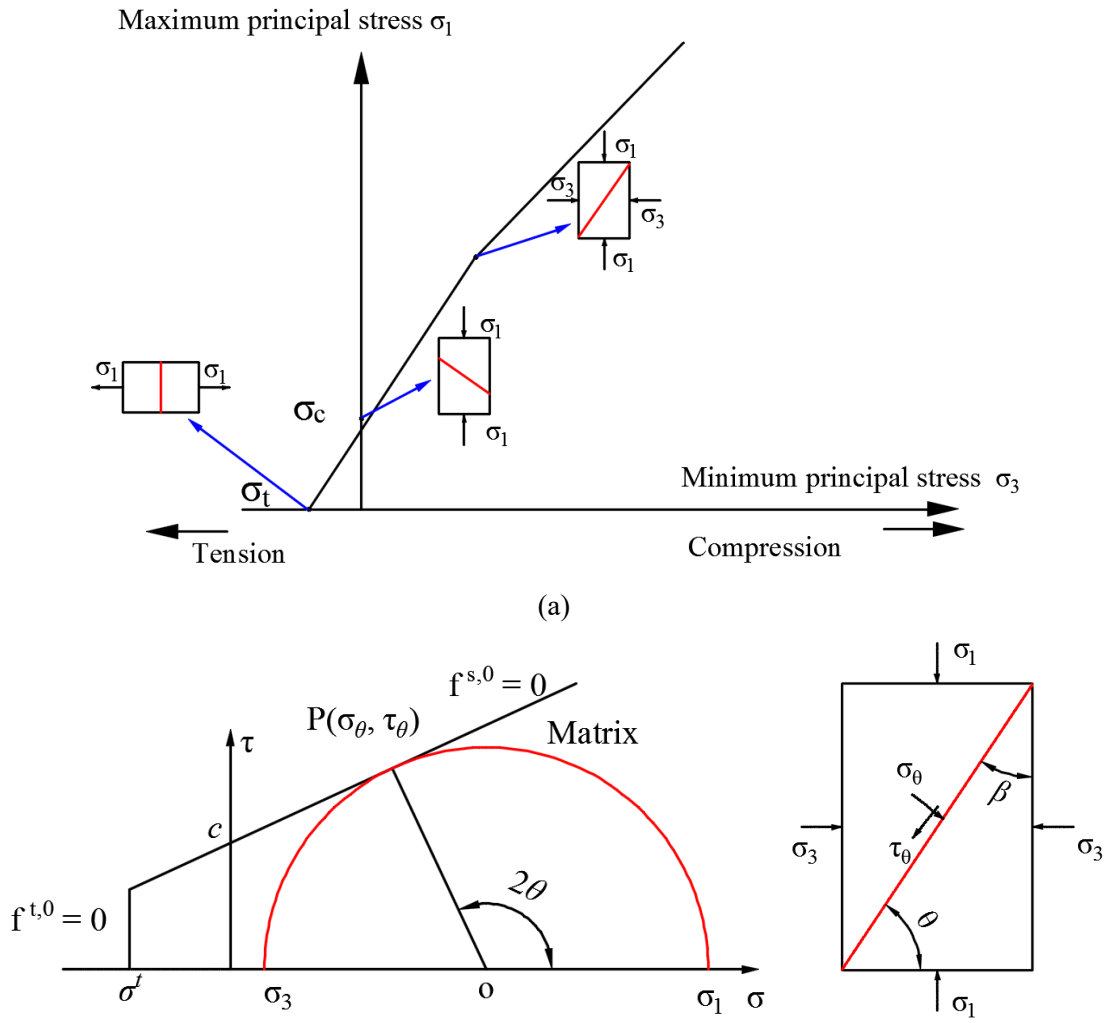

Figure 2.14 Failure and stress states for a jointed model: (a) failure envelope and fracture pattern, (b) Mohr's circle and stress state on failure plane

For a rock specimen which contains a pre-existing joint (see also Equation 2.9) slip will occur along the joint when:

$$\sigma_1 \geq \sigma_3 + \frac{2\,(c_j + |\sigma_3| \tan\phi_j)}{(1 - \tan\phi_j \tan\beta)\sin 2\beta} \qquad (2.25)$$

where c_j is the joint cohesion, ϕ_j is the joint friction angle and β is the joint angle formed by σ_1 and the joint.

For other combinations of c, ϕ, σ_3 and β, the function (2.25) is not satisfied and slip will not occur on the discontinuity. Then failure of the rock matrix may occur according to the Mohr-Coulomb failure criterion:

$$\sigma_1 = \sigma_3 k - 2c\sqrt{k} \tag{2.26}$$

where $k = \dfrac{1+\sin\phi}{1-\sin\phi}$

Under uniaxial compression (σ_3=0), Eqs. (2.25) and (2.26) can be rewritten as:

$$\begin{cases} \sigma_1 = \dfrac{-2c_j}{(1-\tan\phi_j \tan\beta)\sin 2\beta} \\ \sigma_1 = -2c\sqrt{k} \end{cases} \tag{2.27}$$

The maximum stress during an uniaxial compressive test of a jointed specimen can be expressed as:

$$\sigma_c = \begin{cases} \min\left\{ 2c\sqrt{k},\ \dfrac{-2c_j}{(1-\tan\phi_j \tan\beta)\sin 2\beta} \right\} & if\ (1-\tan\phi\tan\beta) > 0 \\ 2c\sqrt{k} & if\ (1-\tan\phi\tan\beta) < 0 \end{cases} \tag{2.28}$$

2.4.3.2 Analytical solution for strength of rock with multiple discontinuities

Figure 2.15 shows a rock specimen containing two pre-existing discontinuities with various joint angle combinations. The joint angle β for joint AB is measured clockwise from the vertical axis. Joint CD is rotated by an angle α measured anti-clockwise from joint AB.

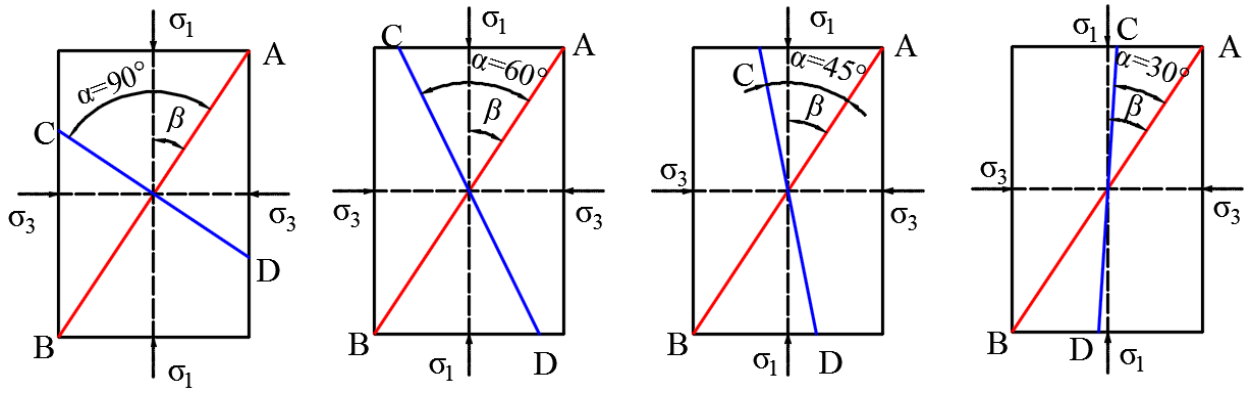

Figure 2.15 Sketch of pre-existing joint combinations

The influence of the second joint CD on the failure of the specimen is estimated by the same procedure as described in chapter 2.4.3.1. It has been assumed that the properties of the two discontinuities are identical, but if required, different sets of properties may be assigned to each joint. Bray (1967) suggests that the overall strength of a rock mass containing several sets of joints is given by the lowest strength envelope of the individual strength relations. The full set of equations defining the uniaxial compressive strength of a rock specimen containing two pre-existing weak planes is listed below in Equation 2.29:

$$\sigma_c = \min\left(2c\sqrt{k}, \frac{2c_{j1}}{(1-\tan\phi_{j1}\tan\beta_1)\sin 2\beta_1}, \frac{2c_{j2}}{(1-\tan\phi_{j2}\tan\beta_2)\sin 2\beta_2}\right) \quad (2.29)$$

The uniaxial compressive strength σ_c calculated by Equation 2.29 determines the minimum strength of a rock mass for various joint combinations. This Equation will serve as an analytical solution in the following chapters.

2.5 Numerical simulation

Considering the complex mechanical behavior of rock masses, it is difficult or even impossible to get analytical solutions for all the complex constellations. With the development of computing capacity, sophisticated numerical methods are used to analyze the mechanical behavior of rock mass having such complex characteristics (Clark et al 2006; Detournay et al. 2016). Modeling

techniques for typical rock mechanical problems such as underground openings or rock slopes have been developed (Wang, 2009; Sitharam, 2009). The effect of discontinuities on the strength and deformability of rock masses has been studied by many researches using numerical methods, such as continuum methods (finite element method, finite difference method, boundary element method) and discontinuum methods (distinct element method, interface element method).

Several software tools are used to simulate deformation and stability of excavations and slopes in jointed rock masses (Verma, 2010; Hammah, 2009). One of the most famous Finite Difference programs in engineering mechanics is FLAC (Itasca 2007). Clark (2006) implemented ubiquitous joint orientations at the zone level (U-J model) into FLAC. Clark combined GSI values and Hoek-Brown parameters. The rock mass consist of intact rock (Mohr-Coulomb solid) with persistent joints or a fault (Figure 2.16 a). A numerical code called RFPA (Jia et al., 2006) based on a combination of FEM and DDA, was used to study the influence of different dip angles of layered joints and the lateral pressure coefficient on the stability of a tunnel in jointed rock masses.

In order to consider the joint density and persistence of heavily jointed rock an Ubiquitious Joint Rock Mass (UJRM) model was developed and used to simulate large-scale rock mass strength anisotropy and scale effects (Sainsbury, 2008). The matrix properties in this UJRM model are deduced from the intact rocks and joint properties are derived directly from the SRM (Synthetic Rock Mass) testing results. The accuracy of calibration relies mainly on the joint cohesion, critical strain and intact rock stiffness.

Sitharam (2009) developed a 3-dimensional equivalent continuum model for deformation analysis of jointed rock masses. The stress-strain behavior of rock mass over a wide range of stress states is nonlinear based on hyperbolic stress-strain relationships. Sitharam proposed a joint factor variable to get accurate rock mass parameters, and he also compared his equivalent continuum model with an explicit interface model. Wang (2009) focused on rock mass with multi-sets of ubiquitous joints, established a corresponding mathematical expression with anisotropy in strength and deformation. Wang also proposed an approach to incorporate existing joint models, e.g. an extended Barton empirical formula was used to estimate the shear strength of joint planes (Wang 2009, 2014). Besides the pre- and post-peak deformation characteristics of the intact rock, Wang

also considered the pre- and post-peak deformation of joints (closure, shear and dilatancy). A new numerical simulation method was developed by Huang (2013) to examine the strength and deformation characteristics of layered rock masses under conventional and true triaxial compression (one joint set as transverse isotropic model). A three dimensional constitutive model was formulated for the deformation analysis of jointed rock masses containing up to three joint sets with arbitrary spatial configurations by Agharazi (2012). He also defined a representative elementary volume (REV) which could represents the deformational response of the rock mass and the constitutive relationships were developed based on the superposition of deformations in the REV components. The model was implemented in FLAC^{3D} (Itasca 2012) and the behavior was compared with the results from a 3DEC (Itasca 2012) model and analytical solutions (Agharazi 2013).

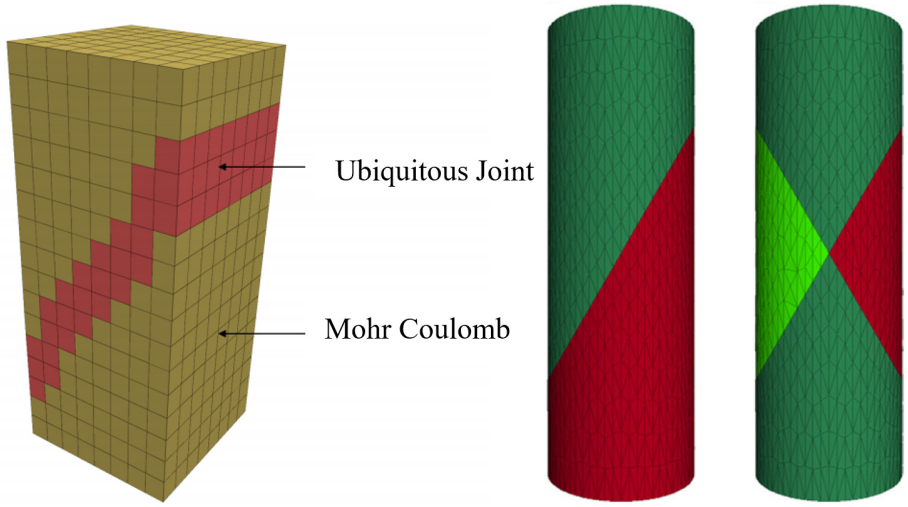

(a) (b)

Figure 2.16 Jointed rock models: (a) continuum model (Clark, 2006), (b) 3DEC model with one and two joints (Chong, 2013)

In contrast to a continuum based approach DEM considers material composed of several individual blocks which are connected and interact with each other. Kim et al. (2007) suggested a method for the determination of the block size considering joint persistence. This method combines the block size with the GSI system. A statistical analyses is used to describe the distribution of rock bridges according to the combination of joint orientation, spacing and persistence which affects the actual size of individual blocks. Various combinations of joints with different geometrical conditions by

orthogonal arrays were generated by Kim et al. Rock fracturing and joint sliding of a single jointed rock mass with an opening under biaxial compression were investigated through experimental and numerical analyses by Sagong et al. (2011). The tested rock models have a persistent joint set with dip angles of 30°, 45° and 60° to the horizontal. Based on the experimental results of Yang et al. (1998) and Kulatilake et al. (2001), Chong (2013) used 3DEC to perform numerical simulations of specimens to study the strength and deformation behavior of a mudstone in unconfined and confined states (Figure 2.16 b). The confined model was extended further to investigate the effects of joint sets and dip angles on the rock mass strength and deformation behavior by incorporating two different joint configurations (one-joint and two-joint) with varying dip angles (0° – 90°). Chong et al (2013). confirmed that two different joint configurations have significant influence on the rock mass strength in a confined state. Scholtès et al. (2012) developed a 3-dimensional DEM model which is dedicated for the simulation of fractured rock masses. Structural defects were explicitly included in the medium to represent pre-existing fractures or discontinuities via a Discrete Fracture Network (DFN). A three-dimensional constitutive model to simulate the behavior of columnar basalt at large scale was developed by Detournay et al. (2016). This model is only applicable when the diameter of columns is much less than the size of rock mass. The matrix of rock mass was modeled as an elastic material and the maximum number of joint sets with arbitrary orientations is four.

3 An equivalent continuum constitutive model for a multi-jointed rock mass

3.1 Introduction

In general there are two different techniques: discontinuous and continuous methods. In the discontinuous methods, the discontinuities inside a rock are considered as explicit joints, while in continuous methods the effect of discontinuities is taken into account in an implicit way (so-called smeared approach). One of the last mentioned ones is the so called ubiquitous-joint model. It assumes a plane of weakness with certain orientation within the continuum. Typically, the joint behavior is embedded in a Mohr-Coulomb solid. A mesh with parameter sets for matrix and joint is illustrated in Figure 3.1.

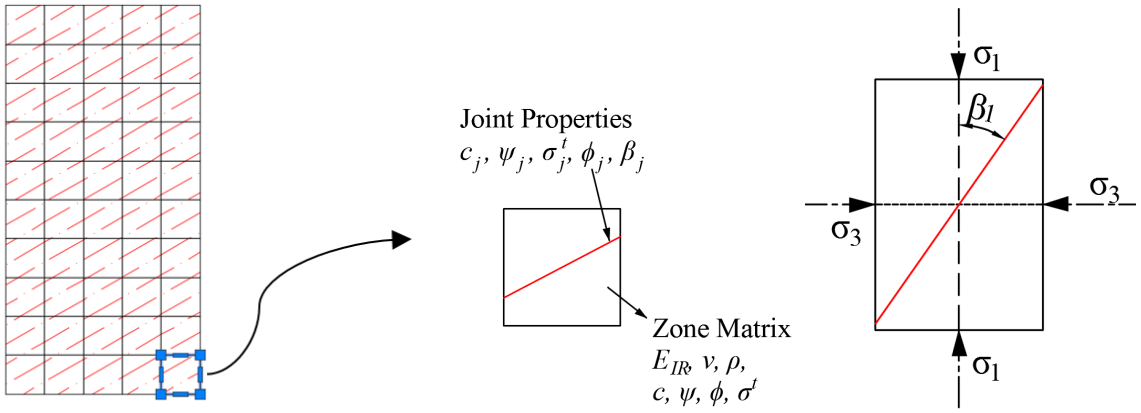

Figure 3.1 Schematic view for a mesh which contains one joint: (a) properties of the weak plane and the intact rock in a zone, (b) equivalent interface model

More advanced UDMs based on the classical ubiquitous joint or strain-harding/softening ubiquitous joint (subiquitous) model are developed in recent years (Sainsbury 2008; Agharazi, 2012; Wang 2009, 2014).

3.1.1 Basic model for a jointed rock

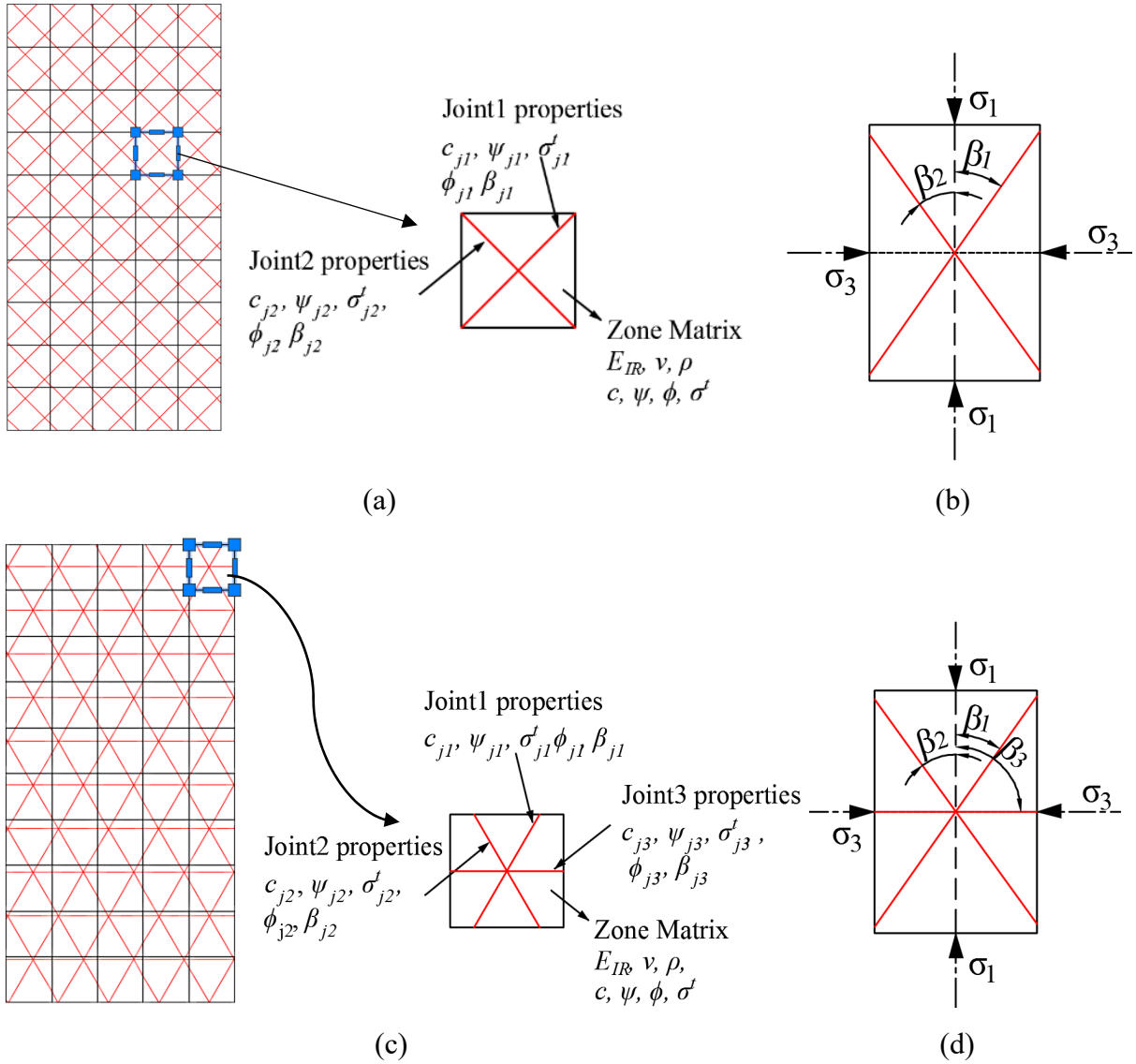

Figure 3.2 Schematic view for a mesh which contains two or three joints: (a), (c) properties of the weak planes and the matrix, (b), (d) equivalent discrete models for two and three joints

The "classical" ubiquitous-joint model describes the anisotropic strength characteristics by considering one joint set only. The effect of several intersecting joints under arbitrary angles needs further research. A new multi-joint model which contains up to three random joints is developed by extension of the "classical" ubiquitous-joint model. Within the basic model joints can have

different strength parameters, but identical stiffness. Also, spatial influence is not considered in this basic model.

3.1.2 Definition of a rock mass

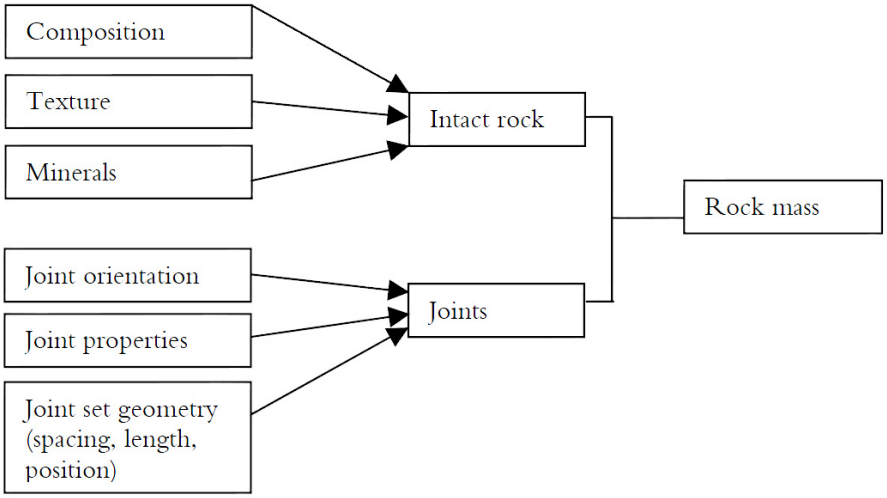

Figure 3.3 Rock mass illustration (Edelbro 2003)

A rock mass (Figure 3.3) is more sophisticated than assumed in the basic joint rock model. Strength and deformation behavior are not only related to the mechanical parameters of the matrix and the joints, but also influenced by the spatial distribution of joints inside the rock material as shown in Figure 3.4.

For a rock mass with more than one joint set new variables have to be introduced. The elastic properties of the weak plane are denoted by the joint normal and shear stiffness parameters k_n and k_s, respectively. The spatial structures of a joint set are represented by the joint orientation and the space between the joints. The aim of this chapter is to describe the developed method which considers these effects in simulating rock masses.

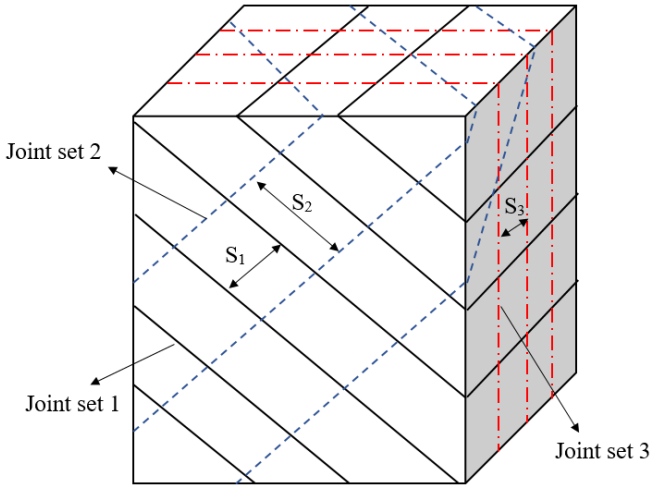

Figure 3.4 Jointed rock mass containing three random joint sets

3.2 Elastic and inelastic behavior of anisotropic materials

The developed model is based on the continuum theory and comprises elastic and plastic elements. The elastic part is already discussed in chapter 2. This section focus on the inelastic part.

3.2.1 Coordinate transformation

Stresses, strains and elasticity tensors of the rock matrix are usually defined in Cartesian coordinates (x-, y- and z-axes) with respect to a fixed global coordinate system. The elasticity tensor for the weak planes is usually defined in a local coordinate system (x'-, y'- and z'-axis) coincident with the material anisotropy (joint) directions (Figure 3.5).

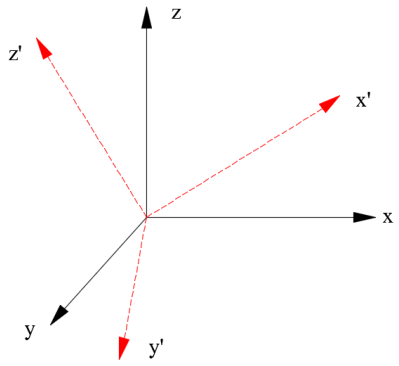

Figure 3.5 Global (x-, y-, and z-) coordinate system and local (x'-, y'-, and z'-) coordinates of the anisotropy plane

Second-order stress and strain components are computed using the transformation rule as follows:

$$\sigma = Q\sigma' Q^T \tag{3.1}$$

and

$$\varepsilon = Q\varepsilon' Q^T \tag{3.2}$$

where Q is the rotation tensor whose three columns are the direction cosines of local coordinates, Q^T is the transpose of matrix Q.

The transformation of the stiffness (D) and compliance matrix (C) are more complicated and can be expressed as follows:

$$C = R_\sigma C' R_\sigma{}^T \tag{3.3}$$

and

$$D = R_\varepsilon D' R_\varepsilon{}^T \tag{3.4}$$

where R_σ and R_ε are the transformation matrices defined by:

$$\tau = R_\sigma \tau' \text{ and } \gamma = R_\varepsilon \gamma' \tag{3.5}$$

For a detailed description of the structure and components of R_σ and R_ε see e.g. Lekhnitskii (1981).

3.2.2 Plasticity of anisotropic materials

Plasticity leads to irreversible deformations after reaching the yield condition. In the classical plasticity theory, two basic functions, namely the “yield surface” and the “plastic potential” are required to formulate the plastic behavior.

3.2.2.1 Yield surface

Different materials have various shapes and sizes of yield surface, most of the yield surfaces are convex and the state of stress inside the yield surface is elastic. The yield surface can be written as a function (F) of stress tensor σ and the plastic strains ε_{pl}:

$$F(\sigma, \varepsilon_{pl}) = 0 \tag{3.6}$$

It can also be expressed by stress invariants as:

$$F(I_1, J_2, J_3, \varepsilon_{pl}) = 0 \tag{3.7}$$

where I_1 is the first principal invariant of the Cauchy stress and J_2, J_3 are the second and third principal invariants of the deviatoric part of the Cauchy stress (Simo & Hughes, 2006).

3.2.2.2 Plastic potential

When the stress reaches the yield surface, the plastic potential function Q is used to determine the direction of plastic strain. Similar to the yield function, the potential function is expressed in the stress space. According to the theory of plasticity it is assumed that the plastic strain increment is proportional to the stress gradients of Q multiplied with the plastic multiplier λ (Owen and Hinton, 1980; Simo and Hughes, 2006), which specifies the strain magnitude. Equation (3.8) is the general expression, Equation (3.9) describes the special case of associated plasticity (plastic potential identical with yield function).

$$d\varepsilon^{pl} = d\lambda \left(\frac{\partial Q(\sigma)}{\partial \sigma} \right) \tag{3.8}$$

$$d\varepsilon^{pl} = d\lambda \left(\frac{\partial F}{\partial \sigma} \right) \tag{3.9}$$

3.2.2.3 Associated and non-associated theory of plasticity

For some materials, such as metals, yield surface F is equal to plastic potential function Q, while, for rocks and soils, $F \neq Q$ (Azadeh, 2008). Figure 3.6 illustrates this for the Mohr-Coulomb model. The plastic strain increments are no longer perpendicular to the flow surface because of the non-associated flow rule.

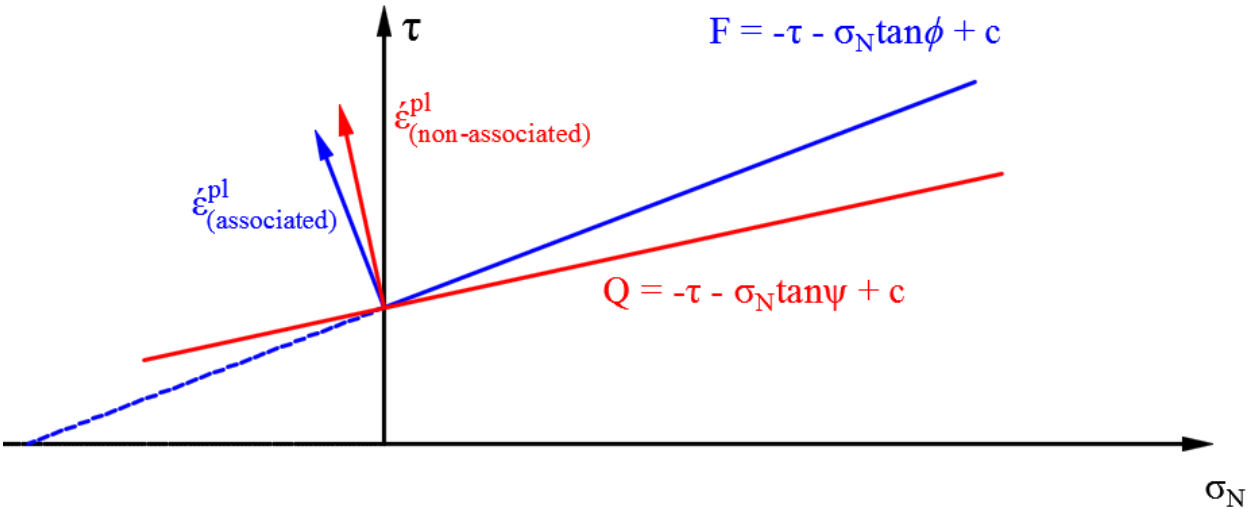

Figure 3.6 Associated and non-associated flow rules for Mohr-Coulomb yield criterion

3.2.2.4 Loading-unloading conditions and consistency condition

The loading/unloading condition obeys the following equations:

$$\lambda \geq 0,\ F(\sigma, \varepsilon_{pl}) \leq 0 \ \text{ and } \ \lambda F(\sigma, \varepsilon_{pl}) = 0 \qquad (3.10)$$

Equation (3.10) are also called the Kuhn-Tucker complementary condition. The first condition means that plastic multiplier λ should be non-negative. The second condition is related to the yield surface and the last one indicates that the stresses should lie on the yield surface during the plastic loading (Huang et. al. 2009). From the Kuhn-Tucker conditions, the consistency requirement can expressed as:

$$\lambda \dot{F}(\sigma, \varepsilon_{pl}) = 0 \qquad (3.11)$$

3.2.3 Elastic properties and plastic behavior of the continuum model

The total principal strain increments can be decomposed into two parts. The superscripts e and p in equation (3.12) refer to the elastic and plastic components, respectively. The plastic components are nonzero only during plastic flow.

$$\varepsilon = \varepsilon^{e} + \varepsilon^{pl} \tag{3.12}$$

A constitutive relation between stress and strain can be defined as:

$$d\sigma = D d\varepsilon^{e} = D(d\varepsilon - d\varepsilon^{pl}) = D_{EP}\, d\varepsilon \tag{3.13}$$

where D is the elasticity matrix.

For Mohr-Coulomb materials, based on Equations (3.8) along with the Kuhn-Tucker condition, the elasto-plastic constitutive matrix becomes:

$$D_{EP} = D - \frac{1}{\zeta} D\left(\frac{\partial Q}{\partial \sigma}\right)\left(\frac{\partial F}{\partial \sigma}\right)^{T} D^{T} \tag{3.14}$$

where: D_{EP} is the elasto-plastic constitutive tensor and

$$\zeta = \left(\frac{\partial F}{\partial \sigma}\right)^{T} D\left(\frac{\partial Q}{\partial \sigma}\right) \tag{3.15}$$

For the derivation of these relations see Will (1999) and Riahi (2008).

3.2.3.1 Algorithm for single yield surface plasticity

The trial elastic stress prediction is:

$$\sigma_{i+1}^{trial} = \sigma_{i} + D d\varepsilon_{i+1} \tag{3.16}$$

For a single yield surface, the active condition of the plasticity surface is the stress state violation of the failure criterion:

If $F^{trial}(\sigma,\varepsilon_{pl})<0$; elastic step (3.17)

If $F^{trial}(\sigma,\varepsilon_{pl})>0$; plastic step (3.18)

When the position of the stress point lies inside (below) the yield surface an elastic stress increment is performed and one can move to the next step. Once the stress level reaches the yield condition, the corresponding yield function and flow rule are mobilized as shown in Figure 3.7.

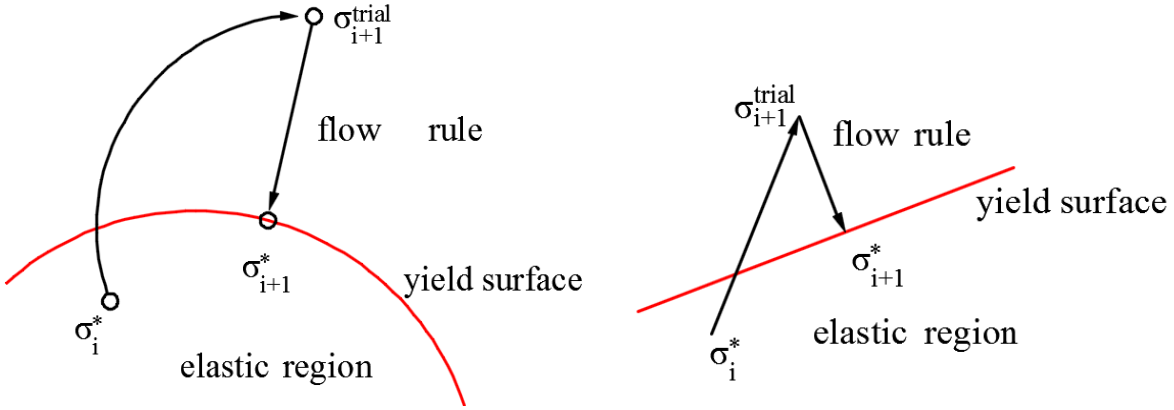

(a) smooth non-linear yield surfaces (b) linear yield surfaces

Figure 3.7 Schematic view of the return mapping procedure for the non-linear/linear yield surface when the stress state reaches the yield condition (valid for a single yield surface)

3.2.3.2 Multi-surface plasticity

In this model, it is assumed that the multi-joint material is composed of an isotropic matrix with one or more sets of joints. Failure of the equivalent continuum can occur due to the failure of any set of joint or failure in the matrix. Each component of the model has separately specified strength parameters and show perfect elasto-plastic behavior. This section concentrates on situations where multiple yield surfaces intersect. Generally, the shape of the yield surface is convex or linear

(Figure 3.8). In the model proposed within this thesis, violations of the Mohr-Coulomb criterion of the matrix are checked first followed by the joint sets.

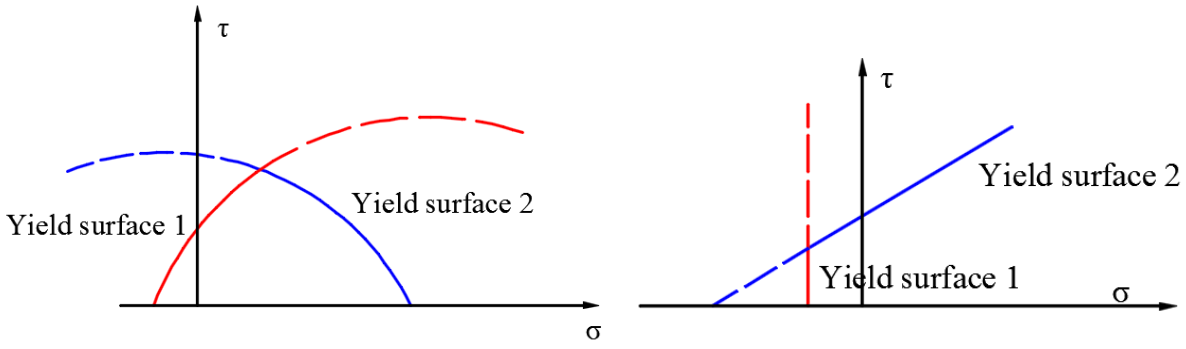

(a) Two convex yield surfaces (b) Two straight yield surfaces

Figure 3.8 Schematic interaction of two yield surfaces

Under multi-surface plasticity condition, the total plastic strain increments are obtained by the sum of the plastic strains of all active plasticity surfaces, as follows:

$$\varepsilon^{pl} = \sum_{j=1}^{n} \lambda_j \left(\frac{\partial Q_j}{\partial \sigma}\right) \tag{3.19}$$

where j denotes the yield surface index, Q is the plastic potential function of the activated yield surfaces j.

Figure 3.9 elucidates possible geometric conditions arising from the intersection of two yield surfaces ($\alpha = 1, 2$) in a multi-jointed model. Several different situations have to be considered (Simo, 1988):

(1) If only one yield condition is violated (region s_4 and s_5), plasticity correction is performed by the corresponding functions F_α and Q_α.

(2) If more than one yield condition is violated, the situation can be categorized as follows:

(a) If $F^{trial}(\sigma,\varepsilon_{pl})>0$ and $\lambda^{\alpha}_{i+1}>0$, for both α =1 and 2 (region s_{12}) both surfaces are active (Azadeh, 2008).

(b) If $F^{trial}(\sigma,\varepsilon_{pl})>0$ and $\lambda^{\alpha}_{i+1}<0$, for α =1 or 2 (region s_1 or s_2) only one of the surfaces are active.

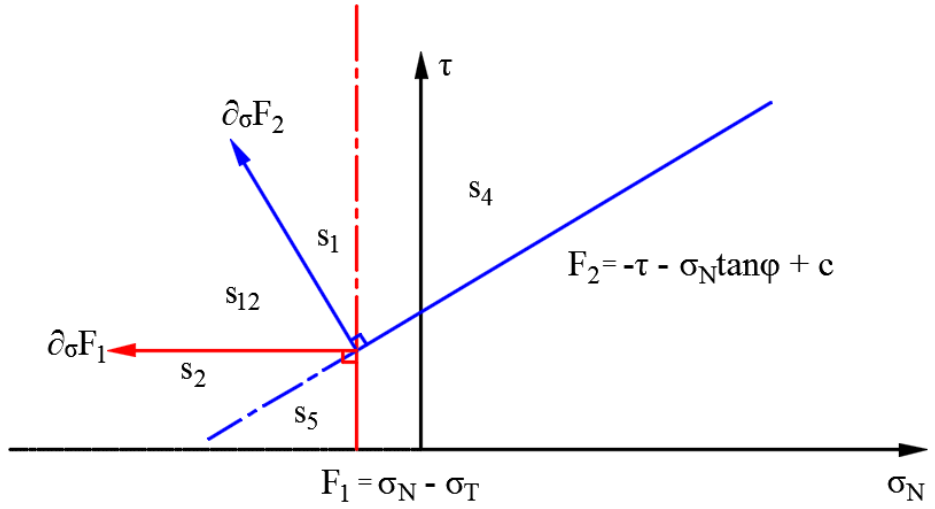

Figure 3.9 Determination of active surfaces and definition the multi-surface regions

3.3 Two different approaches of the equivalent continuum methods for a rock mass

There are two different approaches for the development of an equivalent model. The already existing method starts with the constitutive equations of the equivalent continuum and the representative element volume. The models consider the anisotropy of the joints in the elastic stage, then plastic corrections are performed according to the original ubiquitous or subiquitous model (only one joint participate in the failure criterion). The new developed approach describes the joint parameters by downgrading the rock matrix mechanical parameters to obtain an equivalent continua and treats the rock mass in the elastic stage as an isotrope model; the anisotropic behavior is induced by joint sets and all joints are considered during the plastic corrections.

3.3.1 Already existing approach of equivalent continuum model

3.3.1.1 Anisotropic performance in elastic stage

Several models have been developed based on the first approach (e.g. Agharazi, 2012, Wang 2014). For a representative elementary volume (REV) in this models, first a uniform stress state σ is considered. When subjected to a small stress increment of $d\sigma$, the corresponding incremental strain of the REV is $d\varepsilon$. The overall elastic strain increments are composed of two parts: one is the intact rock deformation $d\varepsilon^I$, the other is the deformation caused by the joint sets (a maximum of three is considered). In a global coordinate system the equation can be written as follows:

$$d\varepsilon = d\varepsilon^I + \sum_{\alpha=1}^{3} d\varepsilon_J^{\alpha} \tag{3.20}$$

The increment of strain can also be calculated by the equivalent compliance matrix of the REV:

$$\Delta\varepsilon = C_{eq}\ \Delta\sigma \tag{3.21}$$

The equivalent elastic compliance matrix of the rock mass can be expressed by summing up the compliance matrixes of the intact rock and three joint sets:

$$C_{eq} = C^I + C_J^{\alpha} + C_J^{\beta} + C_J^{\gamma} \tag{3.22}$$

It is assumed that the intact rock is isotropic. The incremental strain of the intact rock can be related to small increments of stress in the global coordinate system:

$$d\varepsilon^I = C^I\ d\sigma \tag{3.23}$$

where C^I is the elastic compliance matrix of the intact rock.

The elastic compliance of the joint set α is given by the equation below:

$$C_j^{\alpha} = L^{\alpha}\ L^{\alpha}\ \frac{1}{S^{\alpha}}\ D^{\alpha} \tag{3.24}$$

where D^{α} is the element of the compliance matrix associated with the *α-th* joint plane. L^{α} is the transformation matrix composed of directional cosines between local and global coordinates.

Further details on the formulation of this equivalent model can be found by Wang (2014).

3.3.1.2 Flow chart of the first approach

The flow chart shown in Figure 3.10 illustrates the individual calculation steps. This model adopts an elastic-perfect-plastic behavior for the rock matrix and the joint sets. All the three joint sets have stiffness and space parameters, but the joint sets have only one strength parameter set (jcohesion, jfriction, jtension). The first joint set is assumed to have the most critical orientation, no failure check is made for the second and the third joint set (Agharazi, 2013). For a detailed description of the plastic calculation process see (Itasca, 2007).

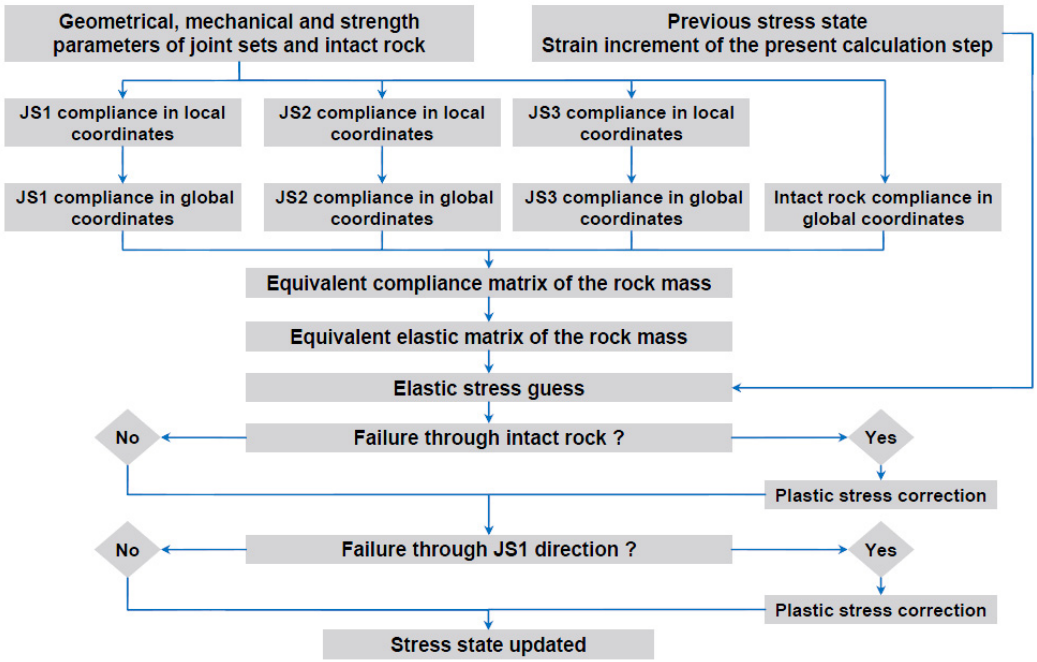

Figure 3.10 Flowchart for the equivalent continuum model (Agharazi, 2013)

3.3.2 The second approach for equivalent continuum models

3.3.2.1 Elastic matrix of the equivalent continuum model

Each component of the multi-jointed model is characterized by a spring-slider-dashpot system as shown in Figure 3.11. The springs represent the equivalent elastic behavior, the dashpot-slider modules represent the visco-plastic behavior.

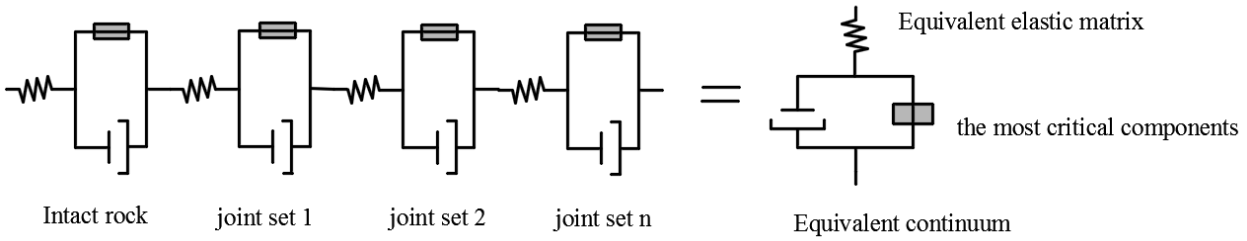

Figure 3.11 Scheme of the multi-joint model based on a spring-slider system

Assuming the rock matrix is isotropic in the elastic stage, the strain-stress relationship of the equivalent continuum model can be written in the following matrix form:

$$\begin{bmatrix} \varepsilon_1 \\ \varepsilon_2 \\ \varepsilon_3 \\ \varepsilon_4 \\ \varepsilon_5 \\ \varepsilon_6 \end{bmatrix} = \begin{bmatrix} \frac{1}{E_{eq}} & -\frac{\nu}{E_{eq}} & -\frac{\nu}{E_{eq}} & 0 & 0 & 0 \\ -\frac{\nu}{E_{eq}} & \frac{1}{E_{eq}} & -\frac{\nu}{E_{eq}} & 0 & 0 & 0 \\ -\frac{\nu}{E_{eq}} & -\frac{\nu}{E_{eq}} & \frac{1}{E_{eq}} & 0 & 0 & 0 \\ 0 & 0 & 0 & \frac{1}{G} & 0 & 0 \\ 0 & 0 & 0 & 0 & \frac{1}{G} & 0 \\ 0 & 0 & 0 & 0 & 0 & \frac{1}{G} \end{bmatrix} \begin{bmatrix} \sigma_1 \\ \sigma_2 \\ \sigma_3 \\ \sigma_4 \\ \sigma_5 \\ \sigma_6 \end{bmatrix} \tag{3.25}$$

In this matrix, E_{eq} is the equivalent deformation modulus of the rock mass, G is shear modulus and v is the poison's ratio of the intact rock. If n is the number of joint sets, S_i is the number of joints per 1 meter for joint set i, K_i is the stiffness of joint set i and E_M means Young's modulus of the intact rock matrix, then the equivalent deformation modulus is obtained:

$$\frac{1}{E_{eq}} = \sum_{i=1}^{n} \frac{S_i}{K_i} + \frac{1}{E_M} \tag{3.26}$$

The corresponding Young's modulus of the rock mass is related to the joint spacing and the joint stiffness. Springs in series representing matrix and joint stiffness will lead to significant reduction in overall stiffness as shown in Figure 3.12 and the whole flow chart of the multi-joint model can be seen in Figure 3.13.

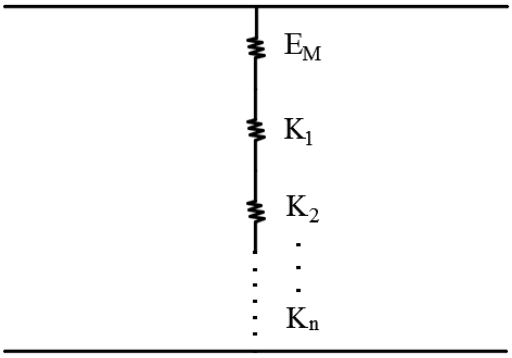

Figure 3.12 Downgraded stiffness for the equivalent continua

3.3.2.2 Calculation flow chart for multi-joint model

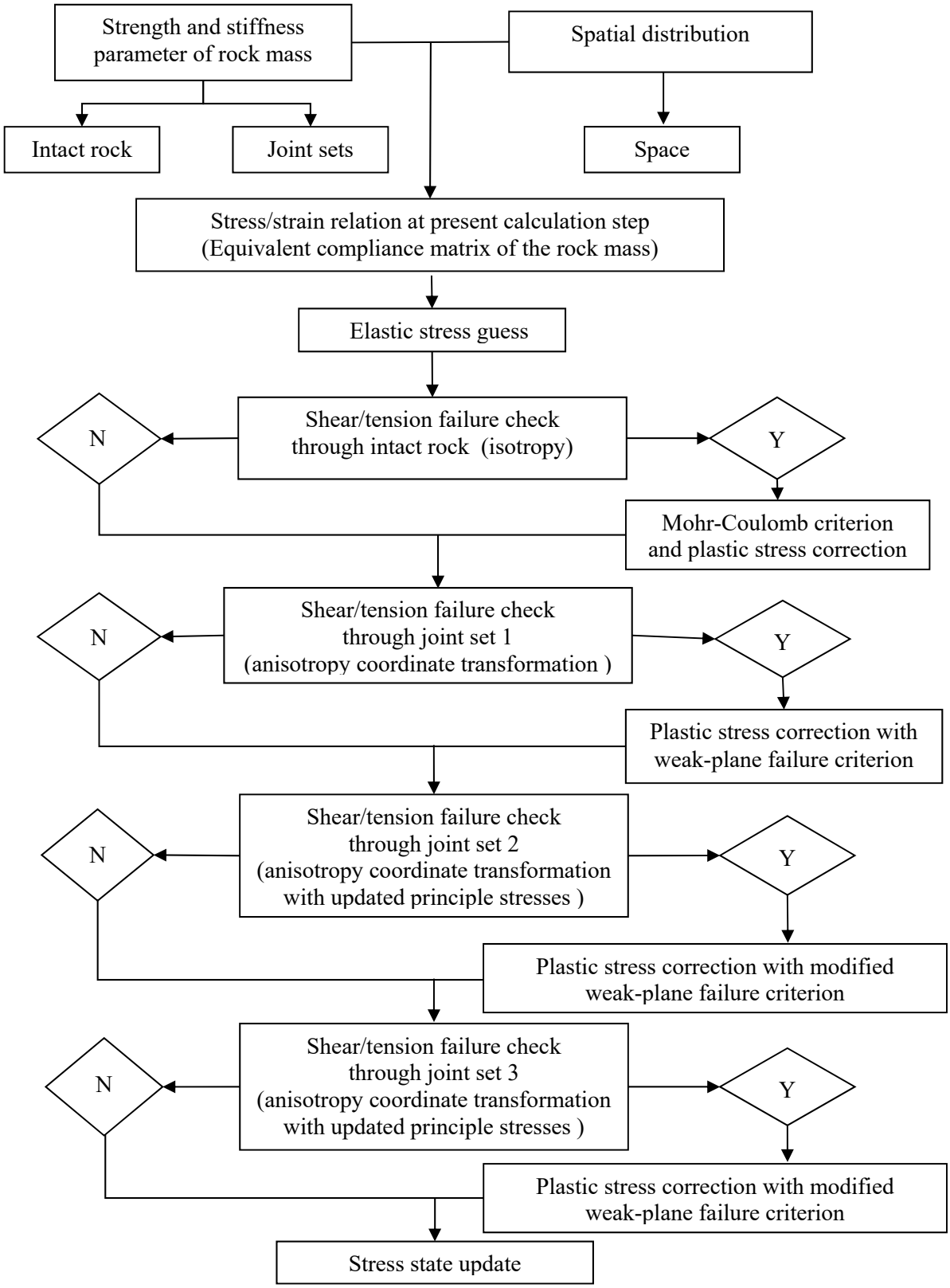

Figure 3.13 Flowchart for the equivalent continuum multi joint model

3.4 The equivalent continuum jointed rock mass model

3.4.1 Anisotropy behavior with one single joint

Jaeger (1960) introduced the plane of weakness model which focus on the shear failure of anisotropic rocks. Although considerable research work is done to propose various failure criteria for anisotropic rock masses, Jaeger's model is still widely used because of its simplicity. Jaeger's model is based on the Mohr-Coulomb criterion. In this section, Mohr's stress circle is used to interpret the jointed rock mass strength for different constellations between joint orientation and direction of loading. In case of uniaxial compression of a rock mass with only one single joint set, Mohr's stress circle representation is shown in Figure 3.14.

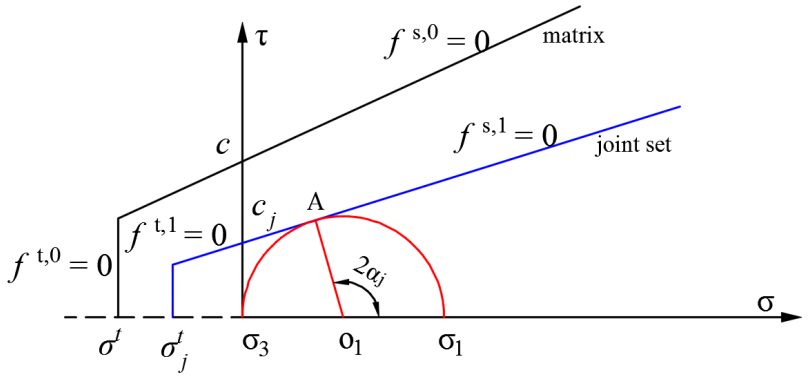

Figure 3.14 Mohr-Coulomb failure criterion with tension cut-off for matrix and joint

The point A indicates the failure stage. The corresponds joint angle α_j identifies the failure plane:

$$\alpha_j = 45^\circ + \frac{\phi_j}{2} \tag{3.27}$$

where ϕ_j is the joint friction angle, α_j is the critical joint angle measured from horizontal direction.

$f^{s,0}$ and $f^{t,0}$ are the shear and tension failure criteria for the rock matrix. $f^{s,1}$ and $f^{t,1}$ are the shear and tension failure criteria of the joint set. The shear strength criterion for this rock mass can be expressed as:

$$f^{s,0} = \frac{1}{2}(\sigma_1 - \sigma_3)\cos\phi + (\frac{1}{2}(\sigma_1 + \sigma_3) + \frac{1}{2}(\sigma_1 - \sigma_3)\sin\phi)\tan\phi - c \tag{3.28}$$

$$f^{s,1} = \frac{1}{2}(\sigma_1 - \sigma_3)\cos 2\alpha_j + (\frac{1}{2}(\sigma_1 + \sigma_3) + \frac{1}{2}(\sigma_1 - \sigma_3)\cos 2\alpha_j)\tan\phi_j^i - c_j^i \tag{3.29}$$

where c and ϕ are cohesion and internal friction angle for the matrix. c_j and ϕ_j are joint cohesion and joint friction angle. With increasing vertical stress, the intersection area between Mohr's stress circle and joint shear failure envelop grows as illustrated in Figure 3.15.

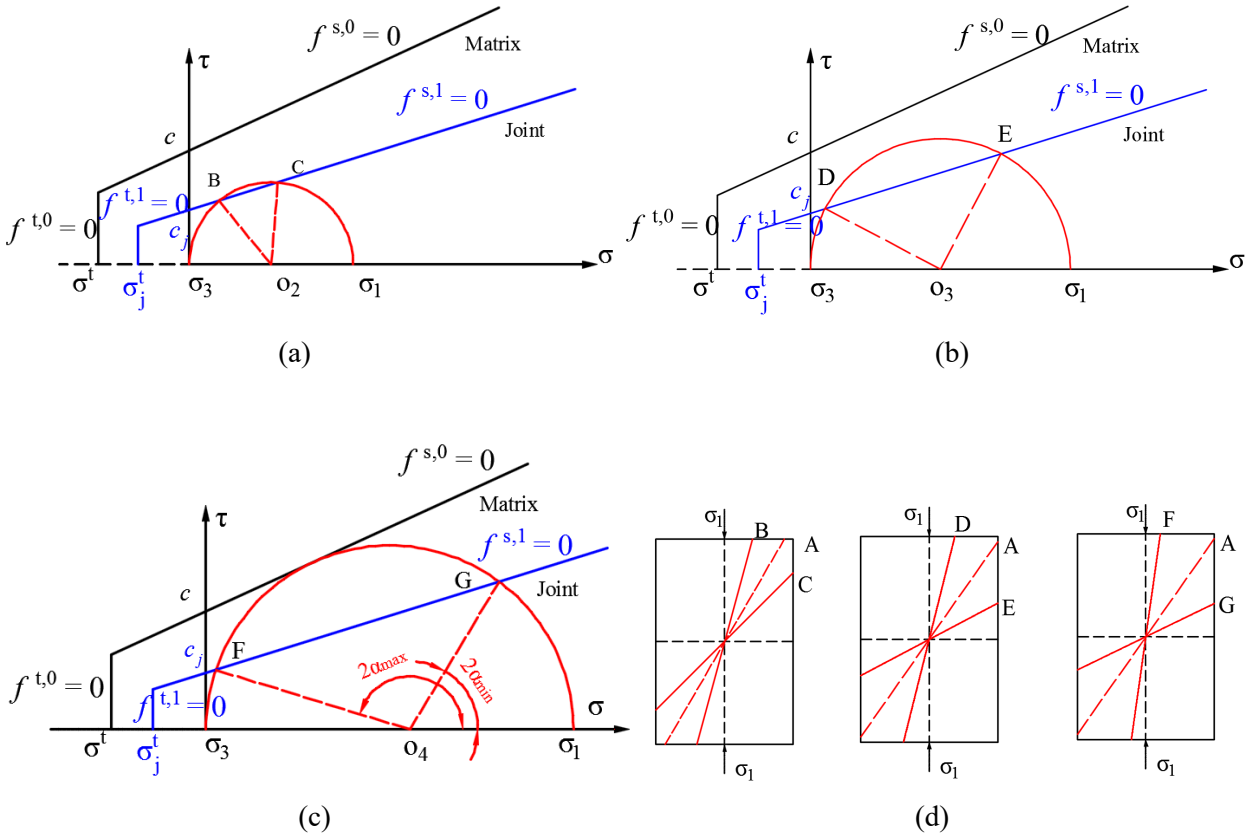

Figure 3.15 Failure criterion for intact rock and joint set in combination with different stress states: (a) Position B and C, (b) Position D and E, (c) Position F and G, (d) illustration of corresponding orientations of weak planes

The general expressions for the maximum and minimum failure angles are:

$$2\alpha_{\min} = \phi_j^i + \sin^{-1}((1 + \frac{(c_j^i \cot\phi_j^i - \sigma_1)(1 - \sin\phi)}{-\sigma\sin\phi + c\cos\phi})\sin\phi_j^i) \tag{3.30}$$

$$2\alpha_{\max} = \pi + 2\phi_j^i - 2\alpha_{\min} \tag{3.31}$$

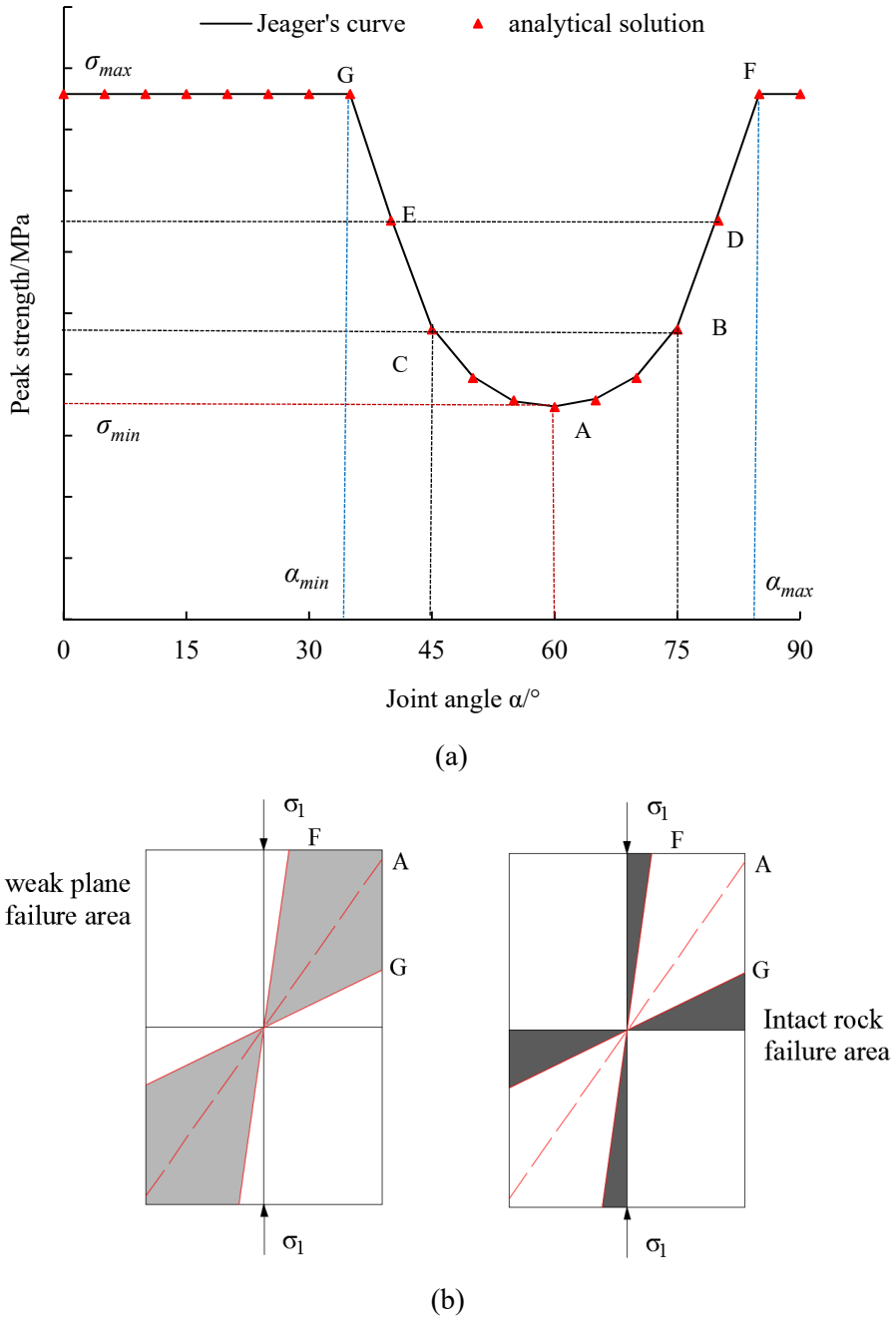

Figure 3.16 Schematic illustration for rock mass strength anisotropy: (a) Jaeger's curve, (b) dominant failure area for weak plane and for rock matrix

Point A indicates the orientation of the plane with minimum strength. Jaeger's complete curve, which shows the relationship between the joint angle and uniaxial compressive strength is shown in Figure 3.16.

3.4.2 Anisotropy behavior with two joint sets

Jaeger's model considers only one single weak-plane. If a jointed rock has more than one sets of joints, the potential failure modes which have to be considered increase. The different joints can have either identical strength parameters but different joint angles, or they have also different strength parameters. For three joint sets, the strength parameters including cohesion, friction angle and tension of the joints have 27 (3^3) possible combinations. Eight typical joint parameters constellations are shown in Table 3.1 and in Figure 3.17.

Table 3.1 Selected possible joint strength parameter combinations for two joints (MC model)

Constellation	Joint cohesion (c_j)	Joint friction angle (ϕ_j)	Joint tension (σ^t_j)
1	$c_j^1 = c_j^2$	$\phi_j^1 = \phi_j^2$	$\sigma_j^{t,1} = \sigma_j^{t,2}$
2	$c_j^1 > c_j^2$	$\phi_j^1 = \phi_j^2$	$\sigma_j^{t,1} > \sigma_j^{t,2}$
3	$c_j^1 > c_j^2$	$\phi_j^1 > \phi_j^2$	$\sigma_j^{t,1} > \sigma_j^{t,2}$
4	$c_j^1 > c_j^2$	$\phi_j^1 > \phi_j^2$	$\sigma_j^{t,1} < \sigma_j^{t,2}$
5	$c_j^1 = c_j^2$	$\phi_j^1 > \phi_j^2$	$\sigma_j^{t,1} < \sigma_j^{t,2}$
6	$c_j^1 > c_j^2$	$\phi_j^1 < \phi_j^2$	$\sigma_j^{t,1} > \sigma_j^{t,2}$
7	$c_j^1 = c_j^2$	$\phi_j^1 < \phi_j^2$	$\sigma_j^{t,1} > \sigma_j^{t,2}$
8	$c_j^1 < c_j^2$	$\phi_j^1 > \phi_j^2$	$\sigma_j^{t,1} > \sigma_j^{t,2}$

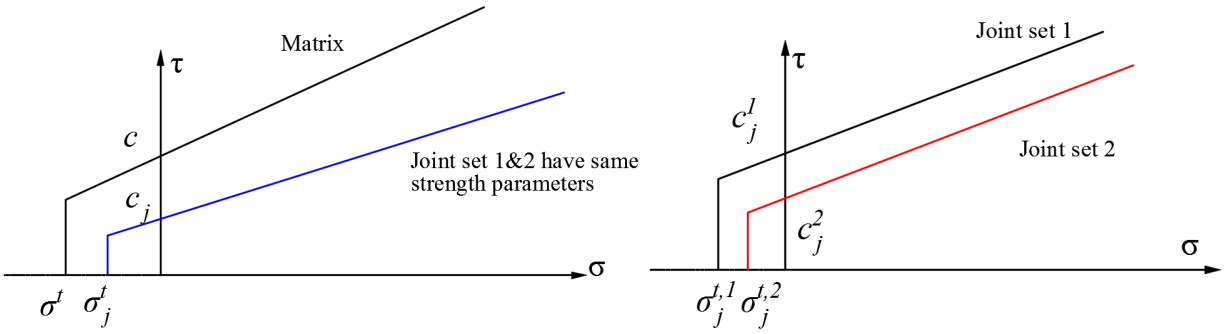

(1) (2)

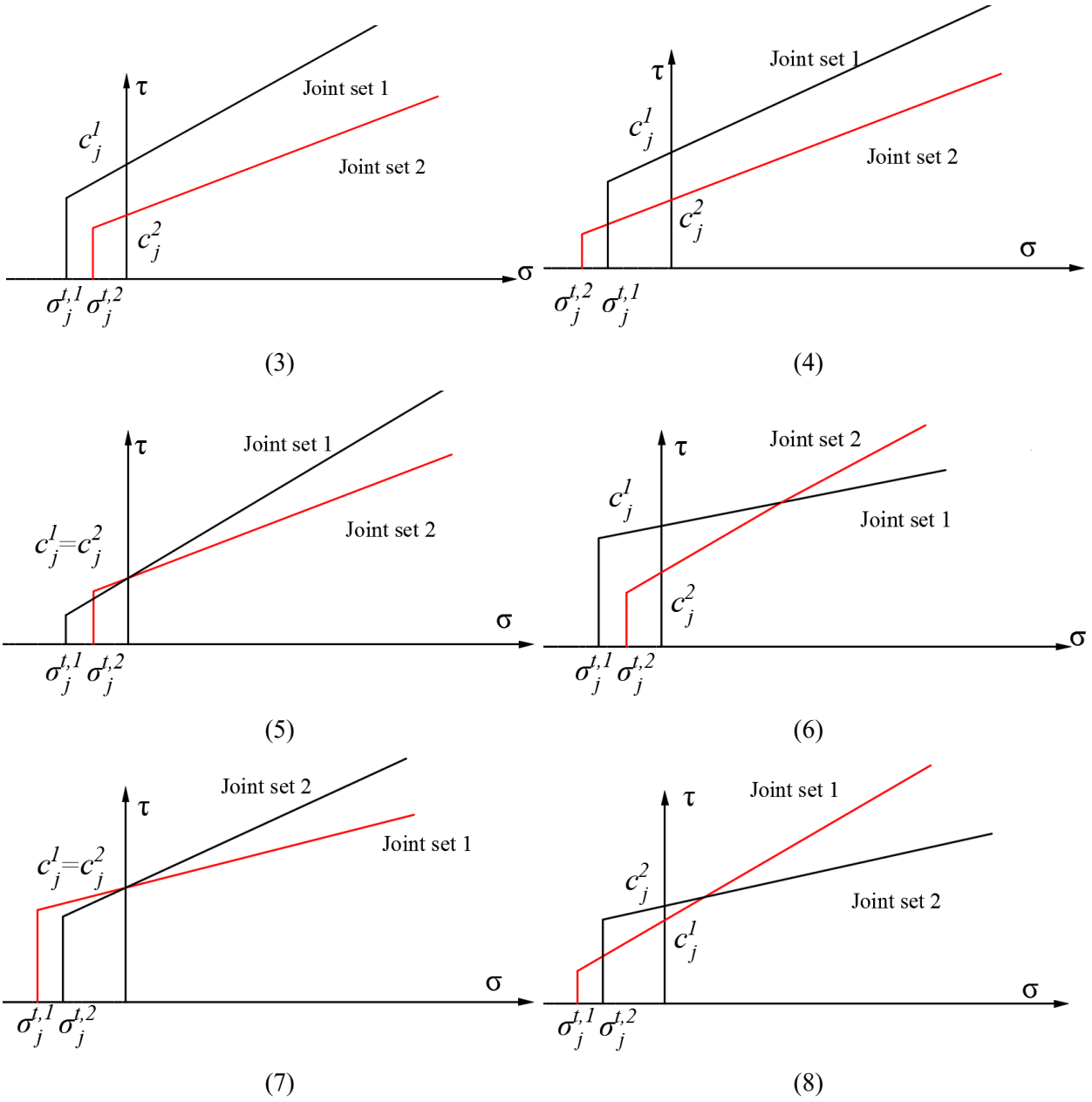

Figure 3.17 Sketch of potential failure envelops for two joints sets

3.4.2.1 Anisotropy performance of two perpendicular joints with identical strength parameters

If the strength properties of two perpendicular joints are identical, the failure area for the two weak planes can be obtained by mirroring at the principal stress axis as shown in Figure 3.18. A complete

Mohr-Coulomb circle is depicted as follows: the points H and I are in symmetrical position to the points F and G.

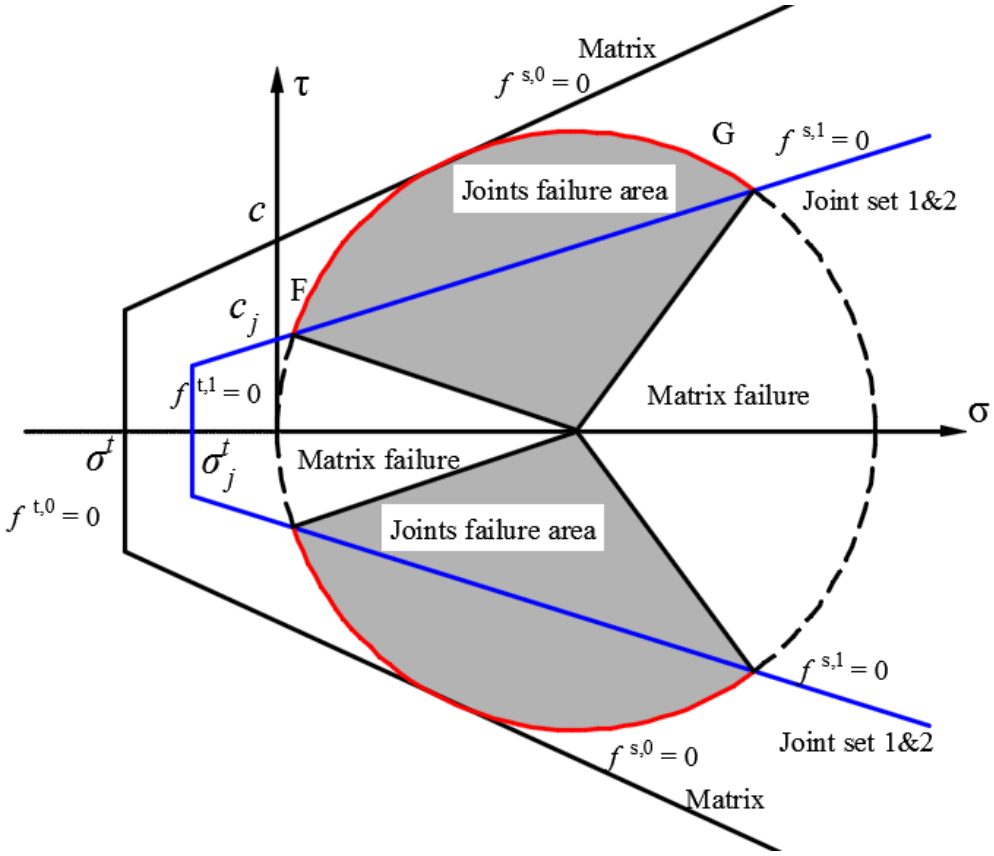

(a)

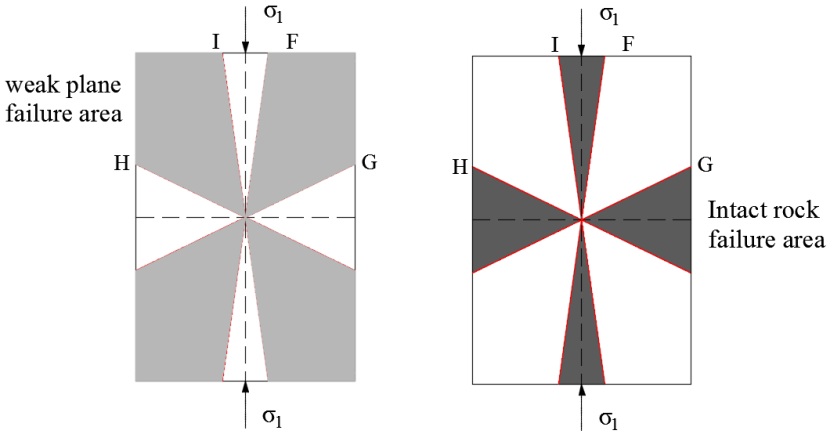

(b)

Figure 3.18 Rock mass with two perpendicular joint sets with identical strength parameters: (a) Mohr's circle representation, (b) illustration of failure and intact areas

3.4.2.2 Anisotropy performance for two joints with different strength parameters

There are two constellations for a rock mass which has two joints with different strength parameters: (I) one joint is weaker in all strength parameters (series 2 - 4 in Table 3.1) and (II) strength parameter have different relations to each other (series 5 - 8). In order to determine the failure region of the two joints, several Mohr's circles and the corresponding schemes are drawn. Figure 3.19 illustrates that joint set 1 has lower strength values compared to joint set 2. In Figure 3.19a the point A represents the least failure angle for joint set 2. At this stage for joint set 1, there is a region from B to C that failed.

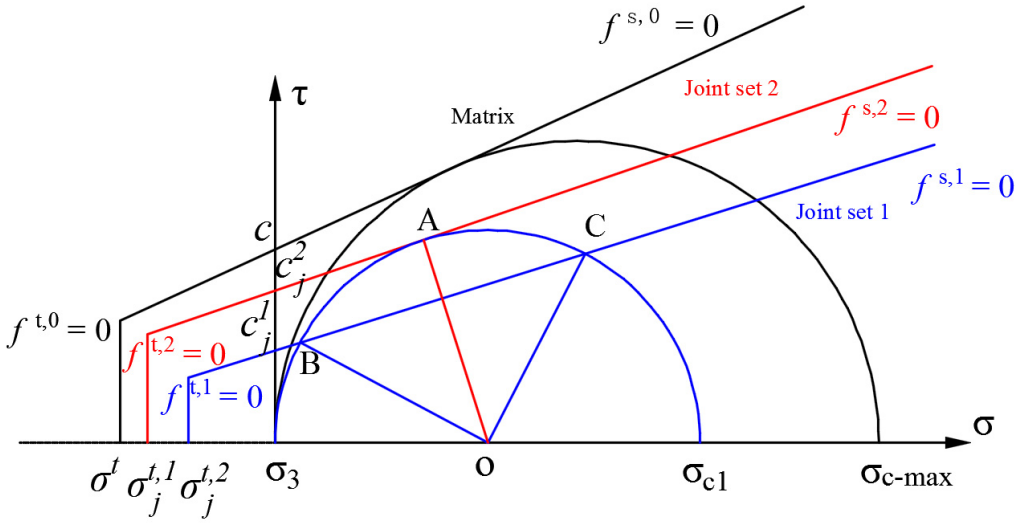

(a) Increasing vertical stress reached a critical state for joint set 2

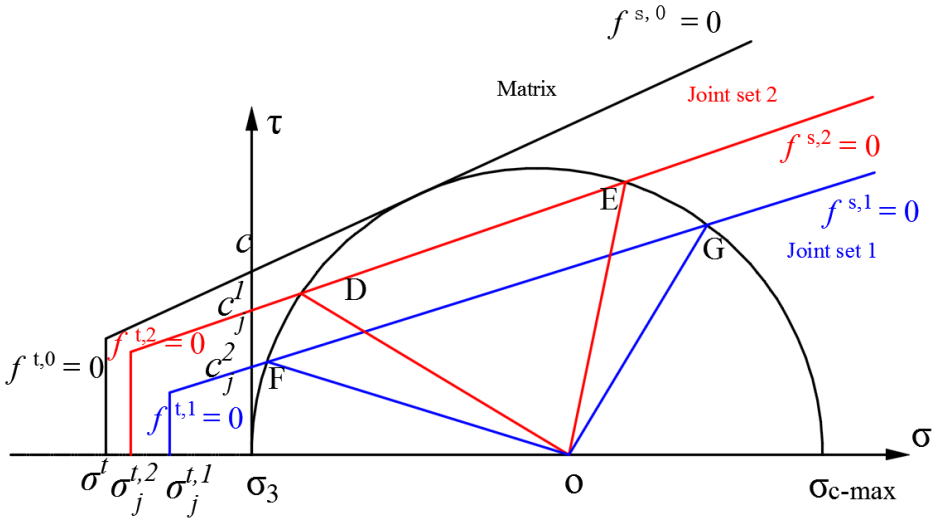

(b) Critical state for rock matrix and failure areas for weak planes

Figure 3.19 Rock mass containing two joint sets

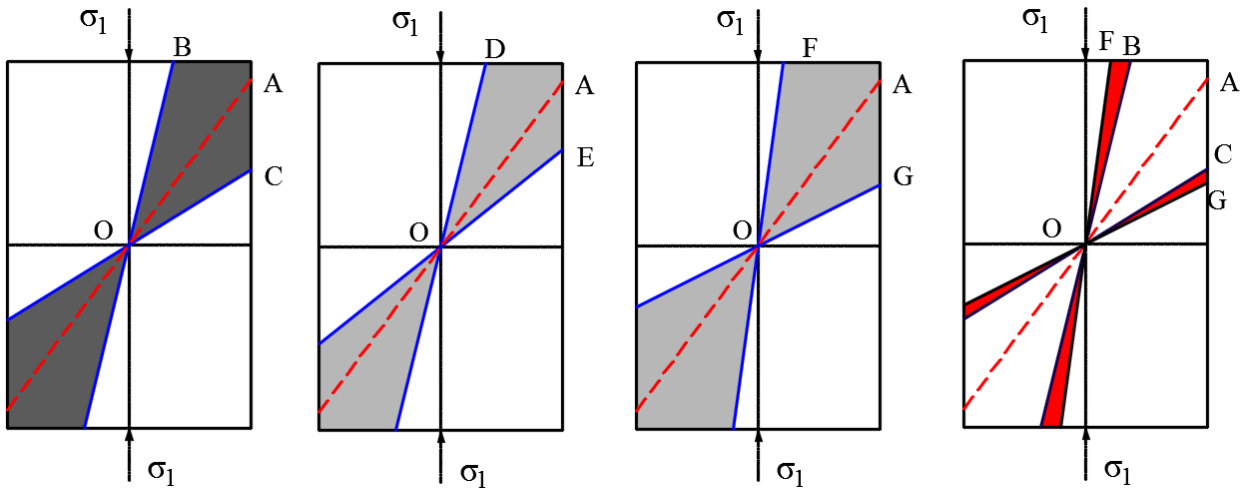

Figure 3.20 Failure areas for weak planes and for rock matrix

When the stress increases to the critical state of the rock matrix, the angle of the failure range for each joint is different (Figure 3.19b). If the jointed rock only has joint set 1, the FOG area in Figure 3.20 is the joint set failure range. If the rock mass has joint set 2 only, the gray area DOE represents the failure area. As can be seen in Figure 3.20, there is a significant difference between the area of DOE and FOG. If both joint sets are in zone BOC, failure usually occurs on joint 1. Compared with the black and grey regions, the joint set 2 might also reach the critical state when joint set 1 is located in region FOB or COG.

3.4.2.3 Anisotropic behavior for two joints with crossing yield surfaces

The most complicated situations for jointed rock mass are joints which shear failure criteria intersect, the effective failure envelope is determined by multiple shear and tension envelopes. The problem is illustrated by Mohr's circles and relevant joints or matrix failure areas in Figure 3.21 and Figure 3.22.

There are three Mohr circles in Figure 3.21a. The vertical (uniaxial) stress for the first circle is σ_{c1}, under this stress state, α_1 and α_2 are the corresponding failure angles for the two joints and $\alpha_1 < \alpha_2$. When the stress reaches stage σ_{c2}, the appeared angles are α_3 and α_4 and $\alpha_3 < \alpha_4$. α_1 and α_4 are the failure joint angles belonging to joint set 1. α_2 and α_3 are related to joint set 2. The third circle is

the critical threshold condition for intact rock, two joint sets failure envelopes are crossing in point A.

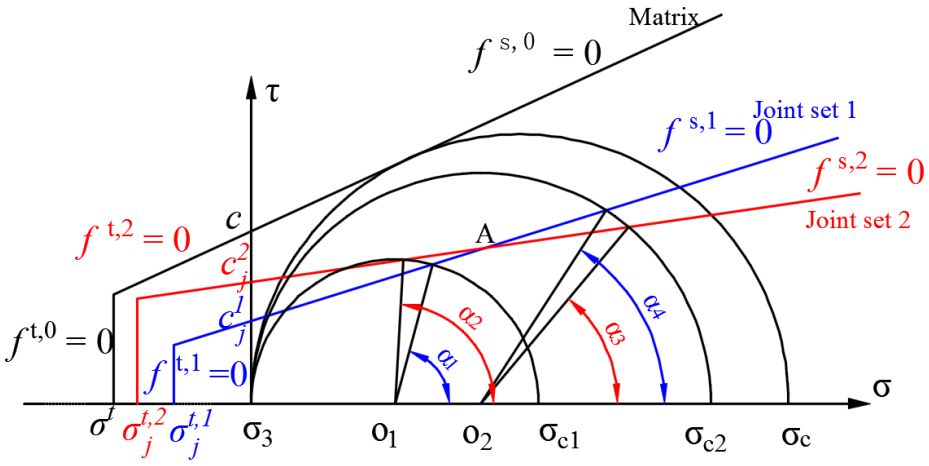

(a) Mohr circles and failure envelopes

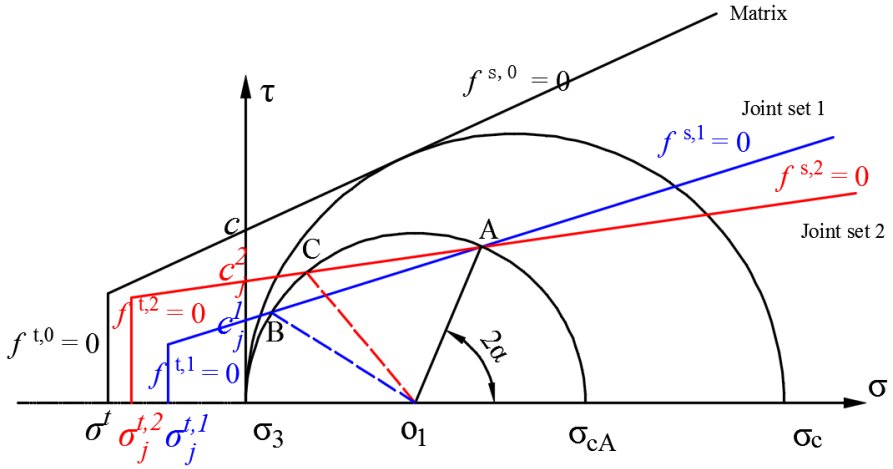

(b) Invalid area for uniaxial stress σ_{cA}

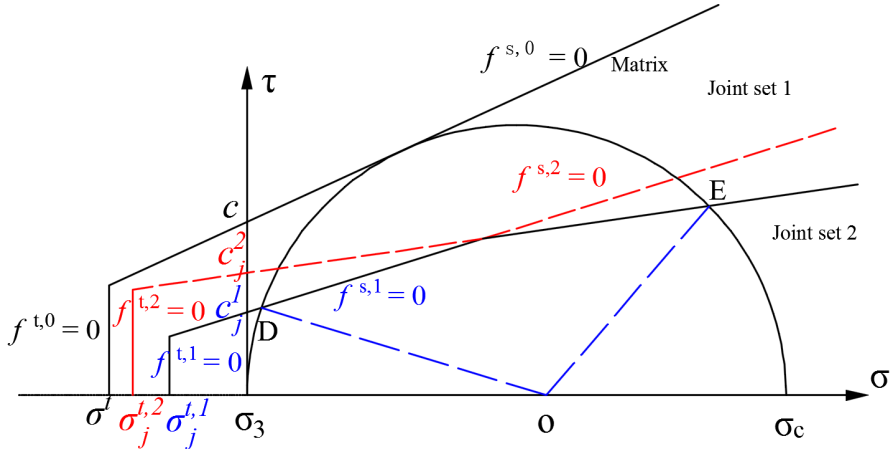

(c) Maximum invalid area for uniaxial stress σ_c

Figure 3.21 Rock mass containing two joint sets with intersecting failure criteria

Figure 3.21b illustrates the significant features of the multi-surface failure envelop: point A and joint angle α. BO_1A and CO_1A are the failure regions for joint set 1 and 2 ($BO_1A > CO_1A$). For same joint angle, joint in zone BO_1A has lower stress state than in zone CO_1A. As can be seen from Figure 3.21c, point D and E are the critical positions for the whole rock mass and DOE is the largest joint failure area. If both joint sets are in zone DOA, failure occurs on joint 1, otherwise in AOE area joint 2 becomes critical (see Figure 3.22).

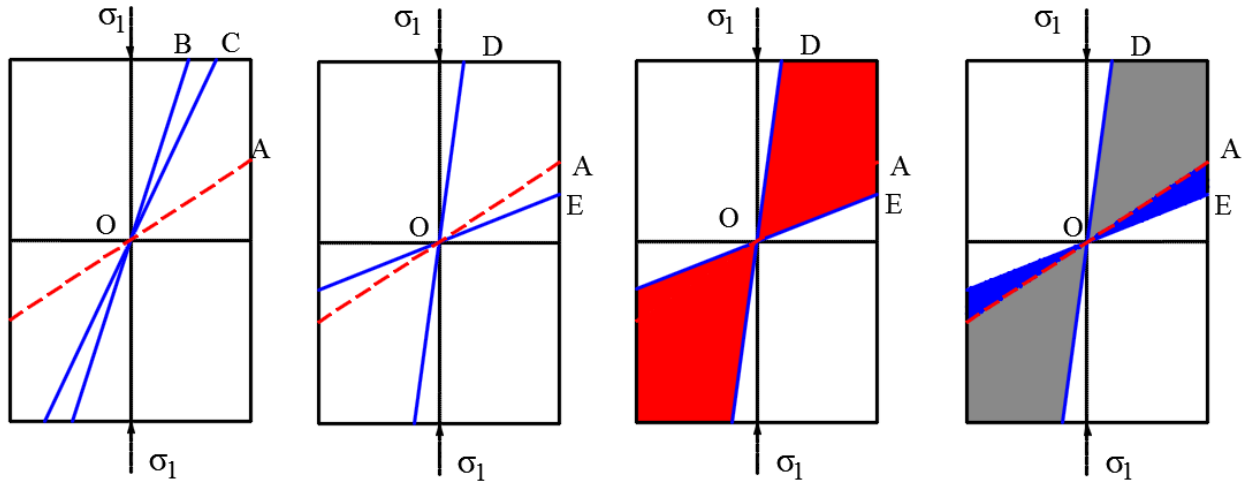

Figure 3.22 Multi-stage failure areas for jointed rock mass

3.4.2.4 Multi-surface plasticity for equivalent continuum jointed rock mass

Two types of joint failure criteria for a rock mass are discussed here. For constellations 1-4 in Table 3.1, a new function h is introduced into the σ-τ-plane in order to solve the multi-surface plasticity problem. This function h is represented by the diagonal between the representation of $f^{s,1} = 0$ and $f^{t,1} = 0$. According to the Figure 3.23a, the failure areas are divided into four sections. If shear failure is reached on the plane in section 1 and 2, the stress point will brought back to the curve $f^{s,1} = 0$. If the stress state belongs to the section 3 or 4, local tensile failure takes place and the stress point will brought back to $f^{t,1} = 0$.

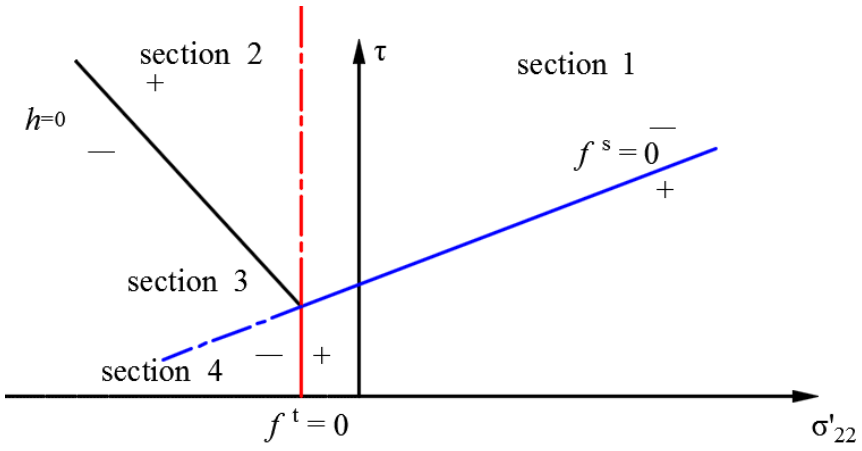

(a) Joint failure criterion for constellations 1-4 (see Table 3.1)

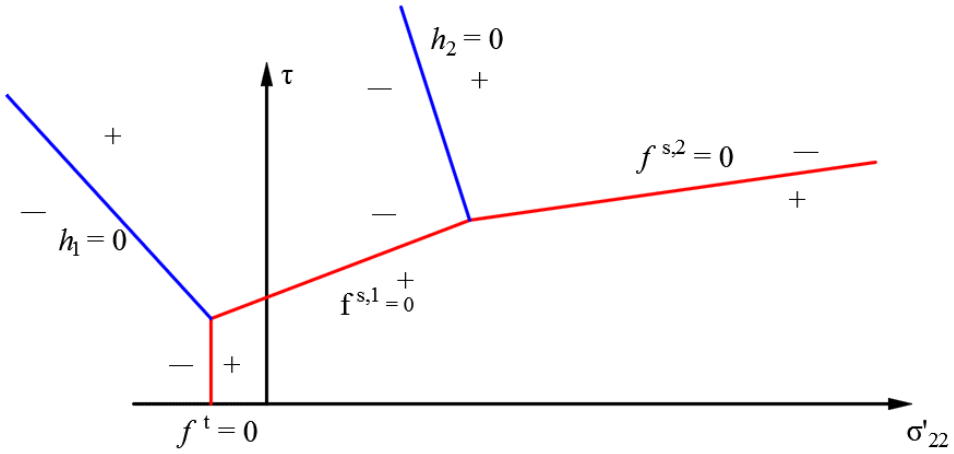

(b) Multi-stage failure criteria for joints having different parameters

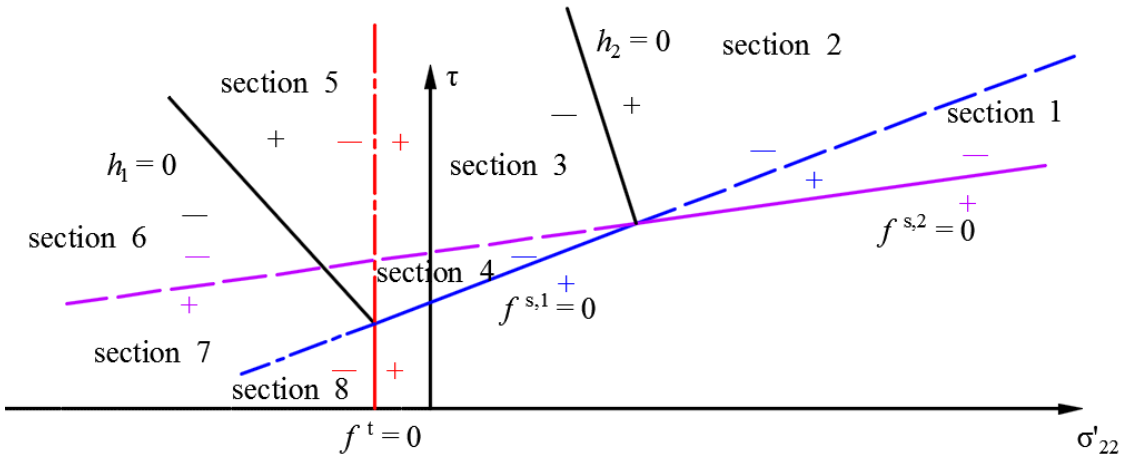

(c) Eight sections for solving the multi-surface plasticity problem

Figure 3.23 Two kinds of joint failure criteria in FLAC for a jointed rock mass

For the constellations 5 - 8 in Table 3.1, two new functions h_1 and h_2 were introduced in the τ-σ-plane in order to solve the multi-surface plasticity problem. Function h_1 represents the diagonal between $f^{s,1} = 0$ and $f^{t} = 0$. Function h_2 represents the diagonal between $f^{s,1} = 0$ and $f^{s,2} = 0$. The stress state which violates the joint failure criteria will be located in sections 1 to 8 corresponding to positive or negative domain of $f^{t} = 0, f^{s,1} = 0$, $f^{s,2} = 0$, $h_1 = 0$ and $h_2 = 0$. According to Figure 3.23c, if for the second joint set shear failure is detected on the plane in section 1 and 2, the stress point will be brought back to the curve $f^{s,2} = 0$. If for the first joint set shear failure is detected in section 3, 4 and 5, the stress point will be brought back to the curve $f^{s,1} = 0$. If the stress state belongs to section 6, 7 or 8, local tensile failure takes place and the stress point will be brought back to $f^{t} = 0$. $f^{t} = 0$ is the minimum tension failure criterion for the two joints inside a rock mass.

3.4.3 Joint parameters influencing the strength of a rock mass

There are many factors which impact the strength of the rock mass. If the effect of external factors such as boundary conditions and load conditions remain the same, then the geometry of the joints and their strength parameters are the most important factors that affect the strength of a rock mass.

The qualitative description of the relation between joint strength parameters and joint failure regions are discussed in this section. The colored parts in Figure 3.24 illustrate the areas where yield can occur at the joints. Gray colored zones stand for the two weak planes with the same parameters. If one of the joints has always stronger strength parameters than the other (constellations 2-3 in Table 3.1), the red regions mark the joint failure area and all regions are determined by the weaker joint. The weaker joint in Figure 3.24b has the same strength parameters as given in Figure 3.24a, which means the areas of the two FOG are the same. The blue colored areas consist of two parts, DOA and AOE. Figure 3.24c indicates two joints with crossing failure areas (constellations 5 - 8 in Table 3.1). Area DOE is larger than that of FOG.

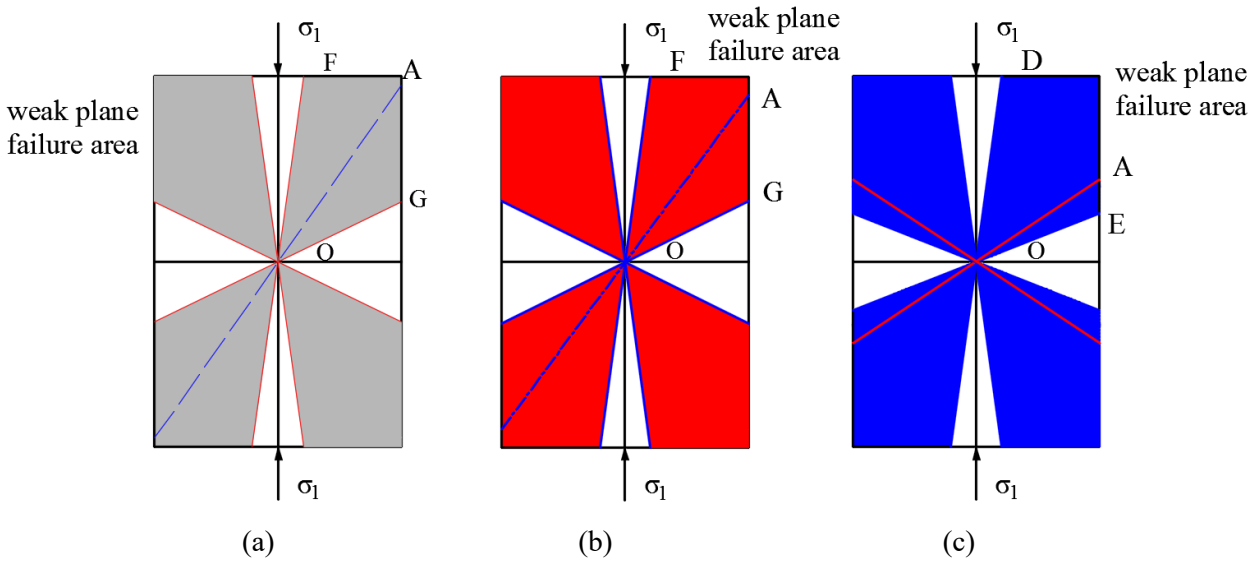

Figure 3.24 Three kinds of joint failure areas defined by joint strength parameters

In terms of Mohr's circle and the colored areas in Figure 3.25: if two joints have same friction angle, the failure areas are determined by the lower joint cohesion. Lower joint cohesion and smaller joint friction angle leads to a large range where the joint may yield.

If the strength parameters for a rock mass are fixed, the geometric nature of joint intersections would be the only factor which influence the mechanical response of the rock. Joints form the weakest component of the rock masses and joint angles can result in a notable decrease in the strength of a rock mass (Hoek, 1983). Figure 3.25a shows a constellation, where two joints have the same strength parameters (both are located in the 1st quadrant). The corresponding Mohr's circle illustrates that the red colored joint (σ_{c1}) is more critical than the blue colored joint (σ_{c2}). In that case, the key element to determine the strength value of the rock mass is the most critical joint angle.

According to the second graph in Figure 3.25, the strength parameters for the two joints are not the same. α_1 and α_2 are the angles for joint position H and I. Joint I is the weaker joint. The corresponding failure strength for the blue colored joint (σ_{c2}) is larger than that of red one (σ_{c1}). More joint combinations for two joint sets are discussed in section 3.6.

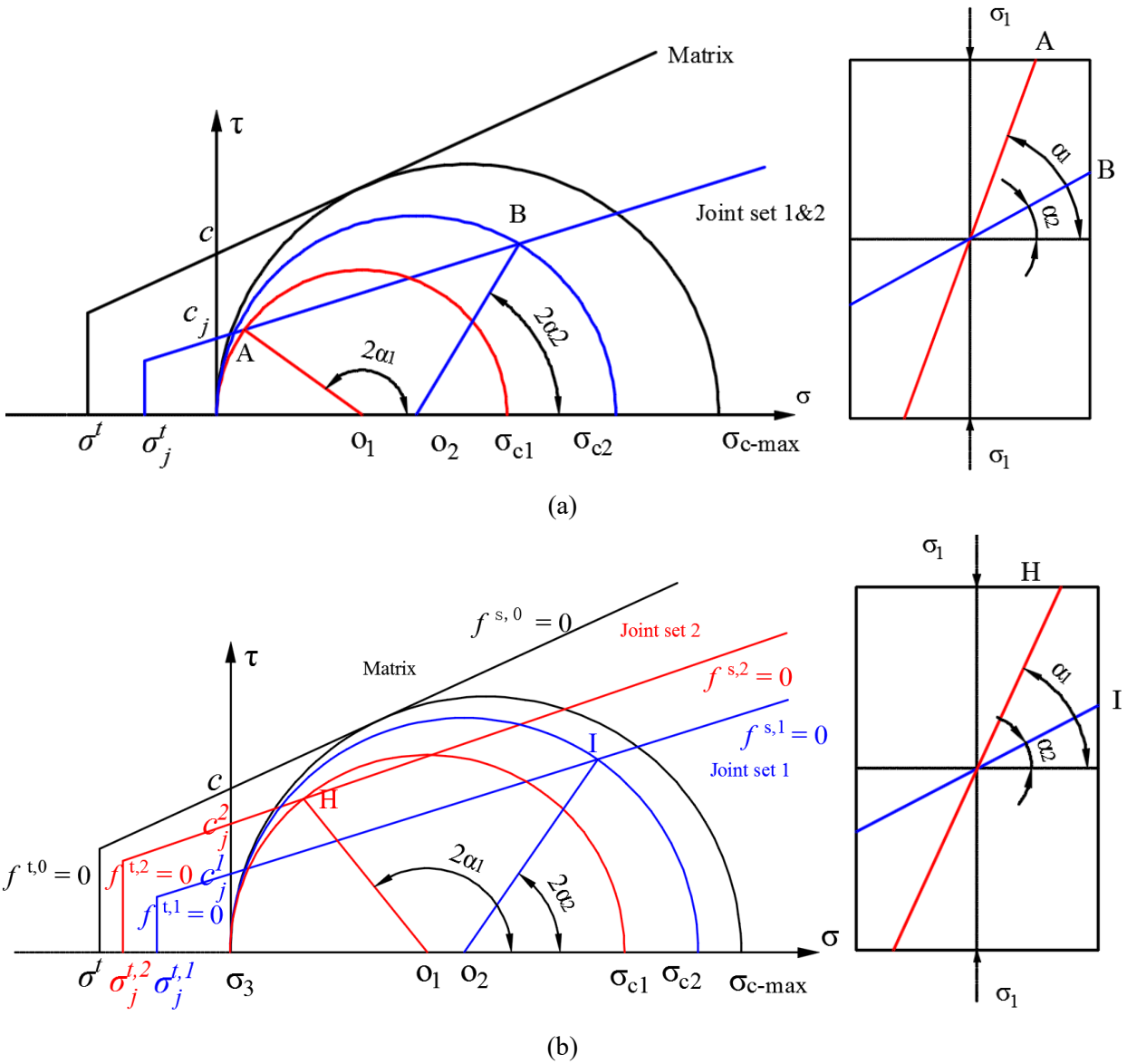

Figure 3.25 Illustration of influence of joint angle and strength parameters on rock mass strength

3.5 Plastic corrections for rock matrix and joints

The constitutive relations of the intact and the joint sets using the new developed multi-joint model are described in this section. The model assumes an elastic-perfect plastic behavior. There are up to three arbitrary joint orientations in the model using the ubiquitous joint formulation.

3.5.1 Global and local coordinate axes for a joint plane in 2D

The joint angles θ_j (j = 1, 3) in the multi-joint model are measured counterclockwise from the global x-axis as shown in Figure 3.26. In this section, a particular joint i is considered as a representative joint. The global stress components σ_{xy} are obtained after the plastic corrections. The local stress components can be expressed as:

$$\begin{cases} \sigma'_{11} = \sigma_{11}\cos^2\theta_j + 2\sigma_{12}\sin\theta_j\cos\theta_j + \sigma_{22}\sin^2\theta_j \\ \sigma'_{22} = \sigma_{11}\sin^2\theta_j - 2\sigma_{12}\sin\theta_j\cos\theta_j + \sigma_{22}\cos^2\theta_j \\ \sigma'_{33} = \sigma_{33} \\ \sigma'_{12} = -(\sigma_{11} - \sigma_{22})\sin\theta_j\cos\theta_j + \sigma_{12}(\cos^2\theta_j - \sin^2\theta_j) \end{cases} \tag{3.32}$$

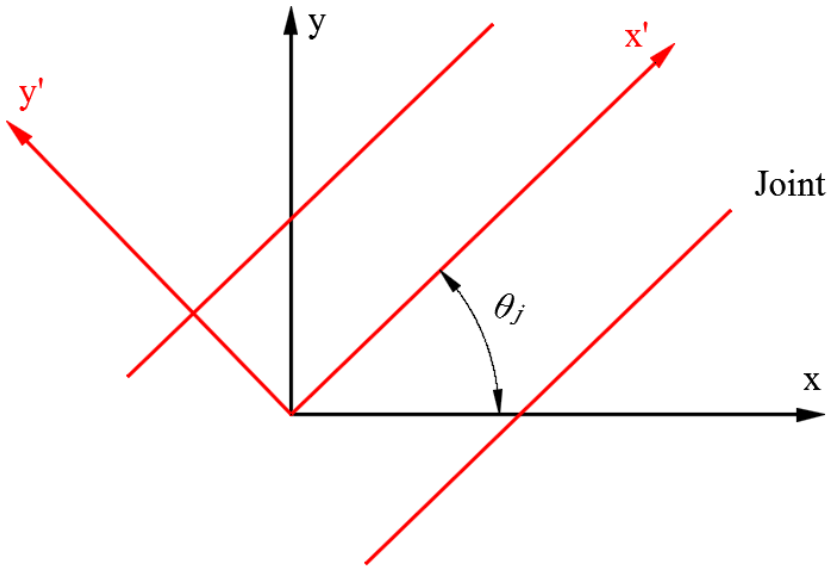

Figure 3.26 A weak plane oriented at an angle θ to the global corrdinate system

There are up to three joint directions in the model, which means totally 12 local stress components participating in the plastic corrections. In the FLAC operational process, the general failure of the Mohr-Coulomb matrix is first detected and the relevant plastic corrections are used to obtain the new stresses. Then failure on joints are checked and analyzed. More detailed information are given below.

3.5.2 Yield criterion for intact material

The failure criterion of the intact rock (matrix) is represented in the plane (σ, τ) and shown in Figure 3.27. Equation 3.33-3.36 are the yield envelopes and potential functions related to the flow rule and failure criterion.

$$f^{s,0} = -\tau - \sigma_{22} \tan\phi + c \tag{3.33}$$

$$f^{t,0} = \sigma^t - \sigma_{22} \tag{3.34}$$

$$g^{s,0} = -\tau - \sigma_{22} \tan\psi \tag{3.35}$$

$$g^{t,0} = -\sigma_{22} \tag{3.36}$$

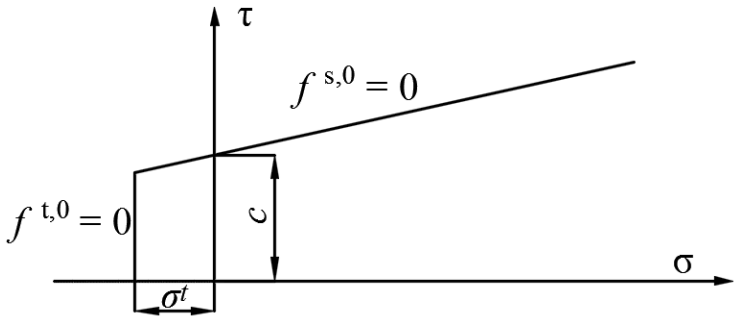

Figure 3.27 Illustration of the intact rock failure criterion

3.5.3 Composite failure criterion for a weak plane

The local yield criterion for a joint is a Mohr-Coulomb failure criterion with tension cut-off. The flow rule for shear failure is non-associated, and the tension flow rule is associated. For the joint set i (i = 1, 3), the local failure envelops are defined as $f^{s,i}$ and $f^{t,i}$ according to the following equations:

$$f^{s,i} = -\tau_j - \sigma'_{22} \tan\phi_j^i + c_j^i \tag{3.37}$$

$$f^{t,i} = \sigma^{t,i} - \sigma'_{22} \tag{3.38}$$

where ϕ_j^i, c_j^i and $\sigma^{t,i}$ represent the friction, cohesion and tensile strength for joint set i. If $\phi_j^i \neq 0$, the tensile strength can be not larger than $\sigma_{\max}^{t,i}$, with $\sigma_{\max}^{t,i} = \frac{c_{ji}}{\tan\phi_j^i}$. $\tau_j^i = \left|\sigma_j'^i\right|$ stand for the magnitude of the tangential stress component of a joint, and the corresponding strain variable is γ_j^i. For the multi-joint model, three joint sets have six failure criterions in the (σ'_{22}, τ) plane, as illustrated in Figure 3.28.

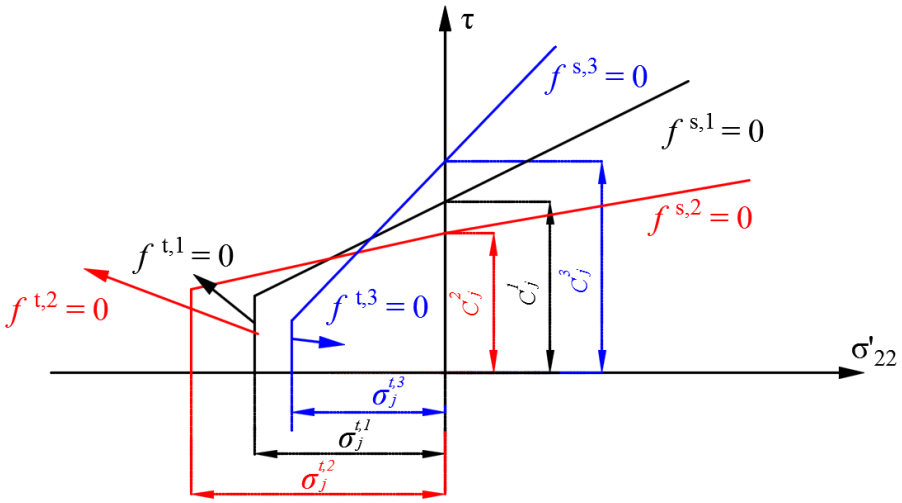

Figure 3.28 Three joint failure criterions in a multi-joint model

In this model, three random joint sets with independent strength parameters are present in a Mohr-Coulomb solid. Yield may occur in either the matrix or as slip or tension failure at the joints, or in combinations. Obviously, various types of failure could happen in each computational step, including single or simultaneous shear yielding on 1, 2 or 3 weak planes, tensile failure on one or more joints as well as combined shear and tensile failure. For each computational step, only one joint exhibiting the most critical situation in shear yielding or tensile yielding is considered for appropriate stress corrections. The shear yielding on joint i corresponds to a non-associated flow rule and the function is:

$$g^{s,i} = -\tau_j^i - \sigma'_{22}\tan\psi_j^i \tag{3.39}$$

where the parameter ψ_j^i is the joint dilation angle of joint set i.

Tensile failure on a joint set corresponds to an associated flow rule, and the potential functions is:

$$g^{t,i} = -\sigma'_{22} \tag{3.40}$$

During each step of the FLAC calculation process, the models obtain the old stress (previous stress state) based on the strain increment of the present calculation step. Then the new stress values for the current step are updated. The new stress state in equation 3.41 can be expressed as the sum of stress increments and the old stress:

$$\sigma_i^N = \sigma_i^O + \Delta\sigma_i \tag{3.41}$$

The stress increments are related to the elastic increments of the rock mass and S_i is a linear function of the elastic strain increments Δe_n^e.

$$\Delta\sigma_i = S_i\,(\Delta e_n^e) \tag{3.42}$$

In the multi-joint rock model holds: when plastic deformation is allowed, for each step the stress increment, the failure of the intact rock and the joint sets are checked, the code also checks for multiple active yield surfaces. After each stress increment, general failure through the intact rock is first checked and if there is any violation of the failure criterion, the corresponding plastic stress correction is applied. According to the updated stress state, a further check is made for the failure of the joint set (Agharazi, 2013). Figure 3.10 shows the algorithm of the multi-joint model during each time step of the calculation in FLAC.

3.5.3.1 Plastic corrections: shear yielding on a joint

If shear failure at the joint occurs, equation 3.39 for $g^{s,i}$ is used. After partial differentiation, the flow rule has the following form:

$$\begin{cases} \Delta e'^{p,i}_{11} = \lambda^{s,i} \dfrac{\partial g^{s,i}_j}{\partial \sigma'^{s,i}_{11}} \\ \Delta e'^{p,i}_{22} = \lambda^{s,i} \dfrac{\partial g^{s,i}_j}{\partial \sigma'^{s,i}_{22}} = -\lambda^{s,i}_j \tan\psi^i_j \\ \Delta e'^{p,i}_{33} = \lambda^{s,i} \dfrac{\partial g^{s,i}_j}{\partial \sigma'^{s,i}_{33}} \\ \Delta \gamma'^{p,i}_j = \lambda^{s,i} \dfrac{\partial g^{s,i}_j}{\partial \tau^i_j} = -\lambda^{s,i}_j \end{cases} \tag{3.43}$$

$\lambda_l^{s,i}$ is given by equation 3.44:

$$\lambda^{s,i} = \frac{f^{s,i}(\sigma'_{22}, \tau^i_j)}{2G + \alpha_1 \tan\phi^i_j \tan\psi^i_j} \tag{3.44}$$

Finally, the global stress corrections for joint shear failure are obtained by transformation of the local stress corrections into the global coordinate system, as expressed below:

$$\begin{cases} \Delta\sigma_{11} = -2\Delta\sigma'^{s,i}_{12} (\cos\theta^i_j \sin\theta^i_j) + \Delta\sigma'^{s,i}_{11} \cos^2\theta^i_j + \Delta\sigma'^{s.i}_{22} \sin^2\theta^i_j \\ \Delta\sigma_{22} = 2\Delta\sigma'^{s,i}_{12} (\cos\theta^i_j \sin\theta^i_j) + \Delta\sigma'^{s,i}_{11} \sin^2\theta^i_j + \Delta\sigma'^{s.i}_{22} \cos^2\theta^i_j \\ \Delta\sigma_{33} = \Delta\sigma'^{s,i}_{33} \\ \Delta\sigma_{12} = \Delta\sigma'^{s,i}_{12} (\cos^2\theta^i_j - \sin^2\theta^i_j) + (\Delta\sigma'^{s,i}_{11} - \Delta\sigma'^{s,i}_{22}) \sin\theta^i_j \cos\theta^i_j \end{cases} \tag{3.45}$$

3.5.3.2 Plastic corrections: tensile yielding on a joint

The tensile flow rule is obtained from partial differentiation of expression $g^{t,i}$ as follows:

$$\begin{cases} \Delta e'^{p,i}_{11} = \lambda^{t,i} \dfrac{\partial g^{t,i}_j}{\partial \sigma'^{t,i}_{11}} \\ \Delta e'^{p,i}_{22} = \lambda^{t,i} \dfrac{\partial g^{t,i}_j}{\partial \sigma'^{t,i}_{22}} = -\lambda^{t,i}_j \\ \Delta e'^{p,i}_{33} = \lambda^{t,i} \dfrac{\partial g^{t,i}_j}{\partial \sigma'^{t,i}_{33}} \\ \Delta \gamma'^{p,i}_j = \lambda^{t,i} \dfrac{\partial g^{t,i}_j}{\partial \tau^{t,i}_j} \end{cases} \tag{3.46}$$

where the $\lambda^{t,i}$ is given by equation 3.48:

$$\lambda^{t,i} = \frac{f^{t,i}_{\min}(\sigma'^{\,t,i}_{22})}{\alpha_1} \tag{3.47}$$

After transformation of local stress into global coordinate system, the stress corrections become:

$$\begin{cases} \Delta\sigma_{11} = (\sigma^{t,i}_{\min} - \sigma'^{s,i}_{22})\,(\dfrac{\alpha_2}{\alpha_1}\cos^2\theta^i_j + \sin^2\theta^i_j) \\ \Delta\sigma_{22} = (\sigma^{t,i}_{\min} - \sigma'^{s,i}_{22})\,(\dfrac{\alpha_2}{\alpha_1}\sin^2\theta^i_j + \cos^2\theta^i_j) \\ \Delta\sigma_{33} = (\sigma^{t,i}_{\min} - \sigma'^{s,i}_{22})\,\dfrac{\alpha_2}{\alpha_1} \\ \Delta\sigma_{12} = -(\sigma^{t,i}_{\min} - \sigma'^{s,i}_{22})\,(1 - \dfrac{\alpha_2}{\alpha_1})\cos\theta^i_j \sin\theta^i_j \end{cases} \tag{3.48}$$

These global stress components are transformed into principle stresses and modified to other joints.

3.5.4 Large-strain update of joint orientation

In the large strain mode, for each zone the joint angle θ_j has to be adjusted to account for rigid body rotations or deformations. The global components of $\Delta[n]^d$ can be obtained from the local corrections parameters $\Delta[n]'^d$ of the joint:

$$\Delta[n]^d = [C]\Delta[n]'^d \tag{3.49}$$

where $[C]$ is a matrix rotation tensor related to three columns of the direction cosines in local coordinate.

3.6 Applications for strength prediction

3.6.1 Strength anisotropy of a rock mass containing two perpendicular joints

There is an unlimited number of joint configurations in terms of their orientation (see conclusions in section 3.4). In order to reproduce Jaeger's curve, some special cases are selected and discussed in this section.

3.6.1.1 Two perpendicular joints with same strength parameters

A series of triaxial compressive tests on samples with two perpendicular joints has been introduced in chapter 2 (Ghazvinian, 2012). The uniaxial compressive strength of a jointed rock sample is a function of the angles formed by the loading direction and the joints. The FLAC verification problem entitled "Uniaxial Compressive Strength of a Jointed Material Sample" (Itasca 2011) is considered here, using the multi-joint model, properties are the same as those documented in the manual which are listed in Table 3.2.

Figure 3.29 compares results obtained from FLAC simulations with two perpendicular joints and the analytical strength predictions (Hoek and Brown 1980) for different joint angles between 0° and 90°. The match is good with a relative error smaller than 1 % for all constellations.

Table 3.2 Mechanical properties of the jointed rock mass

Material parameters	Intact rock	Joint 1	Joint 2
Density	1810 kg/m³	———	———
Young's modulus (E)	20.03 MPa	———	———
Poisson's ratio (v)	0.24	———	———
Cohesion (c)	2 kPa	———	———
Friction angle (ϕ)	40°	———	———
Dilation angle (ψ)	0°	———	———
Joint cohesion (c_j)	———	1 kPa	1 kPa
Joint friction angle (ϕ_j)	———	30°	30°
Joint tensile strength	———	2 kPa	2 kPa
Joint angle	———	α	α + 90°

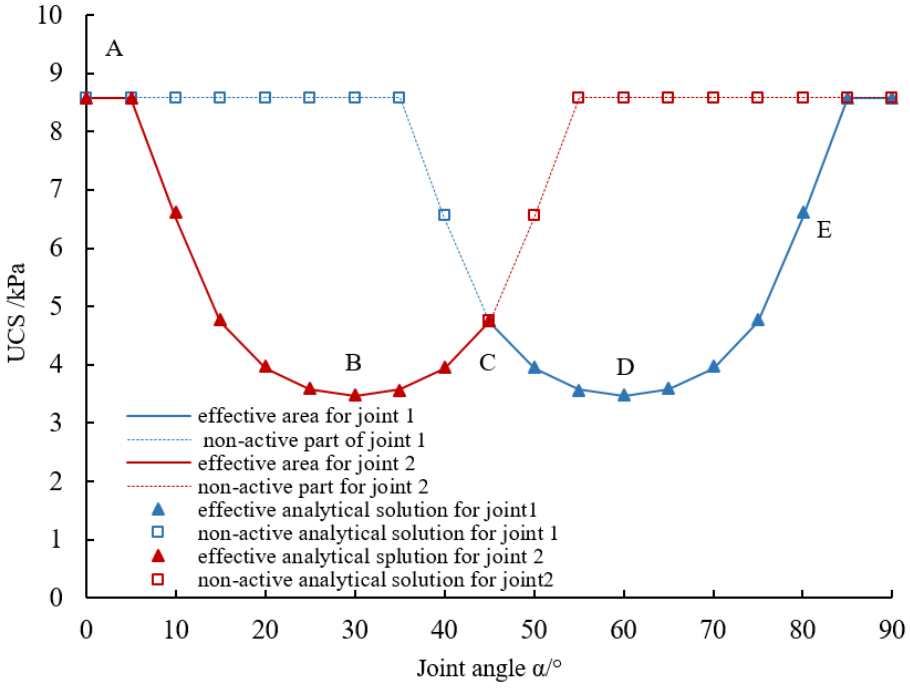

Figure 3.29 Valid and invalid parts of failure envelop for sample with two perpencicular joints according to Table 3.2

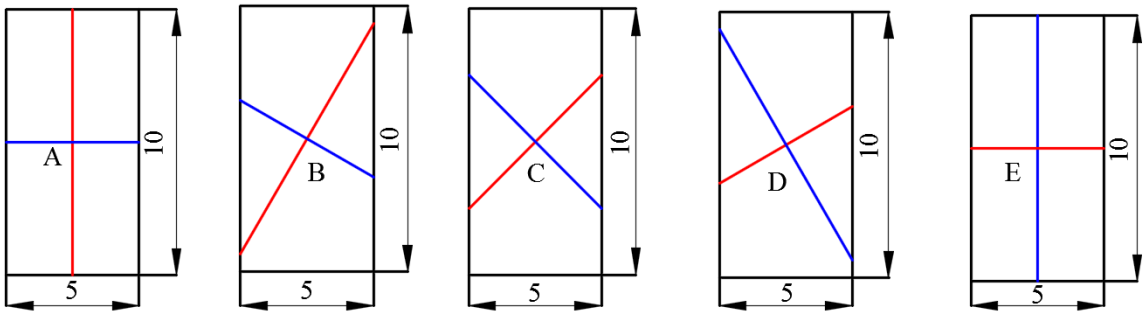

Figure 3.30 Schematic diagram of sample with two perpendicular joints (see Fig. 3.29)

The sample considered in this section has a height to width ratio of 2. The intact rock and the joints behave elastic, perfectly plastic with no strain-hardening/softening. The colored curves in Figure 3.29 correspond to the colored joints shown in Figure 3.30. In Point A and E the two joints are horizontal and vertical, respectively. Points B and D describe the critical joint position. Point C is the inflection point for the two joints. The colored dashed line and the small square in Figure 3.29 mark the areas where both joints are inactive. Joints with unfavourable orientation dominate the strength of the rock mass as shown in Figure 3.31.

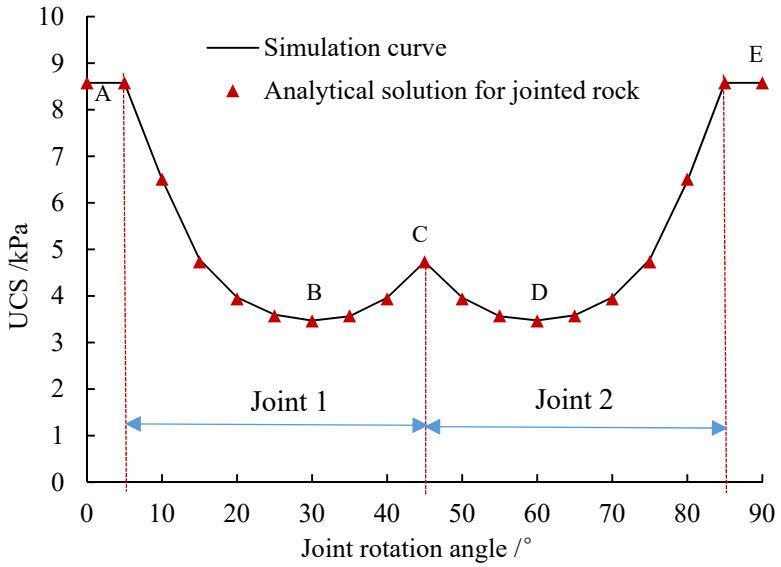

Figure 3.31 Failure envelope for sample with two perpendicular joints vs. joint rotation angle

3.6.1.2 Influence of joint parameters and joint angle on strength of rock mass

In this section, three situations for a sample with two perpendicular joints having different strength parameters are discussed. The two joints can have only different joint friction angles or have various joint cohesion values or both. Specific parameters are listed in Table 3.3 - 3.5. The jointed rock strength behavior is shown in Figure 3.32 - 3.34.

Table 3.3 Mechanical properties of jointed rock mass (different joint friction angle)

Material parameters	Primary joint	Secondary joint
Joint cohesion (c_j)	1 kPa	1 kPa
Joint friction angle (ϕ_j)	10°	40°
Joint tensile strength	2 kPa	2 kPa
Joint angle	α + 90°	α

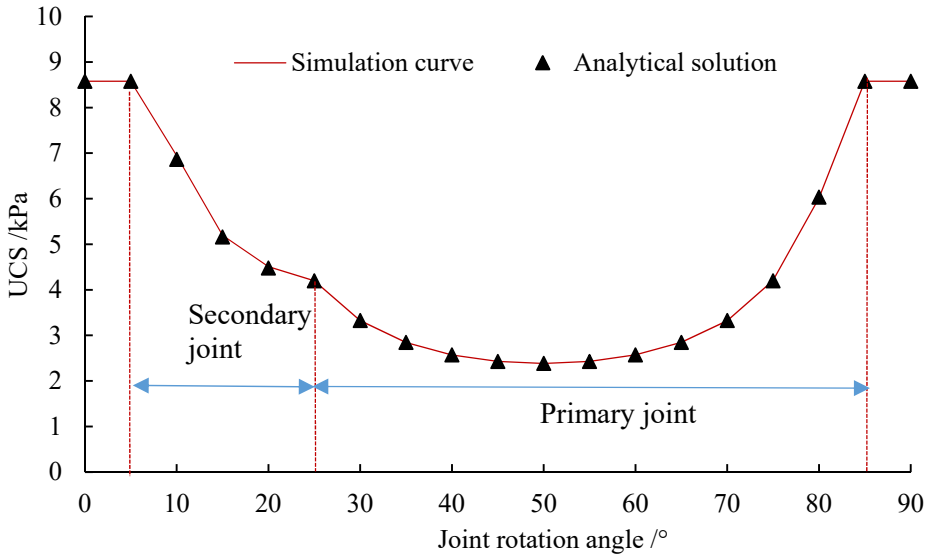

Figure 3.32 Failure envelope for sample with two perpendicular joints with different friction values versus orientation of joint system (see Table 3.3.)

Table 3.4 Mechanical properties of jointed rock mass (different joint cohesion)

Material parameters	Primary joint	Secondary joint
Joint cohesion (c_j)	0.5 kPa	1 kPa
Joint friction angle (ϕ_j)	30°	30°
Joint tensile strength	2 kPa	2 kPa
Joint angle	α + 90°	α

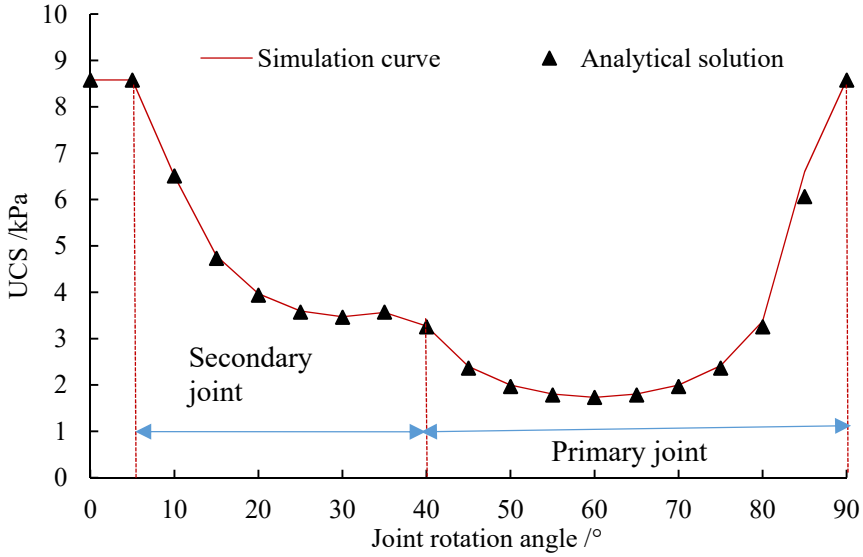

Figure 3.33 Failure envelope for sample with two perpendicular joints with different cohesion values versus orientation of joint system (see Table 3.4)

Table 3.5 Mechanical properties of jointed rock mass (joint cohesion and friction angle are different)

Material parameters	Primary joint	Secondary joint
Joint cohesion (c_j)	1 kPa	0.8 kPa
Joint friction angle (ϕ_j)	10°	40°
Joint tensile strength	2 kPa	2 kPa
Joint angle	α	α + 90°

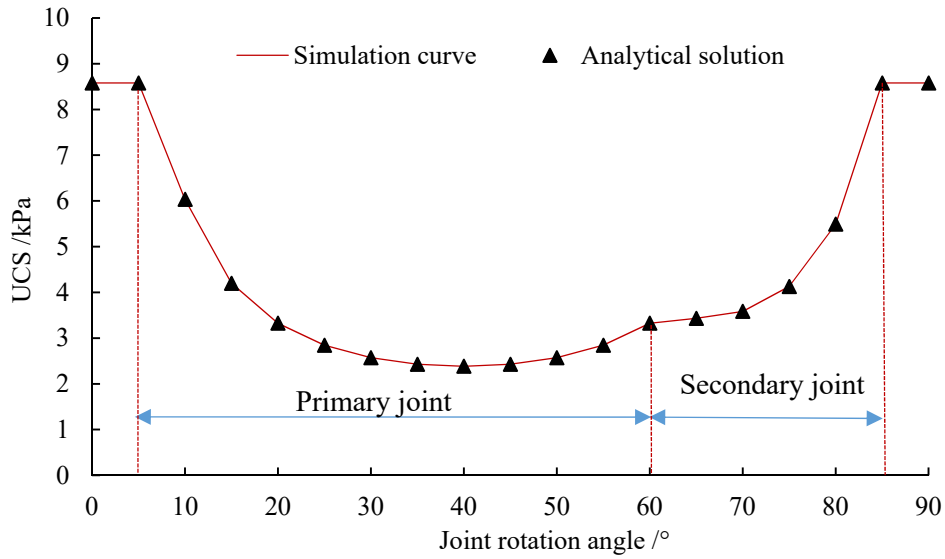

Figure 3.34 Failure envelope for sample with two perpendicular joints with different friction und cohesion values versus orientation of joint system (see Table 3.5)

3.6.1.3 Triaxial tests on anisotropic samples

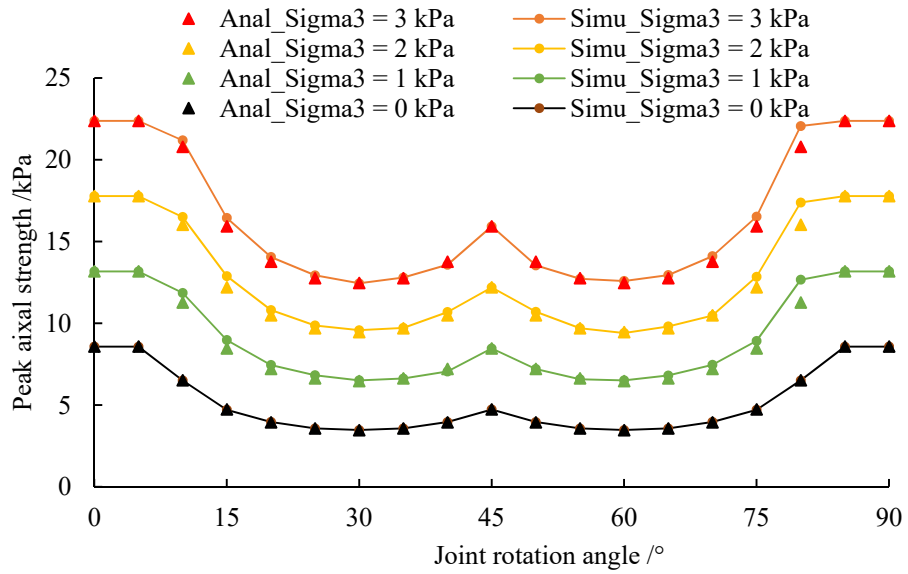

Figure 3.35 Peak strength versus orientation of joint system under various confining pressures

Specimens with different joint orientations are subjected to triaxial compression at various confining pressures. Figure 3.35 compares the multi-joint model simulation results for samples

with two perpendicular joints with corresponding analytical solutions (see section 2.4.3). The jointed rock properties are listed in Table 3.2 (see Figure 3.30). The match is excellent, with a relative error smaller than 1 % for all joint angles.

The black curve demonstrates the anisotropic behavior of the model without confining pressure (uniaxial compression test as shown in section 3.6.1.1). A strength reduction is observed for joint angles from 5° to 30°. A local strength increase is observed for joint angles at 45° ± 15°. Finally, the strength increases for joint angles from 60° to 85°. Increasing confining pressure shifts the failure envelope upwards and the curve shape become more pronounced. Increasing confining pressures leads to a broader curve shoulder (enlargement from 5° to 15° and from 80° to 90°).

3.6.2 Strength anisotropy of a rock mass containing three joints

The height to width ratio of the considered sample is 2. The sample contains three joints (Figure 3.36). The minimum angle between each joint is 30 °. Matrix and joint properties are listed in Table 3.2. According to the Figure 3.37, Point A and D describe the original and final position, point A, B and D describes the critical joint positions. Point C represents the peak strength value. Figure 3.36 compares the multi-joint model with the analytical solution. The match is again excellent with an error below 1% for all values of joint angle. UCS varies from 3.5 kPa to 4.73 kPa, while the maximum UCS for one or two joints is around 8.5 kPa. The strength anisotropy behavior for rock with one joint is characterized by U or V shape (Jaeger's curve). The curve for sample with two perpendicular joints has a W form. In case of three joints, three local peak values appear (see Figure 3.37).

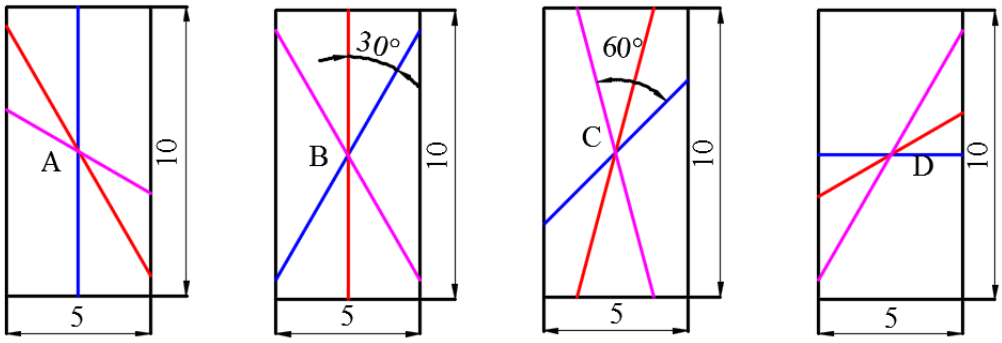

Figure 3.36 Schematic diagram for samples with three joints

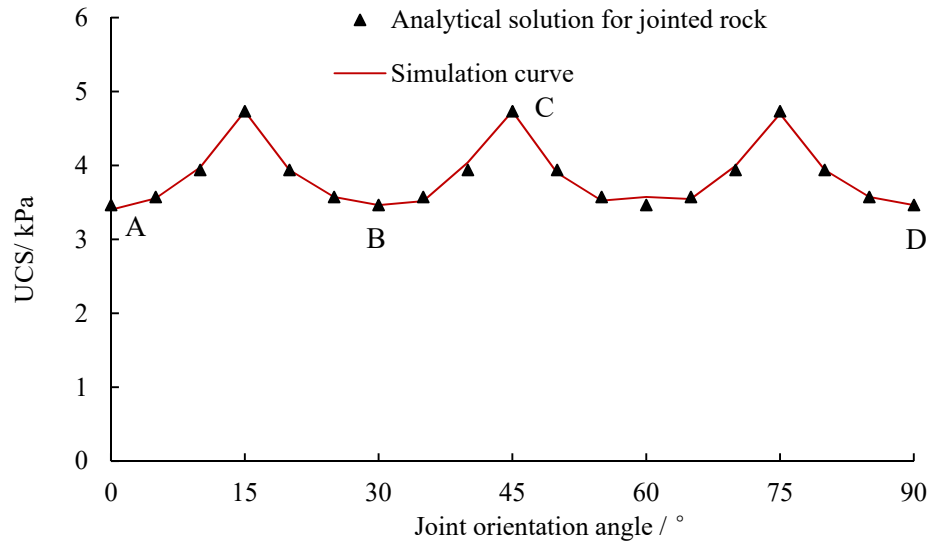

Figure 3.37 UCS for sample with three joints: multi-joint model (line) and analytical solution (triangular) versus joint set angle (see Figure 3.36)

3.6.3 Failure of jointed rock under tensile load

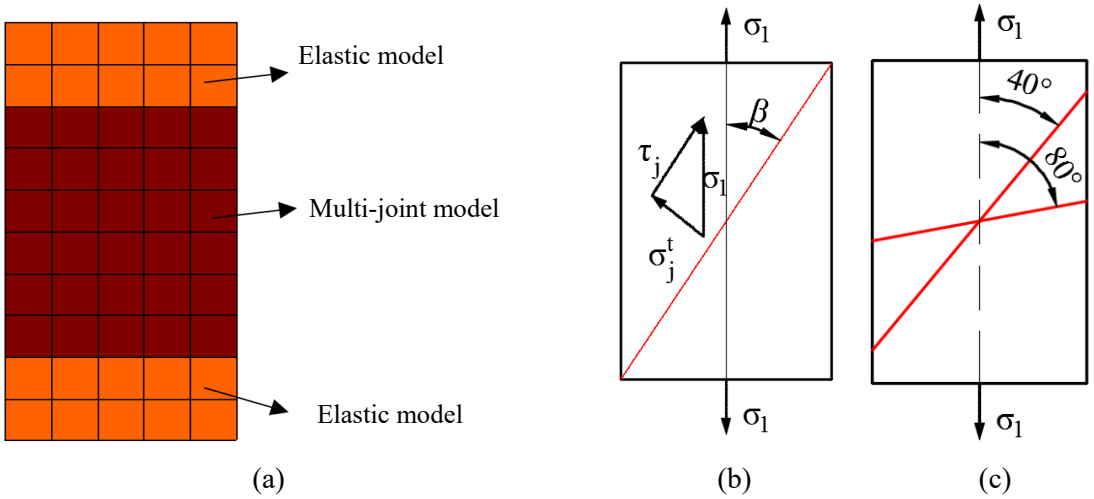

Figure 3.38 Schematic representation of the uniaxial tension model: (a) components and size of the numerical model, (b) sample with one joint, (c) sample with two joints

This section documents simulations of uniaxial direct tensile tests for rock samples with two joints under increasing vertical tensile stress (every 200 steps load increase of 40 Pa). The numerical sample consists of 50 zones and the height to width ratio of this sample is 2. The numerical model

is composed of three parts: an elastic constitutive model is used for the top and bottom of the grid in order to get smooth tensile stresses. In the middle part of the grid the multi-joint model is applied which contains two joints with inclination of 40° and 80° from vertical (Figure 3.38). The parameters for the elastic model part and the rock matrix part of multi-joint model are listed in Table 3.6.

Table 3.6 Numerical simulation parameters for elastic part and rock matrix

Model	E [GPa]	v	ρ [kg/m^3]	c [MPa]	Ψ [°]	ϕ [°]	σ^t[MPa]
Elastic	20	0.23	1810	——	——	——	——
M-J	0.17	0.22	2000	5	0	40	1

According to Figure 3.38b, a simple analytical solution can be used to calculate tensile strength of the sample:

$$\sigma_1 = \frac{\sigma_j^t}{\sin\beta} \tag{3.50}$$

Two groups of jointed rock are tested. In the first group, the two joints have the same strength parameters as shown in Table 3.7. The cohesion of the joint is much higher than the joint tension limit to ensure tensile failure. The only difference is the joint angle: joint 1 is more horizontal and joint 2 is more vertical. It appears that for the joint 1 the tensile strength of the sample is close to the tensile strength of the joint (around 5 kPa). For more vertical orientations (such like joint 2), the tensile strength is much higher.

Table 3.7 Parameters and failure type for numerical simulation of uniaxial tension tests with identical strength parameters for the two joints

Joint	β (°)	ϕ_j [°]	c_j [MPa]	σ_j^t [kPa]	Failure type
1	80	30	1	5	Joint tensile failure
2	40	30	1	5	——

Based on Eq. 3.50, the analytical solution is 5.077 kPa, the simulation gives 5.11 kPa, which is a good agreement. The corresponding strain-stress curve is shown in Figure 3.39.

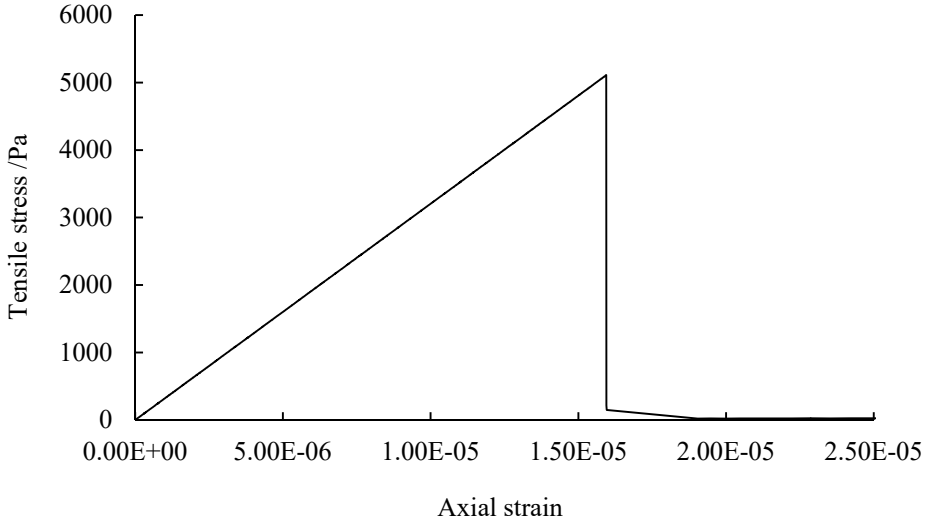

Figure 3.39 Uniaxial tension test with sample containing two joints with same strength parameters (see Table 3.7)

In the second group, the tension limit for the two joints are different as shown in Table 3.8. Based on the analytical solution, the tensile failure for joint 1 is 50 kPa and for the second joint 7.8 kPa. From numerical simulations a tensile strength of 8.6 kPa is obtained. It is clear that the tensile failure happens on joint 2. The stress–strain curve is shown in Figure 3.40.

Table 3.8 Parameters and failure type for numerical simulation of uniaxial tension tests with different strength parameters for the two joints

Joint	β (°)	ϕ_j [°]	c_j [MPa]	σ_j^t [kPa]	Failure type
1	80	30	1	50	——
2	40	30	1	5	Joint tensile failure

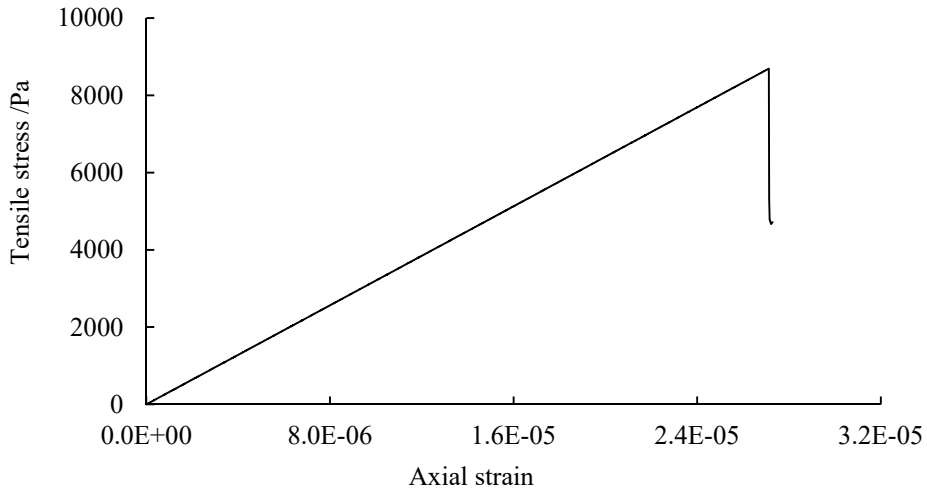

Figure 3.40 Uniaxial tension test with sample containing two joints with different strength parameters (see Table 3.8)

4 Uniaxial compression lab tests with jointed samples

4.1 Introduction

To investigate the behavior of jointed specimen under uniaxial loading and to verify the developed constitutive model special lab tests with artificial rock-like material (gypsum) were performed. Samples with 2 crossing joints covering more than 20 angle configurations and two different property sets are prepared and tested.

4.2 Design of experiments

4.2.1 Material description

Gypsum was chosen as matrix material for sample preparation. Gypsum samples have been used for decades as synthetic rock matrix or as weak planes in combination with other materials such as concrete or cement (Einstein et al., 1969, Shen et al., 1995, Ko et al., 1995, Xiao et al., 2014). The samples are obtained by mixing hemihydrate gypsum powder ($CaSO4 \cdot ½H_2O$) with water. When this hemihydrate is mixed with water, hydrated gypsum ($CaSO4 \cdot 2H_2O$) is formed ($CaSO_4 \cdot ½H_2O + 1½\ H_2O = CaSO_4 \cdot 2H_2O$). The gypsum specimens are then dried at room temperature, but the crystallization water ($2H_2O$) associated with $CaSO_4$ still remains. Environmental scanning-electron microscope (ESEM) images reveal that the average gypsum crystals are less than 5 μm (Wong, 2007), therefore gypsum can be considered as a nearly prefect homogeneous material. The strength properties of gypsum can be described by the Mohr-Coulomb constitutive model.

4.2.2 Material properties

Two kinds of gypsum mixtures are used for the test: white plaster for the rock matrix and colored plaster for the joints. The matrix plaster has higher strength values than the joint plaster. Typical jointed samples are shown in Figure 4.1. At the initial stage of testing, samples without joints were

investigated to obtain strength and stiffness parameters for the matrix. Obtained mechanical properties of the intact rock (matrix) and the joint material are summarized in Table 4.1.

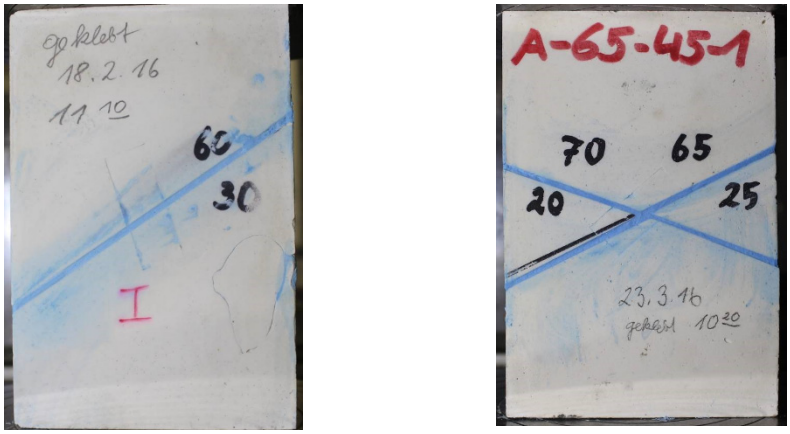

(a) (b)

Figure 4.1 Jointed gypsum specimens: (a) one joint (b) two joints

Table 4.1 Mechanical properties of matrix and joint material

Material parameters	Matrix material	Joint material
Density	1810 kg/m³	———
Bulk modulus [K]	12.84 GPa	———
Shear modulus [G]	8.077 GPa	———
Cohesion [c]	9.1 MPa	———
Friction angle [ϕ]	21.2°	———
Dilation angle [ψ]	10°	———
Joint cohesion [c_j]	———	1.5 MPa
Joint friction angle [ϕ_j]	———	32.8°
Joint tensile strength [σ_j^t]	———	0.5 MPa

4.2.3 Sample geometries

Three types of samples were produced: (1) samples with only one joint; (2) samples with two joints with same mechanical parameters; (3) samples with two joints which have different mechanical parameters. Investigated joint angles cover a range from -90° to +90° degree. Definition of the angles are illustrated in Figure 4.2. As shown in Figure 4.2, there are two types of intersecting

joints: symmetric and asymmetric. More research focus on samples with asymmetric joints. Red or blue solid lines are used to represent the joints in this chapter. All produced specimens have a cuboid shape with the dimensions 150 x 100 x 50 mm (height, length, thickness). A unified format is used to name all samples: CRM_α/β_G_N. CRM represents the categories (type) of the sample, α and β are the joints angles, G stands for the name of the group within each category and N stands for the sample number. Another simple sample name is also used in this thesis: G [α/β]. This type of abbreviation is used in the following sections.

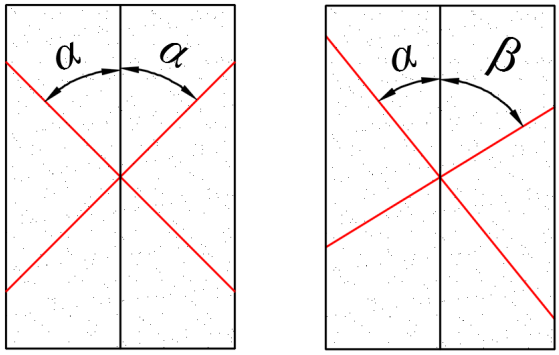

(a) (b)

Figure 4.2 Samples with two joints (a) symmetric type, (b) asymmetric type

4.2.3.1 Samples with one single joint

The single joints have angles of 35°, 45° and 60°. The geometries of category I samples are given in Table 4.2. To avoid confusion, angles are always defined as the angle between the vertical direction and orientation of the joint plane (see Figure 4.3).

Table 4.2 Joint geometry parameters for category I samples

Name	Joint angle α [°]	Joint angle β [°]	Geometry	Abbr.
CI_35/-_A_1	35	———	Fig 4.3A	A [35/-]
CI_35/-_A_2	35	———	Fig 4.3A	A [35/-]
CI_45/-_B_1	45	———	Fig 4.3B	B [45/-]
CI_45/-_B_2	45	———	Fig 4.3B	B [45/-]
CI_60/-_C_1	60	———	Fig 4.3C	C [60/-]
CI_60/-_C_2	60	———	Fig 4.3C	C [60/-]

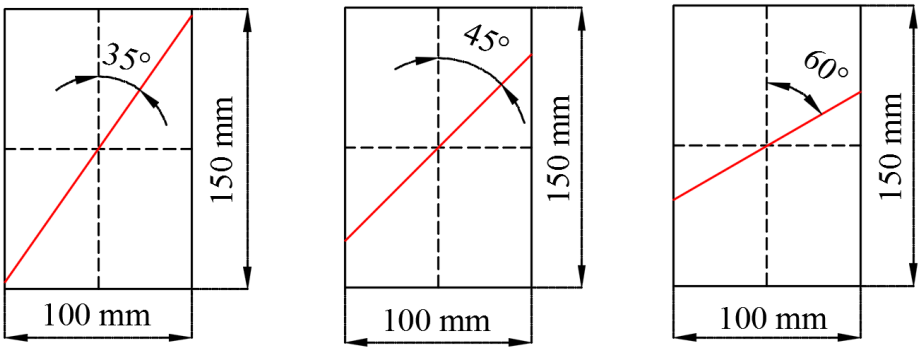

(A) (B) (C)

Figure 4.3 Samples with one single joint

4.2.3.2 Samples with two joints with identical properties

Samples with two intersecting joints were produced, which divide the gypsum block into four discrete pieces. These samples can be subdivided into three groups, which can be characterized as follows:

- Group A: constant angle between the two joints of always 60° (Table 4.3 and Figure 4.4),
- Group B: constant angle between the two joints of always 45° (Table 4.4 and Figure 4.5)
- Group C: constant angle between the two joints of always 45° (Table 4.5 and Figure 4.6).

In each of the three groups samples with more than 10 joint angle combinations are produced and tested.

Table 4.3 Joint geometry parameters for category II samples (group A)

Name	Joint angle α [°]	Joint angle β [°]	Geometry	Abbr.
CII_-30/30_A1_1	-30	30	Fig 4.4 A1	A1 [-30/30]
CII_-30/30_A1_2	-30	30	Fig 4.4 A1	A1 [-30/30]
CII_10/70_A2_1	10	70	Fig 4.4 A2	A2 [10/70]
CII_10/70_A2_2	10	70	Fig 4.4 A2	A2 [10/70]
CII_30/90_A3_1	30	90	Fig 4.4 A3	A3 [30/90]
CII_30/90_A3_1	30	90	Fig 4.4 A3	A3 [30/90]
CII_-60/60_A4_1	-60	60	Fig 4.4 A4	A4 [-60/60]
CII_-60/60_A4_2	-60	60	Fig 4.4 A4	A4 [-60/60]
CII_-45/75_A5_1	-45	75	Fig 4.4 A5	A5 [-45/75]
CII_-45/75_A5_2	-45	75	Fig 4.4 A5	A5 [-45/75]

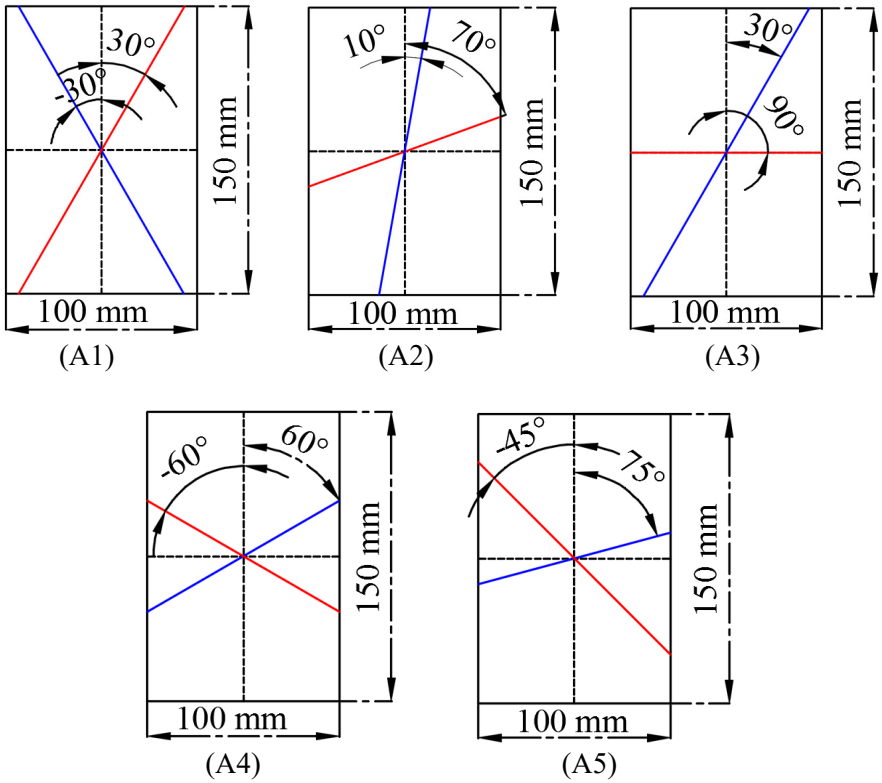

Figure 4.4 Sample geometries for category II group A

There are different types of joint configuration. Some are symmetrical (A1, A4, B6) and in some cases at least one joint reaches the upper and lower boundary of the specimen (A1, A2, A3, B1, B2, C1). In cases A4, A5, B4, B5, B6 and C3 the angle between the joints is at least 45°. Six different joint combinations are shown in Figure 4.5. All of them are asymmetric. The angle of the blue joint in group B varies from 10° to 65°.

Table 4.4 Joint geometry parameters for category II samples (group B)

Name	Joint angle α [°]	Joint angle β [°]	Geometry	Abbreviation
CII_10/55_B1_1	10	55	Fig 4.5 B1	B1 [10/55]
CII_10/55_B1_2	10	55	Fig 4.5 B1	B1 [10/55]
CII_25/70_B2_1	25	70	Fig 4.5 B2	B2 [25/70]
CII_25/70_B2_2	25	70	Fig 4.5 B2	B2 [25/70]
CII_35/80_B3_1	35	80	Fig 4.5 B3	B3 [35/80]
CII_35/80_B3_2	35	80	Fig 4.5 B3	B3 [35/80]
CII_45/90_B4_1	45	90	Fig 4.5 B4	B4 [45/90]
CII_45/90_B4_2	45	90	Fig 4.5 B4	B4 [45/90]
CII_-85/50_B5_1	-85	50	Fig 4.5 B5	B5 [-85/50]
CII_-85/50_B5_2	-85	50	Fig 4.5 B5	B5 [-85/50]
CII_-70/65_B6_1	-70	65	Fig 4.5 B6	B6 [-70/65]
CII_-70/65_B6_2	-70	65	Fig 4.5 B6	B6 [-70/65]

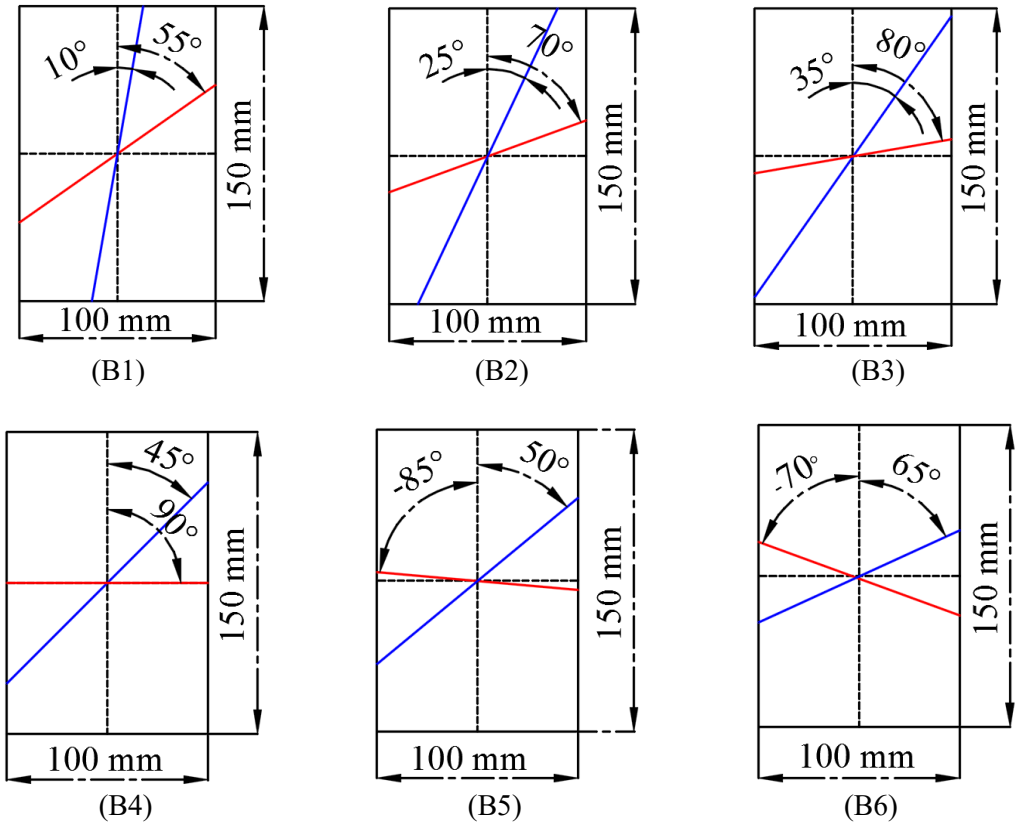

Figure 4.5 Sample geometries for category II group B

Three different joint combinations are shown in Figure 4.6. All of them are asymmetric. The angle of the blue joint in group B varies from 30° to 60°. In this group, joint orientations cover the whole spectrum from 0° to 90°.

Table 4.5 Sample geometry parameters for category II group C

Name	Joint angle α [°]	Joint angle β [°]	Geometry	Abbreviation
CII_30/60_C1_1	30	60	Fig 4.6 C1	C1 [30/60]
CII_30/60_C1_2	30	60	Fig 4.6 C1	C1 [30/60]
CII_35/65_C2_1	35	65	Fig 4.6 C2	C2 [35/65]
CII_35/65_C2_2	35	65	Fig 4.6 C2	C2 [35/65]
CII_60/90_C3_1	60	90	Fig 4.6 C3	C3 [60/90]
CII_60/90_C3_2	60	90	Fig 4.6 C3	C3 [60/90]

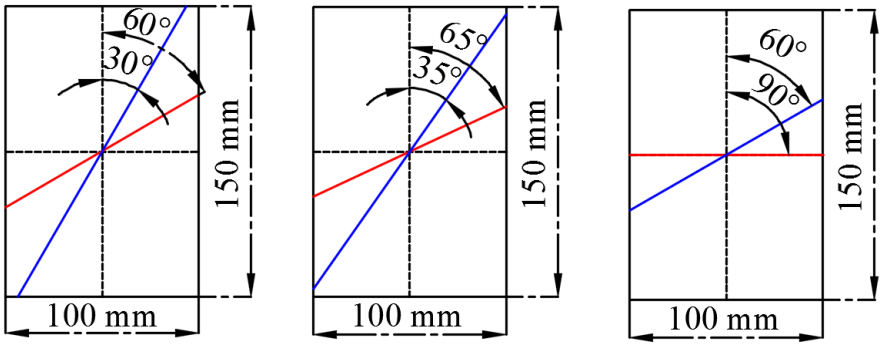

Figure 4.6 Sample geometries for category II group C

4.2.3.3 Samples with two joints with different properties

Three joint angle combinations are considered as shown in Figure 4.7. In this category, the blue line stands for a joint which is much weaker than the red one.

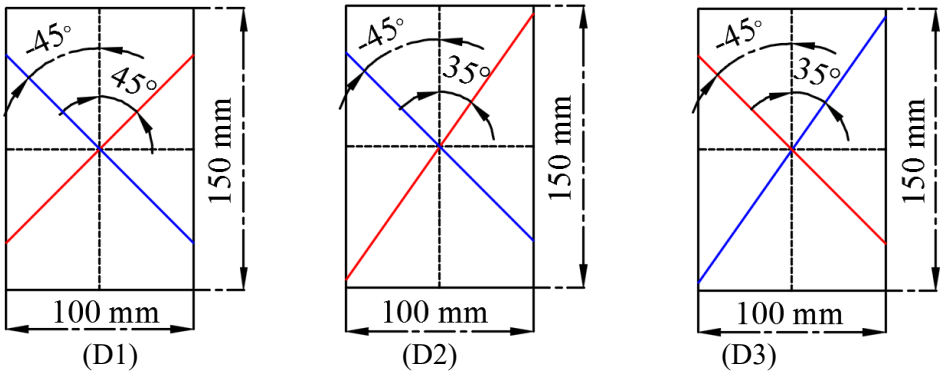

Figure 4.7 Sample geometries for two joints with different parameters (blue: weak joint, red: strong joint)

Table 4.6 Sample geometry parameters for category III group D

Name	Joint angle α [°]	Joint angle β [°]	Geometry	Abbreviation
CIII_30/60_D1_1	-45	45	Fig 4.7 D1	D1 [-45/45]
CIII_30/60_D1_2	-45	45	Fig 4.7 D1	D1 [-45/45]
CIII_35/65_D2_1	-45	35	Fig 4.7 D2	D2 [-45/35]
CIII_35/65_D2_2	-45	35	Fig 4.7 D2	D2 [-45/35]
CIII_60/90_D3_1	-45	35	Fig 4.7 D3	D3 [-45/35]
CIII_60/90_D3_2	-45	35	Fig 4.7 D3	D3 [-45/35]

4.3 Specimen preparation

Samples are prepared with pre-defined joints according to the geometry described in section 4.2. Intact samples were obtained by pouring a mixture of gypsum powder and water into a mold first. After curing black lines were drawn on the specimen to mark the joint orientations. Along the marked lines the plaster samples were cut into pieces. After cutting, a colored plaster was used to glue the blocky parts together, so that cohesive joints are formed as shown in Figure 4.8.

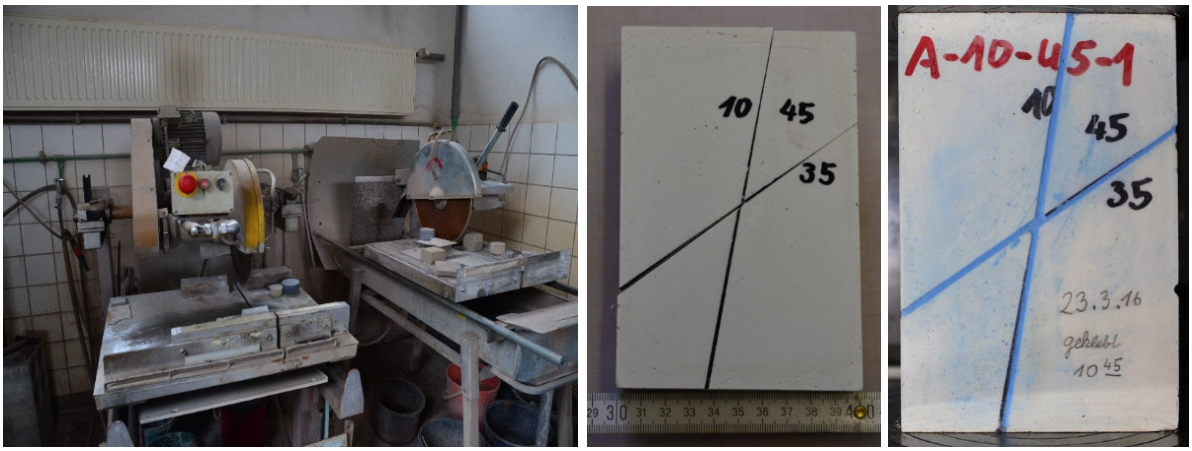

(a) (b) (c)

Figure 4.8 Sample preparation: (a) slicing machine, (b) specimen cut into pieces and (c) final sample with glued joints.

Much research work has been done to investigate the influence of the curing time on the properties. Coquard and Boistelle (1994) found that moisture content significantly affects the mechanical strength of gypsum. If the plaster absorbs 2 % more water, the mechanical strength will decrease by 50 %. Here, water and gypsum powder were mixed with a weight ratio of 1: 3.5. After sufficient mixing to guarantee homogeneity the material was cast into a cuboid box. Finally, the samples were equipped with pre-defined joints of different orientation and strength as described above (Figure 4.8).

Before tests were started, all samples were stored at room temperature and cured for 3 weeks. In order to ensure accuracy of the experiments, each test was performed with two to four samples. In total about 30 individual tests with more than 60 specimens were performed. It is difficult to manufacture more than 10 samples in one day, so the experiments were divided into six batches. In each batch, the same weight ratio and curing time were used to ensure that plaster for the matrix of each sample has the same parameters. For the handmade joints it cannot be guaranteed that each batch of joint has same parameters. More detailed information about joint parameters are given in the data analysis section.

4.4 Uniaxial compression testing equipment

The uniaxial compression tests were conducted in the Rock Mechanical Laboratory of the Geotechnical Institute at the Technical University Bergakademie Freiberg using the TIRA-Test 28500 Rock Testing System (Figure 4.9). The machine consist of a load frame (1 in Figure 4.9) with nominal axial load of 500 kN and a load speed control system (2 in Figure 4.9). Load and displacement data were automatically logged and stored in a data acquisition PC (3 in Figure 4.9). First, the samples are carefully placed and loaded with an initial axial load of 1 kN. Then, the samples are uniaxial compressed with a rate of 1.5 MPa/min until failure. During the loading, the specimen front face was continuously recorded by a Canon digital camera to observe deformation behavior and failure mode.

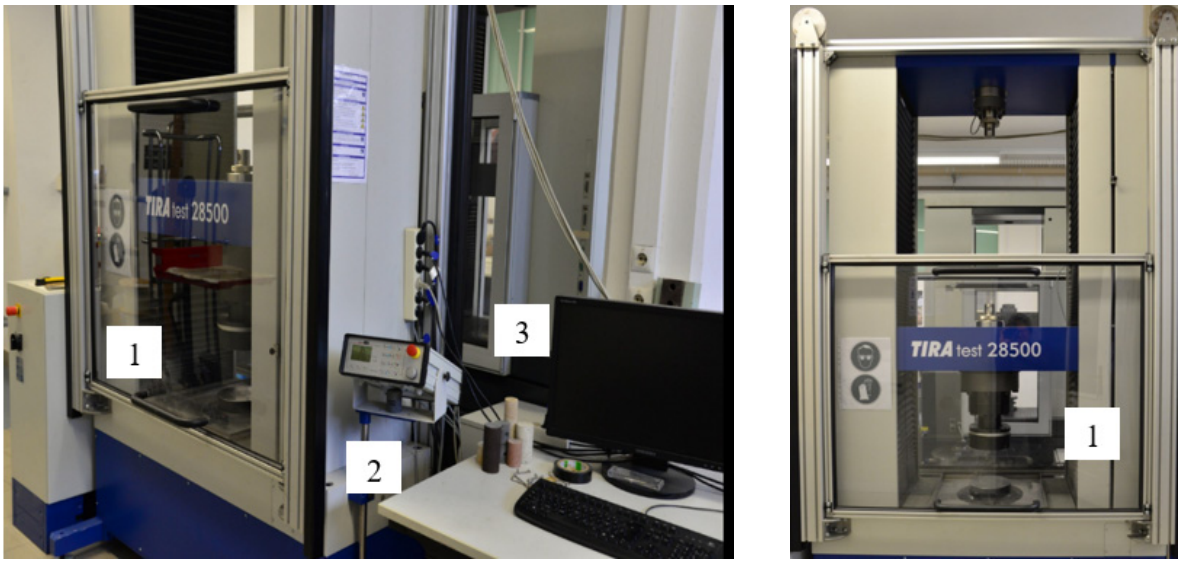

(a) (b)

Figure 4.9 Uniaxial test equipment TIRA test 28500: (a) overview, (b) detailed view

4.5 Data analysis

Only selected test results are shown in detail, but for each test category, qualitative and quantitative data are listed in tables. These data are further analyzed to characterize the fracturing and failure processes. By studying the videos which were taken during the uniaxial compression tests, it is possible to identify the damage pattern of each sample.

4.5.1 Stress-strain characteristics and fracture pattern for sample category I

Category I: Sample with one joint (35°)

Figure 4.10 shows the stress-strain curve. Two specimens were tested and the general behavior is similar, but the peak strengths are different. The points a_1 and a_2 mark the end of the initial loading process. During this stage, although significant axial strain is observed, the increase of axial stress is quite low. b_1 and d_2 indicate the peak stress. The behavior is nearly linear from a_1 to b_1 and a_2 to b_2. After peak stress is reached, sharp stress drop with further increase of strain is observed up to stage c_1 and e_2. One peculiarity is that between the point b_2 and d_2 (sample A2), axial stress drops

to stage c_2, followed by an increase until the peak stress is reached. Damage processes are illustrated in Figure 4.11.

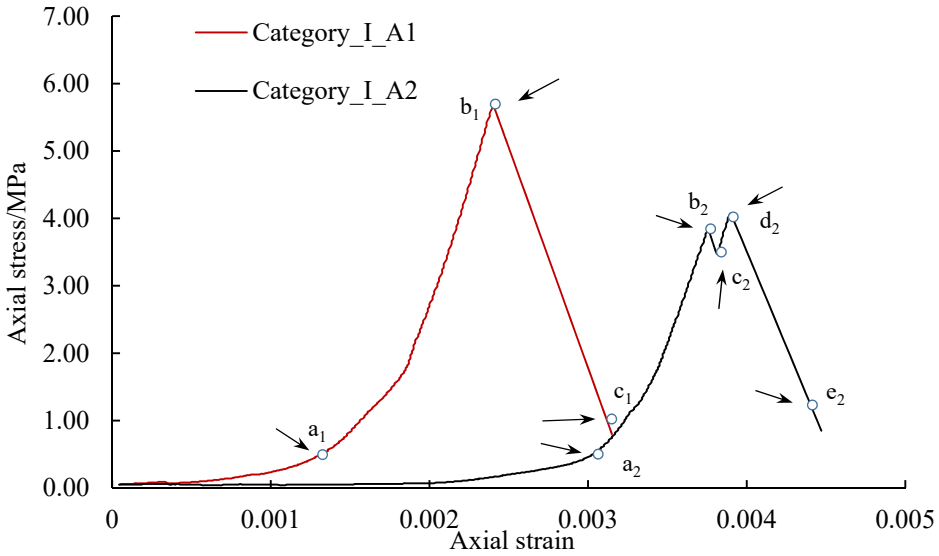

Figure 4.10 Stress-strain curves for samples of category_I_A: [35/-]

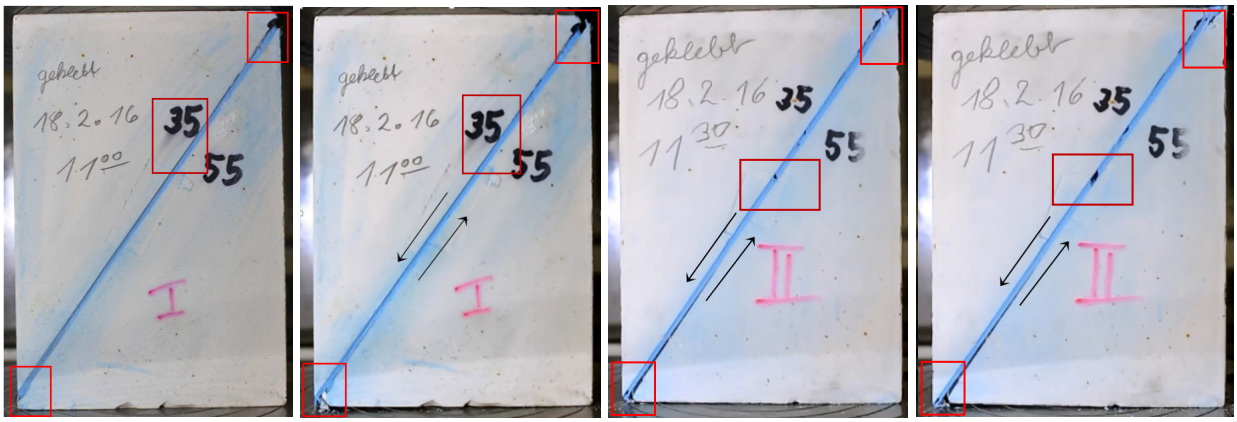

(a) (b) (c) (d)

Figure 4.11 Fotos of category_I_A [35/-]: (a) and (b) are related to the red curve in Figure 4.10, (c) and (d) are related to the black curve in Figure 4.10

Figure 4.11a and b show sample A1, 4.11c and d show sample A2 (see also Figure 4.10). Figure 4.11a and 4.11c show the initial position of the specimen. The fotos of specimen in Figure 4.11 contain three red rectangles, which can be used to recognize the deformation pattern. The joints show no tensile cracking, but with increasing stress, cracks emerge first in the colored plaster, then this tiny cracks extend and form slightly larger cracks. Also, displacement along the joint (Figure 4.11d) is observed. No failure in the matrix is observed.

Category I: sample with one joint (45°)

As shown in Figure 4.12, both tests reveal the stress-strain diagram for one joint samples with a joint angle of 45° . The trend of the two curves are quite different, but the peak stresses are similar. The vertical stress increases slightly before reaching stage a_1, b_1 indicates the peak stress. There is a rapid linear increase in axial stress between the stages a_1 and b_1. The curve for the second test in Figure 4.12 is much more complicated. First, the vertical stress increases linearly with growing vertical strain until the point a_2 is reached, then the stress decreases to stage b_2. A saw tooth like rise from the point b_2 to c_2 followed. Point c_2 indicates the maximum vertical stress. After that, the vertical stress showed a gradually decrease between c_2 and d_2 followed by a rapid decrease until the stage e_2 is reached.

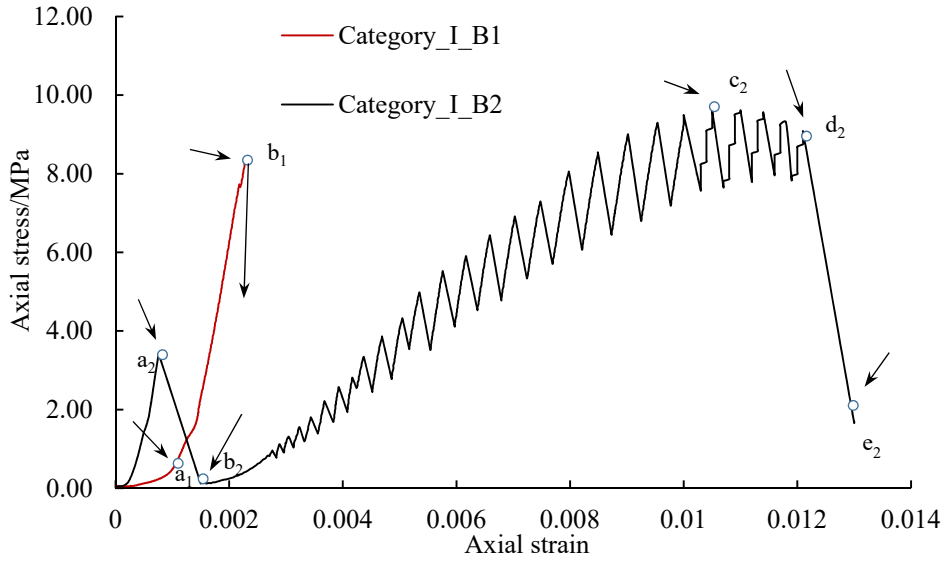

Figure 4.12 Stress-strain curves for sample of category_I_B: [45/-]

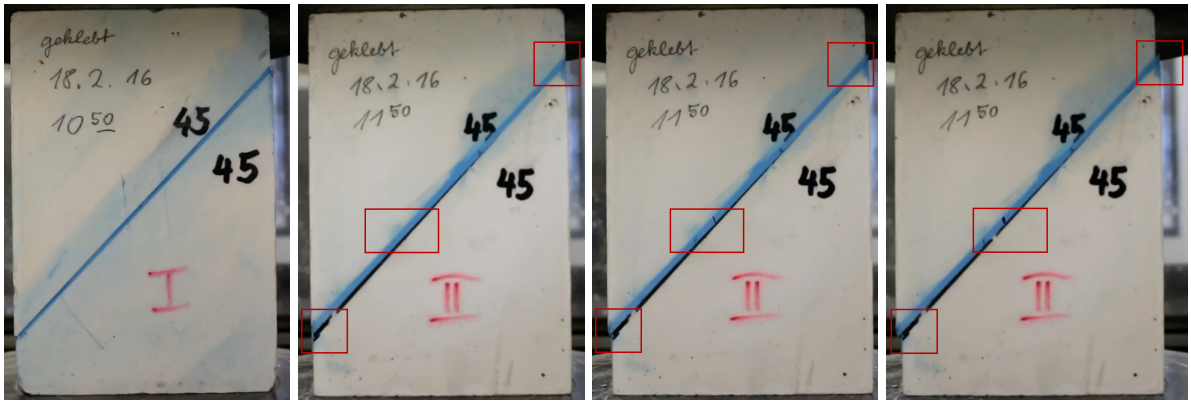

(a) (b) (c) (d)

Figure 4.13 Uniaxial compression test: failure pattern for samples of category_I_B [45/-]: (a) B1 specimen and (b), (c), (d) B2 specimen

Figure 4.13 shows the two plaster specimens before and after the uniaxial compression test. The specimen B1 in Figure 4.13a showed sudden brittle failure and sample was divided into two pieces (red curve in Figure 4.12). Figure 4.13b shows the B2 specimen at the initial stage. Three red rectangles mark areas which make the deformation of the sample during loading visible. First crack emerged on the joint (Figure 4.13c), then several cracks emerged and the width of the first crack increased (Figure 4.13d). Slipping along the surface of the colored plaster occurred without complex damage of the sample. Only after the point d_2 (Figure 4.12) was reached complete sample failure happened.

Category I: sample with one joint (60°)

The stress-strain curves for samples with single joint plane (inclination of 60°) are shown in Figure 4.14. The peak stress is reached at 24.71 MPa and 22.75 MPa, respectively. The loading process started at point a followed by a nearly linear elastic behavior until point b was reached. A slow decrease followed (point b to c) which indicates final failure in the matrix part, but not in the joint. From c to d, a small increase in stress resulted in large deformations. After the peak stress was reached at point d, a stress drop occurred. Damage process and the failure pattern are illustrated in Figure 4.15.

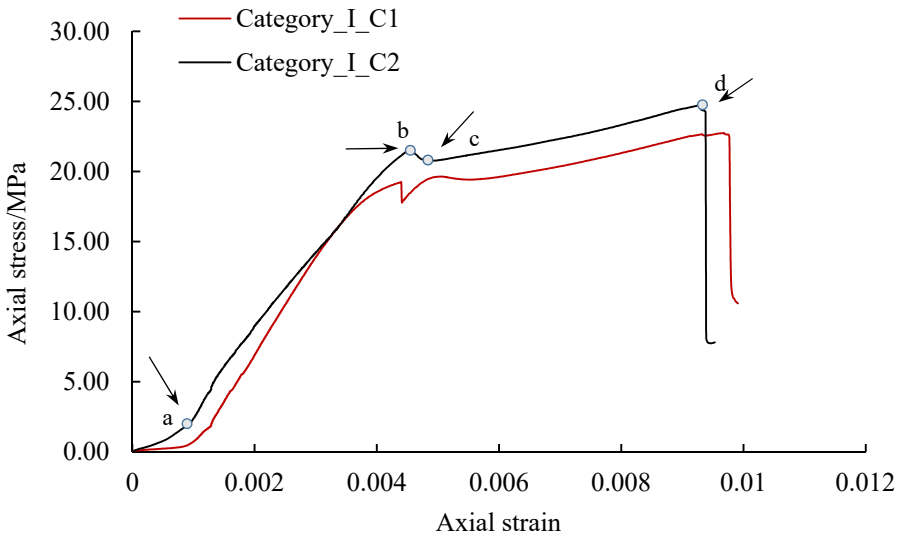

Figure 4.14 Stress-strain curves for samples of category_I_C: [60/-]

Figure 4.15a shows the specimen at the stage a according to Fig. 4.14. As shown in Figure 4.15b, there was no joint sliding but a few tiny cracks emerge first. With the increase of load, small cracks propagated and formed a large crack connected with small displacement along the direction of the crack (Figure 4.15c). Finally, matrix failure was observed and larger slip along the joint occurred (Figure 4.15d). This test showed that plastic failure of the rock matrix happened first followed by sliding along the joint.

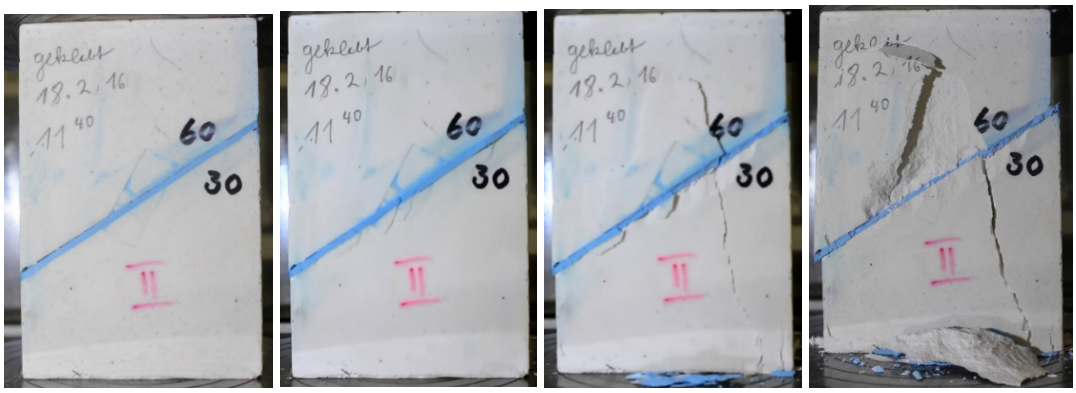

(a) (b) (c) (d)

Figure 4.15 Uniaxial compression test failure pattern for samples of category_I_C [60/-]: (a-d) C2 sample

Rock strength anisotropy data obtained from uniaxial lab testing used to analyse the failure type of samples of category I are listed in Table 4.7 and Figure 4.16.

Table 4.7 Peak stress values and failure mechanisms for samples of category I

Name	UCS [MPa]	Primary failure	Secondary failure	Analytical solution for joint 1 [MPa]	Analytical solution for joint 2 [MPa]
A [35/-]	5.70	Joint sliding	———	5.82	———
A [35/-]	4.17	Joint sliding	———	5.82	———
B [45/-]	8.29	Joint sliding	———	8.44	———
B [45/-]	9.56	Joint sliding	———	8.44	———
C [60/-]	24.70	Matrix failure	Joint sliding	26.28	———
C [60/-]	22.73	Matrix failure	Joint sliding	26.28	———

There are three groups in category I, all the joint angles are located in the first quadrant (joint angle 0° - 90°). The lab test data show good agreement with the analytical solutions. For group A and group B, there is slip failure along the joint. Both, matrix failure and joint sliding occurred on samples of group C. Figure 4.16 documents, a gradual increase in peak stress with increasing joint angle.

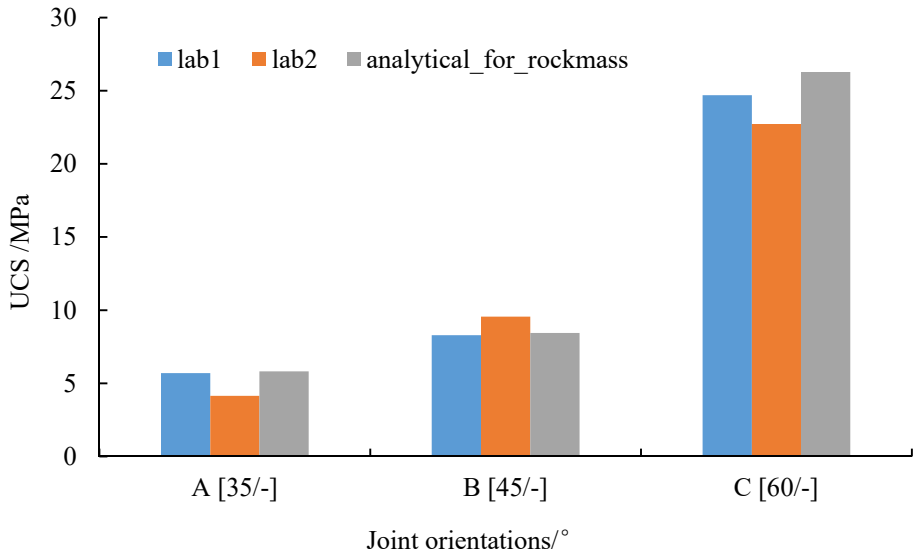

Figure 4.16 Uniaxial compression strength versus joint orientation for samples of category I

4.5.2 Stress-strain characteristics and fracture pattern for sample category II

Category II: samples with 2 joints (group A2)

The stress-strain diagrams for the two experiments of the category II group A2 are shown in Figure 4.17. The angles for the joints are 10° and 70°. The two curves are similar. a_1 and a_2 are inflection points with some minor stress drop. Then, nearly linear response up to stage b_1 and b_2 followed. The points c_1 and b_2 indicate the peak stresses. After reaching the peak stress, a significant decrease of the vertical stresses is recorded with exception of sample A2_2, where a small local stress peak is observed before brittle softening occurred.

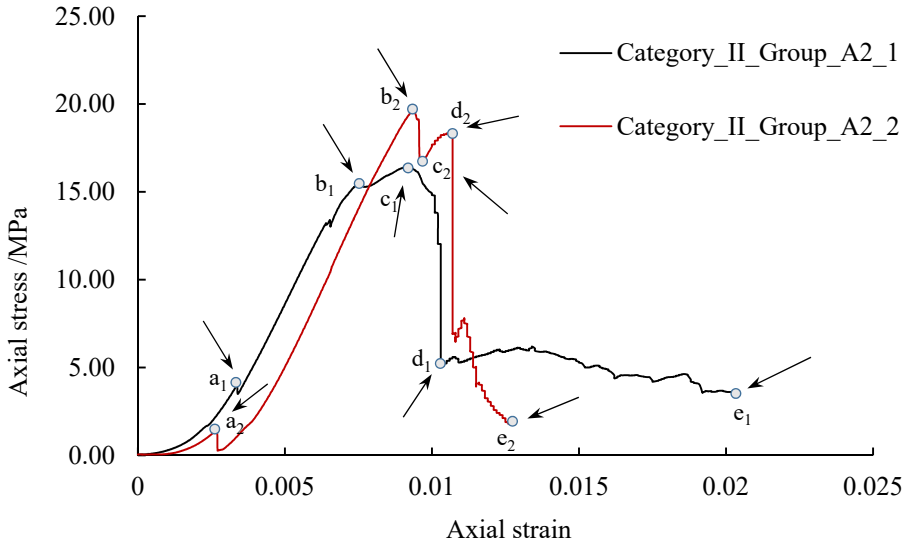

Figure 4.17 Stress-strain curves for samples of category_II_A2: [10/70]

Figure 4.18a shows the initial state of the sample A2_2. Considering the marked red rectangle, it becomes visible that the two parts of the joint with angle is 60° show a small offset at the crossing point. As shown in Figure 4.18b, there is sliding along the 10° joint indicated by black arrows. The joint with angle 10° touches the loading platens, therefore significant sliding along this joint is prevented. A crack emerged first in the matrix at the right side of the specimen. With increasing load, cracks propagate further and joint sliding becomes visible (Figure 4.18c). In the bottom red box, tensile failure is observed indicated by black arrows. Final failure pattern is shown in Figure 4.18d. Both, joint sliding and rock matrix failure are observed.

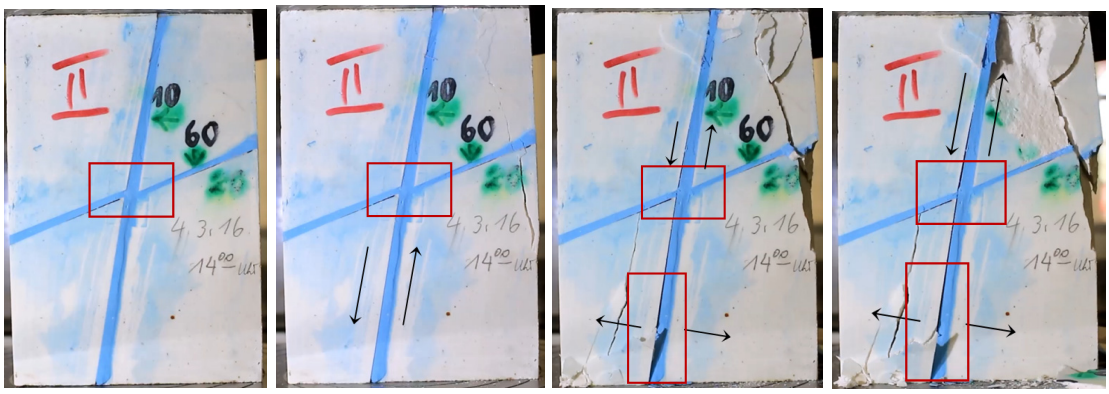

(a) (b) (c) (d)

Figure 4.18 Uniaxial compression test for sample of category_II_A2_2 [10/70]: damage state at different stress levels according to red curve in Figure 4.17

Category II: samples with two joints (group A5)

Figure 4.19 shows the stress-strain curves of the uniaxial compression tests on samples of category II group A5 (see also Figure 4.4). The specimen before testing is shown in Figure 4.20a. There is a nearly linear elastic deformation stage up to a_1 and b_1 followed by a sudden stress drop. Then, vertical stress increases with strong fluctuations until peak stress is reached at d_1 and d_2, respectively. The stages e_1 and e_2 mark the complete failure.

The sample shown in Figure 4.20a shows nearly elastic performance at the begin of the experiment. At the crossing point of the joints (red box in Figure 4.20b), sliding along 45° joint becomes visible and is indicated by black arrows. Also, a tiny crack is generated in the colored joint propagating later into the rock matrix (Figure 4.20c). This final failure pattern of the other sample is shown in Figure 4.20d. In both tests, the joint with angle of 75° remains stable.

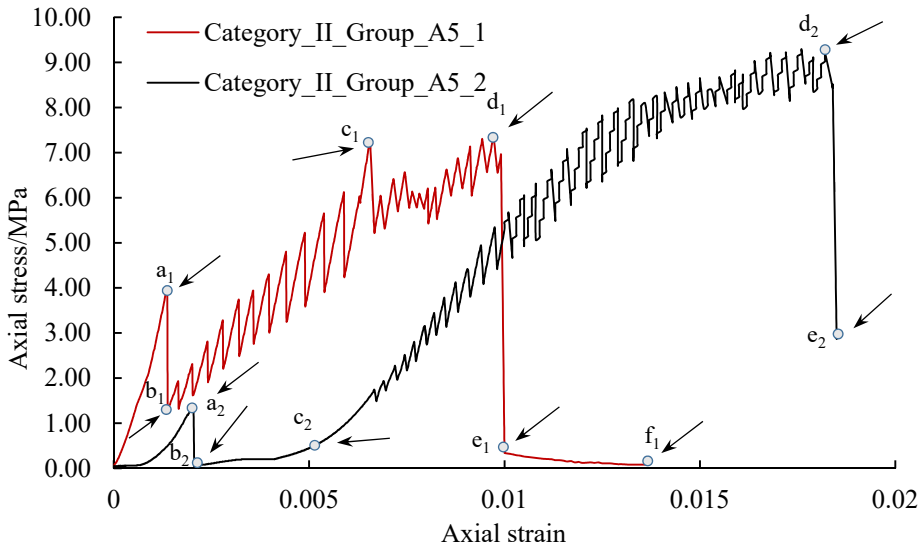

Figure 4.19 Stress-strain curves for samples of category_II_A5: [-45/75]

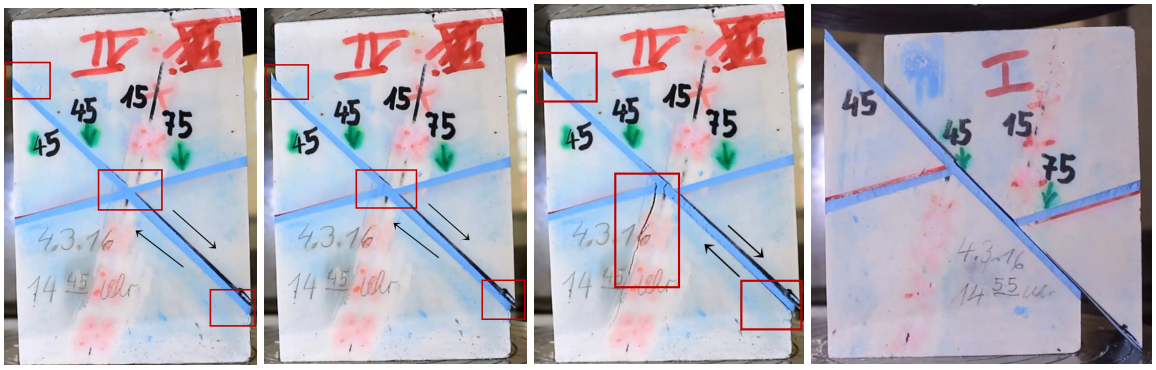

(a) (b) (c) (d)

Figure 4.20 Uniaxial compression test of samples of category_II_A5 [-45/75]: damage state at different stress levels according to curves in Figure 4.19

Test data and failure types of the samples of category II group A are listed in Table 4.8 and Figure 4.21.

Table 4.8 Peak stress values and failure mechanisms for samples of category II group A

Name	UCS [MPa]	Primary failure	Secondary failure	Analytical solution for joint 1 [MPa]	Analytical solution for joint 2 [MPa]
A1 [-30/30]	3.29	Joint sliding	———	5.52	5.52
A1 [-30/30]	5.40	Joint sliding	———	5.52	5.52
A2 [10/70]	16.51	Joint sliding	Matrix failure	10.42	26.28
A2 [10/70]	19.08	Joint sliding	Matrix failure	10.42	26.28
A3 [30/90]	3.36	Joint sliding	———	5.52	26.28
A3 [30/90]	7.93	Joint sliding	———	5.52	26.28
A4 [-60/60]	20.63	Matrix failure	———	26.28	26.28
A4 [-60/60]	19.82	Matrix failure	———	26.28	26.28
A5 [-45/75]	7.27	Joint sliding	———	26.28	8.44
A5 [-45/75]	11.23	Joint sliding	Matrix failure	26.28	8.44

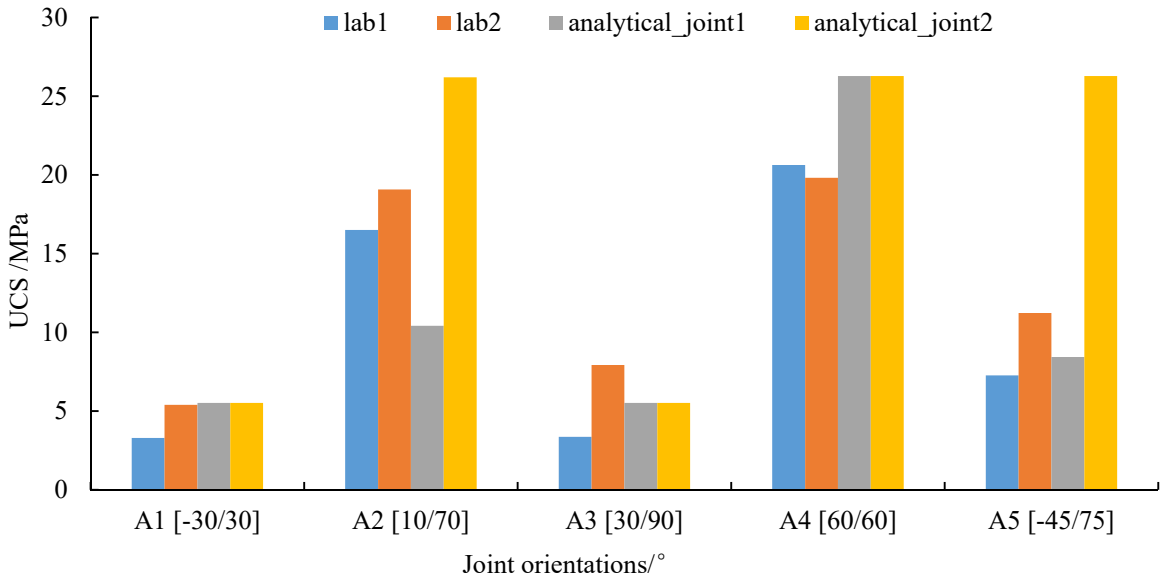

Figure 4.21 Uniaxial compression strength versus joint orientation for samples of category II group A

All of the experimental data showed good agreement with analytical solution results except those from the group A2. Inaccurate handmade joint angle and varying joint cohesion may lead to such deviation. As can be seen from Table 4.8, there is a slip failure along the joint for group A1, A3 and A5. Both, matrix failure and joint sliding occurred in group A2. Samples of group A4 showed matrix shear failure.

Category II: samples with two joints (group B2)

Figure 4.22 shows the recorded stress-strain curves for samples of category III group B1. Joint angles are 10º and 55º. Vertical stress development of sample 1 again shows some fluctuations until peak stress at a1 was reached, followed by strain softening until final state was reached. Sample 2 shows three local stress peaks. The peak stresses observed for these 2 samples are 19.64 MPa and 12.2 MPa. This is the most significant difference in peak stress observed for two samples with same joint pattern during all the experiments.

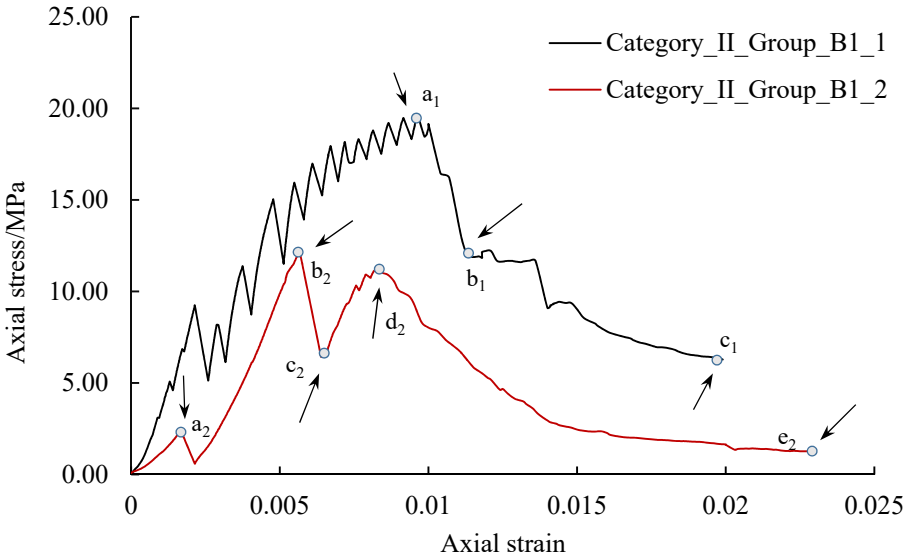

Figure 4.22 Stress-strain curves for samples of category_II_B1: [10/55]

The damage pattern for the two samples are different. According to Figure 4.23a sliding along 55º joint occurs, the other joint remains stable. Matrix failure was observed and some of the joint filling was crushed. With increasing vertical stress, matrix failure and joint sliding increased (Figure 4.23b). The second sample revealed another type of failure: first, there was sliding along the steeper joint (see black arrows in Figure 4.23c). The steeper joint touched the loading platens, therefore, the displacements are very restricted and matrix failure was triggered as shown in Figure 4.23d.

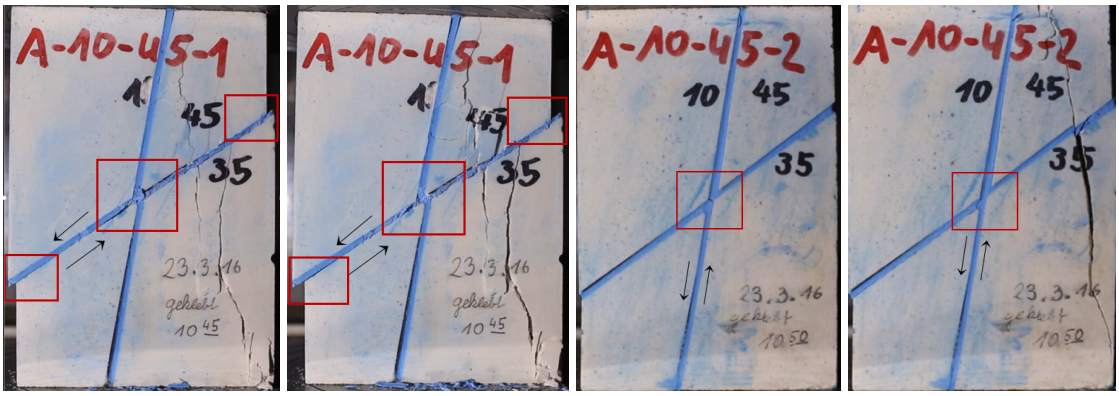

(a) (b) (c) (d)

Figure 4.23 Uniaxial compression test of samples of category_II_B1 [10/55]: damage state at different stress levels according to curves in Figure 4.22

Category II: samples with two joints (group B2)

The stress–strain curves of tested samples with two joint angles of 25° and 70° are shown in Figure 4.24. The two curves show the same trend. a_1 and a_2 are local peak stresses with stress drop behind followed by a nearly linear increase from stage b_1, b_2 to points c_1 and c_2. Points c_1 and c_2 mark the peak stresses followed by strain softening. The corresponding damage process and failure pattern are illustrated in Figure 4.25.

Figure 4.25a shows an initial state of the sample. As can be seen from this picture, the junction of the two cracks were aligned. Then a slight slipping along black arrow direction was observed (see Figure 4.25b). A tiny tension crack emerged inside the junction. In the bottom left of the sample, the intact rock plastic failure and crack emerge were observed. With the increase of load, small crack propagated to form large crack, an apparent displacement occurred along the crack which joint angle is 25° (Figure 4.25c). Ultimately, matrix block failure became conscious as documented in Figure 4.25d. In this test, because of the boundary conditions, sliding at the steeper crack is limited and lead to intact rock failure. The other joint remains stable in the experiment.

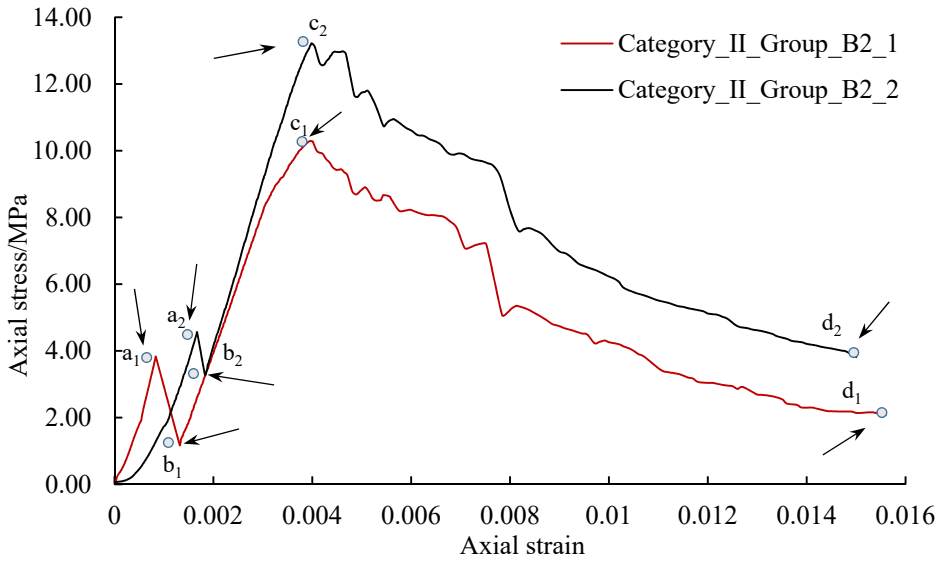

Figure 4.24 Stress-strain curves for samples of category_II_B2: [25/70]

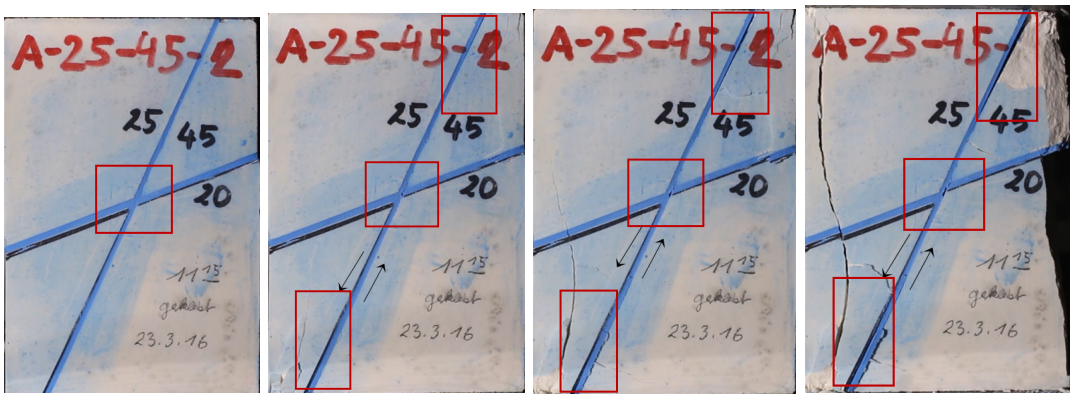

(a) (b) (c) (d)

Figure 4.25 Uniaxial compression test of samples of category_II_B2 [25/70]: damage state at different stress levels according to curves in Figure 4.24

Category II: samples with two joints (group B5)

The stress-strain curves for samples of category II group B5 are shown in Figure 4.26. The joint angles are -85° and 50° (Figure 4.27). The two tests showed different performance. Sample 2 showed nearly linear elastic deformations until peak stress at b_2 was reached. The loading of sample 1 is characterized by a zigzag curve until the peak stress c_1 was reached followed by some softening but still in a zigzag manner. The corresponding failure modes are shown below in Figure 4.27.

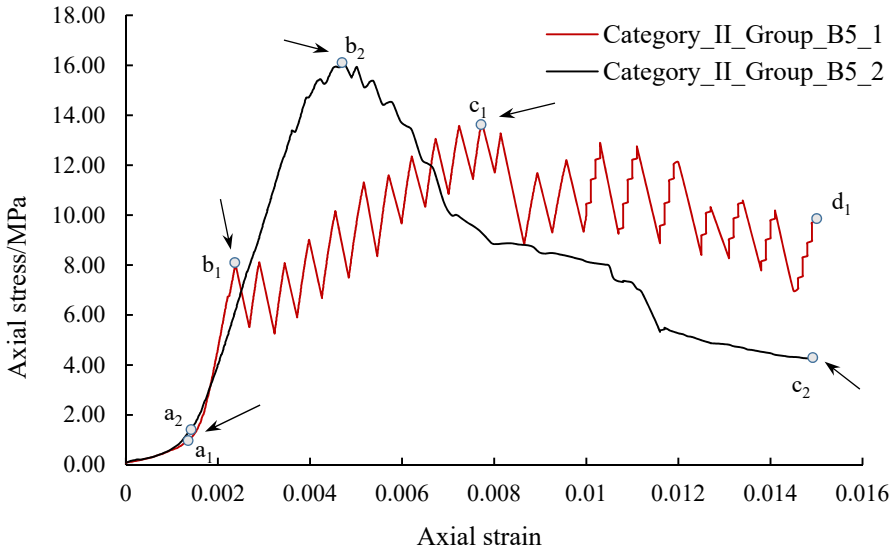

Figure 4.26 Stress-strain curves for samples of category_II_B5: [-85/50]

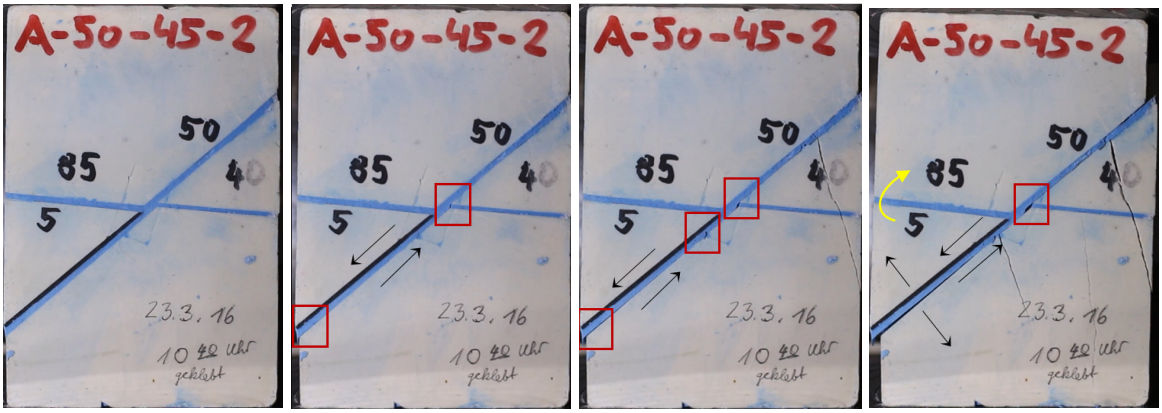

(a) (b) (c) (d)

Figure 4.27 Uniaxial compression test for samples of category_II_B5 [-85/50]: damage state at different stress levels according to curves for sample 2 in Figure 4.26

Figure 4.27a shows the sample in the elastic stage. Figure 4.27b shows the onset of sliding along the 50° joint. Also, at the red middle box a small crack was observed inside the blue colored joint. With ongoing loading, more and more tiny cracks were generated inside the joint and a tensile crack developed at the right part of the sample (Figure 4.27c). As can be seen from the Figure 4.27d, with further increase of load, sliding is accelerating and the upper half of the specimen shows a rotation as indicated by the yellow arrow. The nearly horizontal joint has no influence on the sample failure behavior.

Category II: samples with two joints (group B6)

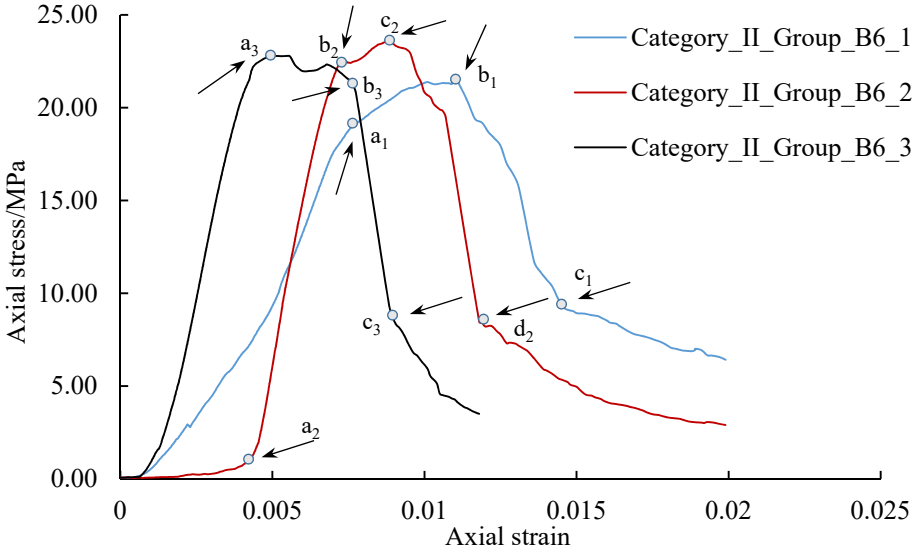

Figure 4.28 Stress-strain curves for samples of category_II_B6: [-70/65]

The stress-strain curves for samples with joint angles of -70° and 65° are shown in Figure 4.28, whereas corresponding failure pattern of the specimen are shown in Figure 4.29. Three samples have been tested with similar results. The maximum stress of all these specimens was over 20 MPa. All tests reveal a pronounced nearly elastic loading phase, a distinguished peak stress followed by softening.

Figure 4.29a shows an initial state of the asymmetric jointed sample. As can be seen in Figure 4.29b, the joints are not sliding and matrix failure is observed. With increasing stress the number of cracks increase and existing cracks grow further, but sliding along the two joints was not observed (Figure 4.29c). As shown in Figure 4.29d, although the rock matrix is partially crushed almost no slipping along the joints was observed in the experiment.

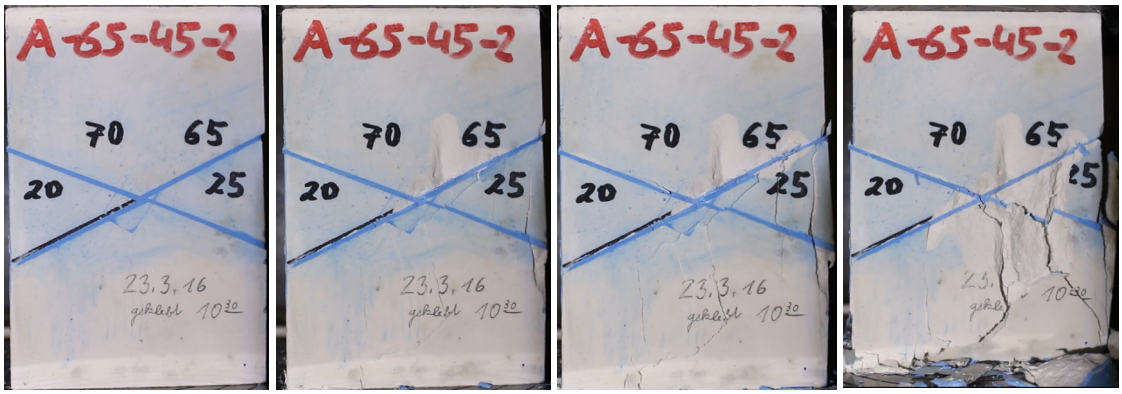

(a) (b) (c) (d)

Figure 4.29 Uniaxial compression test for sample of category_II_B6 [-70/65]: damage state at different stress levels according to curves for sample 2 in Figure 4.28

For specimens in category II group B, the UCS results and the failure state for different geometrical compositions are listed in Table 4.9, Table 4.10 and Figure 4.30.

Table 4.9 Peak stress values and failure mechanisms for samples of category II group B

Name	UCS (MPa)	Primary failure	Secondary failure	Analytical solution for joint 1 (MPa)	Analytical solution for joint 2 (MPa)
B1 [10/55]	19.64	Joint sliding	Matrix failure	13.20	26.28
B1 [10/55]	12.20	Joint sliding	Matrix failure	13.20	26.28
B2 [25/70]	10.29	Joint sliding	Matrix failure	9.67	26.28
B2 [25/70]	12.32	Joint sliding	Matrix failure	9.67	26.28
B5 [-85/70]	13.72	Joint sliding	Joint sliding	26.28	17.51
B5 [-85/70]	16.10	Joint sliding	Joint sliding	26.28	17.51
B6 [-70/65]	22.80	Matrix failure	———	26.28	26.28
B6 [-70/65]	23.65	Matrix failure	———	26.28	26.28
B6 [-70/65]	21.50	Matrix failure	———	26.28	26.28

Table 4.10 Peak stress values and failure mechanisms for samples of category II group B

Name	UCS (MPa)	Primary failure	Secondary failure	Analytical solution for joint 1 (MPa)	Analytical solution for joint 2 (MPa)
B3 [35/80]	5.42	Joint sliding	———	5.82	26.28
B3 [35/80]	4.53	Joint sliding	———	5.82	26.28
B4 [45/90]	6.98	Joint sliding	———	8.44	26.28
B4 [45/90]	9.26	Joint sliding	———	8.44	26.28

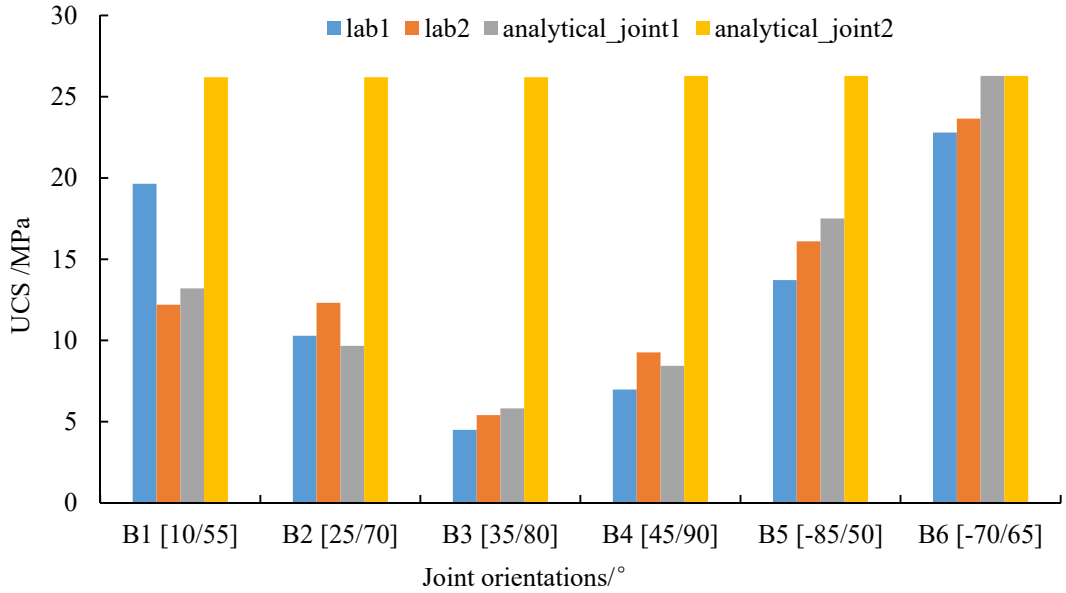

Figure 4.30 Uniaxial compression strength versus joint orientation for samples of category II group B

Table 4.11 Experimental data for the two joints

Sample group	c_j [MPa]	σ_j' [MPa]	ϕ_j [°]	ψ_j [°]	Testing time
B1, B2, B5 and B6	2.5	0.3	32.8	0.24	2016.03.23
B3 and B4	1.5	0.3	32.8	0.24	2016.04.18

The samples in category II group B have joint angles located in the 1st and 4th quadrant (joint angle change from -90° to 90°). All the experiments show good agreement with the analytical solutions. As can be seen from Table 4.3, slip failure along the joints hold for samples of group B3, B4 and B5. Both, joint sliding and matrix failure occurred on samples of group B1 and B2. In this joint angle combination, slip along the joint leads to partial matrix rotation and finally to matrix failure. Samples of group A6 shows matrix shear failure. It should be mentioned, that samples of category

II group B were manufactured in two different periods which lead to different joint strength parameters as shown in Table 4.11.

Category II: samples with two joints (group C)

Figure 4.31 shows the stress-strain curves for sample with two joints (30° and 60°). The two tested specimens show different results (see Figure 4.31). Peak stresses were reached at points a_1 and b_1. Sample 2 shows pronounced strain softening, while sample 1 shows more or less perfect plasticity with fluctuations and small softening. The damage process for sample 1 is illustrated in Figure 4.32.

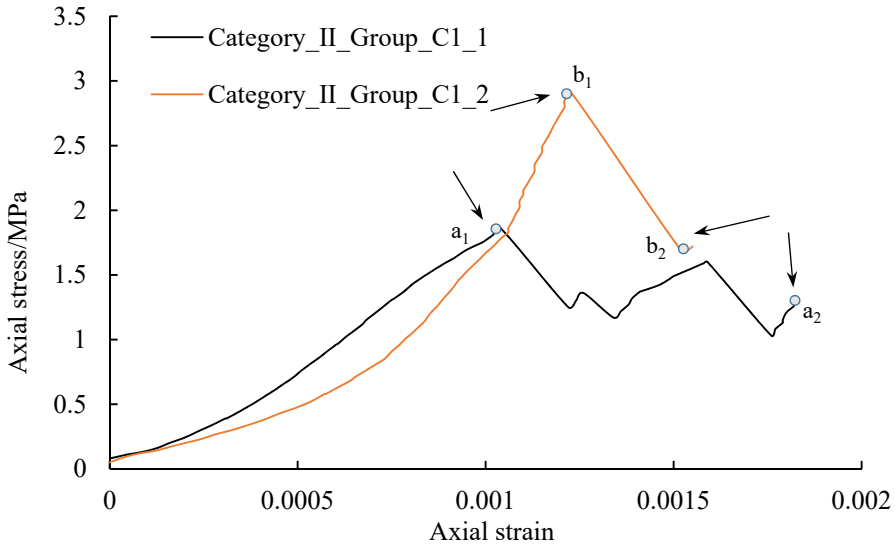

Figure 4.31 Stress-strain curves for samples of category_II_C1: [30/60]

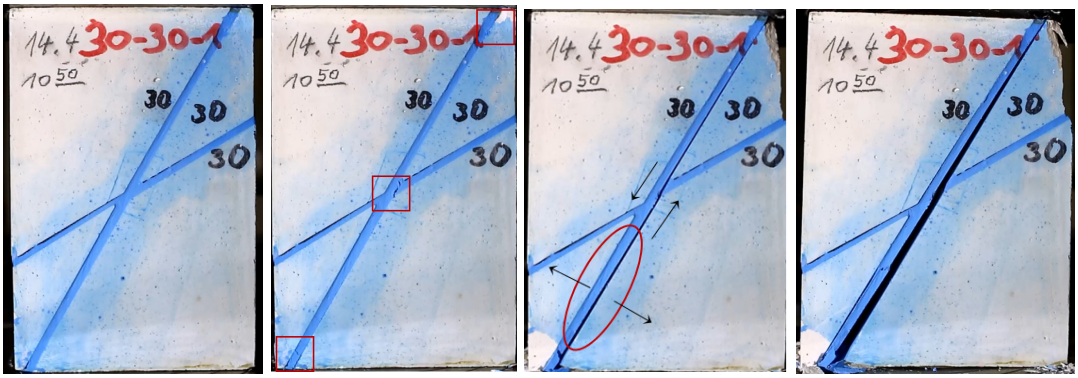

(a) (b) (c) (d)

Figure 4.32 Uniaxial compression test for sample of category_II_C1 [30/60]: damage state at different stress levels according to curve for sample 1 in Figure 4.31

Figure 4.32a shows sample 1 before testing. Three red rectangles mark regions of special interest. In Fig 4.32b (middle red box) a crack emerged inside the blue gypsum at the joint crossing point and matrix failure occurred at the bottom of the specimen. As shown in Figure 4.32c, a joint shear displacement occurs as indicated by the black arrows. Also, a tensile failure at the lower part of joint is observed (see red ellipse). Finally, slip along the steeper joint and matrix fracture were observed.

Table 4.12 Peak stress values and failure mechanisms for samples of category II group C

Name	UCS [MPa]	Primary failure	Secondary failure	Analytical solution for joint 1 [MPa]	Analytical solution for joint 2 [MPa]
C1 [30/60]	2.97	Joint sliding	———	3.68	26.28
C1 [30/60]	4.13	Joint sliding	———	3.68	26.28
C2 [35/65]	4.82	Joint sliding	———	3.88	26.28
C2 [35/65]	3.15	Joint sliding	———	3.88	26.28
C3 [60/90]	20.82	Matrix failure	Joint sliding	26.28	26.28
C3 [60/90]	21.63	Matrix failure	Joint sliding	26.28	26.28

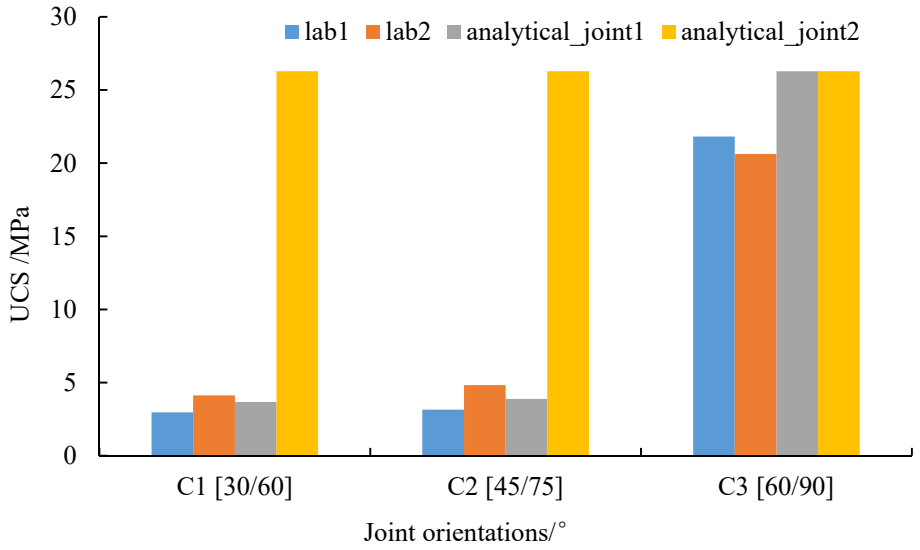

Figure 4.33 Uniaxial compression strength versus joint orientation for samples of category II group C

According to Table 4.12, all of the joint combinations are located in the first quadrant (joint angle: 0° - 90°). Samples of group C1 and group C2 failed by slip along the joint. Both, matrix failure and joint sliding occurred on samples of group C3. Figure 4.33 indicates increasing UCS with increasing joint angle.

4.5.3 Stress-strain characteristics and fracture pattern for samples of category III

Different properties have been assigned to each of the two joints (called primary and secondary joint) in category III samples. There are three joint combinations in category III group D. The joint angles are located in the 1st and 4th quadrant (joint angle vary from -90° to 90°). Most of the experiments show good agreement with the analytical solutions. As Table 4.13 documents, slip failure occurred along the joints in all tests.

The joint configurations for group D2 and D3 are the same, but with different joint cohesion as listed in Table 4.14. Graph 4.34 and Table 4.8 illustrate that if the primary joint has an angle of 35°, the samples have lowest peak stress (below 4 MPa). When the primary joint angle is 45° and the secondary one 35°, the analytical solution for failure at both joints is close to each other. In that case it is not quite clear which joint fails first.

Table 4.13 Peak stress values and failure mechanisms for samples of category III group D

Name	UCS [MPa]	Primary failure	Secondary failure	Analytical solution for joint 1 [MPa]	Analytical solution for joint 2 [MPa]
D1 [-45/45]	2.46	Joint sliding	———	5.63	8.44
D1 [-45/45]	5.57	Joint sliding	———	5.63	8.44
D1 [-45/45]	6.2	Joint sliding	———	5.63	8.44
D2 [-45/35]	5.34	Joint sliding	———	5.63	5.82
D2 [-45/35]	3.74	Joint sliding	———	5.63	5.82
D2 [-45/35]	4.67	Joint sliding	———	5.63	5.82
D3 [35/-45]	3.43	Joint sliding	———	3.88	8.44
D3 [35/-45]	4.03	Joint sliding	———	3.88	8.44
D3 [35/-45]	4.58	Joint sliding	———	3.88	8.44

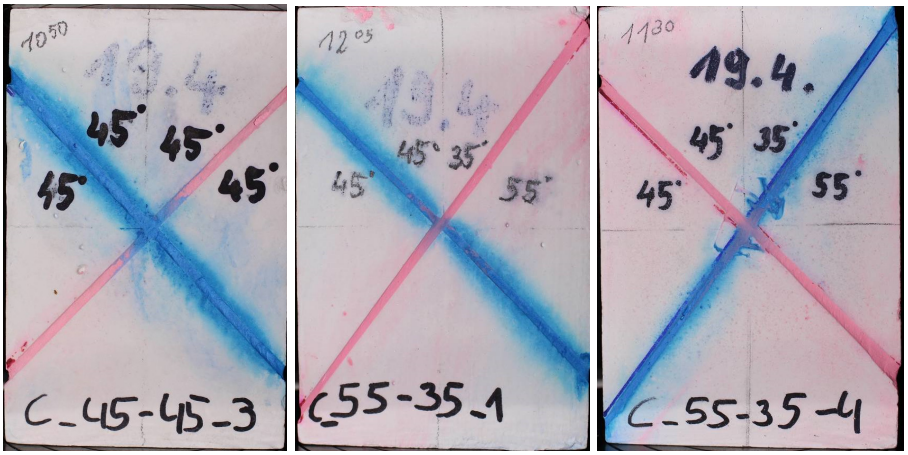

(a)

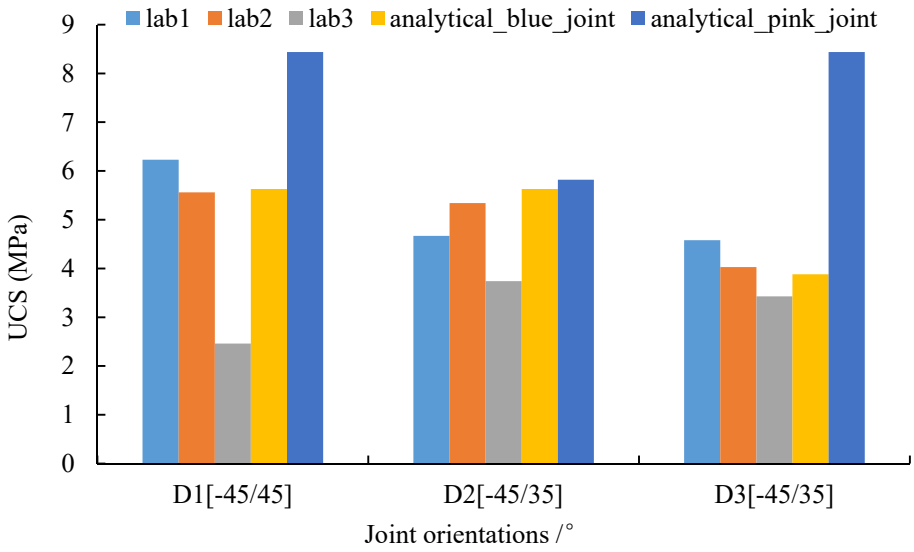

(b)

Figure 4.34 Uniaxial compression test for samples of category_III_D: (a) two different joint angle combinations, (b) uniaxial compression strength versus joint orientation for samples of category III group D

Table 4.14 Back analyzed experimental joint strength data

Joint type	c_j [MPa]	σ_j' [MPa]	ϕ_j [°]	ψ_j [°]
Primary joint	1.0	0.3	32.8	0.24
Secondary joint	1.5	0.3	32.8	0.24

4.6 Conclusions

Based on the uniaxial compression tests of samples of the three categories, the following conclusions can be drawn.

First, a series of experiments to study the behavior of artificial rock samples with weak planes under uniaxial compression was successfully conducted and used to validate a new constitutive model.

Second, the results of the experiments revealed three major failure mechanisms: (1) plastic failure of the rock matrix, (2) slip on a preferred joint plane, (3) both, slip failure at joint and rock matrix failure. Matrix failure is mainly observed when single joint or both joints are nearly perpendicular to applied compressive load (joint angles from 60º to 90º). Specimens with one or more steep joint planes fail by sliding along the steepest joint (steep joint angles are between 35º to 60º) and normally, no failure inside the rock matrix is observed. When the joints are very steep (joint angles between 10º to 35º), the joints touch the platens of the uniaxial compressive testing machine and rock matrix failure with restricted sliding along the joint is observed. Also, in some cases the mechanisms of deformation and failure are controlled by combined movement of the two joints.

Third, jointed rock exhibits strength anisotropy. For category I samples, it is found that UCS is mainly controlled by the joint direction. For category II samples, geometric composition of the two joints control the rock mass strength. When both joint angles are low, rock matrix failure is observed and peak stresses show highest values. When one joint is relatively steep, the peak stress is much lower. The testing of category III samples revealed that anisotropy of a jointed rock does not only depend on joint angle but is also related to shear strength of the joint.

Forth, stress-strain curves obtained by the experiments indicate nearly brittle behavior for joint failure. The zigzag shaped stress-strain curves are based on stick-slip mechanism during joint failure. Some imperfections of the artificial jointed samples and unavoidable scatter in material parameters lead to some deviation between analytical solutions and lab testing results.

Nevertheless, the typical expected features were duplicated by the experiments and confirm the underlying theory.

5 Numerical modeling

5.1 Introduction

In this chapter, the implementation of the multi-joint model into the numerical code is described and the influence of joint strength parameters are analyzed by a series of numerical simulations. Then, lab results obtained by tests with jointed gypsum samples are compared with the numerical predictions. Uniaxial compressive tests for specimens with more than one joint are simulated via the new developed multi-joint model in FLAC. In parallel, the Discrete Element code UDEC (Itasca, 2007) was used to simulate the same tests by explicit consideration of the joints.

The multi-joint model is programmed as a User Defined Model (UDM) which considers joint sets in an implicit manner. In this model, the planes of weaknesses (joints) for each zone are specified by a certain orientation without a fixed location inside the zone similar to the standard ubiquitous joint model. The joints are embedded in a Mohr-Coulomb matrix. The applied failure criterion is based on the Mohr-Coulomb law with tension cut-off and used for both, the joints and the rock matrix. The failure of the intact rock is checked first. Whenever shear or tensile failure is detected, the relevant plastic corrections are applied and the stress state is updated. Then, the new stress state is used to analyze if failure on the joints occur or not.

The dimensions of the modeled jointed rock blocks in FLAC and UDEC were identical: 0.10 × 0.15 m in horizontal and vertical direction, respectively. The FLAC model has 150 zones with gridpoint distance of 0.01m. 4 blocks and a total of 8192 triangular elements are used in the UDEC model as shown in Figure 5.1.

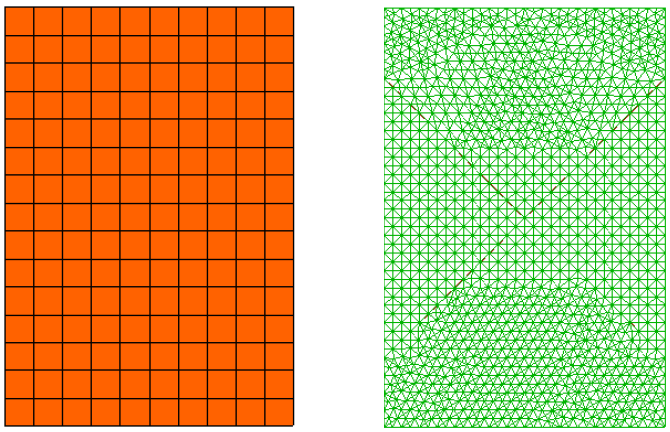

(a) (b)

Figure 5.1 Geometry of the numerical samples: (a) FLAC model and (b) UDEC model

5.2 Elastic parameters (model category I)

First, lab samples without joints were investigated to obtain matrix strength and stiffness parameters. The mechanical parameters of gypsum are listed in Table 5.1

Table 5.1 Mechanical parameters for the gypsum simulation (lab test results)

Gypsum	ρ [kg/m^3]	σ_c [MPa]	σ_t [MPa]	E [GPa]	v [-]
Rock matrix	1810	30	2.26	20.03	0.24

The persistent discontinuities in the multi-joint model and the UDEC model are characterized by the following properties: friction angle, cohesion, tensile strength, dilation angle, normal and shear stiffnesses. High values of stiffness lead to slow solution convergence due to small timesteps. It is proposed to use low stiffness consistent with small elastic joint deformations. A good rule-of-thumb to obtain joint stiffnesses, k_n and k_s, is to multiply the equivalent stiffness of the stiffest neighboring zone with a certain factor (e.g. a factor of 10) according to (Itasca, 2012):

$$k_n = factor \times \left[\frac{K + \frac{4}{3}G}{\Delta z_{\min}} \right] \tag{5.1}$$

where: K and G are the bulk and shear modulus of the matrix, Δz_{min} is the smallest width of an adjoining zone in the normal direction.

The model size in FLAC and UDEC are the same, but the smallest width of an adjoining zone is different according to the mesh size. The maximum normal joint stiffness can be calculated for the FLAC and UDEC model, respectively:

$$k_n \le 10 \times \left[\frac{1.284e10 + \frac{4}{3} 8.10e9}{0.1 / 10} \right] = 2.364e13 \text{ Pa/m} \tag{5.2}$$

$$k_n \le 10 \times \left[\frac{1.284e10 + \frac{4}{3} 8.10e9}{0.005} \right] = 4.728e13 \text{ Pa/m} \tag{5.3}$$

The numerical simulation results obtained from back analysis of uniaxial lab tests are listed in Table 5.2.

Table 5.2 Joint parameters

Model type	k_n [Pa/m]	k_s[Pa/m]	c_j [MPa]	σ_j^t [MPa]	ϕ_j [°]	ψ_j [°]
FLAC	1e12	——	1.5	0.3	32.8	10
UDEC	1e13	1e13	1.5	0.3	32.8	10

In order to determine the influence of the joint stiffness, three different models containing one single 45 ° joint were tested. Table 5.3 and Figure 5.2 show stress and strain simulation results for different stiffness values using UDEC. The strength parameters are the same as shown in Table 5.2. It becomes obvious that the joint stiffness has a great effect on deformation, but does not change strength.

Table 5.3 Influence of joint stiffness values (see Figure 5.2)

Code	k_n [Pa/m]	k_s [Pa/m]	Peak stress [MPa]	Peak vertical strain [-]
UDEC	1e10	1e10	5.6	0.0025
UDEC	1e12	1e12	5.8	0.00050
UDEC	1e13	1e13	5.57	0.00028

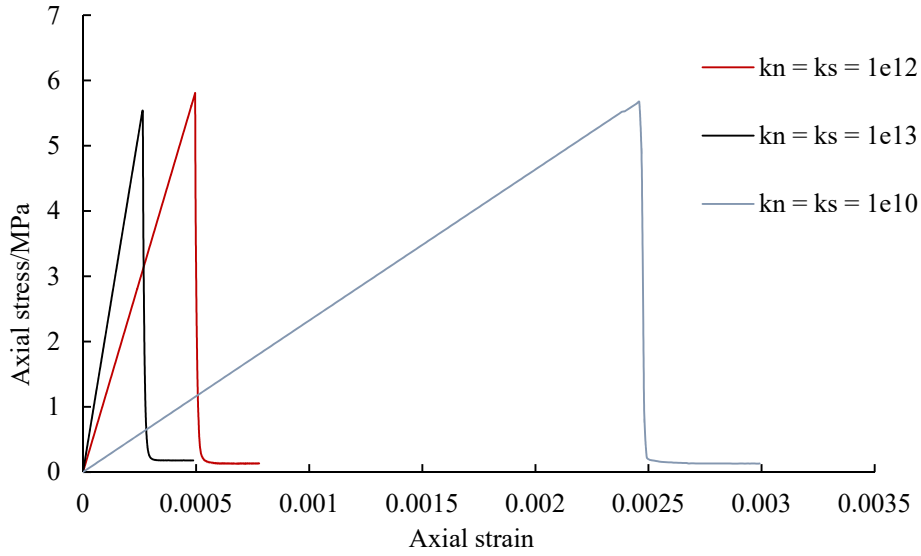

Figure 5.2 Uniaxial compression test: stress-strain behavior obtained by UDEC model using different joint stiffnesses

5.3 Simulation of uniaxial compression test (model category I)

The objective of the presented numerical study is to verify and validate the developed constitutive model by using a sample with a single joint. All other parameters are the same as for the uniaxial compression test given in Tables 5.1 and 5.2.

The simulated stress-strain curves for samples with joint inclination of 60° and 45° are shown in Figure 5.3. The peak stresses obtained from lab tests and simulations are close to each other, but models and lab tests show different vertical strain. As can be seen from Figure 5.3b, FLAC and UDEC models have exactly the same behavior since failure in rock matrix occurs. If a jointed rock has a negative joint angle, there is a significant decrease of the vertical stress in the UDEC model

due to sliding along the joint. The FLAC model is an elastic-perfect plastic model, therefore, stress reaches a plateau after onset of joint sliding.

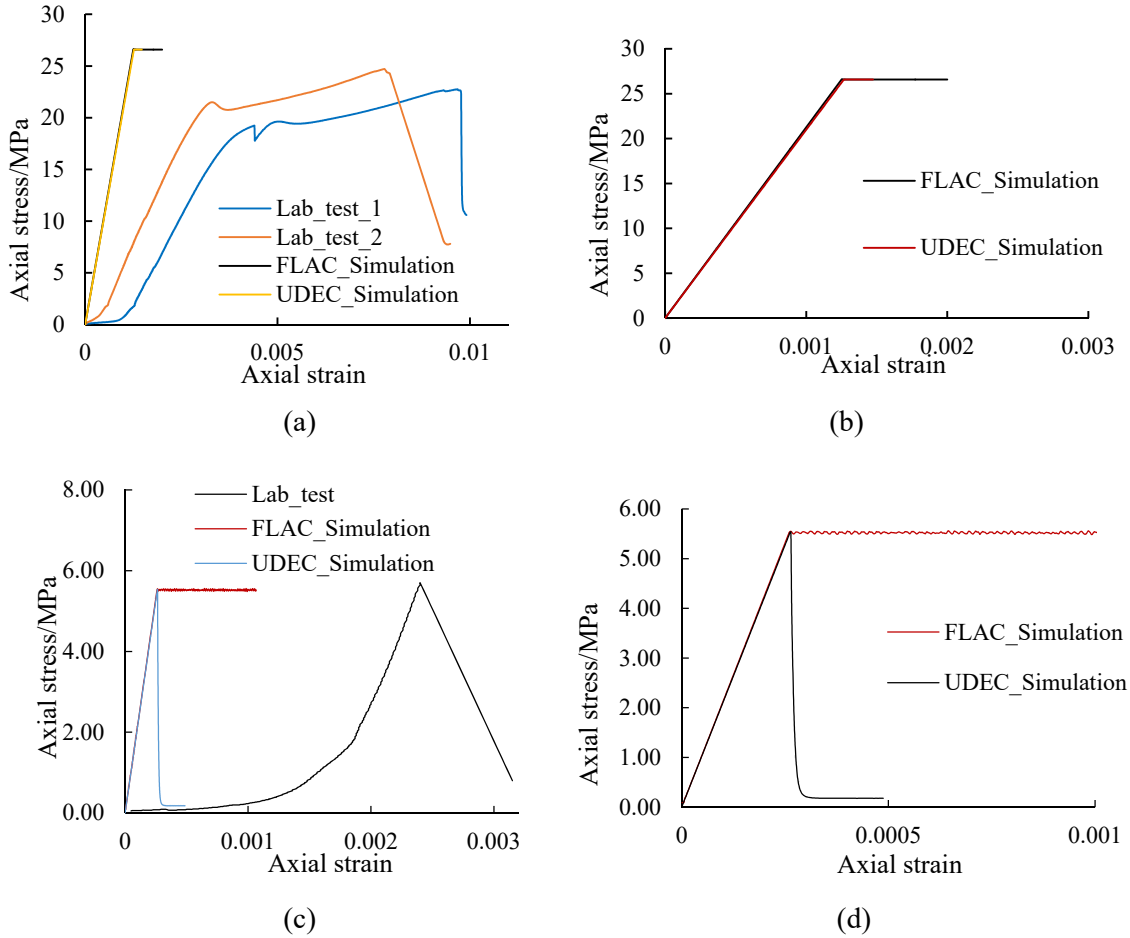

Figure 5.3 Strain-stress curves for uniaxial compression tests: (a) lab testing and numerical modeling for joint with 60°, (b) FLAC and UDEC simulation results for joint with 60°, (c) lab testing and numerical modeling for joint with 45°, (d) FLAC and UDEC simulations for joint with 45°

There are several reasons that lead to the strain difference between the numerical models and the lab tests. First, the joint stiffnesses are usually defined by empirical rules. It is difficult to measure these parameter for real joints. Second, Figure 5.4 provides an overview of strain monitoring for rock samples. In order to get accurate displacements for the rock matrix, the strain gauge should be placed directly on the sample like shown in Figure 5.4 on the right-hand-side. However, the test performed within the framework of this thesis used machine values to measure the strain, that means strain is measured at the loading plates (between A and B as illustrated in Figure 5.4 on the

left-hand-side). The additional interface between sample and loading plate has to be taken into account. The change of monitor position can also result in strain difference (Taheri, 2007; Baumgarten, 2015). Third, joints in UDEC and FLAC models are assumed to be planar, persistent and without thickness, but in the lab experiments, joints have a thickness of about 4 - 7 mm as shown in Figure 5.5. The thickness of the joints and the interface between the sample and the loading plates causes an overall significant softer behavior.

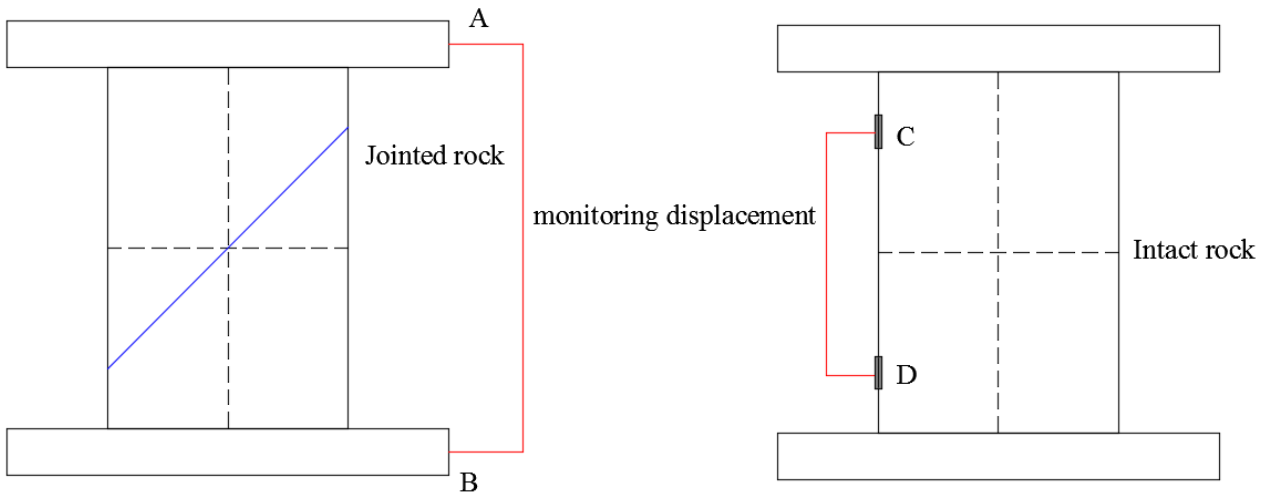

Figure 5.4 Two types of strain measurements (left: between loading plates, right: direct on the sample)

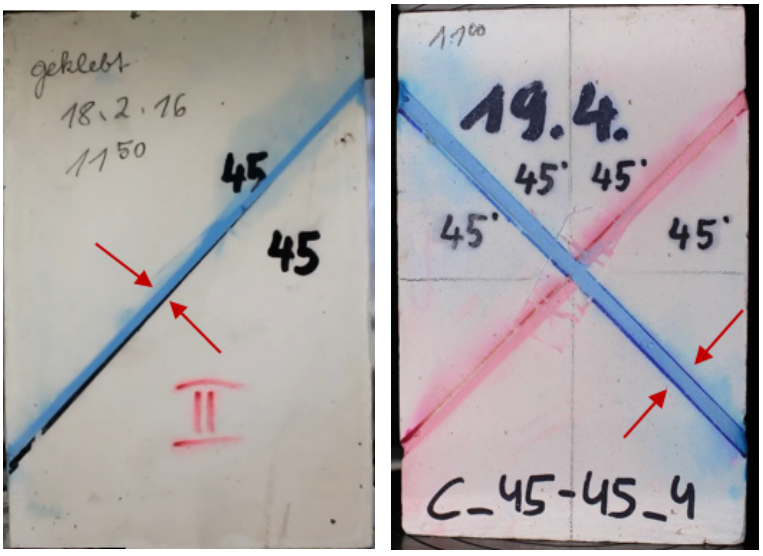

Figure 5.5 Joints thickness for various samples

The numerical simulations provide a straightforward comparison of the peak stress and the failure type of the samples. The UCS values for samples with one joint are given in Table 5.4 and compared graphically in Figure 5.6. For a jointed rock model, failure may occur in either the intact rock or along the joints, or both, dependent on stress state, material properties and angle of the joints.

Models of group A in Figure 5.6 have a 35° joint. Simulated strength is close to lab results and joint sliding failure is recorded. Models of group B have a 45° joint. All the experimentally determined UCS values are slightly higher than the computed results. There is also joint slip failure observed. For models of group C (60° joint angle) all UCS values are over 20 MPa, and matrix failure is observed.

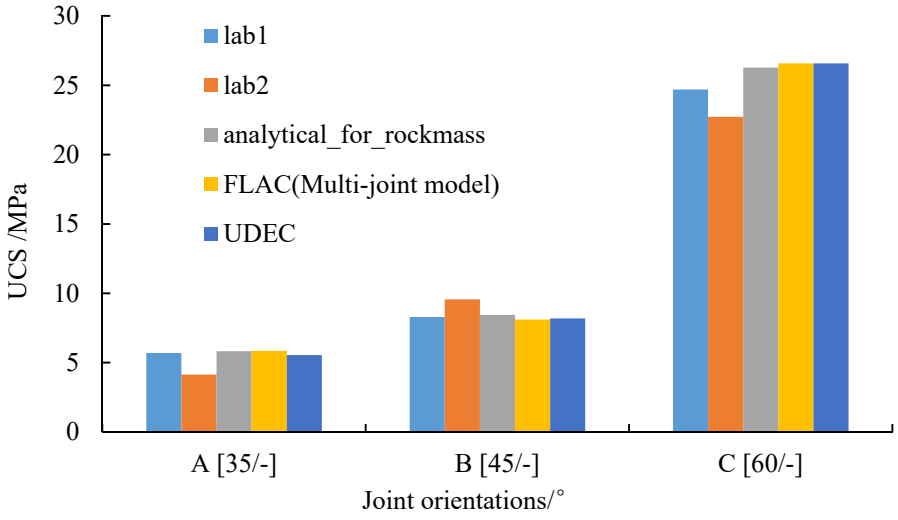

Figure 5.6 Uniaxial compressive strength vs. joint orientation

Figure 5.7 compares the FLAC results obtained by using the multi-joint model with analytical solution for the three model/sample groups. The analytical results show excellent match with the FLAC simulations. The error is below is 1 % for all joint angles. Lab test results for group A and B show good agreement with modeling results. The uniaxial compressive strength obtained by lab test in group C is slightly lower than the simulation results. In the numerical modeling processes, the joint is treated as a persistent plane without considering roughness parameters in an explicit manner.

Table 5.4 Numerical simulation results compared to the lab tests for single joint orientations

Name	UCS [MPa] (laboratory)	UCS [MPa] (analytical)	UCS [MPa] (FLAC)	UCS [MPa] (UDEC)	Failure type
A [35/-]	5.70	5.82	5.84	5.54	Joint sliding
A [35/-]	4.17	5.82	5.84	5.54	Joint sliding
B [45/-]	8.29	8.44	8.11	8.19	Joint sliding
B [45/-]	9.56	8.44	8.11	8.19	Joint sliding
C [60/-]	24.70	26.28	26.58	26.58	Matrix failure
C [60/-]	22.73	26.28	26.58	26.58	Matrix failure

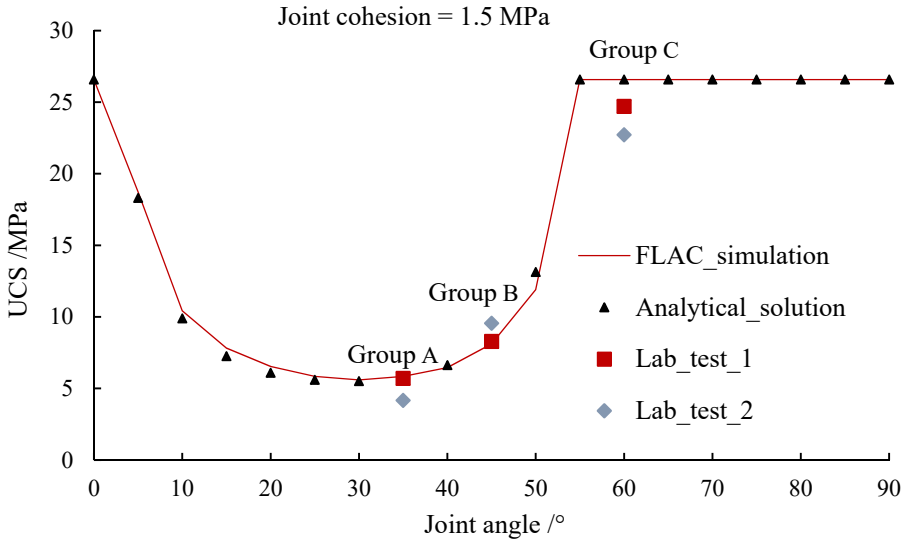

Figure 5.7 Uniaxial compressive strength vs. joint angle

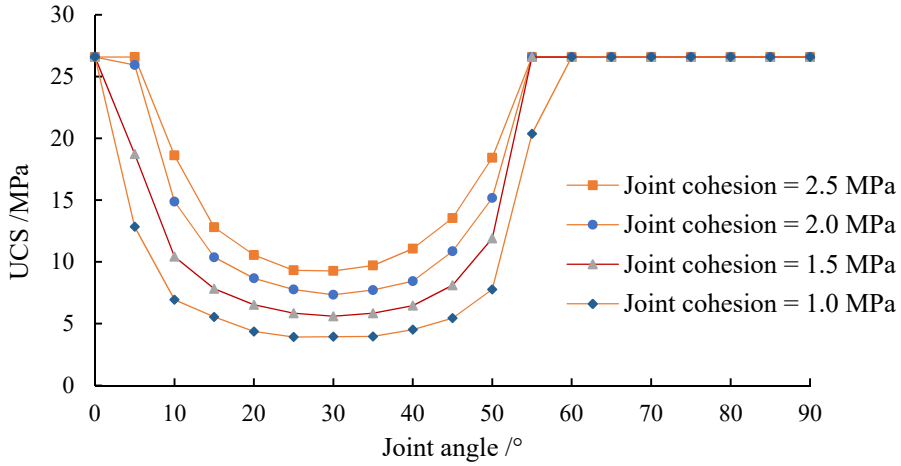

Figure 5.8 Uniaxial compressive strength vs. joint angle for different joint cohesion values

The joints in the artificial lab specimen are handmade by gypsum. It is difficult to guarantee the same joint cohesion for each sample, therefore variations in joint cohesion have to be expected. Figure 5.8 illustrates how uniaxial compressive strength varies for joint angle between 0° and 90° (from vertical to horizontal direction). All curves have the same shape and confirm Jaeger's single plane of weakness theory (Jaeger, 1970). Lower joint cohesion results in lower strength values except the region there only matrix failure is observed. Most significant strength differences are between 0 ° and 10 ° as well as between 50° to 60°.

5.4 Simulation of uniaxial compression test (model category II)

5.4.1 Group A (minimum angle between two joints is 60°)

The numerical simulation results are compared with analytical solutions and experimental data as shown in Table 5.5. The groups A1 and A4 have symmetric joint angles.

Table 5.5 UCS results for non-orthogonal joint set (Group A)

Name	UCS [MPa] (laboratory)	UCS [MPa] (analytical)	UCS [MPa] (FLAC)	UCS [MPa] (UDEC)	Failure type
A1 [-30/30]	3.29	5.52	5.49	5.26	Joint sliding
A1 [-30/30]	5.4	5.52	5.49	5.26	Joint sliding
A2 [10/70]	16.51	10.42	10.06	9.92	Joint sliding
A2 [10/70]	19.08	10.42	10.06	9.92	Joint sliding
A3 [30/90]	3.36	5.52	5.6	5.25	Joint sliding
A3 [30/90]	7.93	5.52	5.6	5.25	Joint sliding
A4 [-60/60]	20.63	26.28	26.58	26.58	Matrix failure
A4 [-60/60]	19.82	26.28	26.58	26.58	Matrix failure
A5 [-45/75]	7.27	8.44	8.19	8.11	Joint sliding
A5 [-45/75]	11.23	8.44	8.19	8.11	Joint sliding

Group A comprises five joint combinations. If one of the two joints has an inclination of 30° (group A1 and A3), the models have lowest strength (around 5 MPa) caused by joint failure. If both of the joints have angles between 60° - 90°, rock matrix failure occurs and the corresponding peak

stress is over 20 MPa (group A4). Results of laboratory experiments are consistent with those of simulations for group A5.

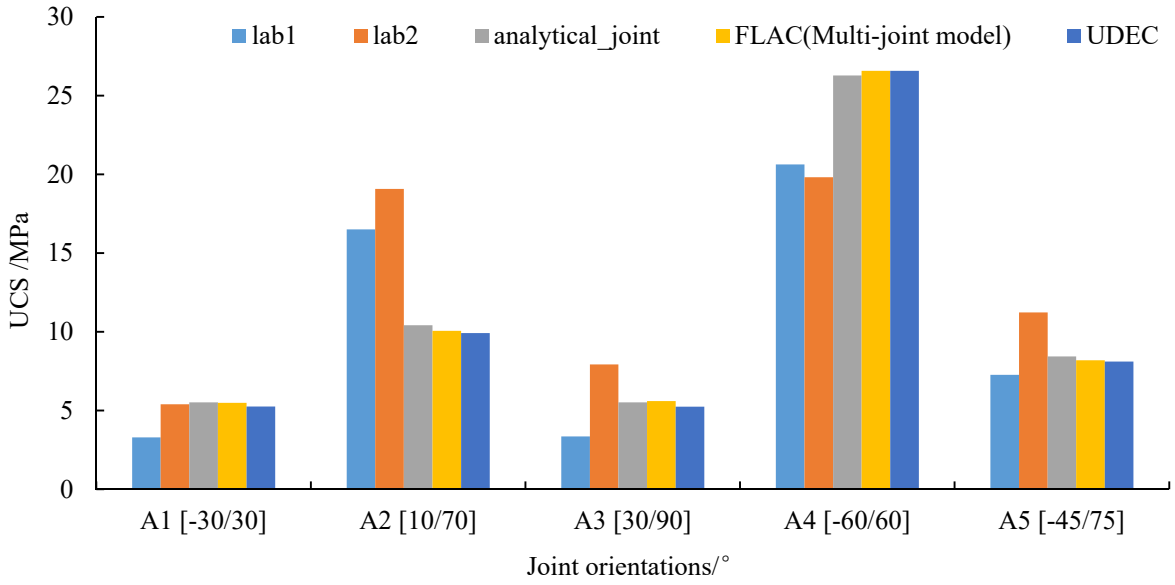

Figure 5.9 UCS vs. joint inclination for group II_A

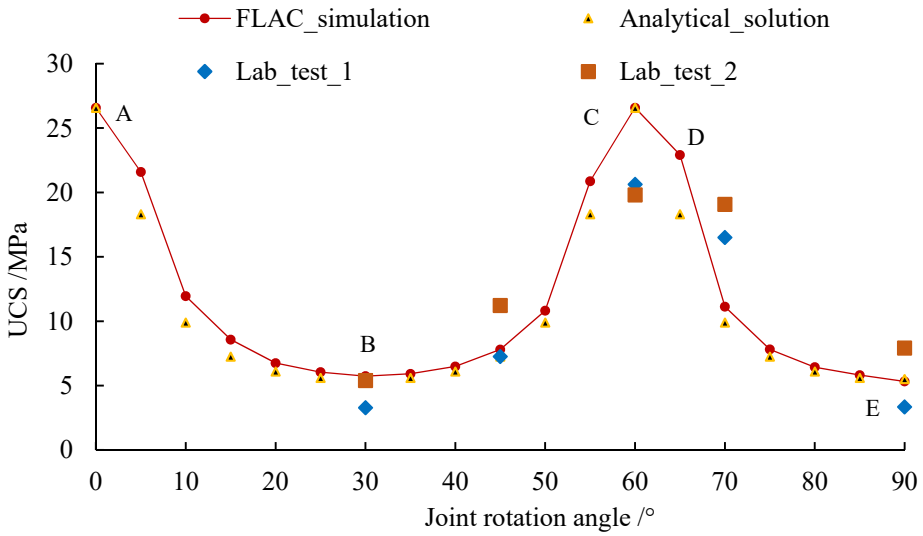

Figure 5.10 UCS vs. rotation angle for group II_A

The observed peak stress obtained by rotation of two crossing joints with constant angle between them of 60° is shown in Figure 5.9 and Figure 5.10. The rotation angle is defined as the minimum angle between the two joints. The deviation between analytical solutions and numerical simulation results is below 5 % for all joint angles. Also, the lab test results confirm the simulations.

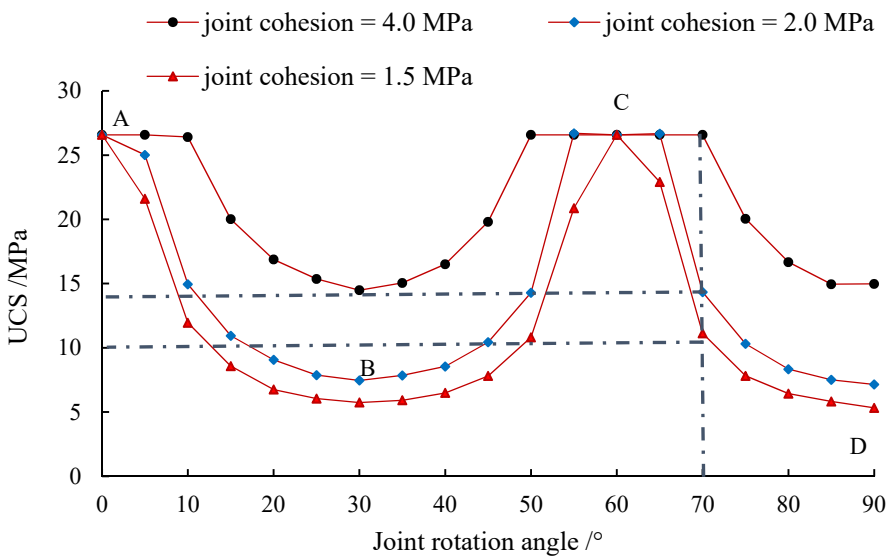

Figure 5.11 UCS vs. rotation angle for group II-A assuming different joint cohesion values

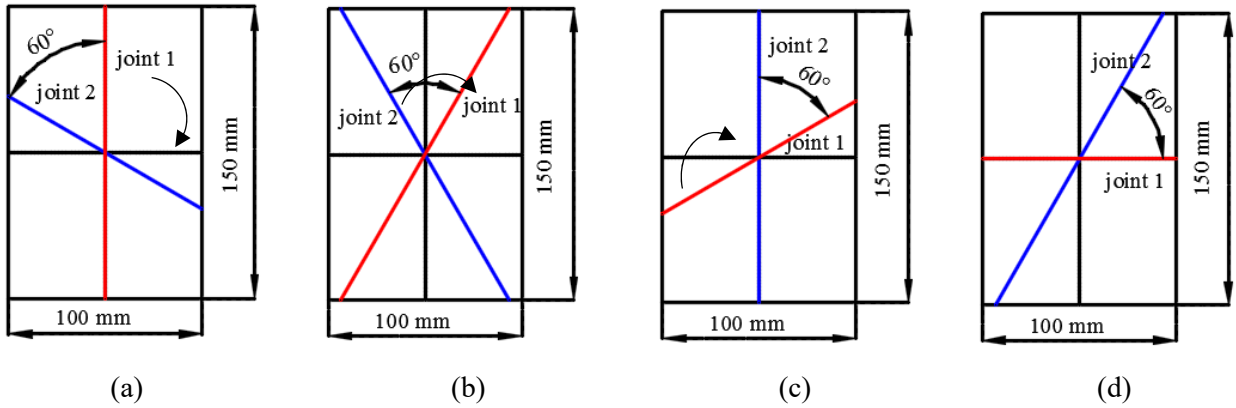

Figure 5.12 Schematic plot of joint pattern for group II_A during rotation

Predicted UCS values for samples with two joints (60° angle between them) are shown in Figure 5.11 for different cohesion values and different rotation angles. Figure 5.12a shows the starting position for this joint configuration and 5.12d gives the final position after 90° rotation. All three curves show the same trend. The strongest strength difference is observed for rotation angles of about 10°, 50° and 70°.

5.4.2 Group B (minimum angle between two joints is 45°)

Simulation results in comparison with analytical solutions and experimental data are shown in Table 5.6. There is no symmetric joint angle combination. When one joint inclination is close to the critical angle joint sliding occurs with dramatic stress decrease.

Table 5.6 UCS results for two non-orthogonal joints (group B)

Name	UCS [MPa] (laboratory)	UCS [MPa] (analytical)	UCS [MPa] (FLAC)	UCS [MPa] (UDEC)	Failure type
B1 [10/55]	19.64	16.5	16.53	16.9	Joint sliding
B1 [10/55]	12.2	16.5	16.53	16.9	Joint sliding
B2 [25/70]	10.29	9.67	9.34	10.08	Joint sliding
B2 [25/70]	12.32	9.67	9.34	10.08	Joint sliding
B3 [35/80]	4.5	5.82	5.76	5.53	Joint sliding
B3 [35/80]	5.4	5.82	5.76	5.53	Joint sliding
B4 [45/90]	6.98	8.44	8.45	8.14	Joint sliding
B4 [45/90]	9.26	8.44	8.45	8.14	Joint sliding
B5 [-85/50]	13.72	17.51	17.62	19.17	Joint sliding
B5 [-85/50]	16.1	17.51	17.62	19.17	Joint sliding
B6 [-70/65]	22.8	26.28	26.58	26.58	Matrix failure
B6 [-70/65]	23.65	26.28	26.58	26.58	Matrix failure
B6 [-70/65]	21.50	26.28	26.58	26.58	Matrix failure

Six joint combinations are considered in this chapter. The joint cohesion for group B3 and B4 is 1.5 MPa. For the other modeling groups the joint cohesion was set to 2.5 MPa. If one joint angle is 35° (group B3), the model shows lowest strength (around 6 MPa) accompanied by joint sliding failure. If both of the joints have inclination between 60°- 90° rock matrix failure occurred and corresponding strength is over 20 MPa (group B6). In general: analytical solutions, UCEC simulation results and FLAC simulations are very close to each other. The lab tests show some minor deviations, but confirm the general trend.

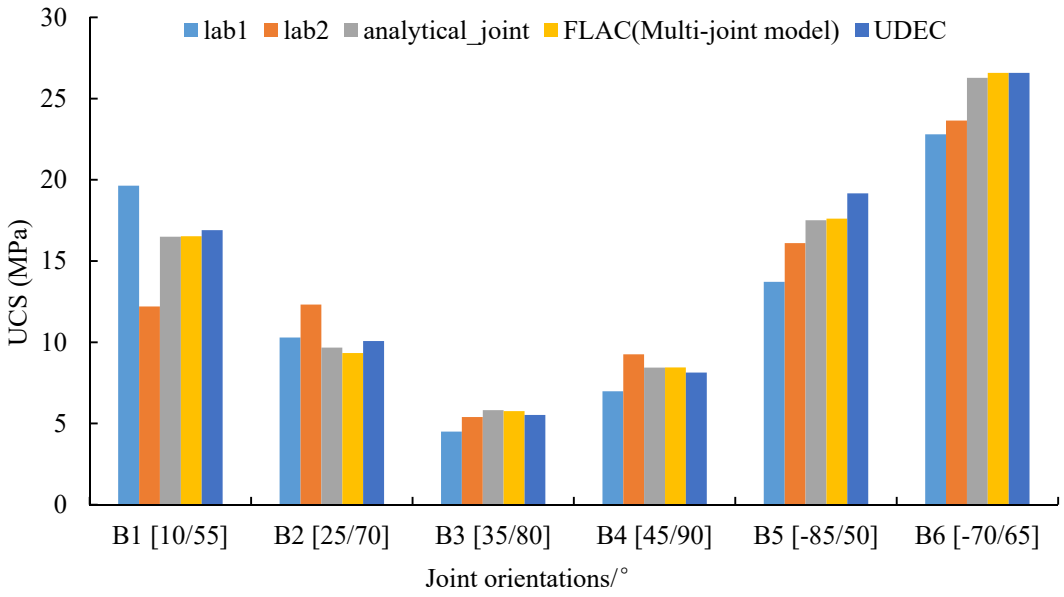

Figure 5.13 UCS vs. joint inclination for group II_B

Figure 5.13 shows a comparison between analytical solutions, lab test results and the multi-joint model results for four groups (one joint angle varies from 0° to 90°). Analytical results are consistent with FLAC simulations with an error below 5 % for all joint angles. The modeling results of group II_B2, II_B3 and II_B4 show good agreement with the lab results. If joint cohesion is 2.5 MPa, the analytical solution gives a maximum strength value close to 22 MPa, which is lower than the matrix failure value (around 26 MPa). If joint cohesion is 1.5 MPa, the maximum UCS is close to 13 MPa, which is significantly lower than the matrix strength (26 MPa).

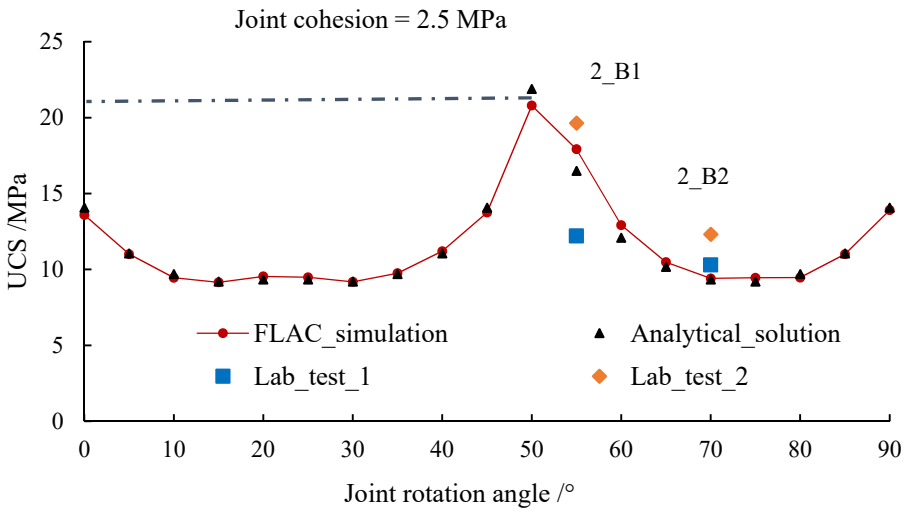

(a)

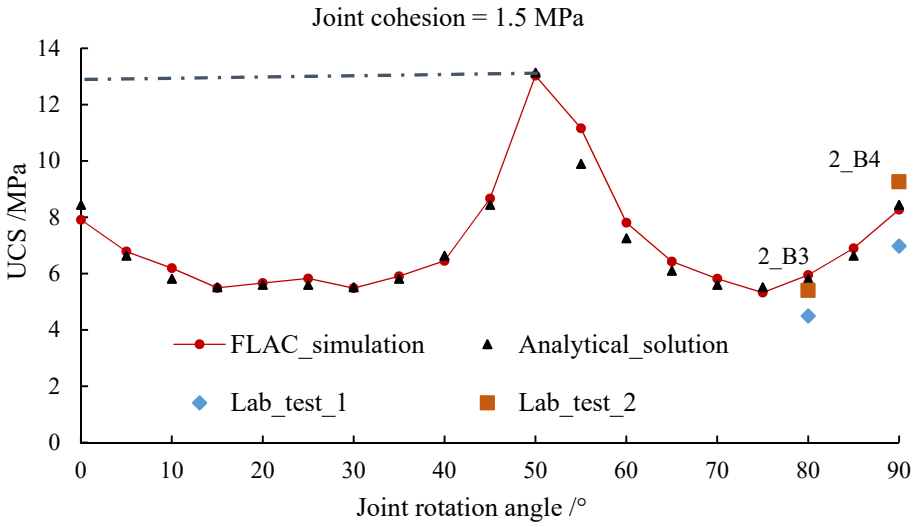

(b)

Figure 5.14 UCS vs. rotation angle for group II_B: (a) joint cohesion of 2.5 MPa, (b) joint cohesion of 1.5 MPa

Figure 5.14 illustrates the observed peak stress obtained by rotation of two crossing joints with constant minimum angle between them of 45°. The predicted strength behavior for different joint cohesion values is shown in Figure 5.15.

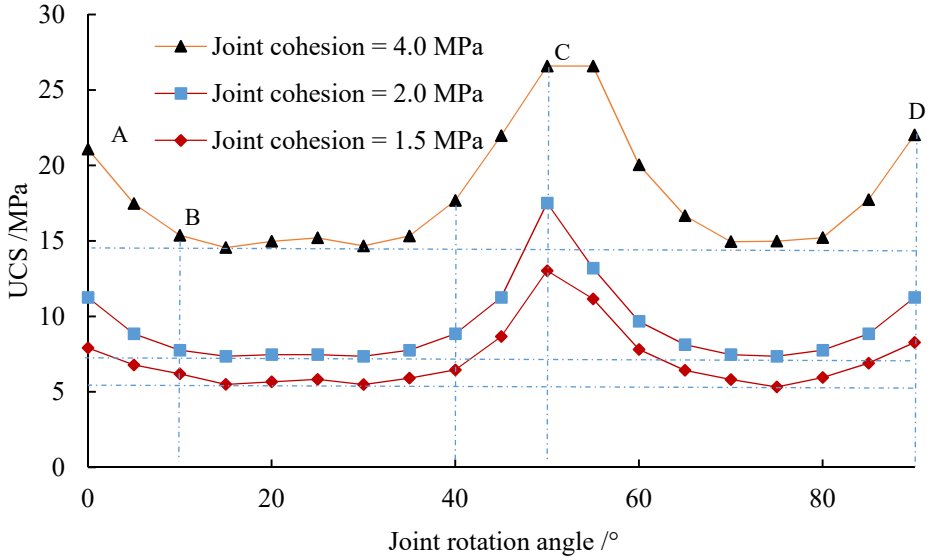

Figure 5.15 UCS vs. rotation angle for group II_B curves assuming different joint cohesion

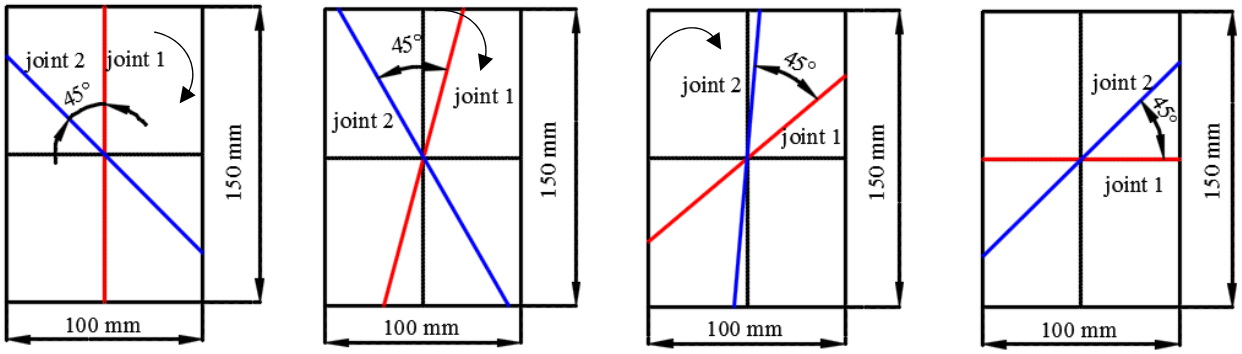

(a) (b) (c) (d)

Figure 5.16 Illustration of joint pattern for group II_B during rotation

Figure 5.16a shows the starting position for this joint configuration and then the two joints rotate in the clockwise direction until the red colored joint arrived at a horizontal position. The UCS changes with the different joint angle combinations. The curves in Figure 5.15 are sufficient for the prediction of the strength anisotropy behavior of a jointed rock which joint angle is 45° for the two weakness planes. The three curves show the same trend. If joint angle of red marked joint increases, the value of UCS first reduces to the position B (joint angle of 10°), then UCS is kept nearly constant until joint angle reaches about 40°. A local UCS maximum is observed at around 50° followed by a U shaped pathway of the strength envelop. There is a significant strength difference for different joint cohesion.

5.4.3 Group C (minimum angle between two joints is 30°)

Table 5.7 shows UCS results obtained from simulations with the multi-joint model in FLAC in comparison to analytical solutions, UDEC simulation results and lab test results. Joint sliding failure appears if one joint inclination is close to 60°. The joint cohesion for category_ II group C modeling is 1.0 MPa.

Table 5.7 UCS results for two non-orthogonal joints (30°)

Name	UCS [MPa] (laboratory)	UCS [MPa] (analytical)	UCS [MPa] (FLAC)	UCS [MPa] (UDEC)	Failure type
C1 [30/60]	2.97	3.68	3.67	3.53	Joint sliding
C1 [30/60]	4.13	3.68	3.67	3.53	Joint sliding
C2 [35/65]	3.15	3.88	3.83	3.59	Joint sliding
C2 [35/65]	4.82	3.88	3.83	3.59	Joint sliding
C3 [60/90]	21.82	26.28	26.58	26.58	Matrix failure
C3 [60/90]	20.63	26.28	26.58	26.58	Matrix failure

If the minimum angle between the crossing joints is 30°, the model has at least a UCS value of around 4 MPa. The results of lab experiments were consistent with those of simulations of models of group C1 and C2. Table 5.7 and Figure 5.17 provide a straightforward comparison of UCS for samples/models of category II_C. Group C3 has an antisymmetric joint configuration with angles of 60° and 90°. All UCS values for group C3 exceed 20 MPa (simulation results are 26 MPa).

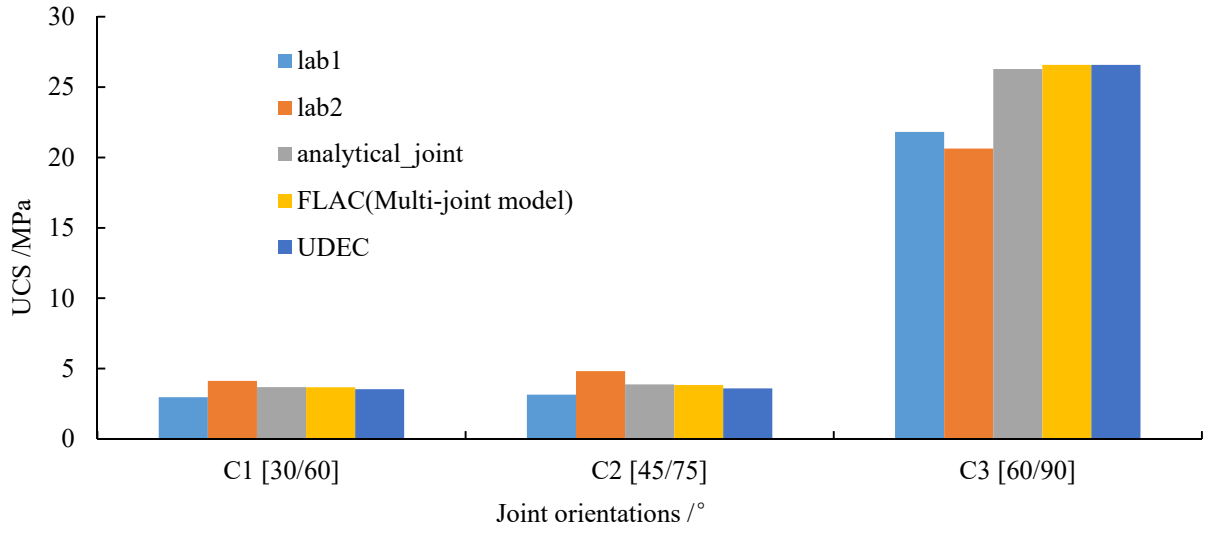

Figure 5.17 UCS versus joint orientation for group II_C

The uniaxial compression strength for various joint combinations for group C (category II) is documented in Figure 5.18. This graph compares the result of the FLAC multi-joint model with those of the analytical solutions, the UDEC simulations and the lab tests. The FLAC results deviate

less than 1 % from the analytical solutions. The lab test results also confirm the simulation results. Predicted UCS values assuming different joint cohesion values are shown in Figure 5.19.

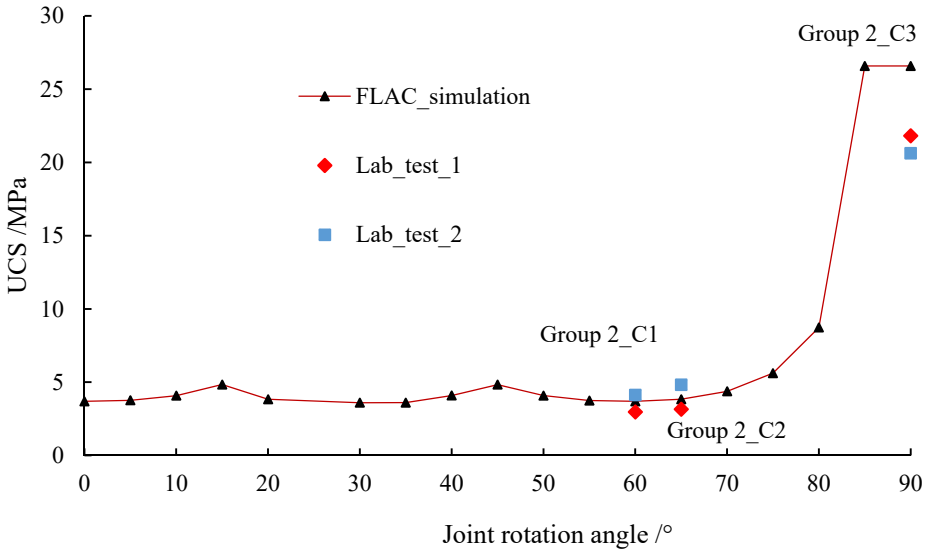

Figure 5.18 UCS vs. rotation angle for group II_C

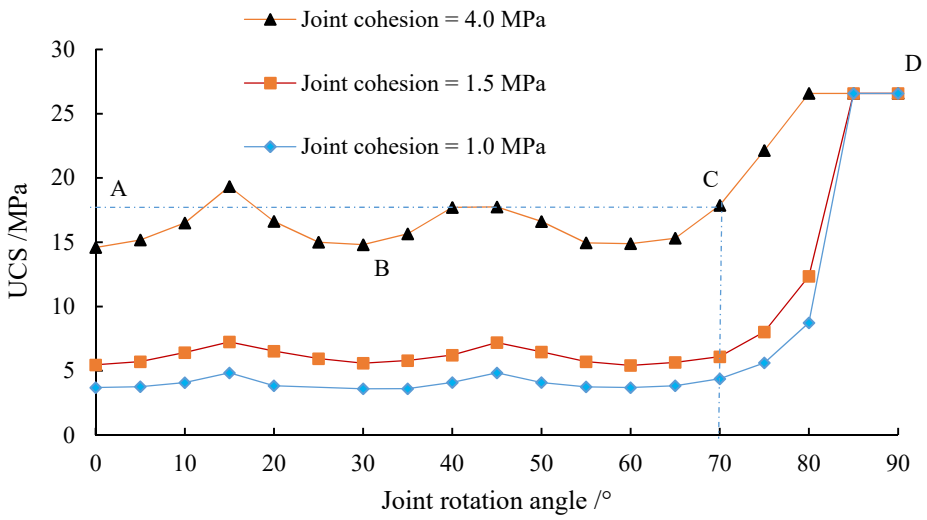

Figure 5.19 UCS vs. joint rotation angle for group II_C assuming different joint cohesion values

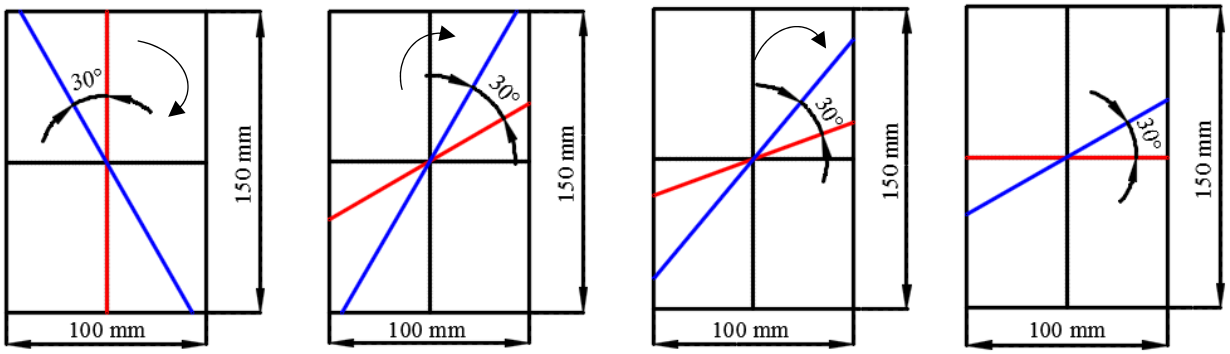

(a) (b) (c) (d)

Figure 5.20 Schematic plot of joint pattern for group II_C during rotation

Figure 5.20 illustrates the joint pattern for different joint rotation angles (from a = 0° to d = 90°). From stage a to c always the minimum UCS values are more or less reached. Afterwards, that means beyond about 75°, significant increase in UCS is observed until peak UCS value of 25 MPa is reached.

5.5 Analysis of two joints with different joint cohesion (category III)

Numerical simulations of models of category III are discussed in this section. Intact rock strength and stiffness parameters remain the same, but strength parameters have changed according to Table 5.8. The primary joint has a lower joint cohesion than the secondary one.

Table 5.8 Strength parameters for models of category III

Joint type	c_j [MPa]	σ_j^t [MPa]	ϕ_j [°]	ψ_j [°]
Primary joint (1)	1.0	0.3	32.8	0.24
Secondary joint (2)	1.5	0.3	32.8	0.24

Table 5.9 UCS results for samples with two joints with different joint cohesion (category III)

Name	UCS [MPa] (laboratory)	UCS [MPa] (analytical)	UCS [MPa] (FLAC)	UCS [MPa] (UDEC)	Failure type
D1 [-45/45]	6.23	5.63	5.47	5.41	Joint 1 sliding
D1 [-45/45]	5.56	5.63	5.47	5.41	Joint 1 sliding
D1 [-45/45]	2.46	5.63	5.47	5.41	Joint 1 sliding
D2 [-45/35]	4.67	5.63	5.45	5.33	Joint 2 sliding
D2 [-45/35]	5.34	5.63	5.45	5.33	Joint 2 sliding
D2 [-45/35]	3.74	5.63	5.45	5.33	Joint 2 sliding
D3 [35/-45]	4.58	3.88	3.85	3.64	Joint 1 sliding
D3 [35/-45]	4.03	3.88	3.85	3.64	Joint 1 sliding
D3 [35/-45]	3.43	3.88	3.85	3.64	Joint 1 sliding

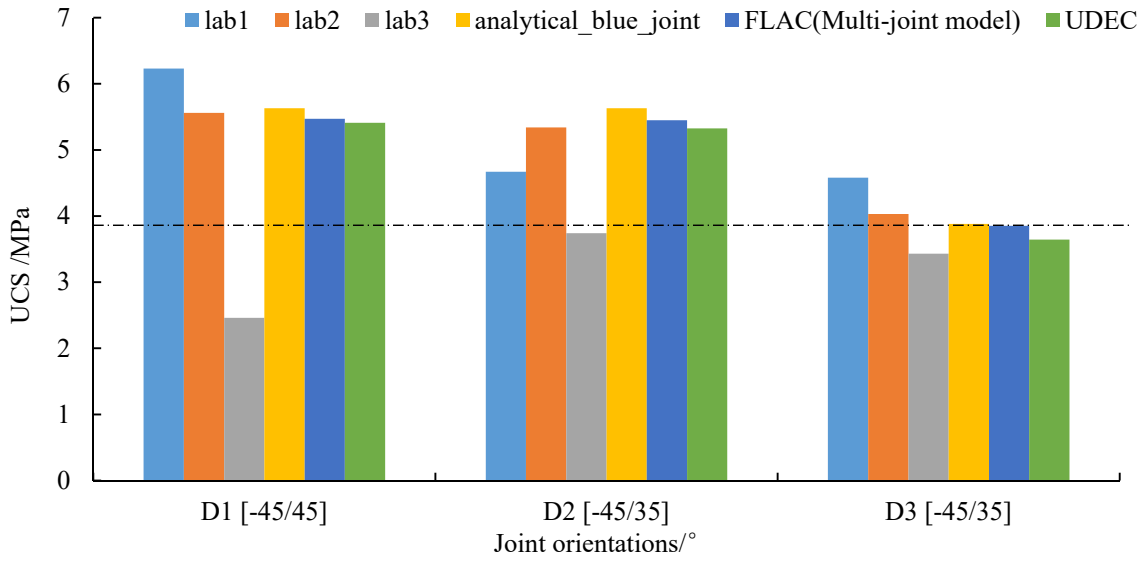

Figure 5.21 UCS vs. joint inclination for samples of category III

Simulation results in comparison with analytical solutions and lab test results are shown in Table 5.9 and Figure 5.21. Group D1 has a symmetric joint pattern in respect to the vertical loading direction. The joint angles are +/- 45°. In this case the sliding failure occurs along the weaker joint plane and the UCS is around 5.5 MPa.

Group D2 and D3 have the same geometrical joint pattern characterized by 35° and -45°, but due to the different joint cohesion values, UCS and failed joint are different. If the primary joint has an inclination angle of 35°, then UCS is slightly below 4 MPa (indicated by the black dotted line in Figure 5.21). When the primary joint angle is 45 ° and the secondary joint angle is 35° and fails, higher UCS values of about 5.5 MPa are obtained.

5.6 Conclusions

In this chapter, uniaxial compressive tests of rock samples with various joint orientation combinations have been analyzed via numerical simulations. Two different simulation approaches are applied: the finite difference method (FDM) and the discrete element method (DEM). In addition the results were validated by lab tests and verified by analytical solutions. The following conclusions can be drawn.

First, for models with one single joint it was found that under the same joint angle, the uniaxial compressive strength is mainly controlled by the joint cohesion c_j. In addition the weak plane orientation α in the range from 10° to 60° has a strong influence on the stress drop. The stiffness parameters k_n and k_s have a strong influence on the magnitude and distribution of the strain. Based on the assumption that the intact rock can be considered as a nearly homogeneous isotropic material, the modeling results show good agreement with the analytical solutions and the experimental data. The results of the numerical models confirm the single plane of weakness theory (Jaeger's theory) and provide a physically justifiable and practical method for simulations.

Second, based on the developed equivalent continuum model (multi-joint model in FLAC), uniaxial compressive simulations for samples with two weakness planes containing the same strength parameters but different constant joint angles were performed. The UCS values versus joint orientation curves are totally different to the classical Jaeger's curve and the failure envelopes have a distinctive shape.

Third, the results of the simulation revealed that two failure mechanisms in the multi-joint model are important: plastic failure of the rock matrix or slip/tension failure on a preferred joint plane. It

was found that failure type and area are mainly controlled by the strength parameters and the joint angles.

To further validate the developed multi-joint model several rock engineering applications are considered: corresponding results are given in chapter 6.

6 Applications of multi-joint model

6.1 Introduction

In this chapter, a simplified slope stability problem is analyzed by the multi-joint model. The factor of safety (FOS) of the slope has been obtained using the strength reduction method (SRM). The failure patterns obtained from SRM for various joint angle combinations are analysed. Also, a circular tunnel driven in an anisotropic rock mass subjected to uniform and non-uniform in-situ stresses has been studied by the multi-joint model.

6.2 Numerical analysis of a slope in jointed rock mass

6.2.1 Model set up

The geometry of the slope and the boundary conditions of the equivalent continuum multi-joint model are depicted in Figure 6-1. The model is 140 m long model with a height of 120 m. Figure 6.1 illustrates the geometry of the slope. The stability for the 80 m high slope with inclination of 1:2.6 is evaluated for the different joint orientations. The rock mass may contain a single closely spaced joint set or two joint sets, those strength parameters are listed in Table 6.1.

For the rock matrix, an isotropic material with Young's modulus of 9.1 GPa and Poisson's ratio of 0.26 was considered. The joints have a normal stiffness, k_n of 10 GPa /m. For the elastic-perfect plastic behavior of the intact rock, a non-associated Mohr-Coulomb failure criterion with a friction angle of 45°, with zero dilation angle, cohesion of 675 kPa and tensile strength of 100 kPa, was considered. The joints exhibit Mohr-Coulomb failure behavior with a friction angle of 40°, zero dilation angle, cohesion of 100 kPa, and tensile strength of 1 kPa. In order to investigate the effect of joint spacing, the elasto-plastic response of the multi-joint model was compared with the results predicted by the ubiquitous joint model, which is the limit case of the equivalent continuum model without considering the joint stiffness.

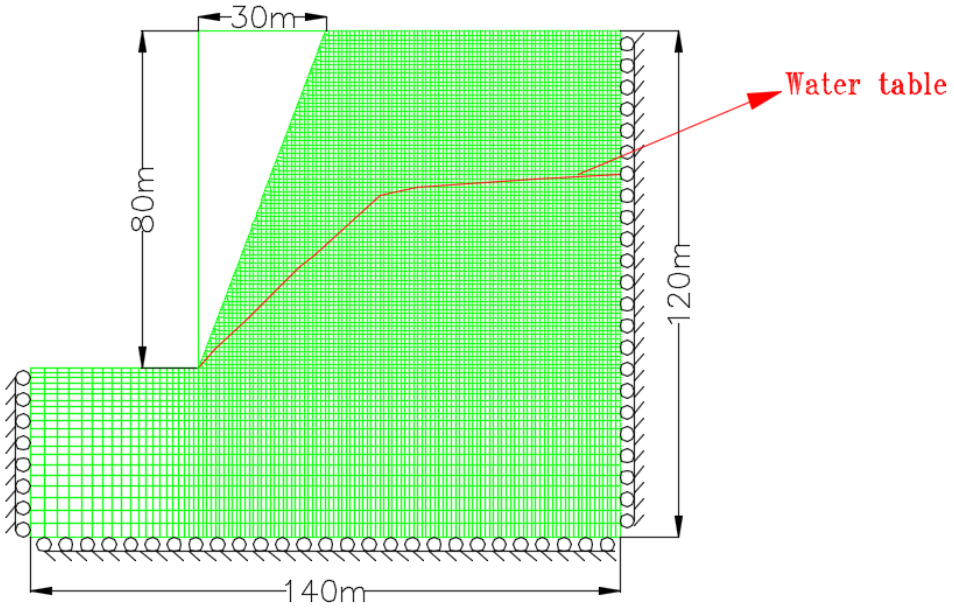

Figure 6.1 Slope geometry and boundary conditions for the multi-joint slope model

6.2.2 Factor of safety calculation

The shear strength reduction method (SRM) has already been used for slope stability analysis as early as 1977 by Zienkiewicz. After that, many researchers (e.g. Cheng et al., 2007; Ma et al., 2014) have applied it for stability and factor of safety (FOS) analysis. Here, an extended version is used including the reduction of the tensile strength. For the intact rock, the reduction equations for these properties are:

$$c^{trial} = \frac{1}{F^{trial}} c \tag{6.1}$$

$$\phi^{trial} = \arctan\left(\frac{1}{F^{trial}} \tan\phi\right) \tag{6.2}$$

$$\sigma^{t(trial)} = \frac{1}{F^{trial}} \sigma^{t} \tag{6.3}$$

where c^{trial} and σ^{trial} are trial values for cohesion and tensile strength, respectively, and ϕ^{trial} is trial value for friction angle.

The reduction equations for the joint properties are:

$$c_j^{i\,(trial)} = \frac{1}{F^{\,trial}} c_j^i \tag{6.4}$$

$$\phi_j^{i(\,trial)} = \arctan\left(\frac{1}{F^{\,trial}} \tan\phi_j^i\right) \tag{6.5}$$

$$\sigma_j^{t,i\,(trial)} = \frac{1}{F^{\,trial}} \sigma_j^{t,i} \tag{6.6}$$

where c_j^{trial} and σ_j^{trial} are the trial values for joint cohesion and joint tensile strength, respectively, and ϕ_j^{trial} is trial value for joint friction angle.

A series of simulations were conducted using trial values for F^{trial} to reduce matrix and joint strength parameters until failure occurs (Table 6.1). The effect of joint orientation on the stability of a rock slope is investigated using the ubiquitous model and the new developed multi-joint model.

Table 6.1 Strength reduction for intact rock and joint parameters

Reduced factor	c (kPa)	ϕ (°)	σ^t (kPa)	c_j (kPa)	ϕ_j (°)	σ_j^t (kPa)
1.0	675	45	100	200	40	1
1.1	614	42.3	91	182	37.3	0.91
1.25	540	38.7	80	160	33.9	0.8
1.5	450	33.7	66.7	133.3	29.2	0.67
2.0	338	26.6	50	100	22.8	0.5
2.5	270	21.8	40	50	18.6	0.4

6.2.3 Slope with one joint set

For comparison, six orientations of the joint sets are investigated: joint angle of 30°, 45°, 60°, - 30°, -45° and -60°, measured from the vertical direction (clockwise is positive, counterclockwise is negative). The strength parameters for the intact rock and the joints are listed in the model set-up section. For comparison, a first simulation is performed neglecting the presence of the joints (Mohr-Coulomb material). The calculated factor of safety for intact rock is 2.42. When joints are included with orientation of -60°, the effect of the joints is negligible. The factor of safety for this case is 2.19 and the failure pattern is similar to the case without joints as shown in Figure 6.2a. At

other joint orientations, the effect of the joints becomes more evident. For the case of 45°, the factor of safety is only 1.18. For a joint orientation of 30°, slip along the joint is the predominant mode of failure, and the factor of safety is 1.03. The factor of safety is 1.53 for the case of -45° joint orientation, the failure surface is more aligned with the angle of the slope indicating a toppling mode of failure as documented by Figure 6.2c. For other joint angles the factors of safety are listed in Table 6.2 and shown in Figure 6.2. The black arrows in Figure 6.2 and 6.3 represent the direction of displacement velocity.

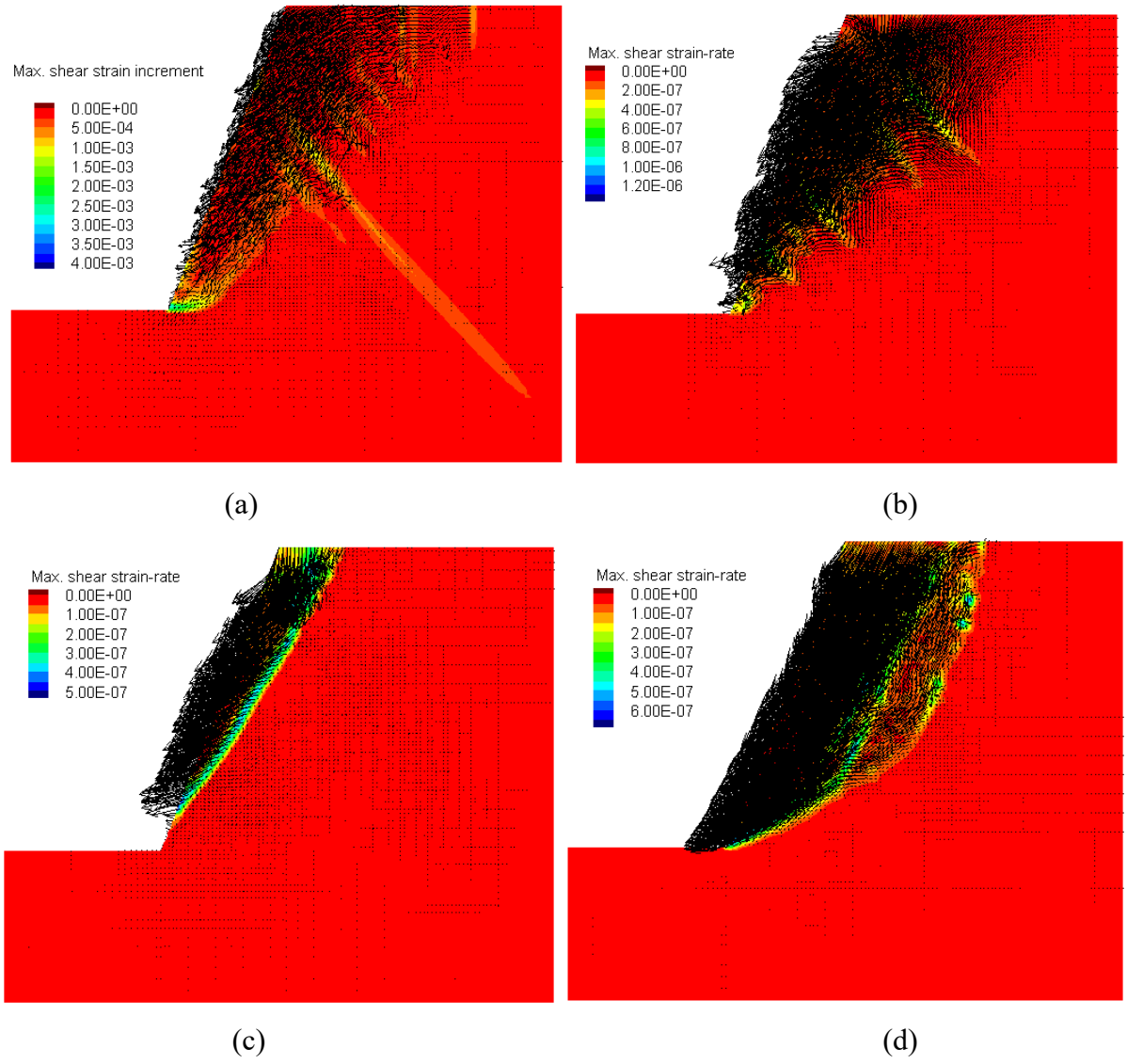

Figure 6.2 Rock slopes at failure for various joint orientations: (a) 30°, (b) 45°, (c) -45°, (b) -60°

Table 6.2 Factor-of-safety results for slope with different joint angles

Joint angle (°)	30	45	60	-30	-45	-60
FOS (ubiquitous- joint model)	1.03	1.18	1.56	1.16	1.53	2.19

6.2.4 Slope with two joints sets

Two models are used to investigate how joint spacing, joint stiffness and joint orientation influence the stability of a slope. The models have the same joint stiffness, joint spacing for one joint set is 0.2 m, and for the other joint sets it is 5 m. Three joint set orientations are tested: joint angle of 60°/ -60°, 45°/ -30°, and 30° /-60°. The failure mechanisms predicted by the multi-joint model are depicted in Table 6.3 and Figure 6.3.

Table 6.3 Factor-of-safety results for slope with two joint combinations

joint angle	FOS for rock mass with joint spacing of 0.2 m	FOS for jointed rock mass with joint spacing of 5 m
60/-60	1.0 - 1.25	1.25 - 1.5
45/-30	1.0 - 1.1	1.0 - 1.25
30/-60	1.0 - 1.1	1.0 - 1.1

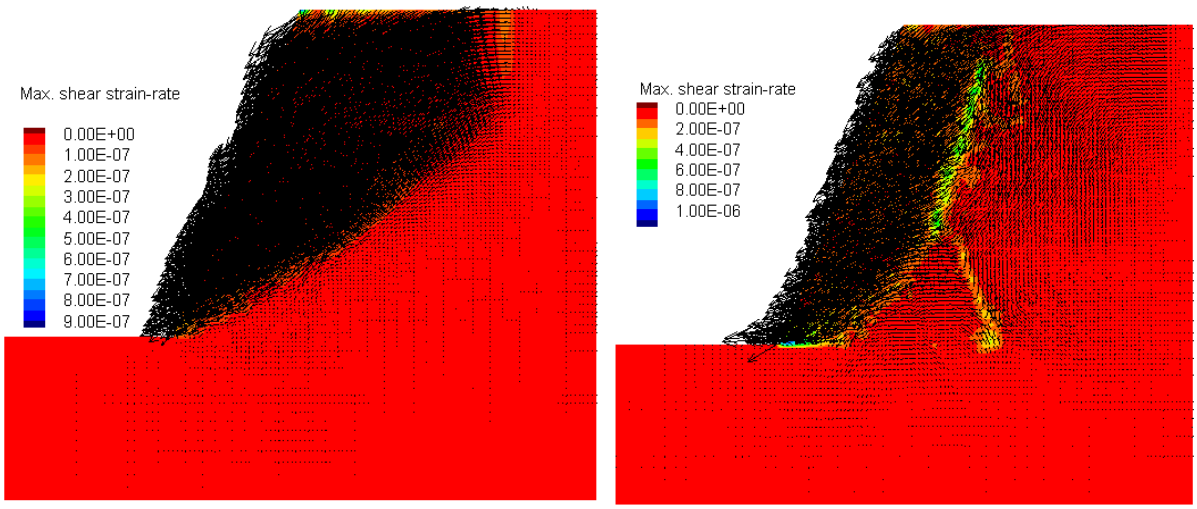

(a) (b)

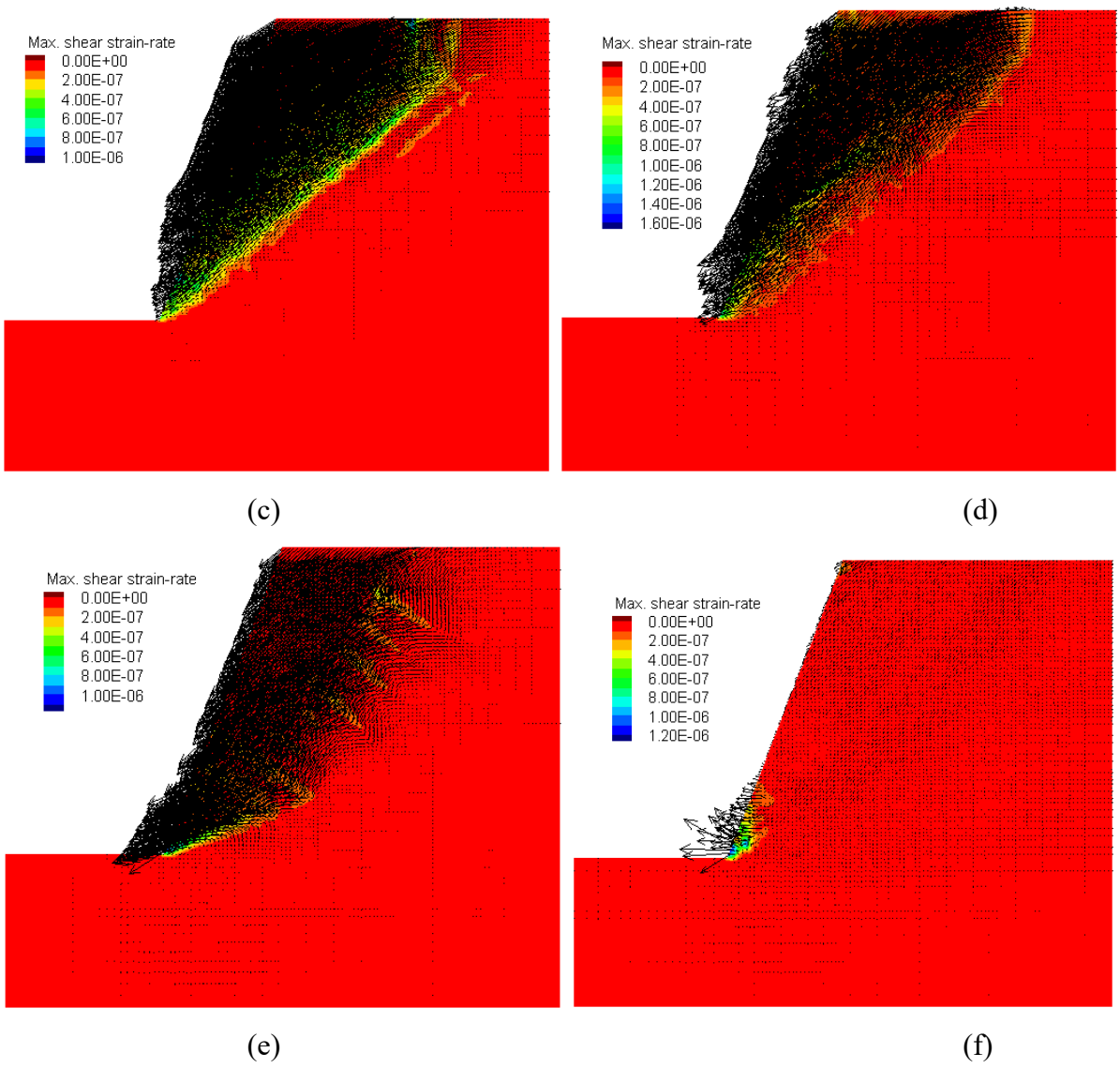

Figure 6.3 Rock slope with various joint set orientations: (a) 60°/ -60° with 0.2 m spacing, (b) 60°/ -60° with 5 m spacing, (c) 45°/ -30° with 0.2 m spacing, (d) 45°/ -30° with 5 m spacing, (e) 30°/ -60° with 0.2 m spacing, (f) 30°/ -60° with 5 m spacing

When the -60° joint orientation is included, failure surface and factor of safety is determine by the other joint set. For the joint angle of 45°, the factor of safety is smaller than 1.25. When a rock mass has 30° joint orientation, slip along the joint is the dominating failure type, the factor of safety is close to 1. Figure 6.3 also illustrates the influence of joint spacing on the failure surface. Closely spaced joints produce a larger failure area than larger spaced joints.

6.3 Numerical analysis of a circular tunnel in jointed rock mass

6.3.1 Model set-up

A circular tunnel subjected to an initial stress state is depicted in Figure 6.4. The objective of this model is to investigate the mechanical response of a circular excavation under either isotropic or anisotropic in-situ stresses. The geometry of the numerical model is characterized by a tunnel with diameter of D = 1.5 m and a model size of W = 10 m. σ_{xx} is set to 1 MPa and the other input parameters are shown in Table 6.4. Three cases are studied by varying the in-situ stress ratio. The vertical earth pressure coefficient κ is set to 1.0, 0.5 and 2.0, respectively (Table 6.5). A value of κ >1 means that in-situ vertical stress is greater than in-situ horizontal stress and vice versa. Constellations with no joint, one joint and two joints were investigated.

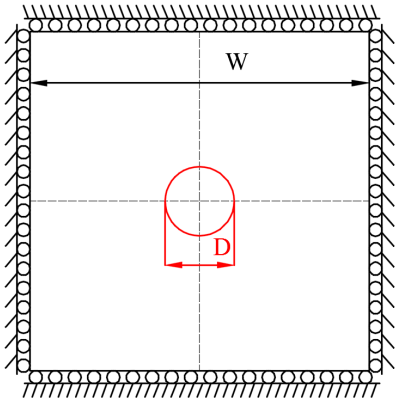

Figure 6.4 Sketch of model geometry and boundary conditions

Table 6.4 Numerical simulation parameters for rock mass

E (GPa)	v	ρ [kg/m^3]	c [MPa]	Ψ [°]	ϕ [°]	σ^t[MPa]	ϕ_j[°]	c_j [MPa]	σ_j^t[MPa]
0.2	0.23	1810	1	10	21.2	0.1	32.8	0.1	0.05

Table 6.5 Stress and joint constellations for tunnel model

Stress ratio	Joint orientation			
	No joint	-60	45/-45	45/-60
κ = 1	$\sigma_{xx} = \kappa\sigma_{yy} = \sigma_{zz}$			
κ = 2	$\sigma_{xx} = \kappa\sigma_{yy} = \sigma_{zz}$			
κ = 0.5	$\sigma_{xx} = \kappa\sigma_{yy} = \sigma_{zz}$			

6.3.2 Simulation results for Mohr-Coulomb matrix without joints

Figure 6.5 shows contour plots of total displacements and plasticity state for the tunnel in a homogeneous Mohr-Coulomb rock matrix without joints for different in-situ stress fields. Increase in vertical initial stress (κ = 2) leads to increasing displacements at the tunnel crown and floor, whereas plastic failure occurs at the tunnel walls (Figure 6.5b). For κ = 0.5 (Fig 6.5c) maximum displacements are recorded at the tunnel walls and plasticifications are not observed.

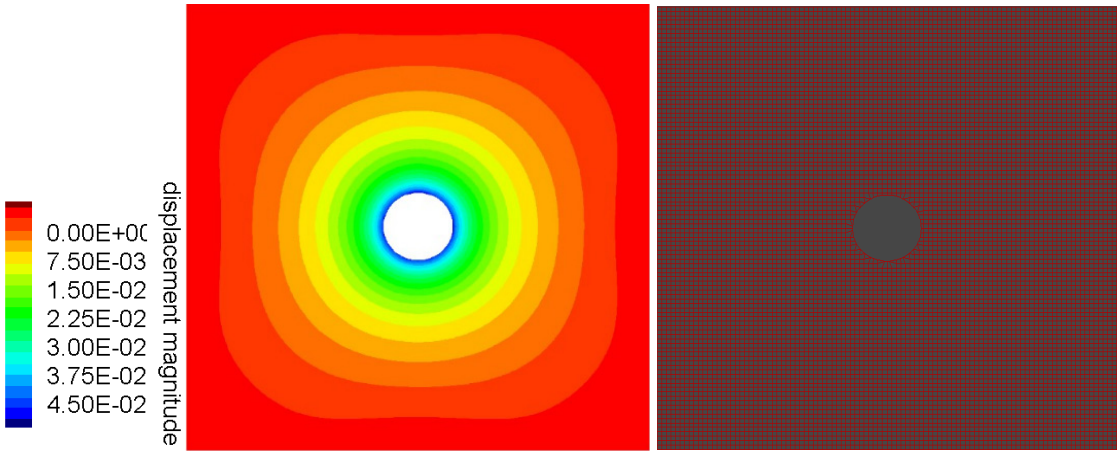

(a) κ =1.0

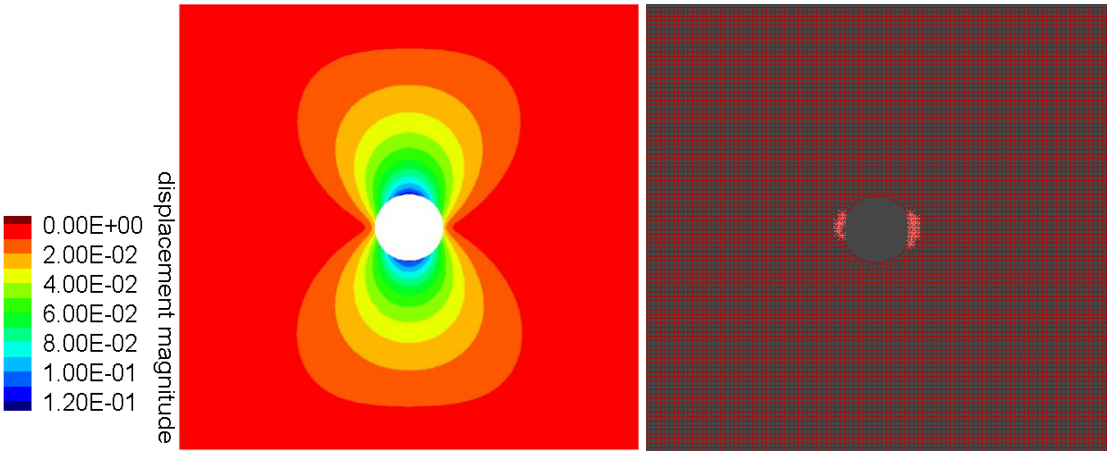

(b) κ =2.0

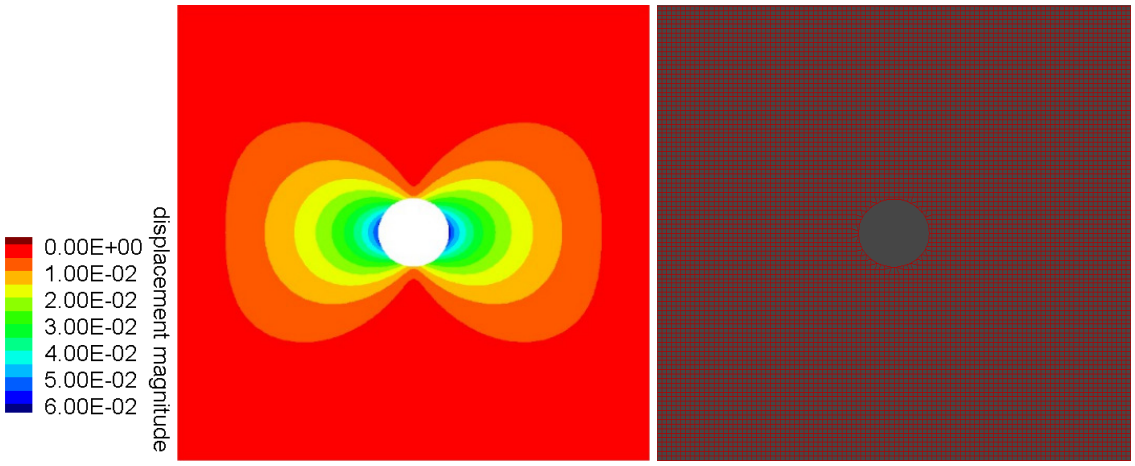

(c) κ = 0.5

Figure 6.5 Displacement contours and and failure pattern for tunnel in Mohr-Coulomb material (no joint) under different initial stress conditions

6.3.3 Simulation results for Mohr-Coulomb matrix with one joint set

Simulation strategy presented in this chapter is similar as outlined in the chapter above but in addition influence of one joint set with angle of -60° (measured from vertical) is considered in detail. Figures 6.6, 6.7 and 6.8 show contour plots of displacement magnitude and stress components as well as the plasticity state for different stress states.

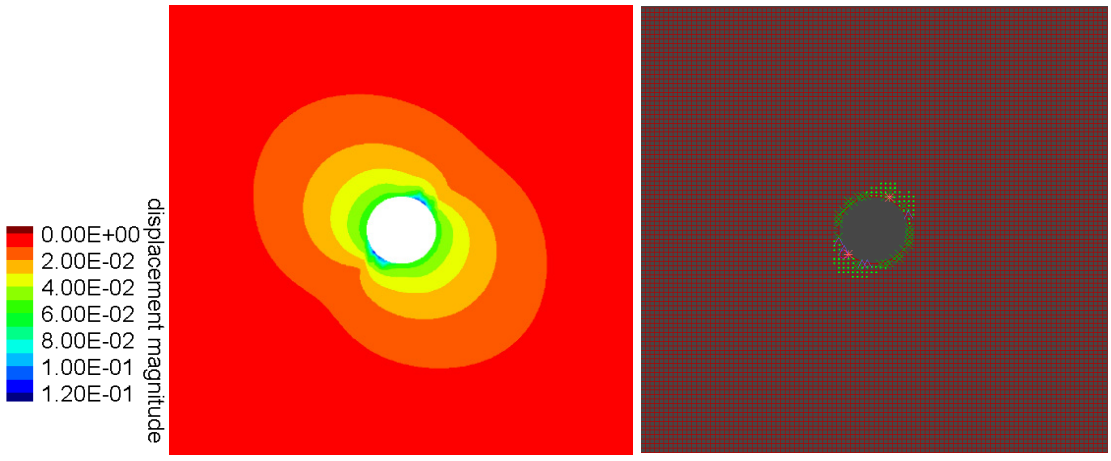

(a) (b)

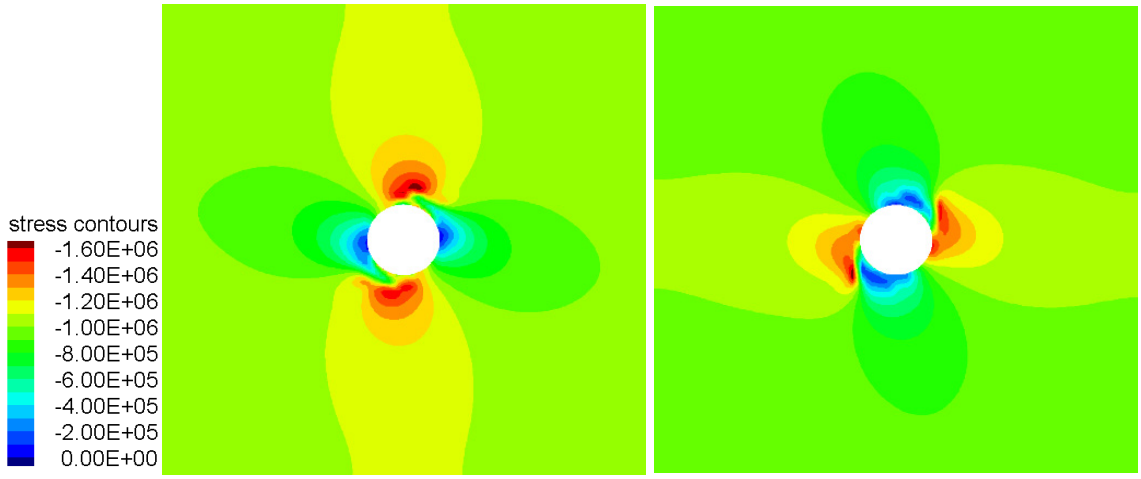

(c) (d)

Figure 6.6 Simulation results for tunnel model with joint orientation of -60° and κ = 1: (a) displacement contours [m], (b) plasticity state, (c) contour plot of horizontal stresses [Pa] and (d) contour plot of vertical stresses [Pa]

Figure 6.6 shows maximum displacements of 0.12 m at the tunnel boundary around 30° inclined to the vertical. Plasticity pattern follows the displacement field. (Figure 6.6a and b). The influence of the joint on the secondary stress field is illustrated by Figures 6.6c and 6.6d.

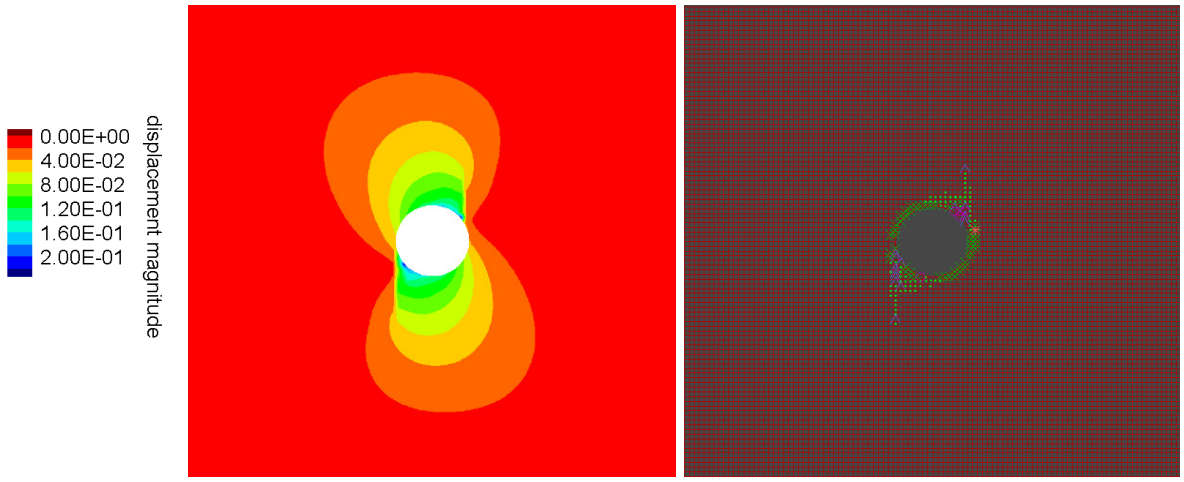

(a) (b)

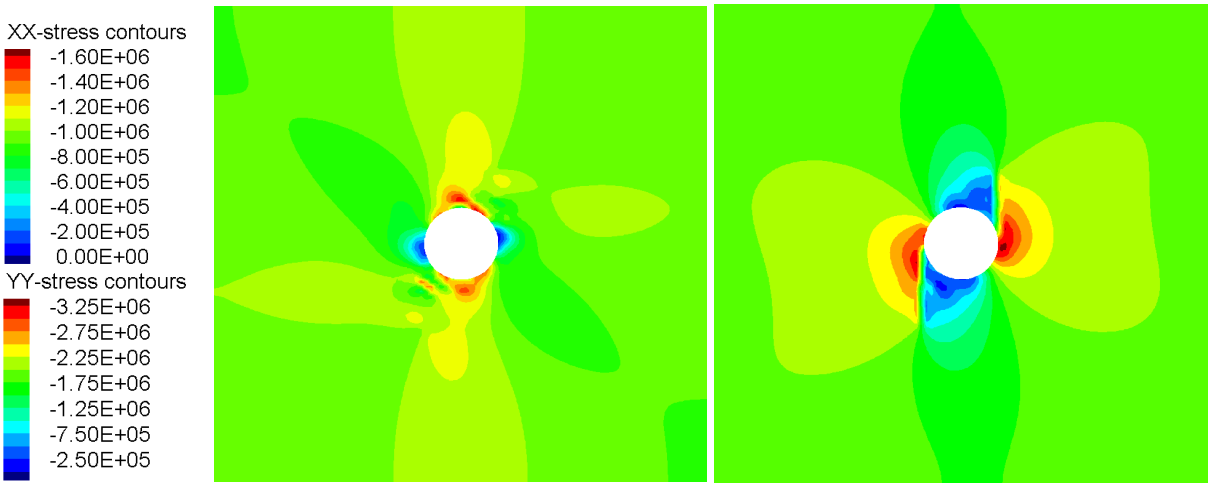

(c) (d)

Figure 6.7 Simulation results for tunnel model with joint orientation of -60° and κ = 2: (a) displacement contours [m], (b) plasticity state, (c) contour plot of horizontal stresses [Pa] and (d) contour plot of vertical stresses [Pa]

As Fig. 6.7 shows with κ = 2.00 the maximum displacements increase to 0.20 m and plasticity pattern changes. The maximum horizontal stress component becomes 1.60 MPa at the tunnel roof and invert. The maximum vertical stress component is 3.25 MPa and occurs at the tunnel sidewalls (Figure 6.7d).

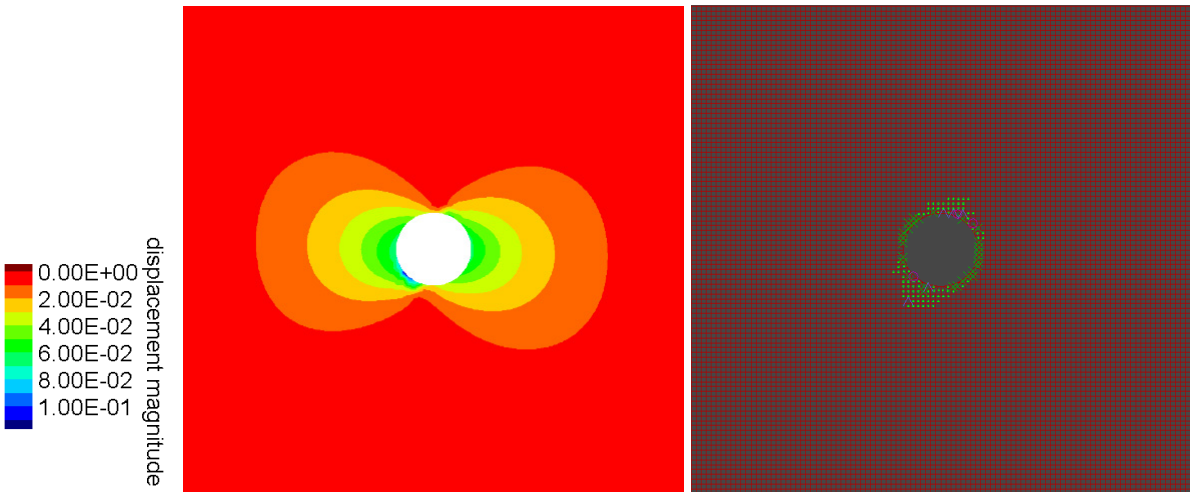

(a) (b)

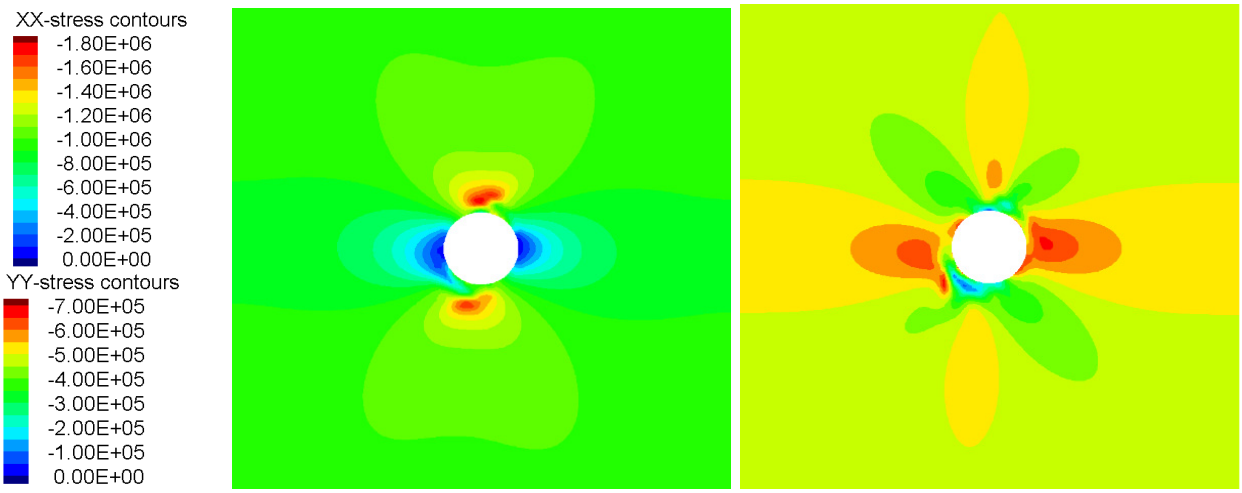

(c) (d)

Figure 6.8 Simulation results for tunnel model with joint orientation of -60° and κ = 0.5: (a) displacement contours [m], (b) plasticity state, (c) contour plot of horizontal stresses [Pa] and (d) contour plot of vertical stresses [Pa]

Figure 6.8 illustrates the situation for κ = 0.5. Due to the lower vertical stress component, the maximum contour displacement is only 0.1 m. The plasticity area is similar to that of the isotropic stress case shown in Figure 6.8b. The maximum horizontal stress value of 1.80 MPa is observed at the tunnel roof and invert. The maximum vertical component of 0.7 MPa is found at the tunnel sidewalls (Figure 6.8d).

6.3.4 Simulation results for Mohr-Coulomb matrix with two joint sets

In this section, the behavior of a rock mass with two joint sets is investigated by using the new developed multi-joint model. Both, symmetric and skew-symmetric interconnected joint sets are considered. Figures 6.9 - 6.14 show stress and displacement fields for given values of initial stress strength parameters and joint orientation. These figures clearly illustrate the anisotropic behavior due to the presence of joints especially under non-uniform stress states.

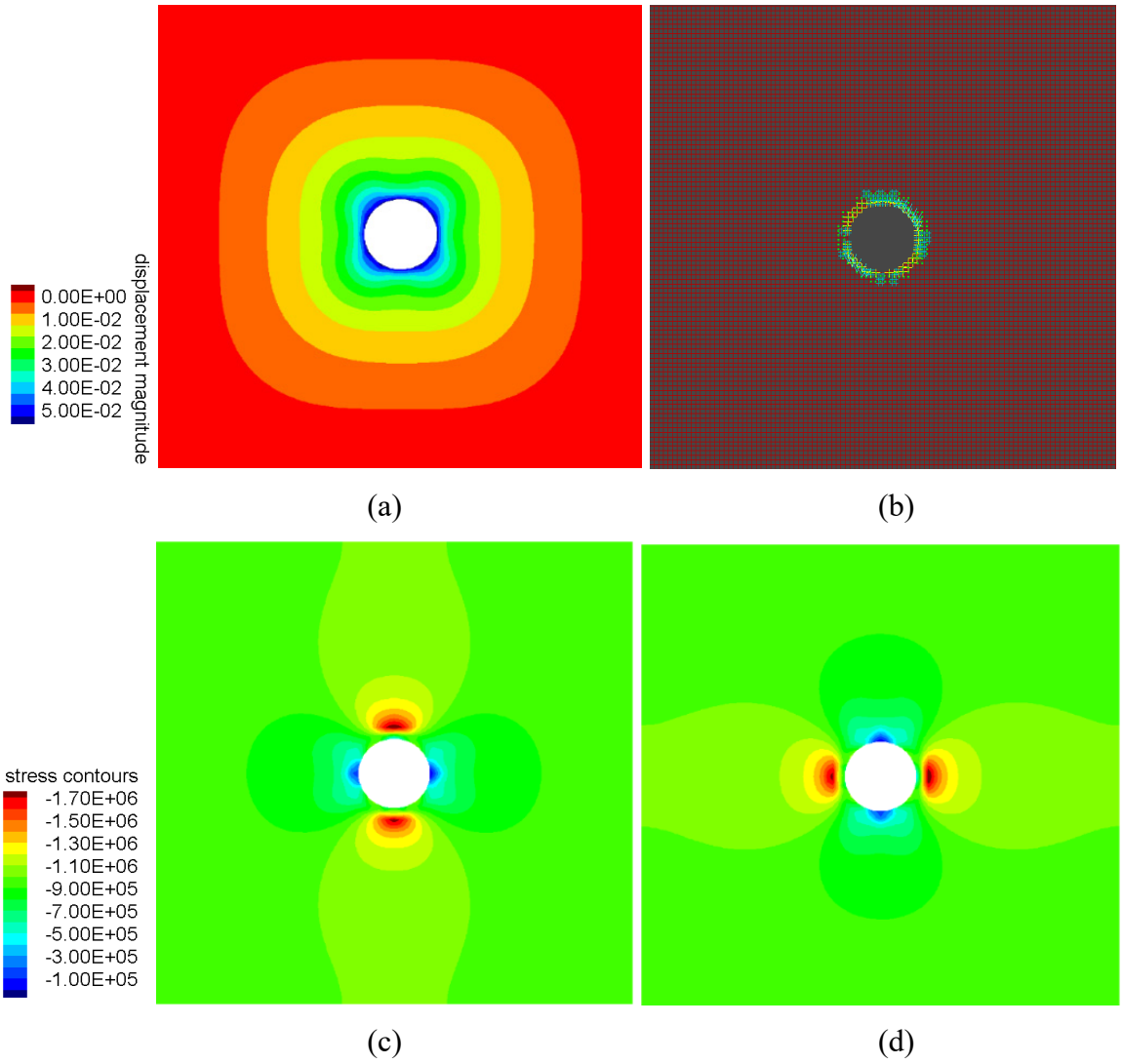

Figure 6.9 Simulation results for tunnel model with two joint sets (45° and -45°) and κ = 1: (a) displacement contours [m], (b) plasticity state, (c) contour plot of horizontal stresses [Pa] and (d) contour plot of vertical stresses [Pa]

The numerical results for κ = 1.0 and joint angle of 45°/-45° are illustrated in Fig. 6.9. Maximum displacement is 0.05 m, plasticity is restricted to immediate tunnel contour (Figure 6.9b). As can be seen from Figure 6.9c and 6.9d, stress components show symmetric pattern similar to displacements and plasticity.

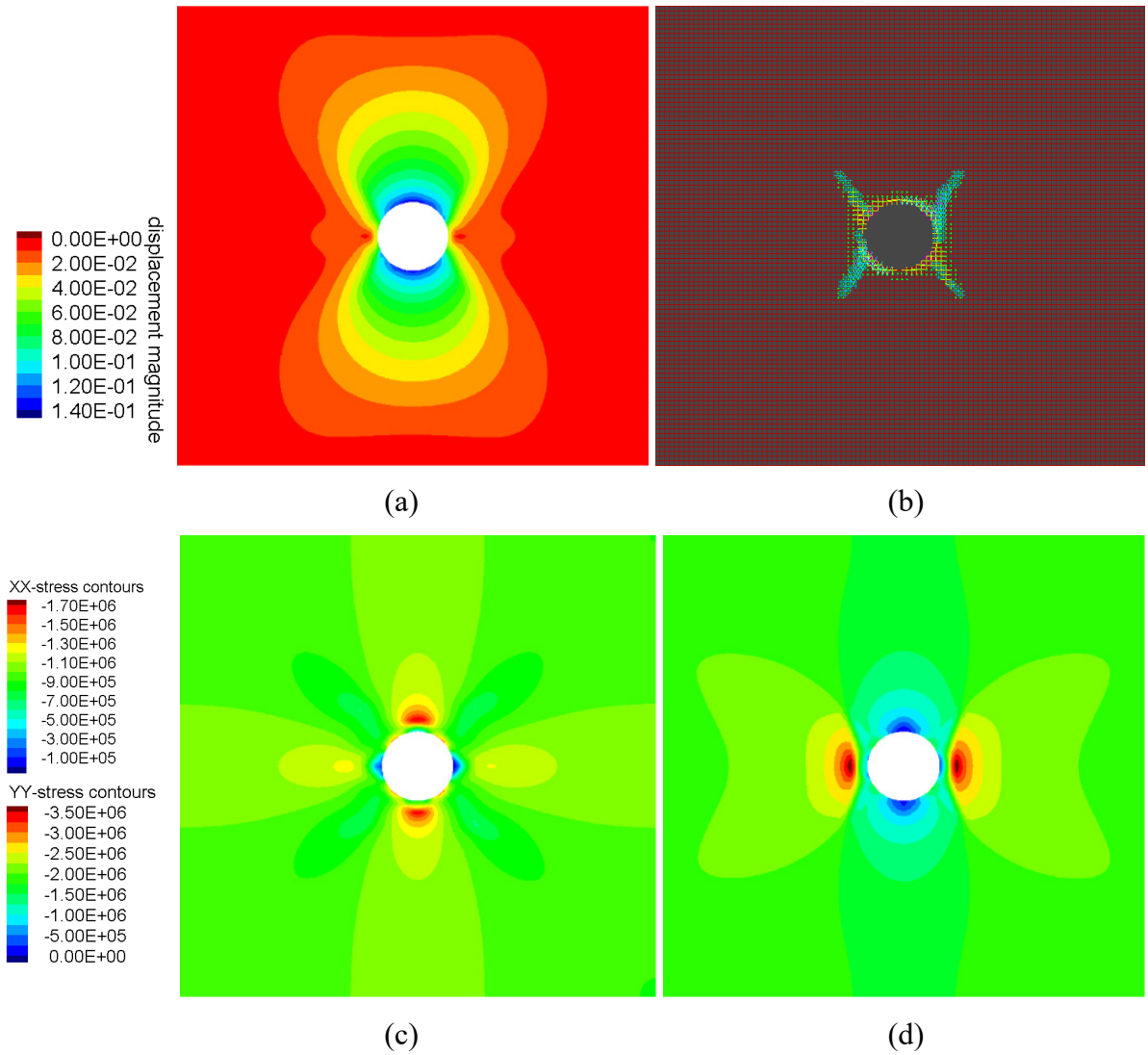

Figure 6.10 Simulation results for tunnel model with two joint sets (45° and -45°) and κ = 2: (a) displacement contours [m], (b) plasticity state, (c) contour plot of horizontal stresses [Pa] and (d) contour plot of vertical stresses [Pa]

Results for κ = 2 and joint angles of 45°/-45° are shown in Figure 6.10. The maximum displacement is 0.14 m as shown in Figure 6.10a. Locally plasticity extends deeper into the rock mass following the joint orientation (Figure 6.10b). The maximum horizontal stress component is 1.70 MPa at the tunnel roof and invert, the maximum vertical stress component is 3.50 MPa and observed at the tunnel sidewalls (Figure 6.10d).

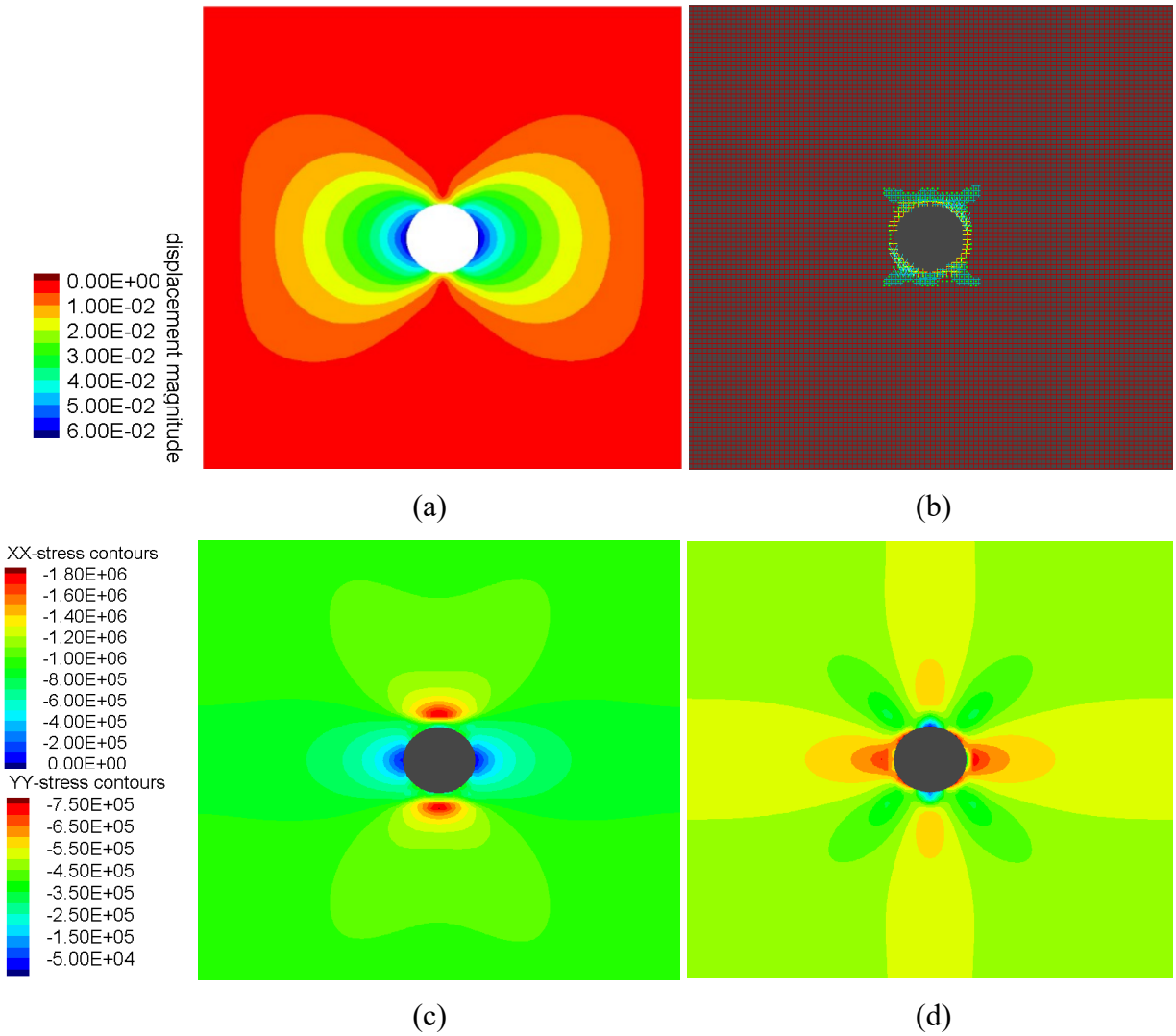

Figure 6.11 Simulation results for tunnel model with two joint sets (45° and -45°) and κ = 0.5: (a) displacement contours [m], (b) plasticity state, (c) contour plot of horizontal stresses [Pa] and (d) contour plot of vertical stresses [Pa]

The simulation results for κ = 0.50 and joint angles of 45°/-45° are shown in Figure 6.11. Maximum displacement is 0.06 m in the sidewalls. The secondary horizontal stress is larger than the vertical stress. This failure area is symmetric as illustrate in Figure 6.11b. The maximum horizontal stress components is 1.80 MPa and situated at the tunnel roof and invert, the vertical stress component is 0.75 MPa and observed at the tunnel sidewalls (Figure 6.11d).

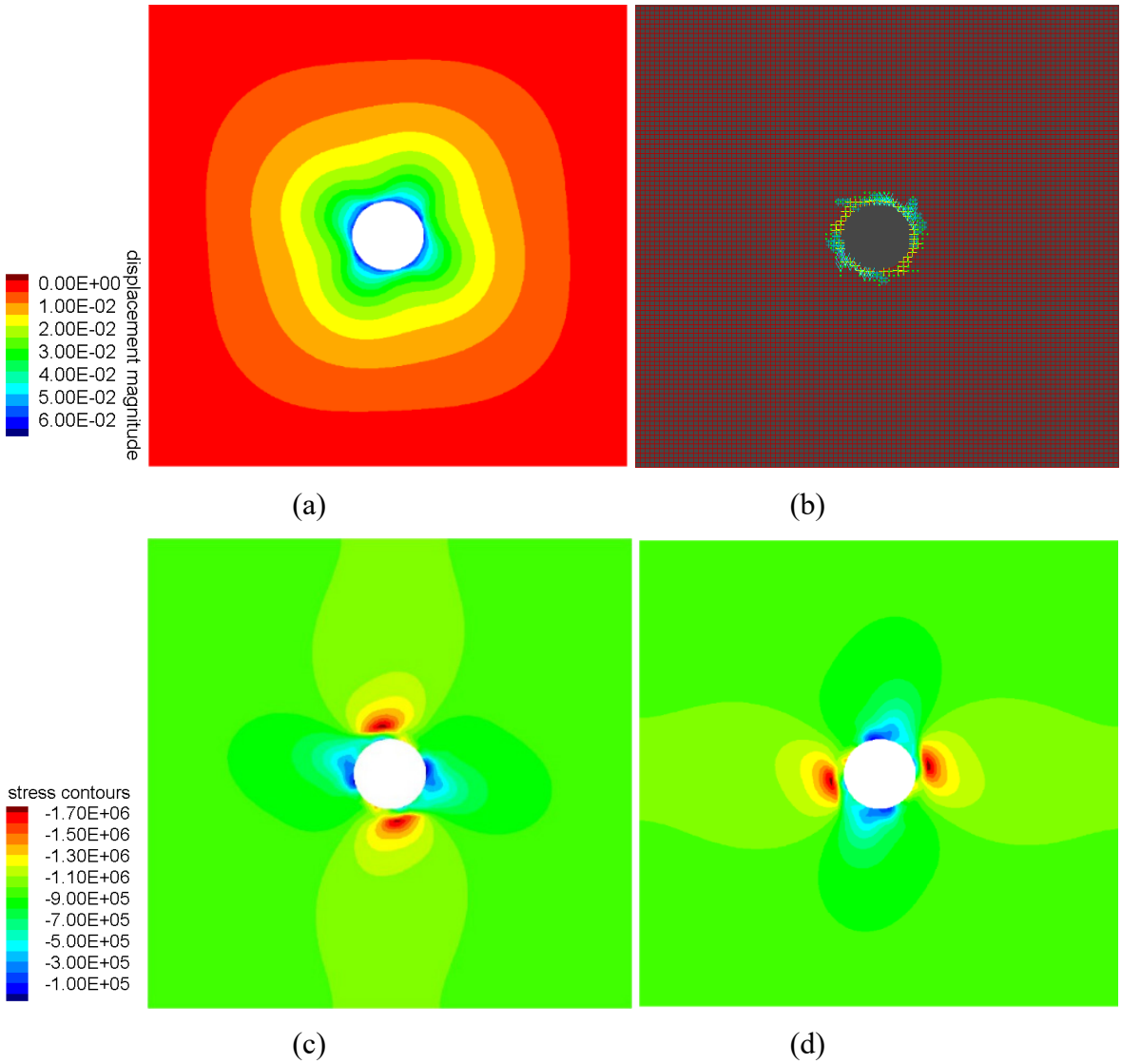

Figure 6.12 Simulation results for tunnel model with two joint sets (45° and -60°) and κ = 1: (a) displacement contours [m], (b) plasticity state, (c) contour plot of horizontal stresses [Pa] and (d) contour plot of vertical stresses [Pa]

The simulation results for κ = 1.0 and joint angle of 45°/-60° are illustrated in Fig. 6.12. Maximum displacement is 0.06 m located in the 30° and -45° directions. Plastic failure areas are in accordance with the displacement field (Figure 6.12b). Figure 6.12c and 6.12d illustrate how joint orientations influence the stress distribution.

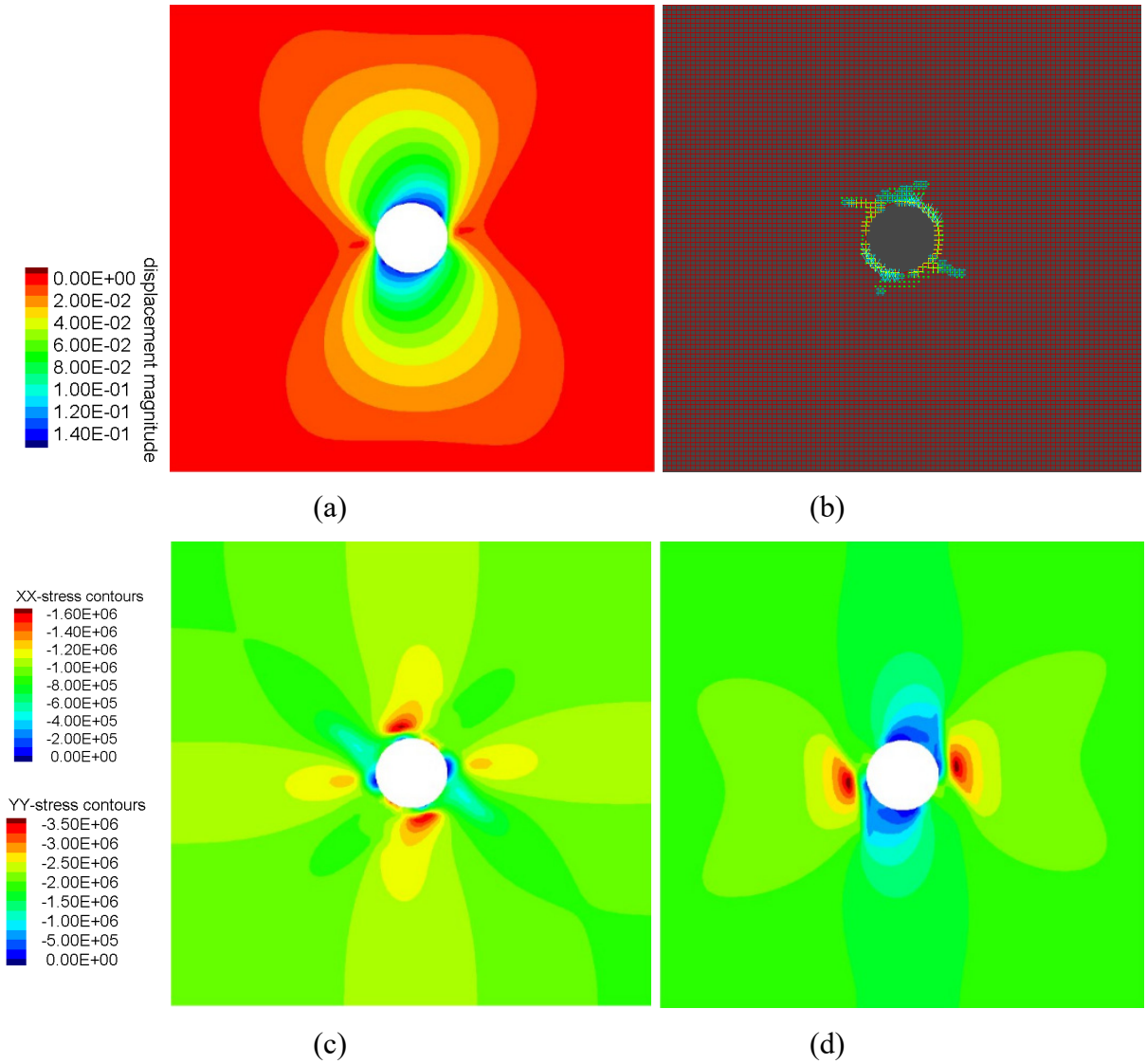

Figure 6.13 Simulation results for tunnel model with two joint sets (45° and -60°) and κ = 2: (a) displacement contours [m], (b) plasticity state, (c) contour plot of horizontal stresses [Pa] and (d) contour plot of vertical stresses [Pa]

Simulation results for κ = 2 and joint angles of 45°/-60° are shown in Figure 6.13. The maximum displacement is 0.14 m (Figure 6.13a). Plastifications extend deeper into the rock mass along four directions (Figure 6.13b). The maximum horizontal stress component is 1.70 MPa and situated at the tunnel roof and invert, the vertical stress component is 3.50 MPa and located at the tunnel sidewalls (Figure 6.13d).

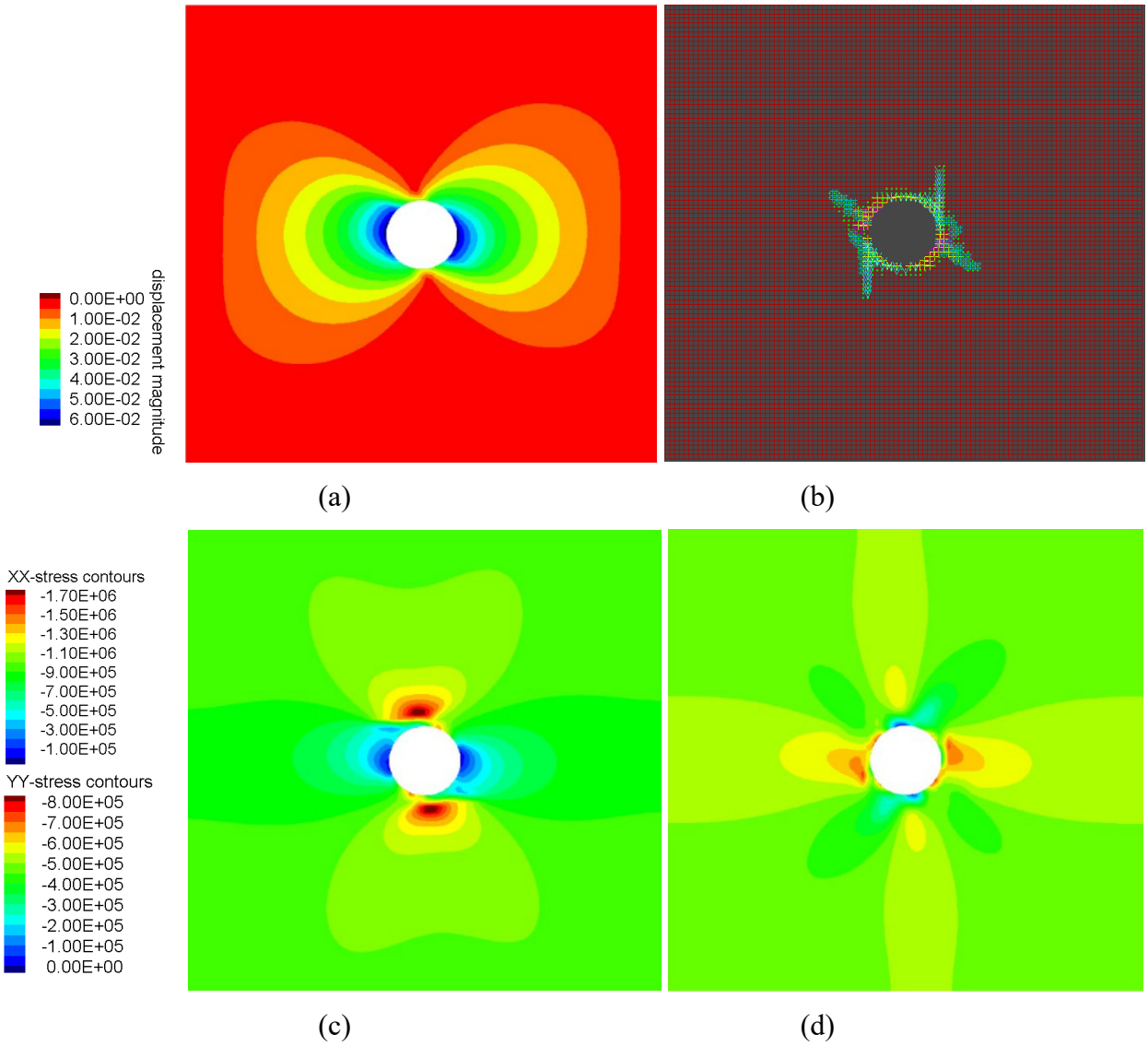

Figure 6.14 Simulation results for tunnel model with two joint sets (45° and -60°) and κ = 0.5: (a) displacement contours [m], (b) plasticity state, (c) contour plot of horizontal stresses [Pa] and (d) contour plot of vertical stresses [Pa]

Simulation results for κ = 0.5 and joint angles of 45°/-60° are shown in Figure 6.14. The maximum displacement is 0.06 m. The horizontal stress is larger than the vertical stress. This failure area corresponds to the two joints orientation (Figure 6.14b). The maximum horizontal stress components is 1.70 MPa and situated at the tunnel roof and invert, the vertical stress component is 0.80 MPa located at the tunnel sidewalls (Figure 6.14d).

6.4 Conclusions

Two simple applications, a slope and a tunnel, are used to test the new developed multi-joint model. For comparison one single joint set and two crossing joint sets were considered as well as pure matrix behavior without joints. It is found, that failure mode, deformation pattern and FOS predicted by the multi-joint model are influenced by the joint orientation and spacing as well as the corresponding strength and stiffness parameters. The simulations of the circular tunnel subjected to isotropic and anisotropic in-situ stresses showed the influence of stress field and joint orientations. The simple models showed reasonable results using the new developed multi-joint constitutive law, although a rigorous verification or validation was not performed.

7 Conclusions and outlook

7.1 Conclusions

In this thesis, the anisotropy behavior of interconnected jointed rock masses has been investigated based on numerical simulations and lab tests. An equivalent continuum based anisotropic model has been implemented into FLAC for the stress-strain analysis of jointed rock masses containing up to three randomly oriented persistent joint sets. The equivalent compliance matrix of the rock mass has been deduced and the Mohr-Coulomb yield criterion has been used to check the failure characteristics of the intact rock and the joints. A series of uniaxial compressive tests on special artificial rock-like materials (gypsum) have been carried out in the lab. The corresponding numerical simulations have not only demonstrated the strength anisotropy response of jointed samples, but also delivered insight into the failure patterns of the specimens. Thus, through these analyses, the following conclusions can be drawn:

(1) The strength anisotropy behavior of the jointed rock mass is closely related to the direction of loading relative to the orientation of discontinuities. The criterion for failure of the matrix and the joints is a Mohr-Coulomb yield criterion with tension cut-off with non-associated shear flow rule and associated tension flow rule. By extensive testing of interconnected joints, it is shown that the multi-joint formulation is as accurate as the discrete method in predicting the strength anisotropy of rock mass with one, two or three joints. Considering the computational efficiency of the method, it can be argued that the intrinsic characteristic of the continuum model leads to a high computationally efficiency.

(2) The potential of yield in the joints and in the rock matrix was considered. Due to the independent Coulomb strength parameters of the joints, the failure envelope of a rock mass can be quite different. Since violation of multiple plasticity surfaces can occur within one calculation step, a consistent elasto-plastic algorithm which automatically identifies the activated surfaces was applied.

(3) The failure envelop for uniaxial compressive loaded sample with two perpendicular joints is 'W' shaped and strongly influenced by joint orientation and joint parameters as illustrated. By a large number of tests such as triaxial compressive, uniaxial compressive and pure tensile simulations, it was shown that the developed multi-joint model exhibits consistent behavior and allows reasonable predictions for the behavior of jointed rock masses.

(4) Rock like material (gypsum) specimens with one or two interconnected joints (with systematically varying interconnected joint orientations and strength parameters) were prepared and tested under uniaxial compressive conditions. Three sample categories containing more than 20 joint angle configurations were considered. For category I samples (single joint) the rock strength is a function of the angle between the main loading direction and the orientation of the joint plane. For category II samples (two joints), geometric composition of the joints controls the rock mass strength. The results of category III (two joints) revealed that anisotropy of a jointed rock not only depends on the joint angle but is also related to the shear strength of the joints. Lab test results were analyzed and compared with continuum and discontinuum based numerical simulations as well as analytical solutions to verify the developed multi-joint model.

(5) The stiffness parameters k_n and joint spacing have a strong influence on the strain magnitude. UCS simulations for samples containing two weakness planes with same strength parameters but different constant minimum joint angles were performed. The failure envelope for samples with two joints are totally different to Jaeger's curve. These curves have their own specific shape and can be used to predict the stability under certain joint angle combinations. Based on the assumptions that the intact rock can be considered as a nearly homogeneous isotropic material and the joints are assumed as smooth, planar and persistent, the modeling results show good agreement with the analytical solutions and the experimental data.

(6) The results of the experiments and simulations revealed three failure mechanisms: plastic failure of the rock matrix; slip on a preferred joint plane; both, slipping and rock matrix failure. Rock matrix failure is mainly observed when orientation of single joint or one of the two joints is nearly perpendicular to the loading direction (angles from 60° to 90°). Specimens with one or more steep joint planes failed by sliding along the steepest joint (joint angle bewteen 35° and 60°).

Normally, no failure of the rock matrix is observed under these circumstances. When the joint plane angle is steep enough (joint angle between 10º to 35º), the joint touches the platens of the uniaxial compressive testing machine, so that joint sliding is mostly prevented and intact rock failure along with very restricted sliding along the joint is observed. The failure type is mainly controlled by strength parameters and joints angles in the sample.

(7) A simplified rock slope model including application of the shear strength reduction technique (SRM) was used to test the new constitutive multi-joint model considering no joint, one joint or two joint sets. Influence of joint spacing, joint parameters and joint orientation on failure pattern was investigated. Also, a circular tunnel in a fractured rock mass was investigated under isotropic and anisotropic in-situ stresses. The mechanical response of a rock mass shows different characteristics in dependence on stress state and joint orientation. Although no rigorous verification or validation was performed, the simulations delivered reasonable results.

7.2 Main contributions of the thesis

- Development of an equivalent continuum model which takes into account up to three joint sets of arbitrary spatial configuration to simulate the anisotropy behaviour of jointed rocks.

- Implementation of a Mohr-Coulomb failure criterion with tension cut-off for intact rock and joints as UDM into the code FLAC including an elasto-plastic algorithm which automatically identifies the activated yield surfaces.

- Comprehensive verification of proposed multi-joint model containing one, two or three joints via uniaxial, triaxial and tensile tests on lab samples, numerical models and analytical solutions.

- Comprehensive verification of sample/model behaviour with joints of different orientations taking into account stress-strain relations and failure patterns.

- Illustration of developed approach on the basis of two simple practical examples.

7.3 Recommendations for future research

Based on the analysis of this research, further work should focus on:

- Extension of the multi-joint model for 3-dimensional analysis with FLAC^{3D}.

- More detailed consideration of the anisotropy in elastic properties due to the existence of joints.

- Developed multi-joint model should be extended to incorporate strain-hardening/softening. Also, roughness of joints should be considered in an explicit manner.

- Additionally, constitutive relations may incorporate thermal and viscous effects.

References

Agharazi, A., Martin, C. D. & Tannant, D. D. (2012). "A three-dimensional equivalent continuum constitutive model for jointed rock masses containing up to three random joint sets." Geomechanics and Geoengineering 7(4): 227-238.

Alireza, A. (2013). "Development of a three-dimensional equivalent continuum model for deformation analysis of systematically jointed rock masses." Doctor dissertation. Department of Civil and Environmental Engineering. University of Alberta: 1-142.

Agharazi, A., Tannant, D. D. & Martin, C. D. (2012). "Characterizing rock mass deformation mechanisms during plate load tests at the Bakhtiary dam project." International Journal of Rock Mechanics and Mining Sciences 49: 1-11.

Allirot, D. & Boehler, J. P. (1979). "Evolution of mechanical properties of a stratified rock under confining pressure." 4th ISRM Congress, Montreux: 15-22.

Arora, V. K. (1987). "Strength and deformational behavior of jointed rocks." Doctor dissertation. Delhi: Indian institute of technology: 1-355

Kim, B. H., Cai, M., Kaiser, P. K. & Yang, H. S. (2007). "Estimation of block sizes for rock masses with non-persistent joints." Rock mechanics and rock engineering 10(2): 169-192.

Bagheripour, M. H. Rahgozar, R., Pashnesaz, H. & Malekinejad, M. (2011). "A complement to Hoek-Brown failure criterion for strength prediction in anisotropic rock." Geomechanics and Engineering 3(1): 61-81.

Bandis, S. C., Lumsden, A. C. & Barton, N. R. (1983). "Fundamentals of rock joint deformation." International Journal of Rock Mechanics and Mining Sciences and Geomechanics Abstracts 20(6): 249-268.

Barton, N. (1986). "Deformation phenomena in jointed rock." Geotechnique 36(2): 147-167.

Barton, N. (2007). "Rock quality, seismic velocity, attenuation and anisotropy." Taylor & Francis Group. CRC Press: 1-756

Baumgarten, L. (2015). "Gesteinsmechanische versuche und petrophysikalische untersuchungen–laborergebnisse und numerische simulationen." Technical University Bergakademie Freiberg:1-205.

Bieniawski, Z. T. (1978). "Determining rock mass deformability: experience from case histories." International journal of rock mechanics and mining sciences & geomechanics abstracts 15(5): 237-247.

Blatt, H., Tracy, R. & Owens, B. (2006). "Petrology: igneous, sedimentary, and metamorphic." W. H. Freeman: 1-530

Bray, J. W. (1967). "A study of jointed and fractured rock." Rock mechanics and engineering geology 5(2-3): 117-136.

Brown, ET. (1970). "Strength of models of rock with intermittent joints." Journal of Soil Mechanics & Foundations Division 96(SM6): 1935-1949.

Brzovic, A. & Villaescusa, E. (2007). "Rock mass characterization and assessment of block-forming geological discontinuities during caving of primary copper ore at the El Teniente mine, Chile." International Journal of Rock Mechanics and Mining Sciences 44(4): 565-583.

Cai, M. & Horii, H. (1992). "A constitutive model of highly jointed rock masses." Mechanics of Materials 13(3): 217-246.

Cai, M., Kaiser, P. K., Tasaka, Y. & Minami, M. (2007). "Determination of residual strength parameters of jointed rock masses using the GSI system." International Journal of Rock Mechanics and Mining Sciences 44(2): 247-265.

Chen, Y., Zhou, C. & Sheng, Y. (2007)."Formulation of strain-dependent hydraulic conductivity for a fractured rock mass." International Journal of Rock Mechanics and Mining Sciences 44(7): 981-996.

Chen, W., Konietzky, H. & Abbas, S. M. (2015). "Numerical simulation of time-independent and-dependent fracturing in sandstone." Engineering Geology 193: 118-131.

Chen, W. & Konietzky, H. (2015, January). "Simulation of Damage Evolution in Rocks Due to Critical and Subcritical Crack Growth." ISRM Regional Symposium-EUROCK 2015, Salzburg: 701-706.

Cheng, Y. M., Lansivaara, T. & Wei, W. B. (2007). "Two-dimensional slope stability analysis by limit equilibrium and strength reduction methods." Computers and Geotechnics 34(3): 137-150.

Chong, W. L., Haque, A., Gamage, R. P. & Shahinuzzaman, A. (2013). "Modelling of intact and jointed mudstone samples under uniaxial and triaxial compression." Arabian Journal of Geosciences 6(5): 1639-1646.

Clark, I. H. (2006). "Simulation of rockmass strength using ubiquitous joints." Numerical Modeling in Geomechanics. 4th International FLAC Symposium, Madrid: 08-07.

Cundall, P. A., Pierce, M. E. & Mas Ivars, D. (2008). "Quantifying the size effect of rock mass strength." Proceedings of the 1st Southern Hemisphere International Rock Mechanics Symposium, Perth: 3-15.

Cundall, P. A. & Hart, R. D. (1992). "Numerical modelling of discontinua." Engineering Computations 9(2): 101-113.

Cundall, P. A. (1971). "The measurement and analysis of accelerations in rock slopes." London, University of London: 1-364

Dawson, E. M. (1995). "Micropolar continuum models for jointed rock." Doctor dissertation, University of Minnesota. Minneapolis: 1-214.

Desai, C. S., Zaman, M. M., Lightner, J. G. & Siriwardane, H. J. (1984). "Thin-layer element for interfaces and joints." International Journal for Numerical and Analytical Methods in Geomechanics 8(1): 19-43.

Detournay, C., Meng, G. & Cundall, P. A. (2016). "Development of a constitutive model for columnar basalt." Applied Numerical Modelling in Geomechanics: 249-264.

Di, S. J., Xu, W. Y. & Shan, Z. G. (2013). "Study of anisotropic equivalent elastic parameters of jointed rock mass." Rock and Soil Mechanics 3: 1-15.

Donzé, F. V., Richefeu, V. & Magnier, S. A. (2009). "Advances in discrete element method applied to soil, rock and concrete mechanics." Electronic Journal of Geotechnical Engineering 8: 1-44.

Donath, F. (1964). "Strength variation and deformational behavior in anisotropic rock." International Conference State of Stress in the Earth's Crust. Santa Monica, California: 281-297.

Edelbro, C. (2003). "Rock mass strength." Dissertation. Lulea University of technology: 1-83.

Edelbro, C., Sjöberg, J. & Nordlund, E. (2007). "A quantitative comparison of strength criteria for hard rock masses." Tunnelling and Underground Space Technology 22(1): 57-68.

Einstein, H. H., Hirschfeld, R. C., Nelson, R. A. & Bruhn, R. W. (1969). "Model studies of jointed-rock behavior." The 11th US Symposium on Rock Mechanics (USRMS), Berkeley: 83-103

Fossum, A. F. (1985). "Effective elastic properties for a randomly jointed rock mass." International Journal of Rock Mechanics and Mining Sciences & Geomechanics Abstracts 22(6): 467-470.

Gerrard, C. M. (1982). "Elastic models of rock masses having one, two and three sets of joints." International Journal of Rock Mechanics and Mining Sciences & Geomechanics 19(1): 15-23.

Gerrard, C. M. (1982). "Equivalent elastic moduli of a rock mass consisting of orthorhombic layers." International Journal of Rock Mechanics and Mining Sciences & Geomechanics Abstracts 19(1): 9-14.

Ghaboussi, J., Wilson, E. L. & Isenberg, J. (1973). "Finite element for rock joints and interfaces." Journal of Soil Mechanics & Foundations Division 99 (10): 849-862.

Ghazvinian, A. & Hadei, M. R. (2012). "Effect of discontinuity orientation and confinement on the strength of jointed anisotropic rocks." International Journal of Rock Mechanics and Mining 55(10): 117-124.

Goodman, R. E. (1976). "Methods of geological engineering in discontinuous rocks." West Information Publishing Group: 1-472.

Goodman, R. E. (1989). "Introduction to rock mechanics." New York: Wiley, 2nd edition: 1-576.

Goodman, R. E., Taylor, R. L. & Brekke, T. L. (1968). "A model for the mechanics of jointed rocks." Journal of Soil Mechanics & Foundations Division 94(3): 637-660

Hammah, R. E., Yacoub, T. E. & Curran, J. H. (2009). "Numerical modelling of slope uncertainty due to rock mass jointing." International conference on rock joints and jointed rock masses. Tucson, Arizona: 7-16.

Hucka, V. (1965). "A rapid method of determining the strength of rocks in situ." International Journal of Rock Mechanics and Mining Sciences & Geomechanics Abstracts 2(2): 127-134.

Hoek, E. (1983). "Strength of jointed rock masses." Geotechnique 33(3): 187-223.

Hoek, E. & Brown, E. T. (1980). "Empirical strength criterion for rock masses." Journal of Geotechnical Engineering Division 106: 1013-1035.

Hoek, E. & Brown, E. T. (1980). "Underground excavations in rock." CRC Press: 1-532.

Hoek, E. & Brown E. T. (1997). "Practical estimates of rock mass strength." International Journal of Rock Mechanics and Mining Sciences 34(8): 1165-1186.

Hoek, E. D., Mark S. (2006). "Empirical estimation of rock mass modulus." International Journal of Rock Mechanics and Mining Sciences 43(2): 203-215.

Huang, J. & Griffiths, D. V. (2009). "Return mapping algorithms and stress predictors for failure analysis in geomechanics." Journal of Engineering Mechanics 135(4): 276-284.

Itasca (2007). "Fast lagrangian analysis of continua, constitutive models." Itasca Consulting Group, Inc. Minneapolis, Minnesota, USA: 1-193.

Itasca (2007). "Fast lagrangian analysis of continua, verification problems, uniaxial compressive strength of a jointed rock sample." Itasca Consulting Group, Inc. Minneapolis, Minnesota, USA: 6-22.

Itasca (2007). "Fast lagrangian analysis of continua, theory and background." Itasca Consulting Group, Inc. Minneapolis, Minnesota, USA: 1-127.

Itasca (2007). "Fast lagrangian analysis of continua, theory and background, choice of material properties." Itasca Consulting Group, Inc. Minneapolis, Minnesota, USA. 2:11-17.

Jade, S. & Sitharam, T. G. (2003). "Characterization of strength and deformation of jointed rock mass based on statistical analysis." International Journal of Geomechanics 3(1): 43-54.

Jaeger, J. (1960). "Shear failure of anistropic rocks." Geological Magazine 97(01): 65-72.

Jaeger, J. C., Cook, N. G. & Zimmerman, R. (2009). "Fundamentals of rock mechanics." Wiley- Blackwell, 4 edition: 1-488.

Jia, P. & Tang, C. A. (2008). "Numerical study on failure mechanism of tunnel in jointed rock mass." Tunneling and Underground Space Technology 23(5): 500-507.

Jing, L. (2003). "A review of techniques, advances and outstanding issues in numerical modelling for rock mechanics and rock engineering." International Journal of Rock Mechanics and Mining Sciences 40(3): 283-353.

Jiang, Y., Li, B. & Tanabashi, Y. (2006). "Estimating the relation between surface roughness and mechanical properties of rock joints." International Journal of Rock Mechanics and Mining Sciences 43(6): 837-846.

Kallu, R. R., Keffeler, E. R., Watters, R. J. & Warren, S. N. (2016). "Development of a highly portable plate loading device and in situ modulus measurements in weak rock masses." Rock Mechanics and Rock Engineering 49(2): 443-454.

Ko, S. C., Olgaard, D. L. & Briegel, U. (1995). "The transition from weakening to strengthening in dehydrating gypsum: Evolution of excess pore pressures." Geophysical Research Letters 22(9): 1009-1012.

Konietzky, H. (2016). "Micromechanical rock models." Rock Mechanics and Rock Engineering: From the Past to the Future. CRC Press: 17-24.

Kulatilake, P. H. S. W., Malama, B. & Wang, J. (2001). "Physical and particle flow modeling of jointed rock block behavior under uniaxial loading." International Journal of Rock Mechanics and Mining Sciences 38(5): 641-657.

Kumar, D. & Das, S. K. (2005). "An experimental study of the parameters influencing ultimate bearing strength of weak floor strata using physical modeling." Geotechnical & Geological Engineering 23(1): 1-15.

Lai, W. M., Rubin, D. H., Rubin, D. & Krempl, E. (2009). "Introduction to continuum mechanics." Elsevier, 4 edition: 1-536.

Le, A. D. & Nguyen, T. S. (2014)."Hydromechanical response of a bedded argillaceous rock formation to excavation and water injection 1." Canadian Geotechnical Journal 52(1): 1-17.

Lee, Y. K. & Pietruszczak, S. (2008). "A new numerical procedure for elasto-plastic analysis of a circular opening excavated in a strain-softening rock mass." Tunnelling and Underground Space Technology 23(5): 588-599.

Lekhnitskii, S. (2011). "Theory of elasticity of an anisotropic body, 1981." Grand Forks, BC, Mir: 1-430.

Li, A. J., Merifield, R. S. & Lyamin, A. V. (2008). "Stability charts for rock slopes based on the Hoek–Brown failure criterion." International Journal of Rock Mechanics and Mining Sciences 45(5): 689-700.

Li, J., Ma, G. & Zhao, J. (2010). "An equivalent viscoelastic model for rock mass with parallel joints." Journal of Geophysical Research: Solid Earth 115 (B3): 1-11.

Lin, H., Cao, P. & Wang, Y. (2013). "Numerical simulation of a layered rock under triaxial compression." International Journal of Rock Mechanics & Mining Sciences 60: 12-18.

Lin, J. S. & Ku, C. Y. (2006). "Two-scale modeling of jointed rock masses." International Journal of Rock Mechanics and Mining Sciences 43(3): 426-436.

Ma, Z., Liao, H., Ning, C. & Feng, Z. (2014). "Stability analysis of a high slope along a loess plateau based on field investigation and numerical analysis." Landslide science for a safer geoenvironment. Springer: 451-458.

Mahabadi, O. K., Lisjak, A., Munjiza, A. & Grasselli, G. (2012). "Y-Geo: new combined finite-discrete element numerical code for geomechanical applications." International Journal of Geomechanics 12(6): 676-688.

Maji, V. B. (2009). "Strength and Deformation behavior of jointed rocks: an equivalent continuum model." Doctoral dissertation. IISc-Bangalore. India.

Marache, A., Riss, J. & Gentier, S. (2008). "Experimental and modelled mechanical behaviour of a rock fracture under normal stress." Rock Mechanics and Rock Engineering 41(6): 869-892.

Min, K. B., Jing, L. & Stephansson, O. (2004). "Determining the equivalent permeability tensor for fractured rock masses using a stochastic REV approach: method and application to the field data from Sellafield, UK." Hydrogeology Journal 12(5): 497-510.

Min, K. B. & Jing, L. (2003). "Numerical determination of the equivalent elastic compliance tensor for fractured rock masses using the distinct element method." International Journal of Rock Mechanics and Mining Sciences 40(6): 795-816.

Misra, A. & Marangos, O. (2010)."Rock-joint micromechanics: relationship of roughness to closure and wave propagation." International Journal of Geomechanics 11(6): 431-439.

Nick, B. (2002). "Some new Q-value correlations to assist in site characterisation and tunnel design." International Journal of Rock Mechanics and Mining Sciences 39(2): 185-216.

Nguyen, V. H. (2013). "Static and dynamic behaviour of joints in schistose rock: lab testing and numerical simulation" Doctoral dissertation. TU Bergakademie Freiberg: 1-173.

Obara, Y. & Ishiguro, Y. (2004). "Measurements of induced stress and strength in the near-field around a tunnel and associated estimation of the Mohr-Coulomb parameters for rock mass strength." International Journal of Rock Mechanics and Mining Sciences 41(5): 761-769.

Oda, M., Yamabe, T., Ishizuka, Y., Kumasaka, H., Tada, H. & Kimura, K. (1993). "Elastic stress and strain in jointed rock masses by means of crack tensor analysis." Rock Mechanics and Rock Engineering 26(2): 89-112.

Owen, D. R. J. & Hinton, E. (1980). "Finite elements in plasticity, (1980)." Pineridge Press Limited, Swansea, UK. 1st edition: 1-450.

Palchik, V. (2006). "Application of Mohr–Coulomb failure theory to very porous sandy shales." International Journal of Rock Mechanics and Mining Sciences 43(7): 1153-1162.

Palmström, A. & Singh, R. (2001). "The deformation modulus of rock masses-comparisons between in situ tests and indirect estimates." Tunneling and Underground Space Technology 16(2): 115-131.

Pande, G., Beer, G. & Williams, J. (1990). "Numerical methods in rock mechanics." Wiley, University of California: 1-327.

Prudencio, M. & Jan, M. V. S. (2007). "Strength and failure modes of rock mass models with non-persistent joints." International Journal of Rock Mechanics and Mining Sciences 44(6): 890-902.

Rafiai, H. & Jafari, A. (2011). "Artificial neural networks as a basis for new generation of rock failure criteria." International Journal of Rock Mechanics and Mining Sciences 48(7): 1153-1159.

Ramamurthy, T. (1993). "Strength and modulus responses of anisotropic rocks." Comprehensive Rock Engineering 1(13): 313-329.

Ramamurthy, T. (2004). "A geo-engineering classification for rocks and rock masses." International Journal of Rock Mechanics and Mining Sciences 41(1): 89-101.

Ramamurthy, T. & Arora, V. K. (1994). "Strength predictions for jointed rocks in confined and unconfined states." International Journal of Rock Mechanics and Mining Sciences And Geomechanics Abstracts 31(1): 9-22.

Riahi, A. (2008). "3D Finite Element Cosserat Continuum Simulation of Layered Geomaterials." Doctor dissertation, University of Toronto: 1-192.

Riahi, A., Hammah, E. R. & Curran, J. H. (2010, January). "Limits of applicability of the finite element explicit joint model in the analysis of jointed rock problems." 44th US Rock Mechanics Symposium and 5th US-Canada Rock Mechanics Symposium. Salt Lake City.

Sagong, M., Park, D., Yoo, J. & Lee, J. S. (2011). "Experimental and numerical analyses of an opening in a jointed rock mass under biaxial compression." International Journal of Rock Mechanics and Mining Sciences, 48(7): 1055-1067.

Sainsbury, B., Pierce, M. & Mas Ivars, D. (2008). "Simulation of rock mass strength anisotropy and scale effects using a Ubiquitous Joint Rock Mass (UJRM) model." International FLAC/DEM Symposium on Numerical Modelling, Minneapolis, USA: 25-27.

Salager, S., François, B., Nuth, M. & Laloui, L. (2013). "Constitutive analysis of the mechanical anisotropy of Opalinus Clay." Acta Geotechnica 8(2): 137-154.

Scholtès, L. U. C. & Donzé, F. V. (2012). "Modelling progressive failure in fractured rock masses using a 3D discrete element method." International Journal of Rock Mechanics and Mining Sciences 52: 18-30.

Scholtès, L. U. C. & Donzé, F. V. (2013). "A DEM model for soft and hard rocks: role of grain interlocking on strength." Journal of the Mechanics and Physics of Solids 61(2): 352-369.

Shen, B., Stephansson, O., Einstein, H. H. & Ghahreman, B. (1995). "Coalescence of fractures under shear stresses in experiments." Journal of Geophysical Research Atmospheres. 100(B4): 5975-5990.

Shi, G. H. (1996). "Simplex integration for manifold method, FEM, DDA and analytical analysis." The First International Forum on Discontinuous Deformation Analysis (DDA) and Simulations of Discontinuous Media, Berkeley: 205-262.

Shi, G. H. (2002). "Single and multiple block limit equilibrium of key block method and discontinuous deformation analysis." 5th International Conference on Analysis of Discontinuous Deformation. Beer Sheva, Israel: 3-46.

Shi, G. H. (1992). "Discontinuous deformation analysis: a new numerical model for the statics and dynamics of deformable block structures." Engineering computations 9(2): 157-168.

Simo, J. C., Kennedy, J. G. & Govindjee, S. (1988). "Non-smooth multisurface plasticity and viscoplasticity. Loading/unloading conditions and numerical algorithms." International Journal for Numerical Methods in Engineering 26(10): 2161-2185.

Simo, J. C. & Hughes, T. J. (2006). "Computational inelasticity." Springer Science & Business Media: 240-271

Singh, M. & Rao, K. S. (2005). "Empirical methods to estimate the strength of jointed rock masses." Engineering Geology 77(1): 127-137.

Singh, B. (1973). "Continuum characterization of jointed rock masses: Part I the constitutive equations." International Journal of Rock Mechanics and Mining Sciences & Geomechanics Abstracts 10(4): 311-335.

Singh, M., Rao, K. S. & Ramamurthy, T. (2002). "Strength and deformational behaviour of a jointed rock mass." Rock Mechanics and Rock Engineering 35(1): 45-64.

Singh, M. (2000). "Applicability of a constitutive model to jointed block mass." Rock Mechanics and Rock Engineering 33(2): 141-147.

Singh, R. K. & Dev, C. (1988). "Strength and modulus tests on jointed specimens of plaster of Paris." M. Tech Thesis, IIT-Delhi, India.

Sitharam, T. G., Maji, V. B. & Verma, A. K. (2007). "Practical equivalent continuum model for simulation of jointed rock mass using FLAC3D." International Journal of Geomechanics 7(5): 389-395.

Sitharam, T. G., Sridevi, J. & Shimizu, N. (2001). "Practical equivalent continuum characterization of jointed rock masses." International Journal of Rock Mechanics and Mining Sciences 38(3): 437-448.

Taheri, A. & Tani, K. (2008). "Development of an apparatus for down-hole triaxial tests in a rock mass." International Journal of Rock Mechanics and Mining Sciences 45(5): 800-806.

Timoshenko, S. P. & Goodier, J. N. 1970, "Theory of Elasticity." McGraw-Hill College: 1-608.

Tiwari, R. P. & Rao, K. S. (2004). "Physical modeling of a rock mass under a true triaxial stress state." International Journal of Rock Mechanics and Mining Sciences 41: 396-401.

Tien, Y. M. & Tsao, P. F. (2000). "Preparation and mechanical properties of artificial transversely isotropic rock." International Journal of Rock Mechanics and Mining Sciences 37(6): 1001-1012.

Tan, X. & Konietzky, H. (2017). "Numerical Study of Biot's Coefficient Evolution During Failure Process for Aue Granite Using an Empirical Equation Based on GMR Method." Rock Mechanics and Rock Engineering: 1-7.

Ünal, E. (1997). "Determination of in situ deformation modulus: new approaches for plate-loading tests." International Journal of Rock Mechanics and Mining Sciences 34(6): 897-915.

Verma, A. K. & Singh, T. N. (2010). "Assessment of tunnel instability—a numerical approach." Arabian Journal of Geosciences 3(2): 181-192.

Vychytil, J. & Horii, H. (1998). "Micromechanics-based continuum model for hydraulic fracturing of jointed rock masses during HDR stimulation." Mechanics of Materials 28(1): 123-135.

Walhlstrom, E. (1973). "Tunneling in rock." Amsterdam. Elsevier 1st Edition. Development in Geotechnical Engineering: 1-263.

Walton, O. R. (1993). "Numerical simulation of inelastic, frictional particle-particle interactions." Mechanics of Materials 25: 884-907

Wang, T. T. & Huang, T. H. (2009). "A constitutive model for the deformation of a rock mass containing sets of ubiquitous joints." International Journal of Rock Mechanics and Mining Sciences 46(3): 521-530.

Wang, T. T. & Huang, T. H. (2014). "Anisotropic deformation of a circular tunnel excavated in a rock mass containing sets of ubiquitous joints: theory analysis and numerical modeling." Rock mechanics and rock engineering 47(2): 643-657.

Will, J. (1999). "Beitrag zur Standsicherheitsberechnung im geklüfteten Fels in der Kontinuums- und Diskontinuumsmechanik unter Verwendung impliziter und expliziter Berechnungsstrategien." Doctor dissertation. Bauhaus-Univ Weimar: 1-137.

Will, J., &T. Bai (2015). "Dynardo technology and applications to well completion optimization for unconventionals." ANSYS Convergence Conference. Houston: 1-29.

Wittke, W. (1984): Felsmechanik – Grundlage des wirtschaftlichen Bauens im Fels, Springer, 1-1051

Wittke, W. (1990): Rock Mechanics – Theory and Applications with Case Histories, Springer, 1-1075

Wong, N., &H. Einstein (2007). "Crack coalescence in molded gypsum and Carrara marble." AGU Fall Meeting Abstracts. MIT: 1-875.

Xiao, W., Deng, R. & Fu, X. (2014). "Model experiments on deformation and strength anisotropy of columnar jointed rock masses under uniaxial compression." Chinese Journal of Rock Mechanics and Engineering 33(5): 957-963.

Xiuli, D. I. N. G., Yaoxu, L. I. & Xin, W. A. N. G. (2010). "Particle flow modeling mechanical properties of soil and rock mixtures based on digital image." Chinese Journal of Rock Mechanics and Engineering 29(3): 477-484.

Xu, T., Ranjith, P. G., Wasantha, P. L. P., Zhao, J., Tang, C. A. & Zhu, W. C. (2013). "Influence of the geometry of partially-spanning joints on mechanical properties of rock in uniaxial compression." Engineering Geology 167: 134-147.

Xu, Q., Chen, J., Li, J., Zhao, C. & Yuan, C. (2015). "Study on the constitutive model for jointed rock mass." PloS one 10(4): 1-20.

Yang, W., Zhang, Q., Li, S. & Wang, S. (2014). "Estimation of in situ viscoelastic parameters of a weak rock layer by time-dependent plate-loading tests." International Journal of Rock Mechanics and Mining Sciences 66: 169-176.

Yang, X. L. & Yin, J. H. (2006). "Linear Mohr–Coulomb strength parameters from the non-linear Hoek–Brown rock masses." International Journal of Non-Linear Mechanics 41(8): 1000-1005.

Yang, Z. Y., Chen, J. M. & Huang, T. H. (1998). "Effect of joint sets on the strength and deformation of rock mass models." International Journal of Rock Mechanics and Mining Sciences 35(1): 75-84.

Yoshida, H. & Horii, H. (2004). "Micromechanics-based continuum model for a jointed rock mass and excavation analyses of a large-scale cavern." International Journal of Rock Mechanics and Mining Sciences 41(1): 119-145.

Zhang, Yujun. (2006). "Equivalent model and numerical analysis and laboratory test for jointed rock masses." Chinese Journal of Geotechnical Engineering 28(1): 29-32.

Zhao, J. (2000). "Applicability of Mohr-Coulomb and Hoek-Brown strength criteria to the dynamic strength of brittle rock." International Journal of Rock Mechanics & Mining Sciences 37(7): 1115-1121.

Zienkiewicz, O. C., Humpheson, C. & Lewis, R. W. (1977). "Discussion: Associated and non-associated visco-plasticity and plasticity in soil mechanics." Geotechnique 27(1): 101-102.

Zienkiewicz, O. C. & Parekh, C. J. (1970). "Transient field problems: two ‐ dimensional and three ‐ dimensional analysis by isoparametric finite elements." International Journal for Numerical Methods in Engineering 2(1): 61-71.

Appendix

Multi-joint model: FLAC ***keywords***

The "multi-joint" model can be loaded in FLAC using the following commands:

config cppudm

model load modelmultijoint.dll (for FLAC version 8.0)

model multijoint

A list of model specific keywords follows:

Parameters for intact rock

bulk_mod	elastic bulk modulus, K [Pa]
shear_mod	elastic shear modulus, G [Pa]
cohesion	cohesion, c [Pa]
dilation	dilation angle , ψ [°]
density	mass density, ρ [kg/m³]
friction	friction angle, ϕ [°]
tension	tension limit, σ^t [Pa]

Parameters for joint set 1

j1angle	joint 1 angle taken counterclockwise from x axis, α_1 [°]
j1cohesion	joint 1 cohesion, c_j^1 [Pa]
j1dilation	joint 1 dilation angle , ψ_j^1 [°]
j1friction	joint 1 friction angle, ϕ_j^1 [°]
j1tension	joint 1 tension limit, $\sigma_j^{t,1}$ [Pa]

Parameters for joint set 2

j2angle	joint 2 angle taken counterclockwise from x axis, α_2 [°]
j2cohesion	joint 2 cohesion, c_j^2 [Pa]
j2dilation	joint 2 dilation angle , ψ_j^2 [°]
j2friction	joint 2 friction angle, ϕ_j^2 [°]
j2tension	joint 2 tension limit, $\sigma_j^{t,2}$ [Pa]

Parameters for joint set 3

j3angle	joint 3 angle taken counterclockwise from x axis, α_3 [°]
j3cohesion	joint 3 cohesion, c_j^3 [Pa]
j3dilation	joint 3 dilation angle , ψ_j^3 [°]
j3friction	joint 3 friction angle, ϕ_j^3 [°]
j3tension	joint 3 tension limit, $\sigma_j^{t,3}$ [Pa]

Parameters for stiffness

kn1	normal stiffness of joint set 1 [Pa/m]
kn2	normal stiffness of joint set 2 [Pa/m]
kn3	normal stiffness of joint set 2 [Pa/m]
spac1	spacing of joint set 1 [m]
spac2	spacing of joint set 2 [m]
spac3	spacing of joint set 3 [m]

```
;*** small example of input: multi-joint model****
new
config cppudm
model load modelmultijoint.dll
g 10 15
gen 0,0 0,0.15 0.1,0.15 0.1,0
        mo multijoint
        pro den 1810 bulk 1.284e10 she 8.077e9 fric 21.2 co 9.1e6 ten 2.26e6 dilation 10
        prop j1co 1.5e6   j1fric 32.8   j1ang 0  j1ten 3e5
        prop j2co 1.5e6   j2fric 32.8   j2ang 90  j2ten 3e5
       step 8000
end
……
```